Engineered bimetallic catalysts for energy and environment applications

by

Jing Shen

A thesis submitted in partial fulfillment of the requirements for the degree of

Doctor of Philosophy

in

Chemical Engineering

Department of Chemical and Material Engineering

University of Alberta

© Jing Shen, 2015

Abstract

Bimetallicity is known to provide synergistic effects and improve catalytic performance of monometallic counterparts in a variety of applications. Conventional impregnation methods for supported catalyst preparation do not allow for the control of bimetallic nanoparticle structure or size, which often leads to considerable difficulties when evaluating metal functions or possible synergism. The presented thesis involves the preparation of bimetallic catalysts with well-defined structures by controlled synthesis of nanoparticles in the presence of a steric stabilizer with the objective of gaining insight into bimetallic effects in selected catalytic reactions. Tightening environmental regulations as well as the increasing demand for premium fuels governed the choice of catalytic applications in this study. Bimetallic catalysts were developed and tested in: (1) low-pressure ring opening of indan as a model reaction in fuel upgrading, (2) hydrodesulfurization of 4,6-dimethyl-dibenzothiophene for the production of ultra-low sulfur fuels, and (3) methane combustion to reduce the greenhouse gas emissions from natural gas vehicles.

Depending on the catalytic application and bimetallic system used, the fate of bimetallic catalysts in the reaction environment and catalytic consequences were found to follow different scenarios.

The first demonstrated example (Pd−Ru catalysts for indan ring opening) showed that a certain bimetallic nanoparticle synthetic strategy allows developing the bimetallic system with such composition and properties that it can be used to replace rare and expensive iridium, known for its outstanding hydrogenolysis performance. A 3-fold and a 2-fold increase in the selectivities toward 2-ethyltoluene and *n*-propylbenzene, respectively, in indan ring opening were achieved by introducing Pd to Ru catalysts. The Ru−Pd system is envisioned as a suitable alternative to the Ir−Pt system for selective hydrogenolysis.

The fate of structure-controlled systems used in a reductive atmosphere of indan hydrogenolysis was different under oxidative conditions. While Pd−Ru catalysts with different surface compositions revealed distinctively different behaviors in indan RO at 350 °C, in methane combustion up to 550 °C such structure control was unnecessary: Originally different structures demonstrated identical activity because of their structural transformation into one structure.

The third scenario of bimetallic effects showed that significant improvements in catalytic behavior could be achieved without intrinsic alloyed nanostructures, even by a mere coexistence of two monometallic particles. The controlled synthesis of the nanoparticles, however, is still paramount. Traditional impregnation and colloidal techniques of bimetallic catalyst preparation yielded monometallic Pd particles on a binary $NiAl_2O_4$ support and Pd and Ni nanoparticles on the parent γ-Al_2O_3, respectively. The colloidal catalyst showed outstanding performance in wet methane combustion versus the conventional one. The catalyst is thus potentially valuable for natural gas catalytic combustion technologies because it dramatically decreased the required temperature for methane combustion with water presence in the feed versus monometallic Pd.

The final addressed bimetallic effect included the improvement of sintering resistance upon metal alloying. The stability enhancement toward Pd sintering was achieved by alloying Ru to a Pd catalyst. The dispersion is responsible for the enhancement of the direct desulfurization (DDS) rate in the hydrodesulfurization of a refractory sulfur compound. A study of the Pd size effect on selectivities confirmed that DDS selectivity depends on Pd dispersions.

Thus, for the majority of applications and catalytic systems, the synergistic effects between two metals were evaluated. Because the nanoparticles were synthesized in the presence of a polymeric stabilizer, its effect on the final catalytic performance was also addressed. The necessity for complete polymer removal depends on the nature of the active metal and also the catalyzed reaction involved. The activities of PVP-stabilized Ru and Ir nanoparticles in an indan RO were not affected by the residual polymer.

To conclude, bimetallic catalysts with improved catalytic performance over conventional catalysts were developed for Pt- and Ir-free ring opening for fuel upgrading, low-temperature wet methane combustion for applications in natural gas vehicles, and ultra-deep hydrodesulfurization of a refractory sulphur compound. The study showed the advantages and limitations of the structure-controlled catalyst preparation, i.e., the ability to save rare and expensive catalysts by replacing them with alternative metals with similar catalytic behavior; the bimetallic nanoparticle stability and structural evolution under reaction conditions; and the effect of a nanoparticle stabilizer on the catalytic functions.

Preface

The introduction in Chapter 1 contains literature review related to the presented research works.

Chapter 2 of the thesis has been published as: J. Shen and N. Semagina, "Iridium- and platinum-free ring opening of indan", *ACS Catalysis* 4 (2014) 268-279. The reaction setup for low-pressure indan ring opening was built by Dr. Cindy-Xing Yin and Dr. Kavithaa Loganathan in collaboration with machine shop and instrument shop in the department of Chemical and Material Engineering, University of Alberta. Dr. Dimitre Karpuzov performed XPS analysis at Alberta Centre for Surface Engineering and Science (ACSES), University of Alberta. NAA analysis was performed by Becquerel Laboratories Inc., Maxxam Analytics, Ontario. The author performed all syntheses, reactions, analyses and other characterizations.

Chapter 3 of the thesis has been published as: J. Shen, H. Ziaei-Azad and N. Semagina, "Is it always necessary to remove a metal nanoparticle stabilizer before catalysis", *Journal of Molecular Catalysis A: Chemical* 391 (2014) 36-40. Dr. Dimitre Karpuzov performed XPS analysis at Alberta Centre for Surface Engineering and Science (ACSES), University of Alberta. The coauthor, Dr. Hessam Ziaei-Azad, performed indan-TPD and CO-TPD experiments. Shiraz Merali performed XRD analysis at the department of Chemical and Material Engineering, University of Alberta. NAA analysis was performed by Becquerel Laboratories Inc., Maxxam Analytics, Ontario. The author performed all syntheses, reactions, analyses and other characterizations.

Chapter 4 of the thesis has been published as: J, Shen, R. E. Hayes, X. Wu and N. Semagina, "100° temperature reduction of wet methane combustion: highly active Pd−Ni/Al_2O_3 catalyst versus Pd/$NiAl_2O_4$", *ACS Catalysis* 5 (2015) 2916-2920. The reaction setup for methane oxidation was originally designed and built by Dr. Long Wu and Dr. Robert E. Hayes. The developed catalysts were tested in methane oxidation with collaboration with a master student, Xiaoxing Wu. Methane oxidation experiments performed by Xiaoxing Wu are: Pd-COL at 450 °C, $PdNi_{12}$-COL at 375, 400 and 415 °C, and $PdNi_{12}$-IMP at 450 °C. Dr. Xuejun Sun collected HRTEM images of $PdNi_{12}$-COL catalyst at the department of Oncology, Alberta Cross Cancer Institute, University of Alberta. Dr. Dimitre Karpuzov performed XPS analysis at Alberta Centre for Surface Engineering and Science (ACSES), University of Alberta. NAA analysis was performed by Becquerel Laboratories Inc., Maxxam Analytics, Ontario. The author performed all syntheses, most of the reactions, analyses and other characterizations.

Chapter 5 of the thesis has been submitted to Applied Catalysis A: General as: "Structural evolution of bimetallic Pd−Ru catalysts in oxidative and reductive applications", J. Shen, R. W. J. Scott, R. E. Hayes and N. Semagina, *Applied Catalysis A: General* (2015). The reaction setup for methane oxidation was originally designed and built by Dr. Long Wu and Dr. Robert E. Hayes. The EXAFS work was performed with technical support by Dr. Ning Chen at the Canadian Light Source, Saskatchewan and Dr. Robert W.J. Scott (and his PhD student, Atal Shivhare) at University of Saskatchewan, Saskatchewan. Dr. Robert W. J. Scott provided training on IFEFFIT software package for EXAFS data processing, as well as collaborated with EXAFS modeling. Dr. Xuehai Tan collected HRTEM images and performed SAED analyses at University of Alberta. Shiraz Merali performed XRD analysis at the department of Chemical and Material Engineering, University of Alberta. NAA analysis was performed by Becquerel Laboratories Inc., Maxxam Analytics, Ontario. The author performed all syntheses, reactions, analyses and other characterizations.

Chapter 6 of the thesis was written as a paper manuscript as "Enhancement of direct desulfurization in the hydrodesulfurization of a refractory sulfur compound", J. Shen and N. Semagina; and it will be submitted for a publication in a due course. The high pressure reaction setup for hydrodesulfurization was built by Dr. Long Wu and Dr. Hessam Ziaei-Azad. The lab view program to communicate with reaction setup was written by Les Dean. Shiraz Merali performed XRD analysis at the department of Chemical and Material Engineering, University of Alberta. NAA analysis was performed by Becquerel Laboratories Inc., Maxxam Analytics, Ontario. The author performed all syntheses, reactions, analyses and other characterizations.

Dr. Natalia Semagina, my supervisor, provided discussions and feedbacks on experimental results, and comments and revisions for all writing work including the present thesis. Dr. Robert E. Hayes and Dr. Robert W. J. Scott provided discussions and feedbacks on methane oxidation and EXAFS analysis, respectively. The rest of the research works, such as experiments, data collection, analysis and interpretation of the experimental results, as well as writing the papers or manuscripts are my own work.

The present thesis includes research projects funded by Institute of Oil Sands Innovation at the University of Alberta (IOSI), Natural Sciences and Engineering Research Council of Canada (NSERC) and Canada Foundation for Innovation.

Dedication

To my beloved mom and dear husband

Acknowledgements

I would like to sincerely thank my supervisor, **Dr. Natalia Semagina**, for her supervision, advices, helps and patience throughout these years. She offered me the opportunity to join her research group and provided brilliant knowledge on catalysis during my PhD program.

I would also love to express my gratitude to:

The committee for my PhD candidacy examination: **Dr. Jingfeng Liu** (Chair), **Dr. Natalia Semagina** (supervisor), **Dr. Arno de Klerk** (supervisory committee), **Dr. Dominic Sauvageau** (supervisory committee), **Dr. Greg Dechaine** (examiner) and **Dr. Yang Liu** (examiner, Civil and Environmental Engineering), for their valuable questions and comments on the early stage of my research.

The committee for my PhD defense: **Dr. Thomas Thundat** (Chair), **Dr. Natalia Semagina** (supervisor), **Dr. Arno de Klerk** (supervisory committee), **Dr. Dominic Sauvageau** (supervisory committee), **Dr. Leijun Li** (examiner, Material Engineering) and **Dr. Ying Zheng** (external examiner, University of New Brunswick) for their valuable questions and comments on the thesis.

Dr. Robert E. Hayes, Professor, Department of Chemical and Material Engineering, University of Alberta, for his knowledge on methane oxidation in the applications of exhaust emission treatment and natural gas heaters.

Dr. Robert W.J. Scott, Associate Professor, Department of Chemistry, University of Saskatchewan, for performing EXAFS analysis, on-site training on EXAFS analysis and modeling, and providing helps in many ways for EXAFS studies.

Dr. Long Wu, for his contribution to the improvement on low-pressure indan ring opening setup and building up the high-pressure hydrodesulfurization system, as well as the discussions and advices in reactor design, catalysis, and other related topics. He is always ready to give me a helping hand whenever I was facing a problem. He was my colleague and is a friend in life.

Dr. Hessam Ziaei-Azad, graduated from Department of Chemical and Material Engineering, University of Alberta, for the team work and sharing experiences and knowledge in the area of reaction engineering, as well as the memorable moments spent throughout our PhD programs. He was my colleague and also is my friend in life.

Dr. Dimitre Karpuzov, **Dr. Shihong Xu** and **Dr. Anqiang He**, Centre for Surface Engineering and Science, University of Alberta, for performing XPS analysis. Special thank to Dr. Shihong Xu, for the one-to-one advice and guidance on XPS peak deconvolution using CasaXPS software.

Dr. Xuejun Sun, and his colleagues, Department of Oncology, Alberta Cross Cancer Institute, University of Alberta, for the training on TEM and performing HRTEM analysis.

Shiraz Merali, Department of Chemical and Material Engineering, University of Alberta, for providing XRD analysis and training on XRD peak identification and data processing using MDI Jade 9.0 software and ICDD database.

Xiaoli Tan and **Jeremiah Bryksa**, Institute for Oil sands Innovations (ISOI), University of Alberta, for providing supports, trainings and helps throughout my entire PhD program.

Ni Yang, Oil Sands and Coal Interfacial Engineering Facility, University of Alberta, for the training and discussion with DRIFTS studies.

Simona Vatamanescu, Becquerel Laboratory of Maxxam Analytics, Ontario, for NAA analysis and providing the analytical conditions.

My colleagues, **Allen Reule** (PhD candidate), **Hanieh Nassiri** (PhD candidate) and **Xiaoxing Wu** (Master student) at Department of Chemical and Material Engineering, University of Alberta, for the helps they provided while working in the lab and the sweet moments we spent together. Special thank to **Xiaoxing Wu** for the collaboration in methane combustion project.

My dear friends, **Dr. Xuehai Tan** and **Ran Ma**, graduated from Department of Chemical and Material Engineering, University of Alberta, for their time and discussion in the area of catalysis and characterizations. Special thank to **Dr. Xuehai Tan**, for collecting HRTEM images and performing SAED analysis.

My dear friend, **Dr. Shaofeng Yang**, Research Associate, Department of Chemical and Material Engineering, University of Alberta, for providing troubleshooting solutions for GC operational problems and advices on instrument maintenances, as well as general knowledge of laboratory equipment, materials, and etc.

Lily Laser, Walter Boddez, **Les Dean**, **Kevin Heidebrecht**, **Andree Koenig** and all other staff at Department of Chemical and Material Engineering, University of Alberta, for their helps and supports.

Financial supports from the **Institute of Oil Sands Innovation (IOSI)** at the University of Alberta, **Natural Sciences and Engineering Research Council of Canada (NSERC)** and **Canada Foundation for Innovation** are gratefully acknowledged.

Table of content

List of Schemes

List of Figures

List of Tables

Nomenclature

d	Mean diameter of nanoparticles
σ	Standard deviation
σ^2	Disorder parameter
ΔE^0	Energy shift parameter
N	Coordination number
R_j	Interatomic distance
R-factor	A measurement of the quality of EXAFS fit
χ	EXAFS function

Abbreviations

AAS	Atomic absorption spectroscopy
ACSES	Alberta centre for surface engineering and science
BT	Benzothiophene
c	core
CGO	Coker gas oil
CN	Cetane number
COL	Colloids
CTAB	cetyltrimethylammonium bromide
DBT	Dibenzothiophene
DDS	Direct desulfurization
DFT	Density functional theory
HYD	Hydrogenation
DMBCH	Dimethyl-bicyclohexyl
DMBP	Dimethyl-biphenyl
DMCHB	Dimethyl-cyclohexylbenzene
DMDBT	Dimethyl-dibenzothiophene
DMHHDBT	Dimethyl-hexahydro-dibenzothiophene
DMPHDBT	Dimethyl-perhydro-dibenzothiophene
DMTHDBT	Dimethyl-tetrahydro-dibenzothiophene
DRIFTS	Diffuse reflectance infrared fourier transform spectroscopy

EDS	Energy dispersive X-ray spectroscopy
EELS	Electron energy loss spectroscopy
EG	Ethylene glycol
EPA	Environmental protection agency
Et	Ethanol
EtOH	Ethanol
EXAFS	Extended X-ray absorption fine structure spectroscopy
XANES	X-ray absorption near edge structure
fcc	Face-centered cubic
FE-TEM	Field emission-transmission electron microscopy
FID	Flame ionization detector
FTIR	Fourier transform infrared spectroscopy
GC	Gas chromatography
G4OH	Generation 4 poly(amidoamine)-hydroxyl dendrimer
hcp	Hexagonal close packing
HDS	Hydrodesulfurization
HRTEM	High resolution transmission electron microscopy
HXMA	Hard X-ray microanalysis
IMP	Impregnation
LCO	Light cycle oil
M	Metal
MBA	2-methylbutan-2-ol
MBE	2-methyl-3-buten-2-ol
MCH	Methylcyclohexane
MCP	Methylcyclopantene
MS	Mass spectrometry
MW	Molecular weight
N	Coordination number
NAA	Neutron activation analysis
NGV	Natural gas fueled-vehicle
ON	Octane number

PAMAM	Polymidoamine
PM	Particulate matter
PVP	Poly-(vinylpyrrolidone)
RO	Ring opening
s	shell
surf	surface
SAED	Selected area electron diffraction
SRGO	Straight run gas oil
STEM	Scanning transmission electron microscopy
TEM	Transmission electron microscopy
TCD	Thermal conductivity detector
TOF	Turn over frequency
TPD	Temperature programmed desorption
TPR	Temperature programmed reduction
TTAB	Tetradecyltrimethylammonium bromide
ULSD	Ultra-low sulfur diesel
UV	Ultraviolet
WHSV	Weight hourly space velocity
XPS	X-ray photoelectron spectroscopy
XRD	X-ray powder diffraction

Chapter 1. Introduction

1.1. Motivation and objective

Due to the rapidly growing demand of oil, natural gas and other energy sources, especially in the developing countries, such as China and India, the earth population is consuming 30% more resources than the earth can actually replenish each year, as reported by the Living Planet [1]. The crude oils in the earth are depleted. The remaining heavy crude oil contains significant amounts of aromatics, nitrogen, sulfur, oxygen and heavy metals. As a consequence of the dramatically booming economy from the past decades, environmental issues have become a critical threat of our everyday beings. Automobiles and power generation emissions contribute to air pollutions, and are major ingredients of "smog" in industrialized cities. Fine particulate matter ($PM_{2.5}$), the key contributor of the smog, is formed by the combination of NO_x, SO_x, NH_3 and volatile organic compounds (VOCs), etc. [2].

The effective control of global environmental issues requires adequate government regulations collaborated with industrial compliance [2]. Strict regulations on diesel fuel quality have been set all over the world, for example, 15 ppm sulfur specification in North America [3, 4] and 10 ppm sulfur in Europe [5], with a maximum polyaromatic hydrocarbon contents at 35 vol.% [6]. In China, a sulfur level less than 350 ppm has been available nationwide since 2011 with some cities and regions following Euro 4 and 5 standards (50 and 15 ppm sulfur, respectively) [7, 8]. A worldwide production of premium fuels is an achieving goal. In addition, further government regulation implementation, by means of reducing methane emission per unit of energy converted, will vitally help increasing fuel efficiency. As a clean alternative to oils, natural gas, containing primarily of methane, comes a rescue of clean energy, bridging to the future. That being said, the demand in natural gas has been growing in a variety of industry applications such as natural gas operated vehicles, heating devices and gas turbines [9]. Although natural gas is the cleanest of all fossil fuels, the release of unburned methane is still an environmental concern since methane is the second largest greenhouse gas with a global warming potential of 23 times higher than that of CO_2.

The presented thesis aims to use catalytic technologies to meet the large demand of high quality fuels and energies, and as a result bringing advanced environmental solutions. The performances of the developed heterogeneous catalysts were investigated in three catalytic processes: (1) selective ring opening of indan as a model reaction in fuel upgrading, (2) hydrodesulfurization of 4,6-dimethyl-dibenzothiophene to produce ultra-low sulfur fuels and (3) methane combustion to reduce the greenhouse gas emission from natural gas vehicles.

Platinum group metals (Pd and Pt) are long known as active catalysts for the above mentioned catalytic processes. However, low sulfur and moisture tolerances, and poor thermal stability have been significant drawbacks of the Pt group metals for the fuel related applications. Numerous studies have focused on increasing the poisoning tolerance and long term stability of Pt group metals via alloying the active component with another metal. In industries, bimetallic catalysts are prepared by a support impregnation with metal precursors followed by calcination and/or reduction steps. Such traditional method for bimetallic catalyst synthesis is known to be inefficient in providing precise size or structure control, which may lead to inefficient metal-metal interactions and impedes understanding of metal functions and/or their possible synergism.

The combination of nanotechnology and advanced material selection allows the design of more efficient catalysts. The success in the colloidal chemistry allows easy preparation of nanoparticles with desired size and bimetallic surface structures. Electronic and geometric properties of the surface atoms are strongly affected by the nanoparticle size and structure modes. Such properties govern the chemisorption strength and mode of the catalytic reaction substrates and deposits. The catalytic properties can be controlled at atomic level by precisely changing the atom position and its surroundings.

The thesis objective is to gain insights in bimetallic interactions in oxidative and reductive catalytic applications and design superior catalysts as compared to the industrial analogues via controlled synthesis of mono- and bimetallic nanoparticles. The basic principles of nanoparticle size and structure controls using colloidal chemistry methods and the concept of efficient catalyst and structural evolution during catalysis, as well as the catalytic reaction mechanisms of indan hydrogenolysis, 4,6-dimethyl-dibenzothiophene hydrodesulfurization and methane oxidation are briefly reviewed in the following sections.

1.2. Metal nanoparticles as catalysts

Metallic nanoparticles (colloids) are referred to isolated particles of sizes between 1−100 nm [10]; those in the range of 1−10 nm with well-defined nanostructures are believed to work as effective catalysts [11]. The preparation of transition metal nanoparticles and their application in catalysis have received much attention in the past decades because of the unique features of nanoparticles, and thus, their catalytic properties [11, 12]. As catalytically active metal atoms are located on the surfaces, smaller nanoparticles are preferred in a variety of industrial applications, due to their high surface-to-volume ratios [11], and so, large amount of active sites per metal loading. The recent advances in nanotechnology and colloidal chemistry allow the easy preparation of nanoparticles with desired size, shape and structures (in the case of bimetallic nanoparticles) [13, 14]. Nanoparticles are usually deposited on a catalyst support, such as metal oxides, zeolites, carbon, etc, to form heterogeneous catalysts. Among the support materials, the oxides-supported metallic nanoparticles are easy to handle and highly preferable in many catalytic processes in industries, involving tubular reaction vessels for gas phase reactions [11]. The large pore volume, low acidity and weak metal support interaction make alumina support preferred for the study of metal functions and active sites in catalysis.

1.2.1. Importance of size control and bimetallic nanocatalyst

Nanoparticles with different sizes have different surface atom distributions; the proportion of atoms on the edges and corners increases with the particle size decreases [15]. Semagina reviewed that many catalytic reactions are structure sensitive, including Suzuki and Heck couplings, hydrogenation, hydrogenolysis, oxidation and electron transfer reactions [16]. The terminology of structure sensitivity is related to the chemisorption strength and mode of the reaction substrates on the active sites of heterogeneous catalysts [16]. Imagine, if the catalytic activity or selectivity is enhanced over some specific atoms, then a monodispersed catalyst will lead to the overall improved catalytic performances. An example of surface sensitive reaction would be acetylene hydrogenation over Pd catalyst. Diminishing activity of Pd was observed with a decrease in Pd particle sizes (< 5 nm), because the complexation of the alkyne and coordinatively unsaturated Pd atoms are too strong [17]. On the other hand, hydrogenolysis rate is faster on the metal atoms with low coordination numbers in small particles than the low index plans present in larger particles [16].

According to the Sabatier's principle, known also as "volcano plot", during catalysis an intermediate formed must be stable enough for chemical transformation on the catalyst surfaces, but not too stable, as it needs to decompose to yield the final product [16]. Hence, the active sites of catalysts should possess appropriate electronic and geometric properties to coordinate with the reaction substrates; such properties can be modified not only by nanoparticle size control, but also more frequently by the incorporation between two metals, for example, alloys. Thus, in addition to the size control, special attentions have paid to the bimetallic systems [18-24] for improved catalytic activity, selectivity and/or stability [21]. The knowledge on structure sensitivity helps to realize the importance of size and structure controls of metal nanoparticles in catalysis, which play an important role in revealing the active sites in chemical reactions [16]. Such concept is far from the traditional way for catalyst preparation that the impregnation of support with metal precursors leading to wide polydispersed catalysts.

1.2.2. Nanoparticle size control

Metallic nanoparticles can be prepared by "bottom up" and "top down" methods. The "bottom up" method usually involves wet chemical nanoparticle preparations such as chemical reduction of metal salts, thermolysis and decomposition of organometallic precursors [13]. While "top down" method relates to the physical pulverization of the bulk metallic mass [24], such as, metal vapour techniques [13]. Among all these synthesis techniques, the colloidal chemistry method with the presence of nanoparticle stabilizer is superior to the others, owning to the facts of simple synthetic procedures, easy tuning in nanostructure size and morphology and better nanoparticle stability [16, 24]. Nanoparticles are thermodynamically unstable, because their surface free energy is excess to their lattice energy. Protecting/stabilizing agents, therefore, are essential to prevent agglomerations during the stepwise formation of nanoclusters involving nucleation, growth and agglomeration to the desired size and morphology [13]. According to the type of protecting shells, the stabilization methods can be summarized as (1) steric stabilization by surrounding the metal center with large organic molecules, such as polymers and surfactants, (2) organic ligands stabilization via P, N, S donors, (3) electrostatic stabilization resulted from the electrical double layer formed by the anions and cations interacting with the metallic nanoparticles and (4) solvent stabilization, for example, by the interaction of nanoparticles with long chain alcohols [13, 16].

Among all the stabilizing agents found in literatures, poly(vinylpyrrolidone) (PVP) is the most commonly employed organic stabilizer for the preparation of various metallic nanoparticles [13, 14], as it fulfills both steric and ligand stabilization requirements, thus allowing the formation of well-defined nanostructures. Figure 1.1 shows the molecular structure of PVP and a schematic diagram of the synthetic procedures for PVP-stabilized Pt nanoparticles [25]. The PVP-stabilized metallic nanoparticles are as small as 2−3 nm and stable for years [14]. Polymeric stabilizers forms many weak bonds on the surface of nanoparticles, instead of less strongly interacting with specific sites of the particles [13] like in the case of shape directing agents (for example, KBr) [26, 27]. Thus, the resulted PVP-stabilized nanoparticles are often in small spherical shapes; however, the final nanoparticle size is known to depend strongly on the synthetic conditions and metal natures. The protecting mechanisms of PVP on metallic nanoparticle surfaces were delivered by a combination of characterization techniques: X-ray photoelectron spectroscopy (XPS) and Fourier transformed infrared spectroscopy (FTIR) [28, 29]. For small clusters (< 7 nm), PVP molecules act as electron donors that cap on the surface atoms of the metallic clusters via their C═O and C−N functional groups [28, 30]; while over large nanoparticles (> 25 nm), charge transfer was from metal to side chain (CH_2) of PVP [31]. In addition to the nanoparticle size control, PVP can be used together with a shape-directing agent (usually bromide ions) for the preparation of for example Pd [27] and Pt [26] nanocubes [32]. During the nanocube formation, PVP participates the formation of small nanoparticle seeds in the nucleation stage; while in the following growth stage, bromide ions selectively bind the (100) faces to promote the nanoparticle growth along the (111) direction [26].

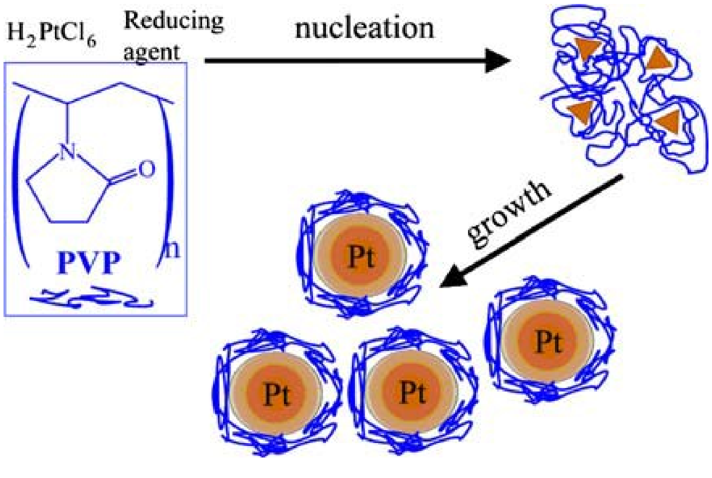

Figure 1.1. The schematic of the synthesis of PVP-stabilized Pt nanoparticles [25]: nucleation, seeds formation and nanoparticle growth. Reprinted with Permission from Ref [25]. Copyright © 2008 Springer Science + Business Media B.V.

To achieve high degree size control, dendrimer templates can be used to synthesize nanoparticles with ultra-small sizes of < 2 nm [33-35]. The dendrimer-templating technique was originally developed by Crooks and co-workers [36]. Poly(amidoamine) (PAMAM) is the most employed dendrimer for the synthesis of transition metal nanoparticles [35]. Figure 1.2 shows the framework of a generation 4 PAMAM dendrimer (G4OH) and the schematic of the employed synthetic scheme [36]. Like PVP, dendrimer meets both steric and ligand stabilization requirements. The internal tertiary amine functional groups act as ligand to interact with metal ions. The G4OH dendrimer has a diameter of ~ 4.5 nm [36]; its unique tree-like structure restricts the further growth of the nanoparticles to large sizes. Ultra-small dendrimer-templated monometallic Au [37], Pd [37, 38], Pt [35, 39] and Rh [35], and bimetallic Pd−Au [40] and Pd−Pt [33, 41] nanoparticles with 1−2 nm diameters have been frequently documented in literatures.

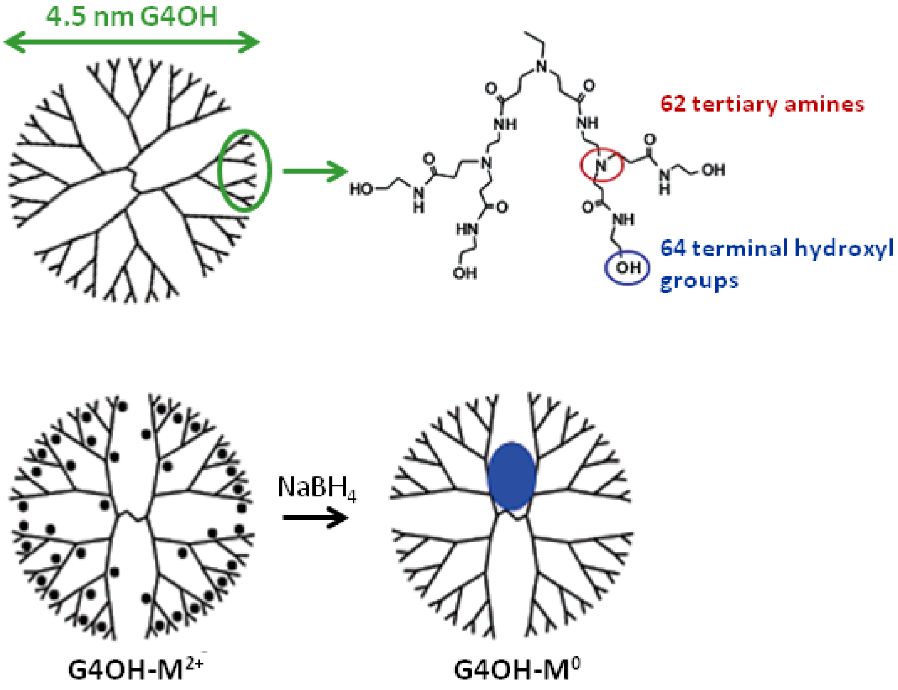

Figure 1.2. The framework of a generation 4 poly(amidoamine) dendrimer terminated by hydroxyl groups (G4OH) (top) and the schematic of the employed synthetic scheme (bottom): complexation and reduction [36]. Reprinted with Permission from Ref [36]. Copyright © 2005 American Chemical Society.

Nanoparticles are usually synthesized by reducing the corresponding metal precursors in low boiling point alcohols under refluxing conditions with the presence of PVP [13, 14]. The mean diameters of monometallic Pd, Pt, Rh, Ag and Au, and bimetallic Pd−Ni, Pd−Au and Pd−Pt nanoparticles are in the range of 2−5 nm if prepared by one-step reduction in alcohol [22, 23, 42, 43, 43]. Alcohol reduction method has the advantage that it acts as both solvent and reducing agent. The size control of nanoparticle depends strongly on the type and concentration of the alcohol used as reducing agent. As a rule of thumb, a higher boiling point alcohol will lead to the formation of smaller nanoparticles than a low boiling point alcohol. The Pd nanoparticles with small diameter were obtained in the order of methanol > ethanol > 1-propanol [44]. In general, an increase in the concentration of reducing agent increases the reduction rate of metal ions to zerovalent metals, thus resulting in smaller particles. However, a too high alcohol concentration will lead to the increase in particle size, due to the slow reduction rate accompanied by low boiling point of the solution [44]. It has been reported that a 40 vol.% alcohol in water is optimal to give the smallest Pd nanoparticles [44].

The choice of reducing agent is not limited to alcohols; and its selection should be on a case-by-case basis. For instance, the reduction of 3d transition metal ions (such as Ni, Fe and Cu) to metallic particles is difficult because their redox potentials are lower than those for noble metals [14]. Thus, a much stronger reducing agent, sodium borohydride ($NaBH_4$), is required [45-47]. Usually solid powders of $NaBH_4$ are introduced into the synthetic system at high temperature that is often provided by high boiling point polyols [46, 48]. Sometimes borohydrides are also used in the reduction of 4d noble metal ions, for example, dendrimer-templated Pt and Pd nanoparticles [36]. A solution of $NaBH_4$ should be prepared at 0 °C to retard the extremely rapid reduction rate [35], and so avoids the formation of irregular nanoparticle morphology. On the other hand, in the formation of Pd nanocubes, a weak reducing agent, such as ascorbic acid, is suitable to provide relatively slow nucleation step [27]. The ratio of the seeds to the remaining metal ions in the solutions is relatively low, so allowing the further growth into large cubes, although the final shape depends on the shape-directing agents [26, 27]. The strategy of synthesis and reducing agent selection are especially important for the bimetallic nanoparticle with controlled surface structures, which will be discussed in the next section.

1.2.3. Synthesis of bimetallic nanoparticles

In the past two decades, Toshima and his coworkers have made great contributions to the synthesis and characterization of bimetallic nanoparticles with precisely controlled size, structure and surface compositions using PVP [14, 19-24]. As shown in Figure 1.3, ideally, bimetallic particles may form core−shell, inverted core−shell and random alloy structures [14], as well as a bimetallic system with one component more abundant in the outermost shell than the other one, if the relative nucleation rates of the two metals are well understood for the applied synthetic method [22]. The synthesis of PVP-stabilized bimetallic nanoparticles can be divided into two methods: successive (or two-step) reduction and simultaneous reduction (or co-reduction) of both metal precursors [14].

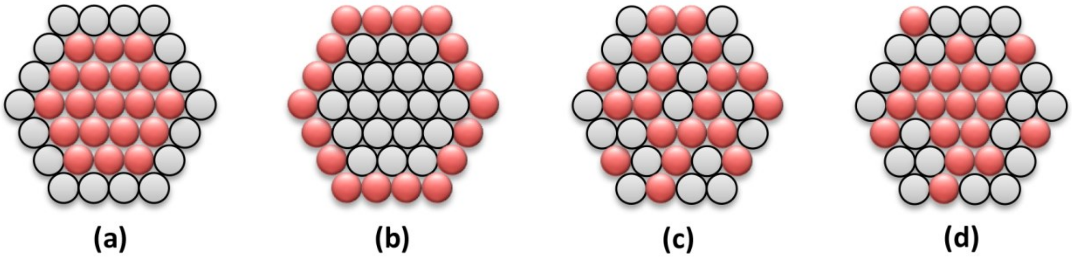

Figure 1.3. Bimetallic structures: core−shell (a), inverted core−shell (b), random alloy (c) [14] and a bimetallic system with one element abundant in the outermost shell (d) [22].

The successive reduction involves the reduction of core metal precursors and followed by the reduction of shell metal precursors on the surface of the metal cores [14], which applies to the preparation of both core−shell (Fig. 1.3(a)) and inverted core−shell (Fig. 1.3(b)) structures. This method becomes especially beneficial when the expensive or active metal with higher redox potential should be formed in the nanoparticle shells for efficient catalysis. Examples of successive reduction include but are not limited to the hydrogen-sacrificial technique for the synthesis of Pd core−Pt shell structure [22], two-step reduction in alcohol (originally employed for the stepwise growth of Pd nanoparticles) [44], and a slow reduction of Au ions on the surface Pd core nanoparticles with ascorbic acid to minimize the secondary nucleation of Au [42, 49]. The application of these synthetic strategies depends strongly on the nature of metal mainly in the viewpoint of their reducibility. The successive reduction allows the formation of complete shell with an accurate coverage of one atomic layer if the amount of the shell metals varies [50]. This requires careful adjustment of core and shell metal molar ratios according to surface atoms and surface sites statistics on metal crystals [15].

The simultaneous reduction of two metal ions with different redox potentials often leads to a surface enrichment with one component [14] (Fig. 1.3(d)). When Pt and Ru precursors are reduced simultaneously in a low boiling point alcohol, Pt^{2+} is reduced to Pt^0 first and then acts as seeds to facilitate the reduction of Ru^{2+} to Ru^0 on Pt surfaces [18]. Without the presence of Pt seeds, the reduction of Ru ions by low boiling alcohols is impossible [18]. Random alloys (Fig. 1.3(c)) can also be formed via simultaneous reduction when metal ratios change. It is important to obtain mixed sites of different compositions on the nanoparticle surface, i.e. complete shell, surface enrichment by one element and random alloys, to understand how the surface configuration affects their performances in catalysis.

1.3. Stabilizer removal for efficient catalysis

As discussed above, nanoparticle stabilizers play important roles for the preparation of well-defined nanoparticle for further use in catalysis. However, the chemisorbed species on metal surfaces block the active sites; thus one cannot have activity without access to the active sites. Such interaction becomes a significant drawback of PVP-stabilized nanoparticles in the field of catalysis. The excess PVP used in synthetic reactions can be washed off by solvents [26], after deposit on catalyst support. However, the removal of chemisorbed polymers from metal surfaces is challenging. It is generally accepted that thermal treatment is the most efficient way to remove stabilizers, comparing to other strategies, such as chemical [26], ultraviolet (UV)-ozone [51] and plasma [52] treatments. The thermal removal of stabilizers from a catalyst that is packed in a tubular vessel for gas phase reaction can be performed in situ without complicating the catalytic processes by additional materials, equipments or steps.

It is known that free PVP decomposes at 330 °C; the presence of metallic nanoparticles could catalyze the combustion of PVP and thus lower the decomposition temperature [53]. It has been found that calcination in dilute oxygen (20% O_2/He) and followed by in situ reduction in hydrogen at 200 °C is a more effective polymer removal way than thermal treatment in inert gas [53]; the observations were made over a monometallic Pt catalyst. As discussed in section 1.2.2, PVP interacts differently with nanoparticles of different sizes: through C═O and C−N functional groups over small particles and side chains over large particles. Thus, the removal of PVP depends on the size of nanoparticles as well as the type of metals being protected, due to the different chemisorption modes and strengths of the pyrrolidone rings on metal surfaces. A stabilizer removal is considered necessary for efficient catalysis. However, the thermal treatment needs to be balanced between clean nanoparticle surfaces and possible size and structural changes of the supported nanoparticles.

1.4. Nanoparticle sintering and structural change during catalysis

Advances in nanotechnologies and colloidal chemistry allow the preparation of ultra-small nanoparticles of ~ 1 nm and the desired compositions in the outer most layers of the bimetallic nanoparticles, as discussed in sections 1.2.2 and 1.2.3. Such structures are usually not preserved; nanoparticles undergo sintering and structural evolution during thermal treatment for stabilizer removal and/or catalysis [54]; this is driven by minimizing surface free energy. Although this thesis did not exclusively study the sintering mechanism or monitoring the structural evolution in the bimetallic surfaces during catalysis, to understand these phenomena (will be discussed below) will greatly help researchers to not only predict the extent of sintering or possible structural changes, but very importantly, to design heterogeneous catalysts toward stable performances in the future.

1.4.1. Nanoparticle sintering

Nanoparticles tend to agglomerate to large sizes during thermal activation and/or catalytic reactions; the lack of stability of nano-scaled catalysts has been frequently documented in literatures [9, 55-57]. Sintering, referred as thermal deactivation, is an important issue for the loss of catalyst activity, which is especially pronounced in some catalytic processes involving high temperatures, like combustion [58], exhaust treatment [59] and reforming processes [57, 60]. Two possible sintering mechanisms of transition metal nanoparticles are coalescence by particle migration and Ostwald ripening [57, 61]. The particle migration leads to coalescence when nanoparticles are in close contact with each other; while Ostwald ripening involves the dissolution of atoms from edge and corner sites (coordinatively unsaturated atoms) of smaller particles and followed by deposition on larger ones [61]. The Ostwald ripening is commonly accepted as the main mechanism for nanoparticle sintering [16, 61], because nanoparticle sintering is related to the movement of atoms rather than particles [62].

Preventing the sintering behaviors of nanoparticles to maintain their high surface-to volume-ratios is indeed challenging. One feasible way is the addition of a second metal to the active one to form alloys; the sintering of the overall bimetallic nanoparticles could be mitigated or even completely suppressed by the nature of the added component, such as high melting point [55]. For example, bimetallic Pt−Rh nanoparticles did not show noticeable sintering up to 850 °C, with its monometallic counterparts displayed severe sintering at about 500 °C [63]. However, it is noteworthy that the choice of the second metal is particular important, as it may alter the overall activity and/or selectivities in catalytic reactions [55], especially when large amount of the second component is introduced to the active metal to achieve stable performance. In addition, surface segregation by one of the two alloyed metals may occur during pretreatment and/or catalysis due to the large difference in melting points, which will be discussed in section 1.4.2.

A binary support is also feasible to enhance the catalyst stability due to the textural and chemical modification of the parent support. Recent studies have shown that the least lattice mismatch between the supported nanoparticles and spinel of magnesium [64] or nickel [65] are responsible for the improved nanoparticle stability towards sintering. Highly dispersed Pt nanoparticles in the range of 1−3 nm were preserved after severe thermal treatment conditions at 800 °C under air for 1 week [64]. The improvement in Pt stability was ascribed to the strong interaction of Pt nanoparticles with the $MgAl_2O_4$ spinel (111) facets [64].

Another approach for nanoparticle stability improvement involves coating the metallic nanoparticles by an inert oxide shell with/without dispersing the particles on inert oxide beads [55]. Examples include Au [66] and Pt [58, 67] nanoparticles encaged by porous silica shells. The silica shells protected the low-coordinated corner and edge atoms from spending in the Ostwald Ripening process [61]. The Pt metal core coated with a mesoporous silica shell revealed high thermal stability and thus allowed superior activity in CO oxidation at high-temperature [58]. Moreover, the CeO_2-coated Pd nanoparticles remained isolated even after treating the catalyst at 850 °C [59].

1.4.2. Structural change in bimetallic catalysts

Thermodynamics is considered as the principal driving force for the structural changes in bimetallic nanoparticles at high temperatures [68]. Bimetallic nanoparticles with same metal ratios but initially different structures may transform into one very same most thermodynamically stable configuration [68]. The metal with lower surface energy segregates to the surface of the bimetallic nanoparticles [69]. For example, the formation energy of the bimetallic structure with Au in the core and Pt in the shell is positive, which demonstrates that they are thermodynamically unstable [68]. When subjecting to thermal treatment, atomic arrangement first occurred at corners and edges; complete inversion of the original Au core–Pt shell structures was observed at 800 K with surface full-filled by Au atoms [68]. The author related the restructuring feature to the large difference of the melting behaviors of the two metals in the bimetallic nanoparticles [68].

In addition to thermodynamics, surface segregation can be also driven by chemically activated selective metal diffusion, due to the different metal affinities to the reaction components [70, 71]. In CO oxidation, the Pd enrichment in the surface of bimetallic Au−Pd nanoparticles was claimed due to the strong adsorption of Pd with CO [71]. Isolated Pd atoms or dimers of Pd atoms were found to exist on the edges of the bimetallic surface, which was related to the rapid loss of activity in the catalytic conversion of CO to CO_2 [71]. The structural change depends strongly on the reaction atmosphere [69]. Y oxides were formed on the surface of a ternary CuPdY alloy in oxygen environment; such surface segregation was not seen in vacuum condition [72]. In another example, the restructuring of the core and shell structure of Rh−Pd nanoparticles is reversible in oxidizing (NO) and reducing (CO) environments [69]. The surface segregation depends also on the two metals involved in the bimetallic structure. The restructuring phenomenon observed in Rh−Pd nanoparticles was not observed in Pt−Pd sample. The initial Pt core−Pd shell structure was maintained in both NO (oxidizing) and CO (reducing) environments, because Pt is much less easily oxidized and has a higher surface energy than Pd [69].

To understand the atomic remodelling in bimetallic structures will not only help researchers to explain the observed loss in catalyst activity or unstable performance during catalysis, but also can be used as an advantage/tool to tune the surface composition at atomic level, and in turn utilizing catalyst efficiency. For instance, bimetallic nanoparticles of Pt shell around Pt−Co core were resulted from annealing the Pt−Co random alloys in CO environment

[70]. The CO-induced surface segregation by Pt atoms is ascribed to the higher adsorption enthalpy of CO on Pt than that on Co [70]. Such intended surface segregation ensures the active and expensive Pt not hidden in the interior of the bimetallic nanoparticles.

Up to here, the understanding to the importance of nanoparticle size and structure control (discussed in section 1.2.1) should not be limited to the optimization of catalyst performances during catalytic reactions; but very importantly, a well-defined nanostructure will allow one to understand the metal functions and active sites during catalysis and to compare with theoretical calculations for future engineering catalyst design. Recent advances in the colloidal chemistry techniques allow researchers to prepare initially well-defined bimetallic structures with uniform sizes and desired surface compositions; thus it enables the experimental studies of the structural evolution or sintering mechanism and rate after thermal treatment and after catalytic reactions. It is practically impossible to gain such insight over conventional catalysts, prepared by impregnating catalyst support with metal precursors, with polydispersed structures and even mixtures of mono- and bimetallic particles. The irregular sampling of the initial nanoparticle structure in the case of conventional catalysts complicates its structural evolution studies. In addition, a combination of the high-tech characterization methods including but not limited to extended X-ray absorption fine structure spectroscopy (EXAFS), X-ray absorption near edge structure (XANES), X-ray photoelectron spectroscopy (XPS), X-ray powder diffraction (XRD), Scanning transmission electron microscopy-electron energy loss spectroscopy (STEM-EELS) and field emission-transmission electron microscopy/energy dispersive X-ray spectroscopy (FE-TEM/EDS) [34, 41, 54, 71, 73, 74] allow the comprehensive study in structural evolution of many bimetallic combinations. However, the limited access of in situ catalyst characterization techniques also complicated the investigation of the nanoparticle structural change during pretreatment or catalysis.

1.5. Indan ring opening

The extensive overcracking of the saturated aromatic rings during conventional hydrocracking limits the production of desirable paraffins. A selective ring opening (RO) of naphthenes is ideal for reducing the aromatic contents and consequently improving the cetane or octane number of fuels [75, 76]. In this thesis, catalytic ring opening of benzocyclopentane (indan) at low pressure was selected as a model catalytic reaction to evaluate the developed catalysts for oil refining purposes. Indan contains a benzene ring fused with a five-carbon ring, which makes it a suitable model compound to study selective hydrogenolysis properties of noble metals and bimetallic effects. Other model compounds such as decaline or tetraline are not suitable for low-pressure ring opening, because of the low reactivity of six-carbon rings over noble metals, and also possible fast dehydrogenation, especially in the case of decaline. A schematic diagram of the indan ring opening is shown Figure 1.4. The desired ring opening products are 2-ethyltoluene and *n*-propylbenzene, where the naphthenic ring is cleaved only once, leaving the carbon number unchanged [77].

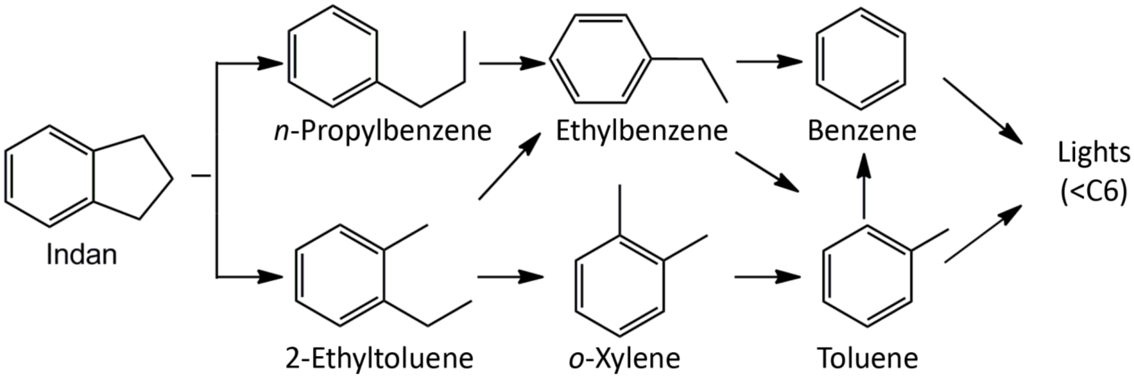

Figure 1.4. Reaction scheme for low-pressure indan ring opening on a metal function [77]. Reprinted with Permission from Ref [77]. Copyright © 2006 Elsevier B.V.

Noble metals supported on alumina are preferable catalysts for selective ring opening reactions over solid acid catalysts. Strong Brønsted acid sites often lead to isomerization, and excessive cracking of naphthene side chains and alkane products. [76, 78-86]. A voluminous pioneering works on the ring opening of methylcyclopentane (MCP) [78, 87-91] and methylcyclohexane (MCH) [78-80] have brought valuable knowledge on ring opening mechanisms and metal functions. The ring opening mechanisms over noble metal catalysts are proposed as perpendicular α-adsorption (or dicarbene), flat-lying π-adsorption and a metallocyclobutane (not in the case of indan ring opening, because of the absence of branches) [92]. Due to the unique adsorption configuration of each mode, dicarbene reaction path results in the cleavage of unsubstituted C−C bond in the ring structures, thus producing highly branched isoparaffins for octane number improvement. The π-adsorption mode results in C−C breakage at the substituted positions, therefore, is desirable for enhancing cetane number [92]. The ring opening mechanisms depend strongly on the type of metal or metal alloy, nanoparticle size and reaction conditions, as well as the structure of reactant molecule.

In either reaction pathway, the selective ring opening reactions are driven by the hydrogenolysis properties of the noble metal catalysts. One of the pioneering works investigated the catalytic performances over 11 transition metals, including Rh, Pd, Ir, Pt, Co, Ni, Ru, Re, Os, Cu and Ag, in selective ring opening of MCP. Ir was found as the most active and selective ring opening catalyst [93]. Later, it was found that Rh, Re, Ru and Ni show similar RO mechanism as Ir through a dicarbene mode in the RO of MCP, but are less selective, due to the secondary cracking of the primary C6-alkane product to C1−C5 paraffins [78, 90]. Pt works in a different way than Ir, that is the RO of MCP is catalyzed through a flat-lying mode over Pt [78, 94]; same π-adsorption mode was also observed in Pd metal [95]. Although Pt is the least active MCP RO catalyst, when alloying with Rh allowed increasing RO performances, reaching the level of Ir catalyst [90]. Alloying two metals is indeed a feasible way to boost the catalyst activity and selectivity in RO. Other examples of bimetallic catalysts reported previously for selective ring opening are Pt−Ru [90], Pt−Ir [96], Pt−Au [97], Rh−Ge [98] and Pd−Ir [99, 100]. The RO activity and selectivity depend on metal nature; the reactant nature and reaction conditions also possess strong impacts on catalyst performances during selective RO. For example, RO of cyclohexane over Ru-based catalysts could proceed at significantly lower temperatures (210−230 °C) as compared with Pt and Rh catalysts at 350−400 °C [101]. In addition, Ru allows higher selectivity (13%) to C7-alkane product than Ir (5%), which is desirable for cetane number improvement [78].

The closest work to ours is the ring opening of indan over bimetallic Pt−Ir catalysts, previously studied by Nylen et al. [77, 102]. The addition of inactive Pt to Ir catalyst showed superior catalyst performances. Ir ensures high RO yields and low coke formation. Pt addition tempers the undesirable cracking by Ir. The addition of Pt is necessary as it also increases sulfur tolerance and resistance to sintering of the bimetallic catalyst [77]. However, the proposed promising ring opening catalysts contain expensive precious metals, such as Pt and Rh, and rare element, like Ir. The high cost and rareness of these metals set limitations on the catalyst exploitation. When selecting new catalyst combinations as alternatives to Pt−Ir, the new system should meet the properties of Pt−Ir catalyst. It is important to keep the Pt-like mechanism of RO via a flat-laying π-mode [78, 94] to prevent undesirable excessive cracking of the ring opening products, and Ir-like metal in the viewpoint of its great hydrogenolysis property. Among the noble metals have been studied frequently in literatures, Pd could be considered as a potential replacement for Pt, because it shows the same flat-lying mode during selective RO [95]. However, owning to the fact that Ir being the most active and selective ring opening catalyst, the search for new alternatives is yet challenging.

The knowledge of metal functions gained for the selective RO reaction at low-pressure is believed to deliver a new class of catalysts when approaching to real industrial conditions. Thus, the catalytic hydrodesulfurization at high pressure will be discussed in the next section.

1.6. Ultra-deep hydrodesulfurization

Sulfur, a natural element in crude oil, is the main contribution to environmental problems and health hazards. According to the new environmental regulations in many countries, sulfur content in diesel fuel must be reduced to an ultra-low level, for example 15 ppm. It has been reviewed that the organic S molecules are mainly benzothiophenes (BT's) and dibenzothiophenes (DBT's), with and without alkyl substituents. These two groups of sulfur compounds are observed in different types of oils, such as straight run gas oil (SRGO) and cracked distillates (light cycle oil (LCO) and coker gas oil (CGO)) feeds, although the compositions may vary from feed to feed [103]. The BT molecules are found to be an order of magnitude more reactive than DBT's. Among all the isomers of alkyl-substituted DBT molecules, the alkyl groups adjacent to sulfur atoms (4 and 6 positions) made the sulfur extraction considerably challenging, as they hinder the interaction between sulfur atoms and the active sites of catalysts. Thus, 4,6-dimethyl-dibenzothiophene (4,6-DMDBT) is generally considered as a suitable candidate to represent the most refractory sulfur compound in the studies of ultra-deep desulfurization in open literatures, whose desulfurization rates is orders of magnitude lower than in the easily-removed S. Thus, as another concern of the presented thesis, ultra-deep hydrodesulfurization refers to the removal of the most refractory organic sulfur molecules left in fuels.

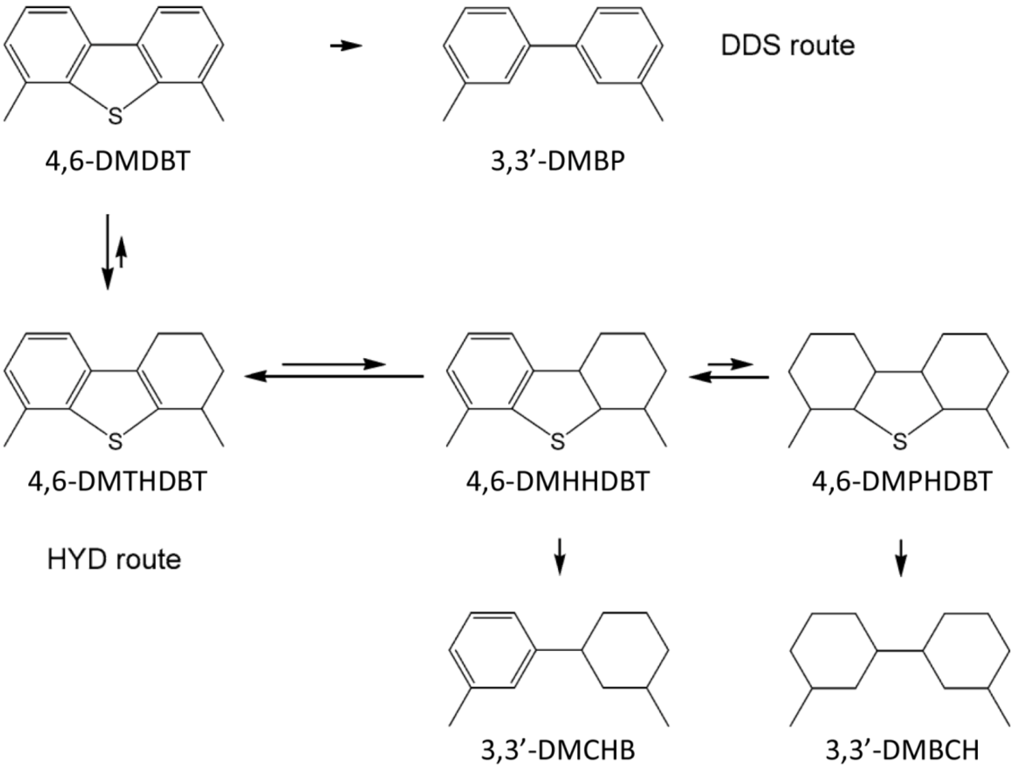

Figure 1.5. DDS and HYD reaction pathways in the hydrodesulfurization of 4,6-dimethyl-dibenzo-thiophene (4,6-DMDBT) at 300 °C and 5 MPa on a metal function [106]. S-free product via DDS route: 3,3'-dimethyl-biphenyl (DMBP); S-free products via HYD route: 3,3'-dimethyl-cyclohexylbenzene (3,3'-DMCHB) and 3,3'-dimethyl-bicyclohexyl (3,3'-DMBCH); and S-containing intermediates via HYD route: 4,6-dimethyl-tetrahydro-dibenzothiophene (4,6-DMTHDBT), 4,6-dimethyl-hexahydro-dibenzothiophene (4,6-DMHHDBT) and 4,6-dimethyl-perhydro-dibenzothiophene (4,6-DMPHDBT). Reprinted with Permission from Ref [106]. Copyright © 2006 Elsevier Inc.

A considerable number of publications have shown the hydrodesulfurization mechanisms of 4,6-DMDBT over noble metal catalysts [103-105]. As shown in Figure 1.5, the two possible sulfur removal mechanisms are direct extraction of sulfur (DDS) and hydrogenation of naphthenic rings followed by hydrogenolysis of the saturated aromatic ring (HYD) [106]. The adsorption modes (α-adsorption and π-adsorption) of the alkyl-substituted DBT molecules on a noble metal catalyst are similar to those discussed for indan ring opening in section 1.5. A perpendicular σ-adsorption of the 4,6-DMDBT molecules via its sulfur atom leads to the DDS mechanism; while a flat-lying π-adsorption through the aromatic rings results in HYD mechanism [106]. It has been reported that the selectivity to DDS mechanism, and thus its hydrodesulfurization rate, for DBT with alkyl groups in the 4 and 6 positions are extremely slow [107]. The sulfur extraction via HYD route dominants the overall desulfurization rate, because the saturation of aromatic rings changes the spatial configuration of the 4,6-DMDBT molecules, with the sulfur atoms more easily to access the catalyst surface [103]. From the thermodynamic point of view [103], catalytic hydrodesulfurization is usually operated at moderate temperature (usually 300 °C) [106] and high hydrogen partial pressures (4.5−6.5 MPa) [106] to promote the hydrogenation reaction for aromatic ring saturation. In addition to the chemical structures of the refractory S-molecules, thermodynamic limitations and other factors present in real feeds, such as H_2S by-product, nitrogen compounds and aromatic contents, could also significantly inhibit the HDS rate by competitive adsorptions on the active sites of catalysts, which make the ultra-deep desulfurization even more challenging for petroleum industries [103].

Conventional Co−Mo and Ni−Mo catalysts play an important role to enhance the sulfur removal and promote hydrodesulfurization in hydrotreating processes [103]; and the activities and selectivities of these catalysts have been already improved significantly [108]. However, at normal operating conditions, Co- and Ni- promoted Mo catalysts are not active enough to desulfurize diesel feeds to ultra-low sulfur level to meet the new regulations on fuel quality. Several times more active catalysts, and increases in operation temperatures [107] and hydrogen pressures [103] have been called for further enhancement of the sulfur extraction rate over conventional Ni- or Co-modified Mo catalysts to meet future fuel standards. However, such increase in operation severities will definitely lead to rapid catalyst deactivation and short cycle length [103], as well as an increase in operating cost. The use of acidic supports (zeolites or amorphous Si−Al) is known to enhance the activities of refractory sulfur molecules; the acidic functions promote isomerization and dealkylation reactions [105]. Even so, the acid solid catalysts discredit themselves due to the undesirable hydrocracking [105] and coke formation.

Metals are much better hydrogenation catalysts than metal sulfides and might be well suited as catalysts for deep HDS [106]. Noble metal catalysts may be used in the second reactor of a two-stage hydrotreating process. In the first stage, the feeds are hydrodesulfurized over conventional metal sulfide catalysts. After the removal of H_2S formed in the first reactor, the first stage product is then further (ultra) desulfurized over noble metal catalysts. The amount of total sulfur entering the second reactor may be low enough for the noble metals to maintain sufficient activity [106]. Noble metals with high hydrogenation properties, such as Pt and Pd, have been well studied in hydrodesulfurization reactions [104-106] using model compounds like DBT and 4,6-DMDBT. For example, a previous study has documented that the catalytic activity of noble metals decreases in the order of Pd ≈ Pt−Pd > Pt > Rh > Ru−Rh >> Ru for 4,6-DMDBT hydrodesulfurization [109]. In HDS of DBT at high pressure (5 MPa), Prins et al. found that Pt has a higher DDS selectivity than Pd. The desulfurization of DBT and 4,6-DMDBT were faster over Pt catalyst than Pd. On the other hand, Pd has a higher hydrogenation activity than Pt, especially for 4,6-DMDBT [106]. Ir was shown to be the most active metal when thiophene hydrodesulfurization was carried out at low pressure [110].

Apart from the outstanding hydrogenation activities of Pt- and Pd- containing catalysts, they also show better sulfur-resistance than other noble metals [105]. Sulfur poisoning of noble metals is the main reason for catalyst deactivation in HDS, which depends strongly on the nature of metals. For instance, Ru binds sulfur too strongly, and the resulted high S coverage (S poisoning) made Ru underperform Pt [111, 112]. In a [^{35}S] DBT radioisotope study, the author has concluded that almost no labile sulfur was accumulated on Pt catalyst [113]. Sulfur resistance of noble metal catalysts is related to the electron density of metal, and could be improved by alloying. The Pd addition to Pt decreases the electron density of Pt, and thus weakens the Pt−S binding [113]. The reason is that alloying Pt with Pd may result in the new active sites with different electronic and geometric properties, and hence optimizes the chemisorption strength and/or mode during HDS reactions. In another work, the author reported that bimetallic Pt−Pd catalysts were much more active than the physical combination of their mono-forms in the HDS of 4,6-DMDBT, which could also be explained by the better sulfur tolerance due to the synergetic effect between the alloyed metals [106].

According to HDS literatures, all examples of noble metal catalysts for ultra-deep hydrodesulfurization were prepared by traditional impregnation method, which does not allow control over nanoparticle sizes or surface composition of the bimetallic particles. For example, the bimetallic Pt−Pd catalyst prepared by dry impregnation for the HDS of 4,6-DMDBT was claimed to have a Pd-rich surface and a Pt-rich core, which makes the use of expensive Pt irrational. As discussed earlier (section 1.2.1), it is believed that the precise structure control of noble metal nanoparticles will bring tremendous improvements in catalyst performances. The rational design for new catalyst combinations or the improvement of existing catalysts will open the unprecedented opportunities for noble metal catalysts in ultra-deep desulfurization at reduced cost.

1.7. Methane combustion

A variety of industrial applications, such as vehicle engines, heating devices and gas turbines [9] use natural gas as an alternative of efficient and clean energy, since the increasing stringent regulations on the quality of fuels and the soaring gasoline and diesel demands. Beside the air pollution by SO_x, NO_x and particulate matters, the production of greenhouse gas (CO_2) from burning fuels poses another environmental concern. Instead, burning methane produces less CO_2 for each unit of heat released, comparing to other hydrocarbon fuels. Substantial carbon dioxide reduction has been already achieved by switching, for example, gasoline and diesel to natural gas. However, methane is the least reactive hydrocarbon molecules and so the most difficult to be oxidized [114]. The release of unburned CH_4 is a serious environmental concern, since methane is the second largest greenhouse gas with a factor of 23 times higher than that of CO_2 [59, 115]. The high combustion temperature in conventional firebox also leads to the emission of harmful pollutants such as nitrogen oxides (NO_x) and carbon monoxides (CO). The use of heterogeneous catalysts encourages complete methane oxidation at relatively low temperatures as compared to thermal combustion, which is concerned in the presented thesis. Newly designed catalysts for complete methane combustion must exhibit high activity at low temperatures and improved thermal stability with the presence of water, as well as better resistance to poisons, which indeed poses significant changes.

Methane combustion has been extensively studied in literatures [59, 115-120]. Complete combustion of unburned hydrocarbons favors lean operating conditions, i.e., with abundant oxygen in the feed [121], which is also the condition of real exhaust gases from natural gas fueled-vehicle (NGV) engine (500−1000 ppm CH_4 and large excess of oxygen [56]). At low CH_4-to-O_2 ratios, complete oxidation of methane produces CO_2 and H_2O [122]. At relatively high CH_4 inlet concentrations, partial oxidation of methane could lead to CO and H_2 formation [123], which is for syngas production (not the concern of the presented thesis). Complete methane combustion must be achieved at low temperature (typically below 500 °C [56]), because the temperature of NGV engine exhausts is in the range of 300−500 °C [124-126]. Low combustion temperatures also prevent toxic NO_x and CO formations versus high temperatures for H_2 and CO formation [123]. The commercial catalysts for emission control are mainly Pd, Pt and bimetallic Pt−Pd supported on γ-Al_2O_3 [9]. As compared to Pt, Pd has higher activities in CO and CH_4 oxidation, a better thermal stability in oxidized form and a lower market price [9]. All these make Pd being largely used in the field of catalytic oxidation of hydrocarbons, as well as a better candidacy for low-temperature methane combustion [9]. However, there is always a significant amount of water vapor (10−15%) present in the lean-burn NGV engine exhaust [56], which is a major issue for unstable performance of Pd. Thus, the engineering design of Pd-based catalysts for emission control becomes remarkably challenging.

The reaction mechanism of catalytic methane oxidation is not as straight forward as those for selective hydrogenolysis and hydrodesulfurization (in sections 1.5 and 1.6), as it involves the transformation of metal/metal oxides in the O_2 and CH_4 environment [9, 56], which depends strongly on temperature, and the stability and volatility of the metal oxides [56]. Therefore, the CH_4 oxidation mechanism is usually explained on the basis of the surface oxidation density of the noble metals, exampled mainly for Pd catalysts due to its excellent CH_4 oxidation activity. Pd catalysts for methane combustion are characterized as the Pd/PdO transformation and the consequent change in surface activity [9, 56, 127]. The activation of CH_4 follows Mars-van Krevelen redox mechanism on site pairs consisting adjacent Pd (oxygen vacancies) and PdO (oxygen atoms) species [9, 128], which involves the reduction of PdO by CH_4 and the reoxidation of Pd by O_2 [129]. The metallic Pd dissociatively adsorbs CH_4 producing H and CH_x species; the PdO is responsible for oxidation [9, 130]. Iglesia and coworkers proposed a reaction mechanism based on the methane dissociation on Pd/PdO site pair over a PdO_x/ZrO_2 catalyst [128], as shown in Figure 1.5. Step 1 is the interaction between CH_4 and an oxygen vacancy site (Pd); step 2 is C−H activation, in which H atoms are abstracted sequentially from chemisorbed CH_4 by the adjacent Pd−O; and step 3 is the formation of surface Pd−OH groups [128]. The author suggested that the rate determining step is the C−H bond activation of CH_4 adsorbed on Pd site by neighboring Pd−O surface species (step 2 in Fig. 1.5) [128]. Whereas, Burch et al. proposed that the decomposition of surface Pd−OH (produced from CH_4 activation and H_2O poisoning) (step 3 in Fig. 1.5) limits the C−H bond activation rate [131]. In agreement with Iglesia, Schwartz proposed that the rate determining step in methane oxidation is the dissociation of CH_4 to H and CH_x species at high temperatures (above 450 °C). But in low temperature range (below 450 °C), Pd−OH decomposition limits the reaction rate [127], which is in line with Burch's conclusion. Nevertheless, in either mechanism, the surface oxygen composition is the key factor for methane activation. The catalyst activity increases when the amount of adsorbed oxygen atoms increases, i.e., high PdO concentration [9, 132].

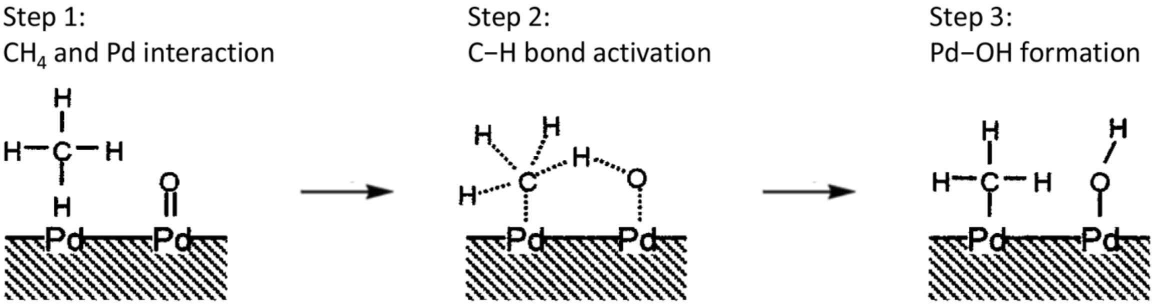

Figure 1.6. Mechanism of CH_4 dissociation on Pd/PdO site pair [128]. Reprinted with Permission from Ref [128]. Copyright © 1998 Academic Press.

Early studies have concluded that methane oxidation is structure sensitive, which is indicated by the large variation in turnover frequency (TOF). This is related to the different behaviors in oxygen activation between small and large metallic particles. It is suggested that stronger Pd−O bonds in small PdO particles lead to a lower surface density of oxygen vacancy sites for CH_4 chemisorption [9]. Hicks et al. evaluated TOFs of alumina-supported Pd catalysts in dry methane oxidation [133]. The reactor was operated at differential conditions (methane conversion below 2%) in the temperature range of 260−370 °C. TOF values were calculated using the particle dispersions obtained from hydrogen chemisorption experiments. The reaction rate depends strongly on Pd dispersion that is associated with metal loading. For small particles of Pd (0.2% Pd loading and 84% dispersion), the TOF is 0.02 s^{-1}; while for large Pd particles (2.3% Pd loading and 10% dispersion), the TOF is 3.3 s^{-1} [133]. Strong correlation between Pd activity and its crystallite size was also observed by other research groups [128, 134, 135]. Fujimoto et al. reported TOFs of 0.012 s^{-1} and 0.003 s^{-1} for ZrO_2-supported Pd catalysts with dispersions of 2.5% and 21.8% (determined by H_2-O_2 titration), respectively; the rate data were obtained at 5% methane conversion [128]. In another study, Roth et al. reported TOFs of Pd catalysts with a wide range of particle sizes in the range of 2−30 nm, determined by H_2 chemisorption [135]. A linear increase in TOF with increasing particle size is observed when Pd particles are smaller than 12 nm. However, for larger particles (> 12 nm), methane oxidation became independent on Pd dispersion [135].

Pd-containing catalyst is no doubt the most qualified candidacy for low-temperature methane oxidation, although catalyst deactivation due to Pd/PdO sintering and water poisoning is still an issue. Species with fast mobility (due to high T) induce fast possible sintering and reconstruction of metal and metal oxides particles during the redox process [9]. Water adsorbed on the active sites could be retained by Pd catalyst (detected by TPD) at temperature ~ 500 °C [56, 136]. Centi summarized that Pd deactivation by water poisoning follows one of the two possible ways: slow rate of surface Pd−OH dissociation or slow recombination to form water [9]. Enormous information from literatures is about the enhancement of catalyst activity and stability of supported Pd catalysts by oxide additives, investigated with and without the presence of water in the feed [137-144]. In early 1990s, Ishihara et al. prepared bimetallic Pd catalysts by co-impregnating $PdCl_2$ with a second metal precursor (in nitrate form) (Ni, Sn, Ag, Rh, Mn, Pt, Co, Fe, Cr, Ce and Cu) on alumina support [137]. The author suggested that oxygen activation is the key for the enhanced catalyst activity. During methane oxidation at lean-burn condition, the metal oxides additives dissociatively adsorb O_2, and then provide O atoms to Pd, which sustained high oxygen concentration on the Pd surfaces [137]. Catalyst supports, like Al_2O_3 or ZrO, could also act as oxygen sources to reoxidize Pd to PdO during the redox mechanism [127]. However, the oxygen exchange between PdO and support was found to be strongly hindered by the presence of water, which explained Pd deactivation [127]. The addition of a second metal to active Pd seems to be more effective than support modification, especially when water presents in the feed (wet methane oxidation).

Among the 11 metal oxides additives, Ishihara concluded that NiO addition to Pd catalyst is the most promising for high CH_4 conversions, because of the easy reduction and oxidation of NiO during the redox process [137]. Later, the addition of Ni to either Pd [138] or Al_2O_3 support [140, 141] has been studied in literatures. Apparently, the addition of Ni in alumina support is not an effective way to enhance Pd activity. For example, a 35 °C reduction in the 90% CH_4 conversion was obtained by adding 36/1 NiO to alumina support [141]. For the Ni-promoted Pd catalysts, they are usually prepared by co-impregnation of Ni and Pd precursors on alumina support [65, 138]. Even when Ni was intended to be added to Pd metal to form alloy or close contact with Pd, after high temperature calcination, Ni was consumed by alumina support and became inactive $NiAl_2O_4$ spinel material, which did not affect the Pd performance in methane oxidation [138]. Recently, Yang's group indicated that adding a large amount of Ni in the support is not necessary. The key factor for effective enhancement of Pd catalyst is ensuring close contact of PdO and NiO particles; however they could not verify their hypothesis because of the use of traditional catalyst preparation method via impregnation and no improvement was observed [144].

1.8. Thesis outline

The objective of the presented thesis is to design Pt- and Ir- free bimetallic catalysts for energy and environment applications. The developed catalysts were investigated in the selected catalytic reactions include selective hydrogenolysis, low-temperature methane combustion and ultra-deep hydrodesulfurization. The advanced nanotechnologies combined with colloidal chemistry allow the preparation of bimetallic nanocatalysts with precisely controlled particle sizes, structures and surface compositions, which is opposed to catalyst preparation by traditional impregnation method followed by calcination and/or reduction steps. It is believed that the structure controlled synthesis of nanocatalysts can enhance the catalytic performances of the existing active catalysts and bring new bimetallic combinations for the above mentioned industrial catalytic processes, with avoiding the use of rare or expensive elements in the earth. Importantly, a well-defined nanostructure also brings deep insight into the metal functions and possible synergism in catalytic reactions. The application of the developed bimetallic catalysts is not limited by the three catalytic processes mentioned in the presented thesis, but may be also beneficial to other industrial processes.

Chapter 2 includes a comprehensive study on the size and structure control of Ru−Pd nanoparticles and the importance of surface composition in selective indan ring opening at atmospheric pressure versus conventional Ir- and Pt-based catalysts. Mono- and bimetallic Ru−Pd nanoparticles were prepared in alcohol media with the presence of a steric stabilizer (PVP) and followed by deposition on alumina support. The synthetic strategies allow the preparation of 2−3 nm bimetallic Ru−Pd nanostructures with varying molar ratios of Ru-to-Pd and different surface compositions including random alloys, Ru-enriched surfaces and complete shells of Ru on Pd cores. The bimetallic nature and the surface enrichment of Ru atoms of the as-synthesized and treated Ru−Pd catalysts (200 °C calcination and 375 °C reduction) were confirmed by temperature programmed desorption of CO (CO-TPD), diffuse reflectance infrared fourier transform spectroscopy of the adsorbed CO (CO-DRIFTS), thermal stability tests and a chemical probe reaction (olefin hydrogenation with only Pd atoms active). The catalytic performances of Ru−Pd in indan ring opening were compared with their monometallic forms to understand metal function of each component, and also with a monometallic Ir catalyst (known as the most active and selective RO metal). Similar to Ir, Ru exhibits a dicarbene path in indan RO and is responsible for the hydrogenolysis property of the bimetallic catalyst. Monometallic Pd is not active, but works through a flat-lying π-adsorbed mode. In the bimetallic structure, Pd dilutes the Ru ensembles and may adsorb the single cleavage products in the flat-lying way, thus preventing further dealkylation. The incorporation of Pd to Ru displayed the same high single cleavage selectivity and as low lights formation as Ir. Chapter 2 discussed the possibility of avoiding rare and expensive Ir by introducing a more available and less expensive alternative bimetallic combinations that allow the same RO selectivity toward single cleavage as Ir.

In Chapter 2, CO chemisorption experiments were performed to check the metallic surface availability after polymer removal by calcination. An interesting finding is that the amount of the adsorbed CO is not indicative of the most optimal pretreatment temperature and does not correlate with the RO activity trends. Thus, in **Chapter 3**, a question arises "Is it always necessary to remove a metal nanoparticle stabilizer before catalysis?" The answer is no, because the balance between resistance to sintering and PVP removal efficiency must be considered before making a conclusion on optimal polymer removal temperature. Chapter 3 studied the effect of different degrees of polymer removal on indan ring opening activity over monometallic Ru and Ir catalysts, calcined at different temperatures. Surprisingly, small amount of PVP residuals did not prevent the adsorption of indan on Ru or Ir surfaces, which is opposed to the chemisorption of CO molecules. A combination of characterization techniques, including XPS, CHN, TEM, CO-TPD and CO chemisorption, also evidenced that polymer-free surface is not necessary. The conclusion is that in some cases a mild stabilizer removal condition is enough. However, the conclusion is limited in indan ring opening at 350 °C, so the necessity for complete polymer removal must be considered on a case-by-case basis.

Chapter 4 involves the modification of a monometallic Pd catalyst by a cheap and abundant metal, Ni; the application is low-temperature methane oxidation with the presence of water. This study addressed the issue with traditional impregnation-calcination method for catalyst preparation, yielding monometallic Pd on inactive $NiAl_2O_4$ binary support, which explains no improvement in catalyst activity during methane combustion as compared to a monometallic Pd catalyst. Whereas, Pd−Ni bimetallic catalyst prepared by colloidal chemistry method allowed significant reduction in methane oxidation temperature with the presence of water in the catalytic system. The Ni addition mode and synthetic strategy have been proved crucial for effective promotion of supported metal nanoparticles to result in excellent performance of Pd-based catalyst. The difference between the catalysts prepared by impregnation method and colloidal technique was shown by temperature programmed reduction (TPR) and supported by XPS analysis. Although there was no direct evidence from XRD or XPS for intrinsic Pd−Ni alloy structure, the hypothetic conclusion is that the close contact of NiO with PdO provided oxygen during the Mars-van Krevelen redox reaction.

It is known that nanoparticles are thermodynamically unstable. In bimetallic nanoparticles, the metal with lower surface energy tends to segregate to the surface, so the well-defined bimetallic surfaces are usually not preserved after high temperature treatment. In **Chapter 5**, bimetallic Ru−Pd catalysts with similar bulk Ru-to-Pd molar ratios were prepared by two different synthetic strategies: an alloy structure with mixed Ru and Pd atoms in the surface and a Pd core−Ru shell structure. The structural evolution of Ru−Pd bimetallic nanoparticles was investigated at three different temperature levels. The initial surface structures of the as-prepared catalysts were characterized by a hydrogenation of an allylic alcohol at room temperature, in which only Pd is active. The distinctively different catalytic behaviors in hydrogenolysis at 350 °C observed over the two different Ru−Pd bimetallic structures indicated the important role of bimetallic structure control for catalytic applications at mild temperatures. Although CO-DRIFTS indicated that the Pd core−Ru shell catalyst went through minor structure change with Pd migration to the surface after treatment at 350 °C, structure-controlled synthesis is still dramatically important for selective hydrogenolysis at moderate temperature. In methane combustion in the 200−550 °C temperature range, Ru−Pd catalysts with initially different bimetallic structures displayed identical activity and stability. The well-defined bimetallic structures were not preserved after calcination at high temperatures, and became one thermodynamically stable structure, i.e., Pd-enriched surface. The bimetallic surface composition control seems not be beneficial in some applications like combustion. The phenomena of structural evolution of the two Ru−Pd catalysts after thermal treatment at 550 °C were confirmed by EXAFS.

In **Chapter 6**, a series of bimetallic Pd−Ru nanoparticles with alloy structures were prepared and investigated in the HDS of 4,6-DMDBT. Pd is long known to be the most active HDS catalyst. Alloying Pd with Ru increased the selectivity toward S-free product formation in both direct desulfurization and hydrogenation routes, because of the improved the thermal stability of the alloyed metals (smaller particle size) and the enrichment of Ru in the bimetallic shell (better hydrogenolysis property than Pd), respectively. The addition of a small portion of Ru to Pd maintained Pd activity, and showed the same S-free product formation rate with a 3-fold increase in the direct desulfurization rate, comparing to the monometallic Pd catalyst. The preliminary conclusion was that the selectivity to DDS depends only and strongly on the nanoparticle dispersions; while the addition of a second metal to Pd improves the C−S cleavage in HYD route.

To validate this hypothesis, the intrinsic size effect in the selectivity toward DDS was then studied over monometallic Pd catalysts with four different dispersions. Ultra-small Pd nanoparticles were prepared using dendrimer-templating technique, and followed by deposition on $MgAl_2O_4$ support, which is known to stabilize noble metals at severe temperatures through metal-support interaction. It was found that by maintaining high Pd dispersion, $MgAl_2O_4$-supported Pd catalyst showed the same high selectivity to DDS as Ru- or Ir- modified Pd catalyst. The addition of Ru or Ir promoted only the selectivity to S-free product via HYD route. The understanding of intrinsic size effect on HDS reaction mechanisms could avoid the use of rare or expensive elements on the earth, which is contrary to most literature findings that HDS proceeds preliminary via HYD route and so requires the addition of second metal for better hydrogenolysis properties. The finding in Chapter 6 may lead to an alternative direction for new catalyst design with cheap and abundant metals for producing ultra-low sulfur fuels.

Last but not the least, the strong binding of S-molecules on coordinatively unsaturated atoms in small Pd particles led to loss in catalyst activity in HDS of 4,6-DMDBT; when considering the 4,6-DMDBT conversion rate and S-free products formation rates, $MgAl_2O_4$ supported Pd catalyst underperformed alumina supported Pd catalyst.

1.9. References

[1] WWF-for a living planet-Living planet report (2008).

[2] D. Hu, J. Jiang, Journal of Environmental Protection. 4 (2013) 746-752.

[3] Environment Canada-Air-Sulphur in Diesel Fuel Regulations, https://www. ec. gc. ca/energie -energy/default. asp?lang=En&n=7A8F92ED-1. (2014).

[4] United State Environmental Protection Agency-Diesel Fuel http://www.epa.gov/OTAQ/fuels/ dieselfuels/index.htm.

[5] TransportPolicy.net-EU: Fuels: Diesel and Gasoline, http://transportpolicy. net/index. php? title=EU:_Fuels:_Diesel_and_Gasoline. (2013).

[6] Directive 2009/30/EC of the European parliament and the council of 23 April 2009, Official Journal of the European Union. L 140/88.

[7] DieselNet-China-Emission Standards, https://www. dieselnet. com/standards/cn/. (2014).

[8] DieselNet-China-Fuel regulations, https://www. dieselnet. com/standards/cn/fuel. php. (2013).

[9] G. Centi, J. Mol. Catal. A. 173 (2001) 287-312.

[10] John C. Berg (Ed.), **An Introduction to INTERFACES & COLLOIDS: The Bridge to Nanoscience**, World Scientific Publishing Co. Pte. Ltd., Singapore, 2010.

[11] N. Toshima, in: Lyshevski, S.E., Contescu, C.I. and Putyera, K. (Eds.), Dekker Encyclopedia of Nanoscience and Nanotechnology, second ed., Taylor & Francis, 2009, pp. 2052-2063.

[12] G. Schmid, in: B. Corain, G. Schmid, N. Toshima (Ed.), **Metal Nanoclusters in Catalysis and Materials Science: The Issue of Size Control** , Elsevier B.V., Amsterdam, 2008, pp. 3-20.

[13] H. Bonnemann, K.S. Nagabhushana, in: B. Corain, G. Schmid, N. Toshima (Ed.), **Metal Nanoclusters in Catalysis and Materials Science: The Issue of Size Control** , Elsevier B.V., Amsterdam, 2008, pp. 21-48.

[14] N. Toshima, H. Yan, Y. Shiraishi, in: B. Corain, G. Schmid, N. Toshima (Ed.), **Metal Nanoclusters in Catalysis and Materials Science: The Issue of Size Control**, Elsevier B.V., Amesterdam, 2008, pp. 49-75.

[15] R. van Hardeveld, F. Hartog, Surf. Sci. 15 (1969) 189-230.

[16] N. Semagina, L. Kiwi-Minsker, Catal. Rev. 51 (2009) 147-217.

[17] A. Molnar, A. Sarkany, M. Varga, J. Mol. Catal. A. 173 (2001) 185-221.

[18] M. Liu, J. Zhang, J. Liu, W.W. Yu, J. Catal. 278 (2011) 1-7.

[19] P. Lu, N. Toshima, Bull. Chem. Soc. Jpn. 73 (2000) 751-758.

[20] P. Lu, T. Teranishi, K. Asakura, M. Miyake, N. Toshima, J. Phys. Chem. B. 103 (1999) 9673-9682.

[21] N. Toshima, T. Yonezawa, New J. Chem. 22 (1998) 1179-1201.

[22] Y. Wang, N. Toshima, J. Phys. Chem. B. 101 (1997) 5301-5306.

[23] N. Toshima, P. Lu, Chem. Lett. 25 (1996) 729-730.

[24] N. Toshima, T. Yonezawa, K. Kushihashi, J. Chem. Soc. , Faraday Trans. 89 (1993) 2537-2543.

[25] M.M. Koebel, L.C. Jones, G.A. Somorjai, J. Nanopart. Res. 10 (2008) 1063-1069.

[26] C.K. Tsung, J.N. Kuhn, W. Huang, C. Aliaga, L.I. Hung, G.A. Somorjai, P. Yang, J. Am. Chem. Soc. 131 (2009) 5816-5822.

[27] M. Jin, H. Liu, H. Zhang, Z. Xie, J. Liu, Y. Xia, Nano Res. 4 (2011) 83-91.

[28] J. Xian, Q. Hua, Z. Jiang, Y. Ma, W. Huang, Langmuir. 28 (2012) 6736-6741.

[29] Y. Borodko, S.E. Habas, M. Koebel, P. Yang, H. Frei, G.A. Somorjai, J. Phys. Chem. B. 110 (2006) 23052-23059.

[30] Y. Borodko, S.M. Humphrey, T.D. Tilley, H. Frei, G.A. Somorjai, J. Phys. Chem. C. 111 (2007) 6288-6295.

[31] L. Qiu, F. Liu, L. Zhao, W. Yang, J. Yao, Langmuir. 22 (2006) 4480-4482.

[32] Y. Xia, Y. Xiong, B. Lim, S.E. Skrabalak, Angew. Chem. Int. Ed. 48 (2009) 60-103.

[33] R.W.J. Scott, A.K. Datye, R.M. Crooks, J. Am. Chem. Soc. 125 (2003) 3708-3709.

[34] M.G. Weir, M.R. Knecht, A.I. Frenkel, R.M. Crooks, Langmuir. 26 (2010) 1137-1146.

[35] W. Huang, J.N. Kuhn, C.K. Tsung, Y. Zhang, S.E. Habas, P. Yang, G.A. Somorjai, Nano Lett. 8(7) (2008) 2027-2034.

[36] R.W.J. Scott, O.M. Wilson, R.M. Crooks, J. Phys. Chem. B. 109 (2005) 692-704.

[37] R.W.J. Scott, O.M. Wilson, R.M. Crooks, Chem. Mater. 16 (2004) 5682-5688.

[38] J.C. Garcia-Martinez, R.W.J. Scott, R.M. Crooks, J. Am. Chem. Soc. 125 (2003) 11190-11191.

[39] H. Ye, R.W.J. Scott, R.M. Crooks, Langmuir. 20 (2004) 2915-2920.

[40] R.W.J. Scott, O.M. Wilson, S.H. Oh, E.A. Kenik, R.M. Crooks, J. Am. Chem. Soc. 136 (2004) 15583-15591.

[41] R.M. Anderson, L. Zhang, J.A. Loussaert, A.I. Frenkel, G. Henkelman, R.M. Crooks, ACS Nano. 7 (2013) 9345-9353.

[42] P. Dash, T. Bond, C. Fowler, W. Hou, N. Coombs, R.W.J. Scott, J. Phys. Chem. C. 113 (2009) 12719-12730.

[43] J.S. Kim, Soft Nanosci. Lett. 13 (2007) 566-570.

[44] T. Teranishi, M. Miyake, Chem. Mater. 10 (1998) 594-600.

[45] H. Hashemipour, M.E. Zadeh, R. Pourakbari, P. Rahimi, Int. J. Phy. Sci. 6 (2011) 4331-4336.

[46] G.G. Couto, J.J. Kleinb, W.H. Schreiner, D.H. Mosca, A.J.A. de Oliveira, A.J.G. Zarbina, J. Colloid Interface Sci. 311 (2007) 461-468.

[47] L. Guo, Q.J. Huang, X.Y. Li, S. Yang, Langmuir. 22 (2006) 7867-7872.

[48] J.M. Khurana, K. Vij, catal. lett. 138 (2010) 104-110.

[49] T. Balcha, J.R. Strobl, C. Fowler, P. Dash, R.W.J. Scott, ACS Catal. 1 (2011) 425-436.

[50] P. Zhang, Y. Hu, B. Li, Q. Zhang, C. Zhou, H. Yu, X. Zhang, L. Chen, B.W. Eichhorn, S. Zhou, ACS Catal. 5 (2015) 1335-1343.

[51] C. Aliaga, J.Y. Park, Y. Yamada, H.S. Lee, C.K. Tsung, P. Yang, G.A. Somorjai, J. Phys. Chem. C. 113 (2009) 6150-6155.

[52] H. Wang, H. Tang, J. He, Q. Wang, Mater. Res. Bull. 44 (2009) 1676-1680.

[53] R.M. Rioux, H. Song, M. Grass, S. Habas, K. Niesz, J.D. Hoefelmeyer, P. Yang, G.A. Somorjai, Top. Catal. 39 (2006) 167-174.

[54] C. Cui, L. Gan, M. Heggen, S. Rudi, P. Strasser, Nat. Mater. 12 (2013) 765-771.

[55] A. Cao, R. Lu, G. Veser, Phys. Chem. Chem. Phys. 12 (2010) 13499-13510.

[56] P. Gelin, M. Primet, Appl. Catal. B. 39 (2002) 1-37.

[57] J. Sehested, A. Garlsson, T.V.W. Janssens, P.L. Hansen, A.K. Datye, J. Catal. 197 (2001) 200-209.

[58] S.H. Joo, J.Y. Park, C.K. Tsung, Y. Yamada, P. Yang, G.A. Somorjai, Nat. Mater. 8 (2009) 126-131.

[59] M. Cargnello, J.J. Delgado Jaen, J.C. Hernandez Garrido, K. Bakhmutsky, T. Montini, J.J. Calvino Gamez, R.J. Gorte, P. Fornasiero, Sci. 337 (2012) 713-717.

[60] D. Mei, V.M. Lebarbier, R. Rousseau, V.A. Glezakou, K.O. Albrecht, L. Kovarik, M. Flake, R.A. Dagle, ACS Catal. 3 (2013) 1133-1143.

[61] T.W. Hansen, A.T. Delariva, S.R. Challa, A.K. Datye, Acc. Chem. Res. 46 (2013) 1720-1730.

[62] J.A. Moulijn, A.E. van Diepen, F. Kapteijn, Appl. Catal. A. 212 (2001) 3-16.

[63] A. Cao, G. Veser, Nat. Mater. 9 (2010) 75-81.

[64] W.Z. Li, L. Kovarik, D. Mei, J. Liu, Y. Wang, C.H.F. Peden, Nat. Commun. 4:2481 (2013).

[65] Y. Liu, S. Wang, T. Sun, D. Gao, C. Zhang, S. Wang, Appl. Catal. B. 119-120 (2012) 321-328.

[66] J. Ge, Q. Zhang, T. Zhang, Y. Yin, Angew. Chem. Int. Ed. 47 (2008) 8924-8928.

[67] I. Lee, Q. Zhang, J. Ge, Y. Yin, F. Zaera, Nano Res. 4(1) (2011) 115-123.

[68] H.B. Liu, U. Pal, J.A. Ascencio, J. Phys. Chem. C. 112 (2008) 19173-19177.

[69] F. Tao, M.E. Grass, Y. Zhang, D.R. Butcher, J.R. Renzas, Z. Liu, J.Y. Chung, B.S. Mun, M. Salmeron, G.A. Somorjai, Sci. 322 (2008) 932-934.

[70] K.J.J. Mayrhofer, V. Juhart, K. Hartl, M. Hanzlik, M. Arenz, Angew. Chem. Int. Ed. 48 (2009) 3529-3531.

[71] B. Zhu, G. Thrimurthulu, L. Delannoy, C. Louis, C. Mottet, J. Creuze, B. Legrand, H. Guesmi, J. Catal. 308 (2013) 272-281.

[72] D.N. Tafen, J.B. Miller, Ö.N. Doğan, J.P. Baltrus, P. Kondratyuk, Surf. Sci. 608 (2013) 61-66.

[73] A.I. Frenkel, Chem. Soc. Rev. 41 (2012) 8163-8178.

[74] S. Alayoglu, P. Zavalij, B. Eichhorn, Q. Wang, A.I. Frenkel, P. Chupas, ACS Nano. 3 (2009) 3127-3137.

[75] C. Song, A.D. Schmitz, Energy Fuels. 11 (1997) 656-661.

[76] H. Du, C. Fairbridge, H. Yang, Z. Ring, Appl. Catal. A. 294 (2005) 1-21.

[77] U. Nylen, L. Sassu, S. Melis, S. Järås, M. Boutonnet, Appl. Catal. A. 299 (2006) 1-13.

[78] G.B. McVicker, M. Daage, M.S. Touvelle, C.W. Hudson, D.P. Klein, W.C.B. Jr., B.R. Cook, J.G. Chen, S. Hantzer, D.E.W. Vaughan, E.S. Ellis, O.C. Feeley, J. Catal. 210 (2002) 137-148.

[79] P.T. Do, W.E. Alvarez, D.E. Resasco, J. Catal. 238 (2006) 477-488.

[80] R. Moraes, K. Thomas, S. Thomas, S. van Donk, G. Grasso, J.P. Gilson, M. Houalla, J. Catal. 286 (2012) 62-77.

[81] S. Dokjampa, T. Rirksomboon, S. Osuwan, S. Jongpatiwut, D.E. Resasco, Catal. Today. 123 (2007) 218-223.

[82] D.G. Blackmond, J.G. Goodwin, J.E. Lester, J. Catal. 78 (1982) 34-43.

[83] D. Kubicka, N. Kumar, P. Maki-Arvela, M. Tiitta, V. Niemi, H. Karhu, T. Salmi, D.Y. Murzin, J. Catal. 227 (2004) 313-327.

[84] C. Marcilly, J. Catal. 216 (2003) 47-62.

[85] M. Santikunaporn, J.E. Herrera, S. Jongpatiwut, D.E. Resasco, J. Catal. 228 (2004) 100-113.

[86] D. Kubicka, M. Kangas, N. Kumar, M. Tiitta, M. Lindblad, D.Y. Murzin, Top. Catal. 53 (2010) 1438-1445.

[87] Z.J. Zhao, L.V. Moskaleva, N. Rösch, ACS Catal. 3 (2013) 196-205.

[88] A. Djeddi, I. Fechete, F. Garin, Catal. Commun. 17 (2012) 173-178.

[89] P. Samoila, M. Boutzeloit, C. Especel, F. Epron, P. Marécot, J. Catal. 276 (2010) 237-248.

[90] P. Samoila, M. Boutzeloit, C. Especel, F. Epron, P. Marécot, Appl. Catal. A. 369 (2009) 104-112.

[91] G. Del Angel, B. Coq, R. Dutartre, F. Figueras, J. Catal. 87 (1984) 27-35.

[92] F.G. Gault, Adv. Catal. 30 (1981) 1-95.

[93] Z. Paal, P. Tetenyi, Nat. 267 (1977) 234-236.

[94] F. Le Normand, k. Kili, J.L. Schmitt, J. Catal. 139 (1993) 234-255.

[95] A.B. Gaspar, L.C. Dieguez, Appl. Catal. A. 201 (2000) 241-251.

[96] C. Poupin, L. Pirault-Roy, C. La Fontaine, L. Tóth, M. Chamam, A. Wootsch, Z. Paál, J. Catal. 272 (2010) 315-319.

[97] G. Espinosa, G. Del Angel, J. Barbier, P. Bosch, V. Lara, D. Acosta, J. Mol. Catal. A. 164 (2000) 253-262.

[98] D. Teschner, L. Pirault-Roy, D. Naudb, M. Guérin, Z. Paál, Appl. Catal. A. 252 (2003) 421-426.

[99] L. Piccolo, S. Nassreddine, M. Aouine, C. Ulhaq, C. Geantet, J. Catal. 292 (2012) 173-180.

[100] H. Ziaei-azad, C.X. Yin, J. Shen, Y. Hu, D. Karpuzov, N. Semagina, J. Catal. 300 (2013) 113-124.

[101] O.M. Masloboishchikova, T.V. Vasina, E.G. Khelkovskaya-Sergeeva, L.M. Kustov, P. Zeuthen, Russ. Chem. Bull. 51 (2002) 249-254.

[102] U. Nylen, B. Pawelec, M. Boutonnet, J.L.G. Fierro, Appl. Catal. A. 299 (2006) 14-29.

[103] A. Stanislaus, A. Marafi, M.S. Rana, Catal. Today. 153 (2010) 1-68.

[104] A. Röthlisberger, R. Prins, J. Catal. 235 (2005) 229-240.

[105] H. Guo, Y. Sun, R. Prins, Catal. Today. 130 (2008) 249-253.

[106] A. Niquille-Röthlisberger, R. Prins, J. Catal. 242 (2006) 207-216.

[107] D.D. Whitehurst, H. Farag, T. Nagamatsu, K. Sakanishi, I. Mochida, Catal. Today. 45 (1998) 299-305.

[108] C. Song, Catal. Today. 86 (2003) 211-263.

[109] A. Ishihara, F. Dumeignil, J. Lee, K. Mitsuhashi, E.W. Qian, T. Kabe, Appl. Catal. A. 289 (2005) 163-173.

[110] M.J. Ledoux, O. Michaux, G. Agostini, J. Catal. 102 (1986) 275-288.

[111] H. Wang, E. Iglesia, ChemCatChem. 3 (2011) 1166-1175.

[112] H. Wang, E. Iglesia, J. Catal. 273 (2010) 245-256.

[113] W. Qian, Y. Yoda, Y. Hirai, A. Ishihara, T. Kabe, Appl. Catal. A. 184 (1999) 81-88.

[114] B. Liu, M.D. Checkel, R.E. Hayes, Can. J. Chem. Eng. 79 (2001) 491-506.

[115] W. Liu, D. Guo, X. Xu, China Petroleum Processing and Petrochemical Technology. 14 (2012) 1-9.

[116] J. Chen, X. Zhang, H. Arandiyan, Y. Peng, H. Chang, J. Li, Catal. Today. 201 (2013) 12-18.

[117] C.K. Ryu, M.W. Ryoo, I.S. Ryu, S.K. Kang, Catal. Today. 47 (1999) 141-147.

[118] T. Shimizu, A.D. Abid, G. Poskrebyshev, H. Wang, J. Nabity, J. Engel, J. Yu, D. Wickham, B. Van Devener, S.L. Anderson, S. Williams, Comb. and Flame. 157 (2010) 421-435.

[119] R. Strobel, J.D. Grunwaldt, A. Camenzind, S.E. Pratsinis, A. Baiker, Catal. Lett. 104 (2005) 9-16.

[120] B. Van Devener, S.L. Anderson, T. Shimizu, H. Wang, J. Nabity, J. Engel, J. Yu, D. Wickham, S. Williams, J. Phys. Chem. C. 113 (2009) 20632-20639.

[121] P.J. Mitchell, R.M. Siewart, US Patent. US5131224 A (1992).

[122] Y.H. Chin, D.E. Resasco, Catal. 14 (1999) 1-39.

[123] R. Lanza, S.G. Jaras, P. Canu, Appl. Catal. A. 325 (2007) 57-67.

[124] T. Ando, Y. Isobe, D. Sunohara, Y. Daisho, J. Kusaka, JSAE Review. 24 (2003) 33-40.

[125] M. Zanolettia, D. Klvana, J. Kirchnerovaa, M. Perriera, C. Guya, Chem. Eng. Sci. 64 (2009) 945-954.

[126] R. Abbasi, L. Wu, S.E. Wanke, R.E. Hayes, Chem. Eng. Res. Des. 90 (2012) 1930-1942.

[127] W.R. Schwartz, L.D. Pfefferle, J. Phys. Chem. 116 (2012) 8571-8578.

[128] K. Fujimoto, F.H. Ribeiro, M. Avalos-Borja, E. Iglesia, J. Catal. 179 (1998) 431-442.

[129] C.A. Muller, M. Maciejewski, R.A. Koeppel, A. Baiker, Catal. Today. 47 (1999) 245-252.

[130] J.N. Carstens, S.C. Su, A.T. Bell, J. Catal. 176 (1998) 136-142.

[131] R. Burch, D.J. Crittle, M.J. Hayes, Catal. Today. 47 (1999) 229-234.

[132] G. Groppi, C. Cristiani, L. Lietti, P. Forzatti, Stud. Surf. Sci. Catal. 130 (2000) 3801-3806.

[133] R.F. Hicks, H. Qi, M.L. Young, R.G. Lee, J. Catal. 122 (1990) 280-294.

[134] C.A. Muller, M. Maciejewski, R.A. Koeppel, A. Baiker, J. Catal. 166 (1997) 36-43.

[135] D. Roth, P. Gelin, A. Kaddouri, E. Garbowski, M. Primet, E. Tena, Catal. Today. 112 (2006) 134-138.

[136] D.L. Mowery, M.S. Graboski, T.R. Ohno, R.L. McCormick, Appl. Catal. B. 21 (1999) 157-169.

[137] T. Ishihara, H. Shigematsu, Y. Abe, Y. Takita, Chem. Lett. (1993) 407-410.

[138] K. Persson, A. Ersson, K. Jansson, N. Iverlund, S. Jaras, J. Catal. 231 (2005) 139-150.

[139] K. Sekizawa, K. Eguchi, H. Widjaja, M. Machida, H. Arai, Catal. Today. 28 (1996) 245-250.

[140] H. Widjaja, K. Sekizawa, K. Eguchi, H. Arai, Catal. Today. 35 (1997) 197-202.

[141] H. Widjaja, K. Sekizawa, K. Eguchi, H. Arai, Catal. Today. 47 (1999) 95-101.

[142] L. Yang, C. Shi, X. He, J. Cai, Appl. Catal. B. 38 (2002) 117-125.

[143] X. Pan, Y. Zhang, Z. Miao, X. Yang, J. Energy Chem. 22 (2013) 610-616.

[144] X. Pan, Y. Zhang, B. Zhang, Z. Miao, T. Wu, X. Yang, Chem. Res. Chin. Univ. 29 (2013) 952-955.

Chapter 2. Iridium- and platinum-free ring opening of indan[1]

2.1. Introduction

Ring opening (RO) of naphthenic rings, when only one C−C bond is cleaved, maintaining the same number of carbon atoms [1], is an attractive reaction for improving fuel quality. Although RO does not necessarily result in the cetane number improvement because of the formation of highly branched products via cleavage of unsubstituted C−C bonds (as opposed to the RO at the substituted positions) [2], it offers other potential benefits to refineries, such as volume increase, improvement of cloud point, and decrease of the polynuclear aromatics content. Catalytic metal function is paramount for RO, as an acid function, necessary for a preliminary six-ring contraction of aromatics to the five-ring, leads to excessive cracking [3-11]. Metal catalysts offer three RO mechanisms: dicarbene, π-adsorbed olefin, and metallocyclobutane reaction paths [12]. The dicarbene path results in the cleavage of unsubstituted secondary C−C bonds, producing highly branched isoparaffins, with π-adsorbed olefin and metallocyclobutane pathways, leading to C−C opening at the substituted positions.

The most active RO catalyst is iridium, which, in most examples, works through the dicarbene mechanism [4, 13, 14]. Platinum has very low activity, but in the RO product distribution, it may be more selective toward unbranched products via π-adsorbed olefin or metallocyclobutane paths. Ir based systems are probably the most studied and reported RO catalysts, with the bimetallic Ir−Pt catalyst being used in refineries as one of the naphtha reforming catalysts [15]. The search for less expensive alternatives driven by the oil industry is getting more complicated, as the fuel regulations have become more stringent with the

---

[1] Chapter 2 of the thesis has been published as: **J. Shen** and N. Semagina, "Iridium- and platinum-free ring opening of indan", *ACS Catalysis* 4 (2014) 268-279. The reaction setup for low-pressure indan ring opening was built by Dr. Cindy-Xing Yin and Dr. Kavithaa Loganathan in collaboration with machine shop and instrument shop in the department of Chemical and Material Engineering, University of Alberta. Dr. Dimitre Karpuzov performed XPS analysis at Alberta Centre for Surface Engineering and Science (ACSES), University of Alberta. NAA analysis was performed by Becquerel Laboratories Inc., Maxxam Analytics, Ontario. The author performed all syntheses, reactions, analyses and other characterizations. This paper was reprinted with Permission from Ref [51]. Copyright © 2014 American Chemical Society.

simultaneous decrease in the quality of crude oil. Iridium, which is one of the rarest elements on Earth, is sought to be replaced by a catalyst with high hydrogenolysis activity to maintain high RO yields and to prevent catalyst coking [16], while the role of platinum in forming products with higher cetane numbers and its hydrogenation ability should not be lost, either.

The objective of this work was to develop less expensive iridium- and platinum-free alternatives for RO. Only metal function is targeted in the current work. The search for an Ir alternative is complicated by its highest known RO activity [1]. A recent density functional theory (DFT) study revealed that the activation barrier for MCP RO increases in the order of Rh < Ir ≪ Pt < Pd, which is consistent with experimentally observed activities [17]. Rh, Re, Ru, and Ni show a similar RO mechanism as Ir (i.e., rupture of unsubstituted C−C bonds), but they are found to be less selective than Ir because of the extensive secondary cracking of the primary C6-alkane RO products to C1−C5 paraffins, especially in the case of Ru [1, 18]. Catalytic properties are also greatly affected by the reactant nature [3]. In pentylcyclopentane RO, the RO selectivities follow the trend Ir (92%) > Rh (87%) > Ru (82%) > Pt (68%) [1]. In methylcyclohexane RO, the trend is Ir (87%) ≫ Pt, Ni and Ru (4−5%) [1], but in the C7-alkane product distribution, n-hexane is produced in higher amounts by Ru (13%) than by Ir (5%). This indicates that Ru might be a valid alternative to Ir, and it could even outperform Ir in terms of cetane number improvement in real complex feeds, as compared with simple model compounds.

A feasible way to bring up the selectivity of Ru toward single cleavage products, at least to the level of Ir, is to add a second component, creating a bimetallic catalyst [19]. A variety of bimetallic catalysts were reported for RO [18, 20-26]. Among them, a Pt−Rh bimetallic catalyst allowed for the increasing RO activity and selectivity, which were similar to those of Ir catalysts [20], but the cost of Rh sets limitations on the catalyst exploitation. The addition of Ru to Pt improved Pt RO activity only when there was a high Ru portion in the bimetallic system; the bimetallic Pt−Ru catalyst favored deep hydrogenolysis compared with the catalytic behavior of the monometallic Pt catalyst, regardless of the Ru content [18].

In selecting the second metal for the alternatives to the currently used Pt−Ir system, it is paramount to keep the Pt-like mechanism of RO via a flat-lying mode [1, 27]. Only Pd follows a similar mechanism [28]. It was not studied as frequently as Pt in RO because of its very low activity [17, 29]. The substitution of Pt by Pd in Ir-based bimetallic RO catalysts was addressed in some recent works. In our study of indan RO, Pd was shown to serve only as a dispersing agent to Ir, without contributing to its intrinsic activity or selectivity, as long as an ensemble of two Ir atoms required for the dicarbene path was not destroyed by Pd addition, resulting in activity loss [24]. Another study included tetralin hydroconversion in the presence of ppm amounts of H_2S and revealed that the catalytic activity increased with Pd content, while the selectivity to RO/contraction products reached the maximum at Ir55−Pd55 composition [25].

Thus, a Ru−Pd system may be envisioned as a prominent alternative to the Ir−Pt system, as soon as the high hydrogenolysis activity of Ru, resulting in lower selectivity as compared with Ir, can be reduced by Pd addition. Notably, the d-level occupancy of Ir is in between the levels for Ru and Pd; thus, it seems feasible to create a Ru−Pd bimetallic system with a similar surface free energy as Ir. Both Ru and Pd have close atomic radii, and the bimetallic crystal structure may be predicted to change from the fcc structure of Pd to the hcp structure of Ru with increasing Ru content, as shown for Pt−Ru systems [30]. We recently addressed the probability of using some Ru−Pd catalysts in indan RO [31], which showed that their activity and selectivity decreased as compared with their monometallic counterparts and were lower than those of Ir, but the used bimetallic nanoparticle sizes were significantly larger than those of monometallic ones, and the applied synthetic methods were different. The previously applied procedure to prepare Ru-rich nanoparticles resulted in Pd abundance in the nanoparticle outer shell, as confirmed by ion scattering spectroscopy, with Pd being responsible for poor activity. Still, motivated by the system potential, we extended our quest to the mono- and bimetallic nanoparticles of similar size of ~ 2−3 nm, but with wide ranges of Pd-to-Ru ratios and various loci of the two atom types in a nanoparticle. The modified synthetic techniques allowed us to enrich the nanoparticle shell with Ru atoms for some catalysts. It should be noted that the used abbreviations only reflect the molar composition of final catalysts (such as Ru4Pd1) or the mode of a catalyst preparation (such as Pd(core)Ru(shell)), and they should not be considered as a phase composition or a real structure of the nanoparticle. As will be shown below, the developed nanoparticle synthetic techniques yielded a Ru−Pd catalyst with as high selectivity as Ir in a model RO reaction of indan (Scheme 2.1) and suppressed lights formation as compared with Pt.

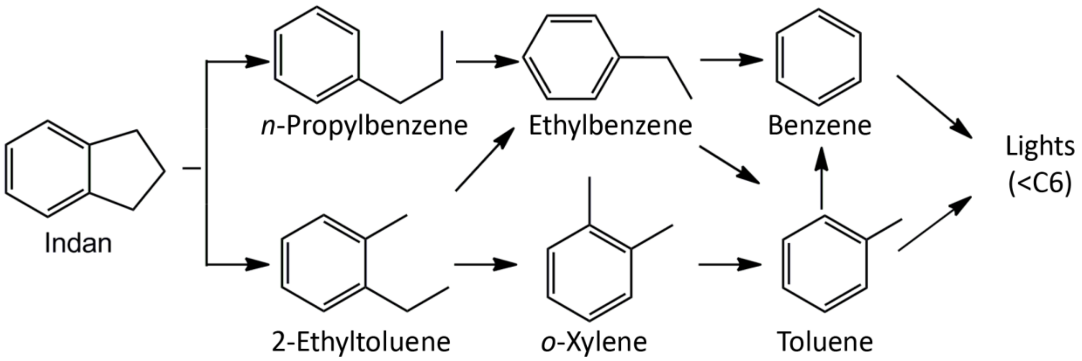

Scheme 2.1. Reaction scheme for low-pressure Indan RO on a metal function [37]; Reproduced with Permission from Ref [37]. Copyright © 2006 Elsevier.

2.2. Experimental section

2.2.1. Materials

Ruthenium(III) nitrosylnitrate ($Ru(NO)(NO_3)_3$, Alfa Aesar), palladium(II) chloride solution ($PdCl_2$, 5% w/v, Acros), hydrogen hexachloroiridate(IV) hydrate (H_2IrCl_6, 99.98%, Sigma-Aldrich), chloroplatinic acid solution (H_2PtCl_6, 8 wt.% in H_2O, Sigma-Aldrich), poly(vinylpyrrolidone) (PVP) (MW 40,000, Sigma-Aldrich), reagent alcohol (ethanol, 95 vol.%, Fisher Scientific), ethylene glycol (EG, 99.8%, Sigma-Aldrich), gamma-aluminum oxide (γ-Al_2O_3, 150 mesh 58 Å pore size, Sigma-Aldrich), acetone (99.7%, Fisher Scientific) and 2-methyl-3-buten-2-ol (MBE, 97%, Acros Organics) and benzocyclopentane (indan, 95%, Sigma-Aldrich) were used as received. Argon, hydrogen, 10% hydrogen in helium, 10% oxygen in argon, and 3% carbon monoxide in helium of ultrahigh purity 5.0 were purchased from Praxair. Milli-Q water was used throughout the work.

2.2.2. Catalyst preparation and pretreatment

All catalysts were prepared by growing 2−3 nm nanoparticles in a colloidal dispersion in the presence of PVP, followed by precipitation on γ-Al_2O_3 with 5.8 nm pores and high-temperature PVP removal. As opposed to our previous work, in which large nanoparticles were obtained with the PVP/metal(s) molar ratio of 10/1 [31], in this work, the ratio was kept at 20 (unless indicated otherwise), and the synthetic procedures were modified, which allowed for us to produce ~ 2−3 nm nanoparticles with various loci of the two atom types in a nanoparticle.

Table 2.1. Summary of the synthesized nanoparticles and γ-Al_2O_3-supported catalysts.

metal precursor(s)	reducing agent[a]	synthesized nanoparticles[b]	size distribution, nm	metal loading in supported catalyst, wt.%
Pd^{2+}	Et/H_2O	Pd	2.0±0.5	0.231
	EG	Pd	~ 7	not used for catalysis
Ru^{3+}	Et/H_2O	no reduction		N/A
	EG	Ru	2.0±0.3	0.300
high molar ratio of Pd^{2+}/Ru^{3+}	Et/H_2O (Scheme 2.2)	Ru4Pd1	2.2±0.5	Ru: 0.166, Pd: 0.046
		Ru2Pd1	2.6±0.6	Ru: 0.154, Pd: 0.065
		Ru1Pd1	3.1±0.7	Ru: 0.111, Pd: 0.090
		Ru1Pd2	2.8±0.5	Ru: 0.082, Pd: 0.143
	EG[c]	(Ru4Pd1)[c]	2.9±0.6[c]	N/A[c]
		(Ru1Pd1)[c]	3.6±1.2[c]	
		(Ru1Pd2)[c]	5.3±0.9[c]	
high molar ratio of Ru^{3+}/ Pd^{2+}	EG	Ru10Pd1	2.1±0.4	Ru: 0.267, Pd: 0.028
		Ru8Pd1	2.0±0.3	Ru: 0.275, Pd: 0.034
		Ru6Pd1	2.0±0.3	Ru: 0.206, Pd: 0.039
Pd^0 (2 nm) and Ru^{3+}	Et/H_2O (Scheme 2.3)	Pd(c)Ru(s), Ru/Pd = 1.6	2.3±0.7	Ru: 0.140, Pd: 0.095
Ir	EG	Ir	1.7±0.3	0.173
Pt	EG	Pt	3.2±0.4	0.205

[a] Et, ethanol; EG, ethylene glycol. [b] Numbers in the catalyst notation correspond to the rounded molar ratio of the two metals in the supported catalysts, as determined by NAA. [c] These catalysts were synthesized and reported for the same catalytic reaction in our previous work [31].

A summary of the prepared catalysts is presented in Table 2.1. Monometallic Pd nanoparticles were synthesized by Teranishi and Miyake's one-step alcohol (ethanol/water system) reduction method [32] with some modifications. A mixture containing 0.712 mL (0.2 mmol) of 5% w/v $PdCl_2$ aqueous solution, 170 mL of ethanol/water ([ethanol] = 41 vol.%), and 0.444 g of PVP (MW 40,000) was stirred and refluxed in a 500 mL 3-neck round-bottom flask for 3 h under air. The PVP stabilized monometallic Ru, Ir, and Pt nanoparticles were prepared using the ethylene glycol (EG) reduction method [33, 34]. At room temperature, 0.2 mmol of metal precursor salt ($Ru(NO)(NO_3)_3$, H_2IrCl_2 or H_2PtCl_6) and 0.444 g of PVP (MW 40,000) were well dissolved in 200 mL of EG in a 500 mL single-neck round-bottom flask. The reduction temperature was increased from room temperature to the reflux point of EG (198 °C), and then it was maintained at 198 °C for 3 h. After reactions, transparent dark-brown macroscopically homogeneous colloidal dispersions of monometallic Ru, Pd, Ir and Pt nanoparticles were obtained without any precipitate.

In this study, three different synthesis techniques were applied to produce Ru−Pd bimetallic nanoparticles: (1) to obtain catalysts with high Ru-to-Pd molar ratio, a simultaneous reduction of both Ru and Pd precursors was applied using the synthetic procedure for monometallic Ru nanoparticles. Three different metal molar ratios were synthesized: Ru10Pd1, Ru8Pd1, and Ru6Pd1 (Ru/Pd molar ratios = 10/1, 8/1, and 6/1, respectively). The total amount of Ru and Pd precursors in each synthesis was 0.2 mmol, while all other experimental conditions were kept the same. (2) To obtain catalysts with lower Ru-to-Pd molar ratio but Ru-enriched surfaces, we used a modified general synthetic procedure for the synthesis of Ru−Pt nanoparticles, proposed by Liu et al. [35] (Scheme 2.2). The experimental conditions followed the preparation method for monometallic Pd nanoparticles in an ethanol/water system, with 0.2 mmol of Ru and Pd in each reaction. A series of Ru−Pd nanoparticles with different compositions were prepared by varying Ru-to-Pd molar ratios: Ru4Pd1, Ru2Pd1, Ru1Pd1, and Ru1Pd2. (3) To obtain the Pd(core)−Ru(shell) nanoparticles (Scheme 2.3), Teranishi and Miyake's stepwise growth reaction method was applied [32]. A 42.5 mL portion of colloidal solution containing 0.05 mmol of PVP-stabilized Pd core nanoparticles was prepared using the synthesis method of monometallic Pd nanoparticles. A 0.032 g portion of $Ru(NO)(NO_3)_3$ precursor (0.1 mmol) and the presynthesized Pd core colloidal solution were dissolved in 170 mL of ethanol/water ([ethanol] = 41 vol.%) at room temperature. This mixture was then heated up to its reflux point. During the shell preparation step, no more fresh PVP was added. A dark brown macroscopically homogeneous colloidal dispersion of Pd(c)Ru(s) nanoparticles was obtained after refluxing for 3 h without any precipitate.

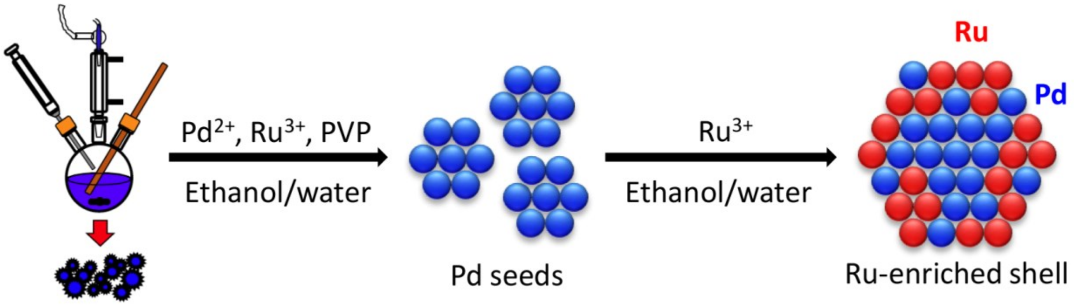

Scheme 2.2. Synthesis of Ru4Pd1, Ru2Pd1, Ru1Pd1, and Ru1Pd2 Catalysts with Ru-Enriched Shells.

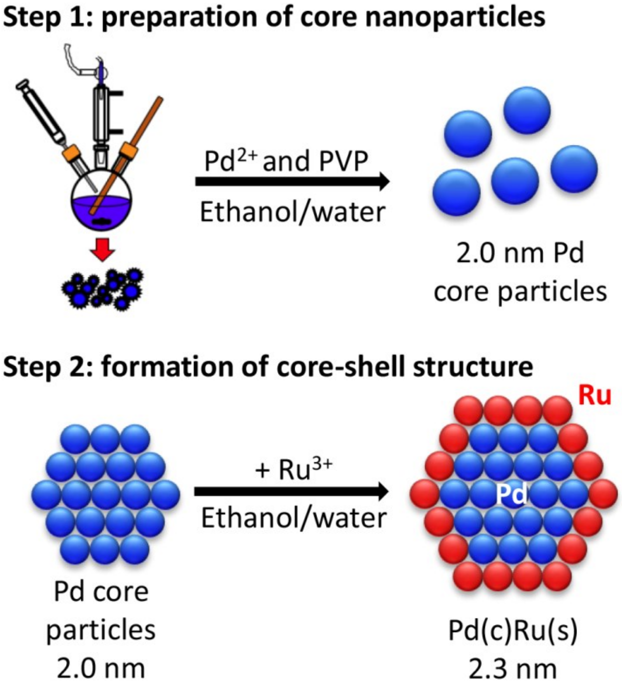

Scheme 2.3. Formation of Ru−Pd Bimetallic Nanoparticles with Pd (Core)−Ru (Shell) Structure.

2.2.3. Catalyst characterization

Transmission electron microscopy (**TEM**), neutron activation analysis (**NAA**), and X-ray photoelectron spectroscopy (**XPS**) of as-prepared metal nanoparticles and/or supported catalysts were performed as described earlier [31]. For the TEM, 100−200 particles per sample were counted from TEM images using ImageJ software.

Temperature Programmed Reduction (**TPR**). TPR experiments of supported catalysts were performed with H_2/Ar gas mixture using an AutoChem 2950HP instrument (Micromeritics, U.S.A.) equipped with a thermal conductivity detector (TCD). To eliminate any effects arising from PVP removal, a series of oxidation-reduction-oxidation-reduction were performed, and the reported results refer to the final reduction step. Prior to the analysis, the catalysts with as deposited nanoparticles were calcined at 200 °C in air for 2 h; 0.5 g of precalcined catalysts were loaded in a quartz reactor. The precalcined catalysts were reduced in a flow of 10% H_2/Ar (50 mL/min) at 375 °C for 1 h. These conditions simulate the pretreatment procedure before the RO reactions. After the calcination-reduction pretreatment, the samples were flashed with inert (He) for 30 min at 375 °C and cooled down to ambient temperature under inert. The catalysts were then heated in a flow of 10% O_2/He gas mixture at a linear rate of 10 °C/min from room temperature to 400 °C (to make sure that all PVP was removed as its decomposition temperature is 350 °C) and then flashed with inert (Ar) for 30 min at 400 °C and cooled down to room temperature in Ar. This oxidation procedure was then followed by a TPR analysis from room temperature to 400 °C (i.e., heating in 10% H_2/Ar gas stream at 10 °C/min). The TCD signals for TPR profiles are reported as inverted signals; thus, positive peaks refer to the consumption of hydrogen (due to relative thermal conductivities of Ar and H_2).

CO Chemisorption. The catalyst samples were calcined at five different temperatures: 200, 250, 300, 350, and 400 °C, followed by the reduction 375 °C as described above in TPR sample preparation. Dynamic CO pulse chemisorption analyses were performed by dosing 3% CO/He gas mixture at room temperature with an AutoChem 2950HP instrument. The volumetric flow rates of CO/He loop gas and He carrier gas were 10 mL/min and 50 mL/min, respectively. The amount of catalyst varied from 0.2 to 2 g to obtain equally sized TCD peaks within 10 doses. CO uptake per gram of pure support (γ-Al_2O_3) was also evaluated using 2 g of alumina, which was subtracted from the values for the supported catalysts.

Temperature Programmed Desorption of CO (**CO-TPD**). PVP-stabilized nanocatalysts were calcined at 350 °C for 1 h to efficiently remove surface polymers, according to the CO chemisorption results. The precalcined catalyst (0.75−0.80 g) was packed in the quartz reactor and reduced in 10% H_2/Ar at 375 °C for 1 h. The reduced sample was outgassed at 375 °C under Ar for 30 min and then cooled down to room temperature in Ar. Then, 3% CO/He was passed through the sample for 30 min with a flow rate of 50 mL/min. The physically adsorbed CO was removed by flashing the sample with He for 30 min. The sample was then heated up under He flow (10 mL/min) from room temperature to 400 °C with a ramping rate of 10 °C/min, while the TCD signals of CO desorption were recorded as a function of temperature. Two controlled runs were made on the γ-alumina support and a mono-Ru/γ-alumina catalyst without CO treatment. Additionally, CO chemisorption of bare support has proven that the amount of CO adsorbed by γ-alumina is negligible, which is less than 1 mol.% of the CO molecules adsorbed by the supported catalyst. Thus, the observed TCD signals correspond only to desorption of CO molecules from metallic surfaces.

Diffuse Reflectance Infrared Fourier Transform Spectroscopy of the adsorbed CO (**CO−DRIFTS**). Diffuse reflectance infrared spectra were obtained using NEXUS 670 FT-IR fitted with a Smart Diffuse Reflectance accessory. The catalysts were prepared with an expected metal loading of 2 wt.%. The PVP-stabilized mono- and bimetallic Ru−Pd catalysts were calcined at 200 °C for 1 h to imitate the conditions of pretreatment before the catalytic reaction, reduced in 10% H_2/Ar flow at 375 °C for 30 min, then purged with Ar at 375 °C for 30 min and finally cooled down to room temperature in the inert gas. Then 3% CO/He was passed through the sample for 30 min with a flow rate of 50 mL/min. Finally, the gas phase CO was removed by purging Ar for 30 min. DRIFT spectra were recorded against a KBr standard with 256 scans and a resolution of 4 cm^{-1}. Each sample was measured three times to ensure repeatability. Resolution enhancement and data processing were performed with OMNIC software. The absorption bands were deconvoluted using Origin software.

Chemical Reaction Probe for Surface Pd. To elucidate whether some Pd atoms are present in the outermost layer of bimetallic nanoparticles, a reaction was selected that was catalyzed by Pd and that did not show any conversions on Ru, which was the hydrogenation of 2-methyl-3-buten-2-ol to a corresponding saturated alcohol (Scheme 2.4).

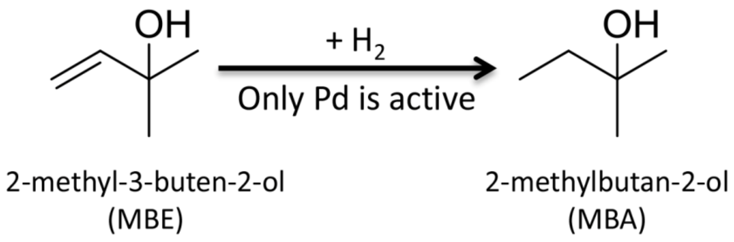

Scheme 2.4. Chemical Reaction Probe for Surface Pd Atoms

The reactions were carried out in a semibatch stainless steel reactor (300 mL autoclave, Parr Instruments 4560 mini Bench Top Reactor) equipped with a high-temperature fabric heating mantle, a gas buret for the continuous isobaric hydrogen supply, and thermocouple, as described previously [36]. The hydrogenation of MBE was conducted at 40 °C and 0.45 MPa absolute pressure. The reactor was filled with 0.04 M MBE in 200 mL of ethanol and 0.5 g of as-prepared catalyst, flashed with nitrogen, and stirred to reach the reaction temperature. Once the desired reaction temperature was achieved, the reactor was then flashed and pressurized with hydrogen. The stirring speed was 1,200 rpm. The experimental conditions have previously confirmed the absence of mass transfer limitations [36]. During the reaction, hydrogen pressure in the gas buret and the reactor's internal temperature were recorded. At least three catalytic trials were performed for most of the catalysts. The initial reaction rate was considered as the consumption rate of hydrogen; it was calculated from the slope of the hydrogen consumption graph once the hydrogen dissolution had completed.

2.2.4. Low pressure RO of indan

Low-pressure indan RO (Scheme 2.1) was performed in a packed bed reactor according to our previous study, with some modifications in the experimental conditions [31]. The PVP-stabilized monometallic Pd, Ru, Ir and Pt, and bimetallic Ru−Pd catalysts were calcined at 200 °C in an oven under air for 2 h. Catalysts were then reduced in situ at 375 °C under a hydrogen flow (80 mL/min) for 1 h. The precalcined catalyst loading to the reactor corresponds to 4 mg active metal(s), unless stated otherwise. Indan was fed into the catalytic system by bubbling 120 mL/min (STP conditions) H_2 through indan at a constant temperature bath at 10 °C. An indan flow rate of $(4.7\pm0.6)\times10^{-6}$ mol/min was confirmed by GC, which was calibrated using a gas cylinder containing indan with a known concentration. A high H_2-to-indan molar ratio, 900−1,500 $\mathrm{mol_{H_2}/mol_{indan}}$, was used to avoid coke formation. The reactions were performed at an internal temperature of 350 °C and 1 atm pressure. The outgoing stream was analyzed online with a Varian 430-GC-FID every 24 min after the reaction was started. The detailed GC conditions can be found elsewhere [31]. In the previous study, we reported that the RO products are 2-ethyltoluene, *n*-propylbenzene, *o*-xylene, ethylbenzene, toluene, benzene, and lights (mainly methane and ethane), which are in agreement with the results published by Nylen et al. [37] The desired RO products are 2-ethyltoluene and *n*-propylbenzene, in which the naphthenic ring has been cleaved only once. Further dealkylation to toluene, benzene, and lights, is undesirable.

A steady state was achieved at 80 min time on stream. Raw GC results were corrected for indan impurities, and all calculations for catalytic performances were based on the corrected GC results. The selectivities are reported on a mass basis as molar selectivity can give a distorted picture of indan utilization, because up to 9 moles of methane may be produced per mole of indan. Reported selectivities are integral selectivities that were calculated as the ratio of the amount of each RO product formed to the total amount of RO products (impurities are not included). The GC-FID response factors for 2-ethyltoluene, *n*-propylbenzene, *o*-xylene, ethyltoluene, and lights were found using calibration cylinders with a known concentration for each component; GC areas for benzene and toluene were calibrated using a bubbler by assuming saturation in H_2. Catalytic properties at 100 min time on stream are reported.

2.3. Results and discussions

2.3.1. Characterization of as-prepared nanoparticles

TEM. To avoid possible size effects in the catalytic performance of different mono- and bimetallic nanoparticles, our goal was to develop nanoparticles with similar sizes (within 2−3 nm range) as monodispersed as possible. Metal nanoparticle stabilization with PVP is a well-known method [32, 38, 39], and we modified the generally known synthetic procedures to ensure the size consistency between the different metals, as the size control was found to be dependent on the metal(s) used.

Table 2.1 summarizes the synthetic procedures and size of prepared nanoparticles and their metal loading after deposition on γ-Al_2O_3. The TEM images and size distribution histograms of monometallic particles are shown in Figure 2.1, and the same for the Ru−Pd materials can be found in Figures 2.2. For TEM analysis, 100−200 nanoparticles per sample were counted from TEM images using ImageJ software. The numbers in the catalyst notation (such as Ru4Pd1) correspond to the rounded molar ratio of the two metals in the deposited catalysts as determined by NAA. Pd(c)Ru(s) refers to Pd(core)Ru(shell) and is an abbreviation to show a different catalyst preparation method (Ru reduction on the preformed Pd nanoparticles).

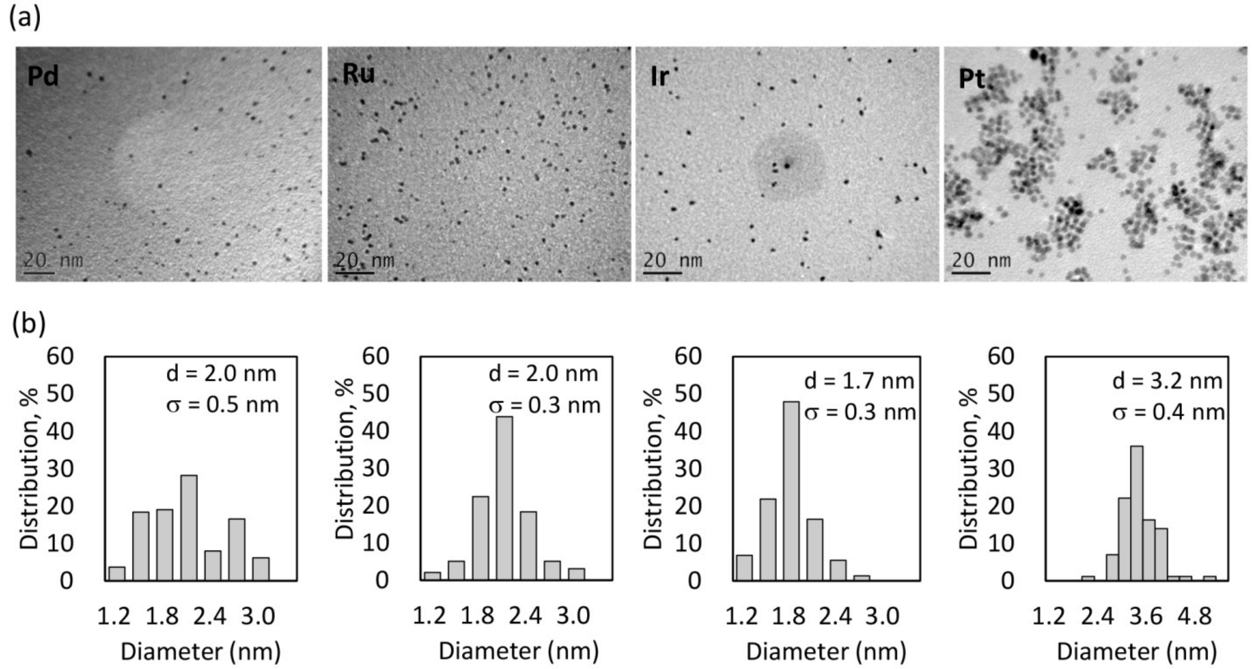

Figure 2.1. TEM images of PVP-stabilized Pd, Ru, Ir and Pt colloids (a) and corresponding size distribution histograms (b).

The obtained bimetallic nanoparticle sizes with the selected reducing methods are consistent with their intrinsic bimetallic nature. When monometallic Pd is reduced by ethanol (Et), 2 nm nanoparticles are observed, while the reduction by ethylene glycol (EG) produces ~ 7 nm particles. Monometallic Ru can be reduced only by EG to 2 nm particles, and no nanoparticle formation was observed in Et. To ensure the reduction, when bimetallic nanoparticles were prepared with high a Ru/Pd molar ratio (Ru10Pd1, Ru8Pd1, and Ru6Pd1), EG was used as a reductant. An average mean diameter of 2.0±0.3 nm was obtained among all the three Ru−Pd bimetallic nanoparticles; if monometallic Pd nanoparticles were present, the 7 nm particles would have been observed. This suggests the bimetallic nature of the nanoparticles, instead of the physical mixtures of 2 and 7 nm particles, corresponding to Ru and Pd, respectively.

However, EG reduction is only an effective method for high Ru content in the Ru−Pd bimetallic system; otherwise, Ru−Pd bimetallic particles reveal not only large particle sizes but also irregularity in particle shapes, and the latter is most likely attributed to the different lattice structures of Pd (fcc) and Ru (hcp). For Pt−Ru systems, the bimetallic crystal structure was found to change from the fcc structure of Pt to the hcp structure of Ru with increasing Ru content

[30]. Indeed, in our previous work [31], when Ru and Pd precursors at a high Pd/Ru ratio were reduced in EG, particles of up to 6 nm diameter were observed (see Table 2.1), and they did not show promising catalytic activity in the RO reaction. In this work, to gradually increase the Pd fraction in the bimetallic structures and preserve their monodispersity, an ethanol/water reduction method [35] was introduced (Ru4Pd1, Ru2Pd1, Ru1Pd1, and Ru1Pd2 in Table 2.1 and Fig. 2.2), that is, the sequential reduction of Pd and then Ru precursors (Scheme 2.2). It is well known that Pd precursor can be easily reduced to Pd metal at a low temperature in alcohol solutions and that the reduced nanoparticles exhibit high monodispersity and a near-spherical shape [32]. Contrary to Pd, the reduction of Ru requires relatively high temperatures; no Ru particles were obtained in low boiling point solvents, such as ethanol/water, which has been examined experimentally (Ru precursor reduction does not occur in ethanol). However, when Pd was present in the Ru^{3+}/ethanol system, Ru precursor was successfully reduced. On average, Ru4Pd1, Ru2Pd1, Ru1Pd1, and Ru1Pd2 prepared by Et reduction have a mean diameter of 2.7 nm. Larger bimetallic particles, as compared with Pd prepared with the same procedure, are indicative of the reduction and growth of Ru atoms on the surface of Pd seeds, and, thus, the bimetallic nature of the synthesized nanoparticles.

We did not elucidate the mechanism of the bimetallic nanoparticle formation. Autocatalytic surface-growth mechanism has been discussed for the formation of noble-metal clusters, when the aggregation of metal ions to small clusters may occur without reducing electrons; the growing oxidation state of the cluster enhances its electron affinity [40]. This may explain why the Ru precursor could be reduced by ethanol in the presence of palladium: Pd^{2+} is easily reduced by ethanol and forms seeds for the further crystal growth by Ru^{3+} deposition followed by facilitated reduction. The order of the reduction is also in line with the standard electrode potentials: +0.915 eV for Pd^{2+}/Pd and +0.68 eV for Ru^{3+}/Ru. The metal (Pd) with the highest potential is reduced first and forms the seeds. Similarly, Liu et al. observed that if there are metallic seeds available, for example, Pt nanoparticles, the reduction of Ru^{3+} can take place on the surface of the seeds to produce zerovalent Ru metal nanoparticles autocatalytically [35].

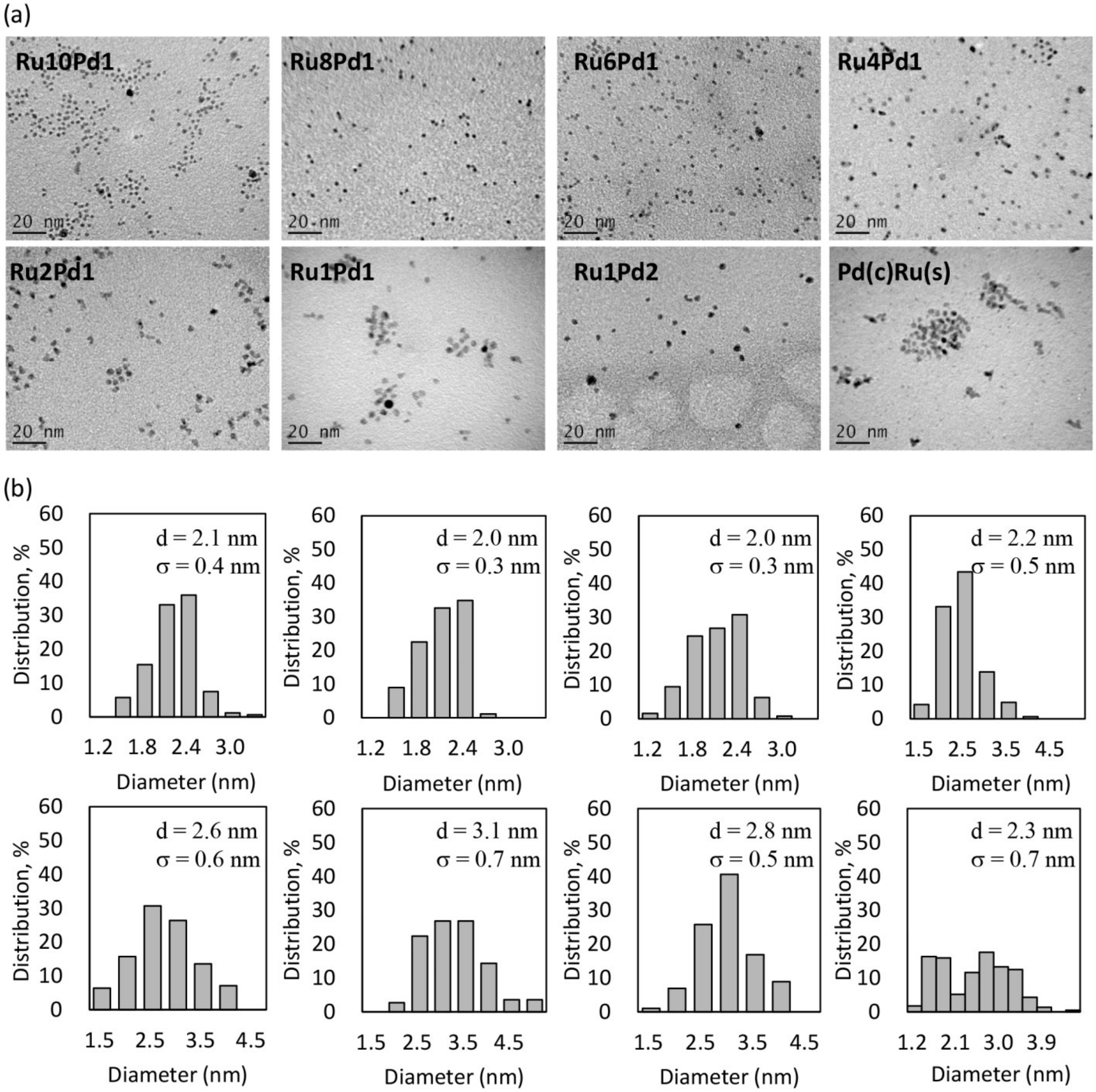

Figure 2.2. TEM images of PVP-stabilized bimetallic Ru−Pd colloids (the scale bar is 20 nm) and corresponding size distribution histograms.

A different 2-step alcohol reduction synthesis for Pd core−Ru shell nanoparticles was used to place Ru atoms only in the nanoparticle shell. Monometallic Pd nanoparticles were synthesized first with an average diameter of 2 nm. Ru precursor was then added to the Pd colloidal dispersion, followed by the reduction of Ru^{3+} and deposition on Pd core particles (Scheme 2.3). The obtained Pd(c)Ru(s) nanoparticles have an average mean diameter of 2.3 nm

(Table 2.1 and Fig. 2.2). The nanoparticles increase in size with the addition of Ru precursors, indicating that Pd nanoparticles in the solution serve as nuclei for larger core−shell particles [32]. According to the metal crystal statistics [41], the 2 nm Pd nanoparticles correspond to an fcc cuboctahedron with 3 atoms on the crystal edge, and to build one more full shell of Ru atoms (which have a similar diameter to Pd), the 2-to-1 Ru-to-Pd molar ratio is required. The ratio determined by NAA of the deposited Pd(c)Ru(s) nanoparticles is 1.6-to-1, which implies that all Ru atoms are mostly likely 100% dispersed on the Pd core nanoparticle. The formation of monometallic Ru particles is unlikely, as no Ru nanoparticles were observed when the Ru precursor alone was treated in ethanol/water.

Chemical Probe Reaction. To further confirm the bimetallic structure of the as-prepared nanoparticles, they were deposited on γ-Al_2O_3 and used without any further pretreatment in a chemical probe reaction, which was the three-phase hydrogenation of 2-methyl-3-buten-2-ol (MBE) to 2-methylbutan-2-ol (MBA, Scheme 2.4) at 40 °C in ethanol. Pd is known for high catalytic activity in this reaction, while Ru at the same conditions is not active, both in the presence and absence of a stabilizer. Single atoms of Pd (not ensembles) are known as active sites in this reaction [36, 42], and because the stabilizer (PVP) and its amount (20/1 molar ratio to the metal) is the same for all the catalysts studied, the Ru, Pd and Ru−Pd systems could be compared in terms of the exposed Pd atoms in the outermost shell of the bimetallic materials. Note that because the stabilizer may affect the catalytic performance, we do not report the turnover frequencies; instead we discuss a qualitative trend based on the observed hydrogenation rates.

Three-phase hydrogenations are well-known for their high susceptibility to mass transfer limitations. The absence of gas-liquid and liquid-solid mass transfer limitations was previously verified by our group for the chosen conditions [36]. In the first step of this investigation, three-phase hydrogenation of MBE to MBA was tested over monometallic Pd and Ru nanoparticles. Pd is extremely active (2.7 $mol_{H_2}/mol_{Pd}/min$), while Ru shows no activity. Thus, MBE hydrogenation can be regarded as an effective chemical probe for surface Pd presence in the Ru−Pd bimetallic surfaces.

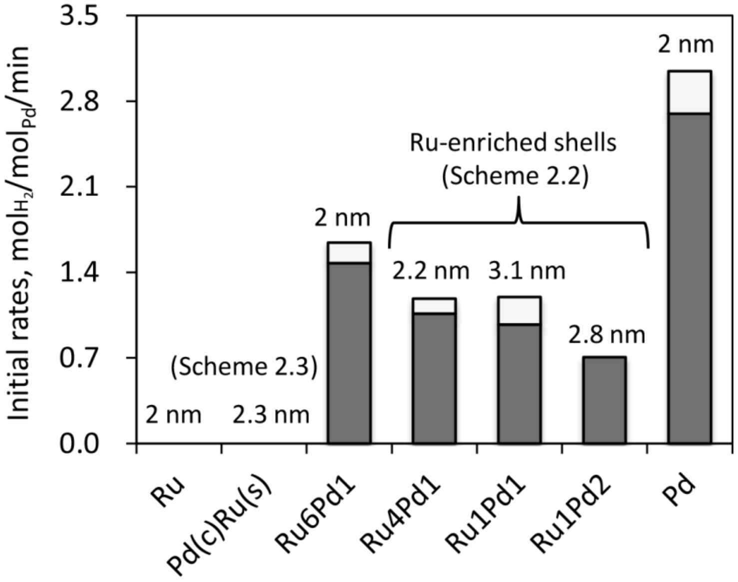

Figure 2.3. MBE hydrogenation reaction rate per Pd atoms in the bimetallic Ru−Pd catalysts (refer to Scheme 2.4). The light gray rectangles correspond to one standard deviation.

The MBE hydrogenation rates were determined at 10% MBE conversion and presented in Figure 2.3 as calculated per total moles of Pd. The Pd(c)Ru(s) catalyst displays zero activity, confirming the coverage of Pd atoms with an inactive Ru shell. Other Ru−Pd compositions show intermediate activities between Pd and Ru even at the same nanoparticle size (such as 2.0−2.2 nm for Ru6Pd1, Ru4Pd1, and monoPd), indicating the presence of both atoms on the nanoparticle surface. If monometallic Pd and Ru particles were formed instead of the bimetallics, the rates would be the same for Ru6Pd1, Ru4Pd1 and mono-Pd, since the nanoparticle sizes are similar. The fact that Ru4Pd1, Ru1Pd1 and Ru1Pd2 catalysts display lower activity than Ru6Pd1 is consistent with their proposed structure as per the synthesis method (Scheme 2.2), which allows for the formation of the Ru-enriched shell. Thus, although the bulk Pd content is the lowest in the Ru6Pd1 catalyst, the proportion of Pd in the outermost atomic layer is higher than in the Ru-enriched shell of Ru4Pd1, Ru1Pd1 and Ru1Pd2, which increases its activity. Some differences in the activities of Ru4Pd1, Ru1Pd1, and Ru1Pd2 catalysts may be attributed to the size effect and the reaction’s structure-sensitivity [36]. The MBE hydrogenation was shown to proceed on (111) and (100) terraces of Pd nanoparticles with different turnover frequencies [36]. We believe that the three latter catalysts possess different relative amounts of the Pd atoms on these surfaces, which contributes to the activity differences. However, all the three catalysts display the lowest activity (after the monoRu and Pd(c)Ru(s) particles), indicating their surface enrichment with Ru. Thus, the chemical probe results are consistent with the proposed bimetallic structures of the as-synthesized nanoparticles as per their synthetic methods (see Table 2.1, Schemes 2.2 and 2.3).

2.3.2. Catalyst characterization after high-temperature treatment

The as-deposited catalysts were subject to high-temperature treatments in air (up to 400 °C) and hydrogen (375 °C) with the purpose of PVP removal (its decomposition temperature is 350 °C) and as preparation for the indan RO reaction that occurs in the gas phase at 350 °C. As ruthenium may form volatile oxides, NAA of the monometallic Ru and bimetallic Ru4Pd1 samples was performed after 400 °C calcination and 375 °C reduction. Ru content before and after the treatments was found as 0.27 wt.% and 0.28 wt.% in the monometallic Ru sample, respectively, and did not change for the bimetallic sample either.

The high-temperature treatments are expected to affect the bimetallic nanoparticle structure and size, altering the Ru-to-Pd ratio in the outermost atomic layers as compared with the freshly prepared nanostructures discussed above. The heat of vaporization of Pd (380 kJ/mol) is lower than the one for Ru (580 kJ/mol), so Pd atoms will tend to migrate to the nanoparticle surface driven by the minimization in the nanoparticle's surface energy. A higher Pd fraction is expected to be in the nanoparticle's shell after the high-temperature treatment, as compared with the as-synthesized nanoparticles. The structural transformations are known to depend on the original nanoparticle size, composition, structure and temperature. They were shown to become significant at ~ 1600 K for Pt−Pd nanoparticles of 3 nm size [43]. In the presence of oxygen, the temperature will be lowered because of the significantly lower melting point of metal oxides.

However, for example, under our pretreatment conditions before the catalytic reaction (200 °C calcination, 375 °C reduction), two Ru1Pd1 composites with the same Ru-to-Pd molar ratios and similar particle size (3.1−3.6 nm) but prepared by two different methods (Et reduction resulting in Ru-enriched shells and EG reduction; see Table 2.1) showed significantly different activities in the indan RO. The EG reduced Ru1Pd1 catalyst was an order-of-magnitude less active [31] than the one reduced by Et (see the catalytic results section below), indicating a different Pd-to-Ru ratio in the outermost nanoparticle layer (the RO activity of monoRu is higher than that of monoPd). This suggests that the applied pretreatment temperature does not result in the very same bimetallic structure starting from two different structures but of the same size and Pd-to-Ru molar ratio. In the current work, we did not attempt to study the structural transformation process upon heating. The following physicochemical characterization of the materials was performed after the same treatments, and the results were correlated with the observed catalytic reaction results.

CO-TPD. CO-TPD was performed after the polymer removal at 350 °C (decomposition temperature of PVP) in air followed by 375 °C reduction. No peaks were detected either for pure γ-alumina support or for a monometallic Ru catalyst with the absence of CO treatment. Figure 2.4 shows a series of CO-TPD profiles for the selected catalysts. Two CO desorption peaks from Pd nanoparticles centered at 74 and 174 °C could be assigned to the desorption from different Pd sites and/or bridged and linear CO complexes on the nanoparticle surface. A much higher CO desorption temperature centered at 265 °C with strong intensity was observed for the mono-Ru catalyst.

Both Pd(c)Ru(s) and Ru4Pd1 samples reveal a single CO desorption peak at higher temperatures than those of mono-Ru nanoparticles and no low-temperature peaks characteristic for Pd. As per the synthesis techniques (Schemes 2.3 and 2.2, respectively), the nanoparticle shell enrichment with Ru is expected, keeping in mind the possible Pd atoms diffusion to the surface because of the high-temperature treatment. Both profiles show a negligible presence of Pd atoms in the outermost layer. The shifts in the Ru peak to higher temperatures may be attributed to the electronic modifications on Ru by Pd in bimetallic nanoparticles. Electron affinity of Ru is higher than that of Pd (101 kJ/mol vs. 54 kJ/mol), so the electron transfer from Pd to Ru may be expected, resulting in different CO chemisorption strength and further catalytic properties as compared with monometallic Ru.

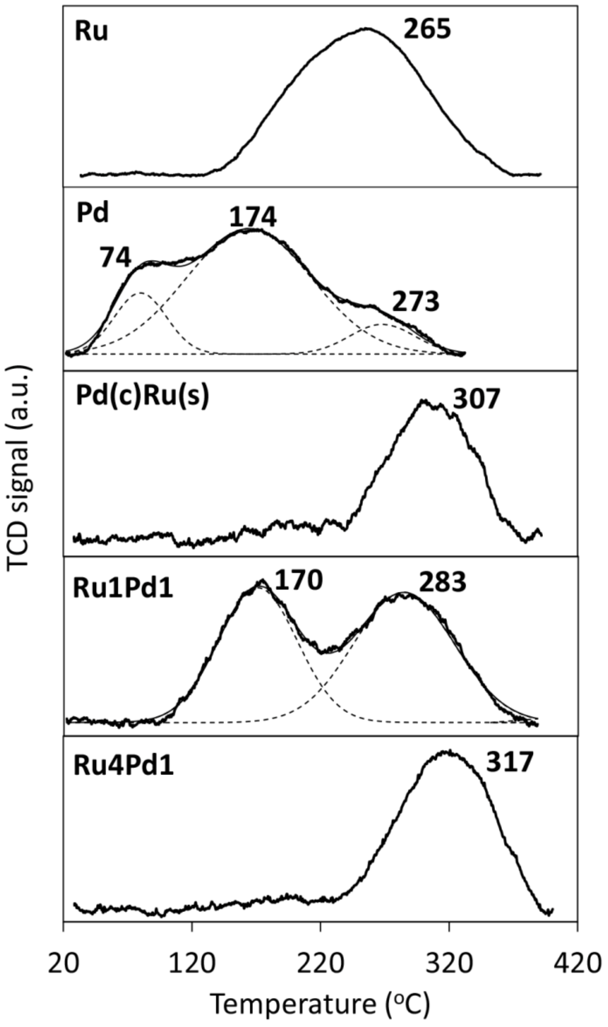

Figure 2.4. CO-TPD profiles for mono- and bimetallic Ru−Pd catalysts.

The CO-TPD profile of the Ru1Pd1 catalyst indicates the significant presence of Pd atoms, but not the monometallic Pd particles, as only one of the Pd peaks is present (170 °C). Note that the catalyst composition (1:1) is close to the Ru/Pd = 1.6 in the Pd(core)−Ru(shell), but after the high-temperature pretreatment, the structures are drastically different (there is negligible Pd in the shell of the core−shell sample), confirming that the molar composition does not control the structure at the applied pretreatment conditions. Less significant shifts in the peaks for the Pd1Ru1 catalyst supports the hypothesis of different loci of Pd and Ru atoms in the selected catalysts. Thus, the CO-TPD results confirm the nanoparticle's bimetallicity and enrichment of the outermost layer of Pd(c)Ru(s) and Ru4Pd1 particles with Ru atoms.

TPR. TPR was carried out also after the high-temperature calcination to ensure polymer removal. Pd could be easily reduced and form Pd hydrides below room temperature [44] while the system waits for a stable TCD signal baseline, thus showing only a hydrogen evolution peak centered at 80 °C (Figure 2.5). The reduction of Ru oxide occurs at 85 °C. The Ru−Pd samples showed one peak at the same temperature (80−85 °C). Typically, a conclusion on the nanoparticle's intrinsic bimetallicity is made based on the peak shifts in bimetallic catalysts as compared with the monometallic forms [20, 37, 45-47]. Because the same peak maxima exist for monometallic Ru and Pd, the TPR was not helpful in elucidating the nanoparticles' structure.

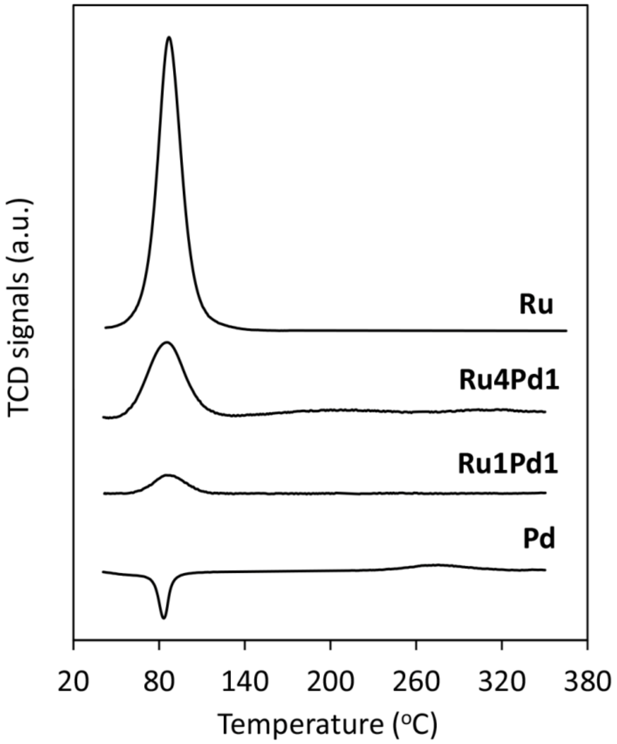

Figure 2.5. TPR profiles of selected mono- and bimetallic Ru−Pd catalysts in H_2/Ar flow (the TCD signal is inverted so that the positive peaks correspond to hydrogen consumption).

CO-DRIFTS. DRIFTS of the adsorbed CO was performed after the pretreatment applied before the catalytic reaction, that is, calcination at 200 °C and reduction at 375 °C. Figure 2.6 shows the vibrational stretching features of the CO probe in the range of 1850−2200 cm^{-1} frequency (the gas-phase CO band occurs at 2143 cm^{-1}). Two controlled experiments performed on bare alumina support and PVP/alumina showed spectral bands in the frequency below 1700

cm^{-1} that do not interfere with the bands related to the adsorbed CO on the metallic surfaces (2000−2130 cm^{-1} for linear and 1800−2000 cm^{-1} for bridged complexes [46, 48, 49]. Both Ru and Pd monometallic catalysts display adsorption bands at similar 2110 and 2116 cm^{-1} for the linear mode, with additional 2070 cm^{-1} peak for monoRu, which could be ascribed to the same linear adsorption but on a different surface atom type (i.e., vertex vs. terrace). The bridged adsorbed CO bands occur at 1946 cm^{-1} for Ru and 2026 and 1995 cm^{-1} for Pd. The Pd(c)Ru(s) sample exhibits a peak at 2098 cm^{-1}, which is closer to the linear CO adsorption on monometallic Ru than it is to the one of monoPd, as well as a peak at lower wavenumber. The latter could be deconvoluted into the 1951 cm^{-1} peak characteristic of a bridged CO complex with monometallic-like Ru atoms and a larger-intensity peak at 1980 cm^{-1} that was observed neither for monoPd nor monoRu, and indicates the formation of new CO adsorption sites. These might be either ensembles of Pd and Ru atoms or monoatoms with properties altered by the presence of a second metal; in both instances, this indicates the formation of intrinsic bimetallic nanoparticles. The 2026 and 1995 cm^{-1} peaks for monometallic Pd could not be fitted during the deconvolution. No obvious conclusion on the Ru or Pd enrichment of the surface could be made based only on the DRIFTS of adsorbed CO; however, the CO desorption temperature is indicative of the Ru shell formation, as discussed in the CO-TPD results above.

The Ru4Pd1 spectrum after deconvolution shows peaks at 1955 cm^{-1} (bridged CO adsorption on Ru), 2116 cm^{-1} (linear CO adsorption on either Ru or Pd) and a 2065 cm^{-1} peak that is similar to the linear adsorption on monoRu. These indicate that the Ru4Pd1 surface is mainly governed by Ru presence but at the same time the relative intensities of linear-to-bridged adsorption peaks are much higher for the Ru4Pd1 catalyst than for monoRu, which implies Ru surface dilution with Pd atoms, that is, bimetallicity. The CO desorption temperature was also different as compared with the monometallic catalysts. These results are in line with the applied synthetic procedure: monometallic Ru nanoparticles cannot be formed in ethanol; rather, they can be formed only in combination with Pd present as seeds.

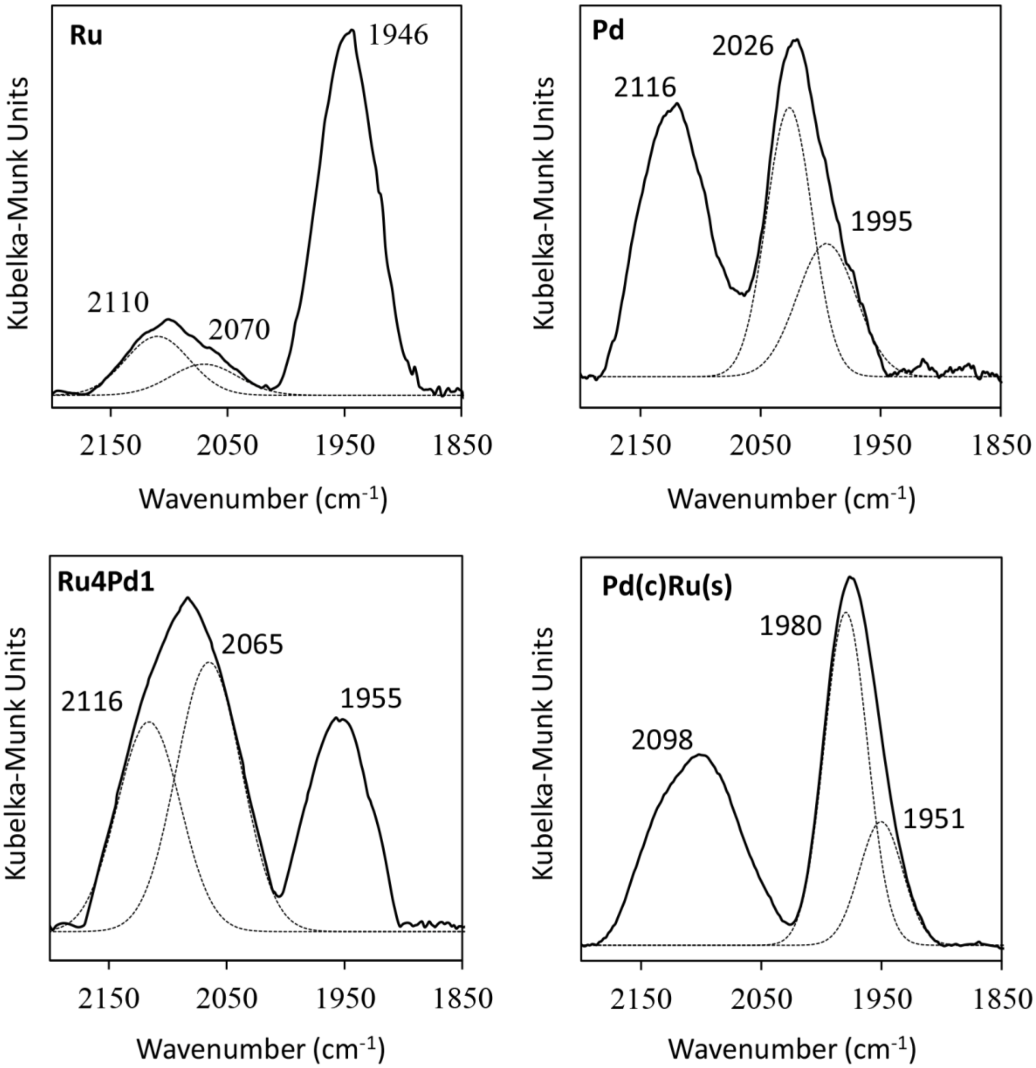

Figure 2.6. DRIFT spectra of CO adsorbed on mono- and bimetallic Ru−Pd catalysts.

Thus, a combination of the applied characterization techniques after the high-temperature treatment confirmed the intrinsic bimetallicity of the catalysts and indicated the shell enrichment with Ru atoms for Pd(c)Ru(s) and Ru4Pd1 samples.

TEM. TEM of supported calcined catalysts was performed to evaluate possible sintering of nanoparticles after the high temperature treatment. The results may be also indicative of intrinsic bimetallicity because the addition of a second metal often allows for better thermal stabilities of the resulting bimetallic catalysts. An example of the beneficial effect on thermal stability by alloying two metals has been previously reported by Strobel et al. [44]: both pure Pd and Pt sintered to a large extent, while the addition of a very small amount of Pt stabilized the Pd particles and prevented sintering at 800 °C [44]. Figure 2.7 shows exemplary TEM images of selected catalysts after calcination. Monometallic Pd and Ru are not resistant to sintering and showed agglomerates in the 300−400 °C range. For the bimetallic sample Ru4Pd1 (this catalyst was found as the most promising in indan RO, as reported below), the nanoparticle sintering did not occur after 400 °C calcination and 375 °C reduction in H_2. This improved thermal stability upon alloying Ru with Pd can be considered as another piece of evidence for intrinsic bimetallicity in Ru4Pd1 sample.

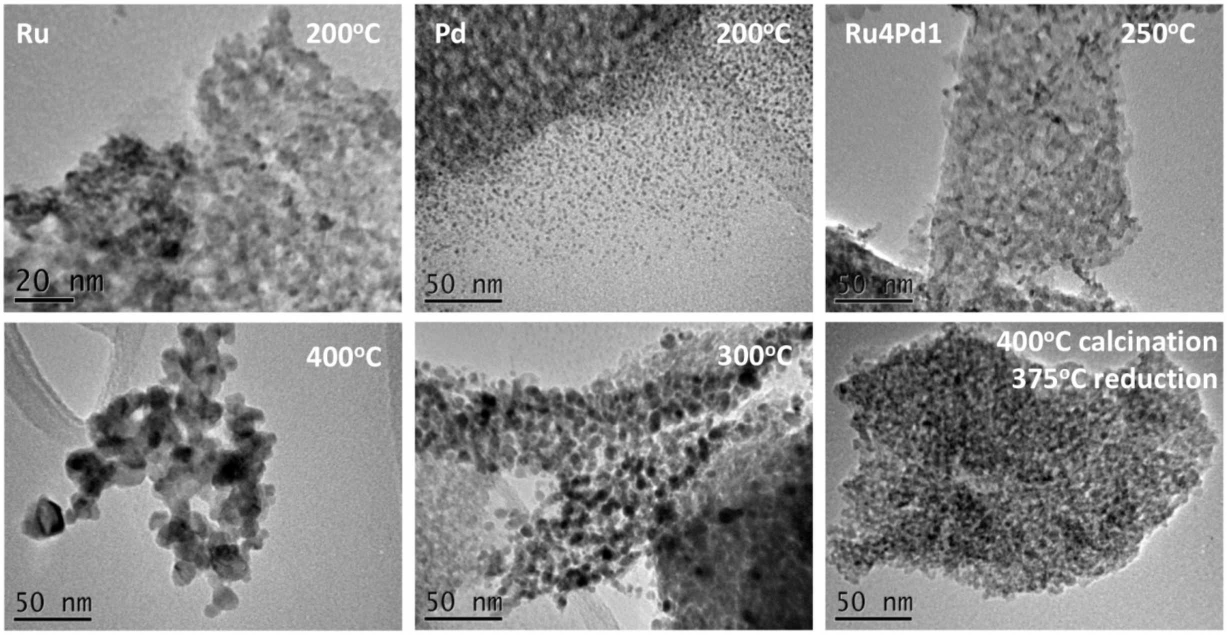

Figure 2.7. TEM images of Ru/γ-Al_2O_3 (left), Pd/γ-Al_2O_3 (center), and Ru4Pd1/γ-Al_2O_3 (right) catalysts after precalcination in air at different temperatures and reduction in hydrogen at 375 °C.

CO Chemisorption. To verify the effect of the calcination treatment on the nanoparticles' agglomeration, CO chemisorption was performed for Ru and Ru4Pd1 catalysts calcined at different temperatures and reduced at 375 °C (Figure 2.8). CO chemisorption of the alumina support is negligible ($< 0.1\ \mu mol_{CO}/g_{alumina}$). The obtained CO uptakes were corrected for the support uptake. As expected from the TEM results on the nanoparticles' sintering, for the monoRu, the dispersion drops significantly starting at 300 °C, with maximum dispersion at 250

°C. Ru4Pd1, on the other hand, at 350 and 400 °C showed highest dispersions of < 40% that corresponds to < 2.3 nm particles. The dispersion value is obtained assuming 1:1 CO:metal stoichiometry, which overestimates particle size since bridged CO is also present (as evidenced by DRIFTs). Thus, the obtained overestimated value of 2.3 nm confirms the particles' thermal stability, since the original size of the as-synthesized nanoparticles is 2.2±0.5 nm (Table 2.1). Very low amounts of adsorbed CO after 200 °C calcination for both samples are due to the residuals of PVP, which prevents the CO chemisorption. The XPS analysis of the Ru4Pd1 catalyst after the 200 °C calcination-375 °C reduction treatment showed that the N/Ru molar ratio was reduced from 2.5 (fresh) to 1.1 (calcined), confirming the presence of PVP residuals on the catalyst surface.

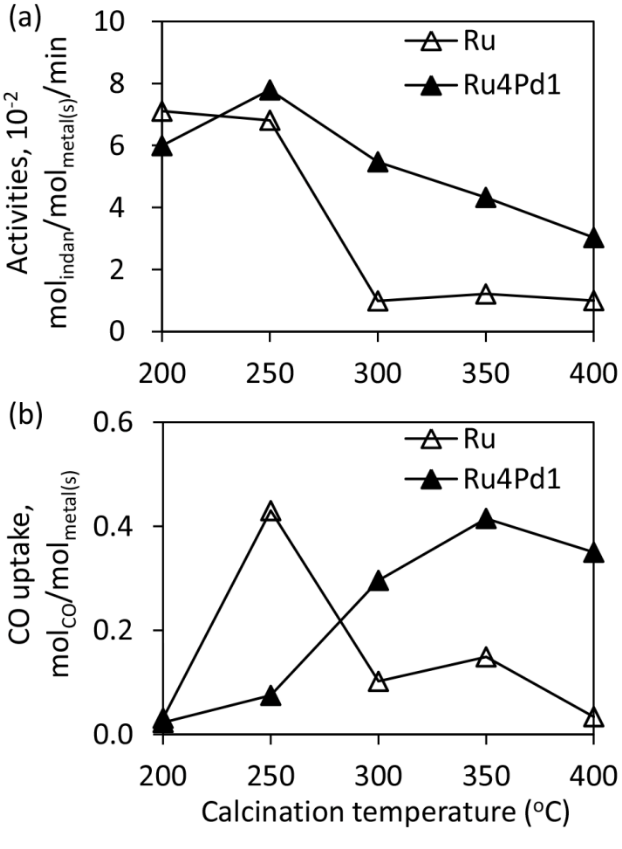

Figure 2.8. Effect of calcination temperatures on catalytic activities in indan RO (a) and CO uptakes from CO chemisorption (b).

However, before concluding on the optimal calcination temperature as one that balances between resistance to sintering and PVP removal efficiency, the catalytic activities must be taken into consideration. For example, Rioux et al. found that the ethylene hydrogenation activity on PVP-stabilized Pt-nanoparticles was maximized with an in situ oxidation-reduction cycle at 200 °C [50]. The indan RO activity was evaluated as a function of the catalyst pretreatment conditions (Figure 2.8). As seen, the amount of the adsorbed CO is not indicative of the most optimal pretreatment temperature and does not correlate with the RO activity trends. The reasons of such behavior are under investigation and will be reported separately. The RO activity of Ru4Pd1 catalyst was maximized at 200−250 °C calcination. Combining the CO chemisorption and TEM results, as well as the indan RO activities, the mono- and bimetallic Ru−Pd catalysts to be used for the indan RO reaction should be calcined at a temperature not higher than 250 °C.

2.3.3. Catalytic behavior in RO

Figure 2.9 shows the selectivity to selective RO products (2-ethyltoluene and *n*-propylbenzene) as a function of indan conversion, over a monometallic Ru/γ-Al_2O_3 catalyst. It can be seen that the selectivity to selective RO products decreases as indan conversion increases. Such trend becomes less pronounced as indan conversion approaches to higher values (above 20%), i.e., the selectivity to selective RO products becomes similar (20±10 wt.%) at indan conversions in the range of 20−45%. Thus, the following selectivity comparisons (in Table 2.2 and Figure 2.10) at indan conversions of 30±11% are valid to reflect intrinsic bimetallic effects with negligible indan conversion impact.

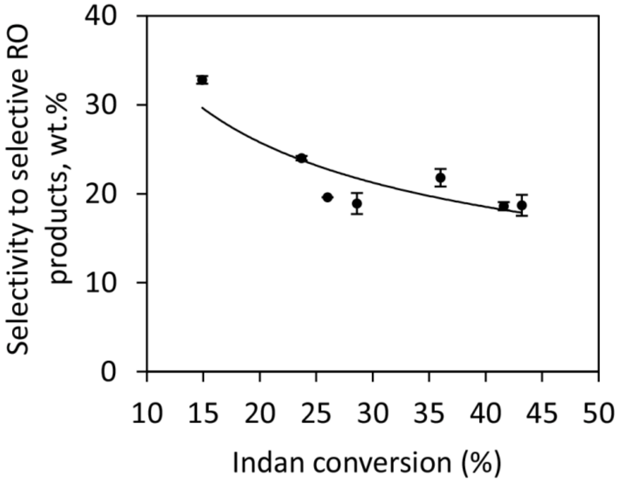

Figure 2.9. Selectivity to selective RO products (2-ethyltoluene and *n*-propylbenzene) vs. indan conversion over a monometallic Ru/γ-Al_2O_3 catalyst. Different indan conversions were obtained by performing low-pressure indan RO over varying amount of Ru/γ-Al_2O_3 catalyst (1.2−4 mg active Ru).

Table 2.2 and Figure 2.10 compare activities and selectivities in indan RO for the developed catalysts. Ir is the most active catalyst, and Ru shows one-fourth of the activity of Ir in indan RO, whereas Pd and Pt reveal the lowest activities, which are the expected trends for these metals. Iridium also results in the lowest lights formation among all monometallic catalysts. Pt allows the highest ratio of *n*-propylbenzene to 2-ethyltoluene, which is in agreement with a known adsorbed flat-lying olefin mechanism for Pt. Pt results in the highest toluene (57%) and lights formation, which is a drawback in terms of single cleavage products. Pd displays poor RO activity but the highest single cleavage selectivity (sum of 2-ethyltoluene and *n*-propylbenzene selectivities) at this low conversion. Monometallic Ru favors deep hydrogenolysis, resulting in high *o*-xylene (40%) and lights formation (21%).

When Pd is added to Ru, it tempers its undesirable hydrogenolysis activity with a simultaneous decrease in activity. Figure 2.10 is plotted in terms of the Pd-to-Ru molar ratio in the catalysts and is grouped into two regions of conversion range, as the high Pd amount results in low conversion, which does not allow for direct selectivity comparison at higher conversions for high Ru amount. Between 0 and 0.25 Pd-to-Ru ratio, the selectivity to 2-ethyltoluene improves 3-fold with corresponding 3-fold suppression in lights formation, reaching the values for monometallic Ir. With the further ratio increase, no further selectivity improvement is observed; it is undesirable from the viewpoint of activity. It is important to note that the bimetallic nanoparticle structure control is paramount: the Pd(core)−Ru(shell) catalyst falls off the trend because of the abundance of Ru atoms despite of high bulk Pd-to-Ru ratio. Its activities and selectivities approach the values for the Ru10Pd1-Ru6Pd1 systems, confirming the shell enrichment with Ru.

The incorporation of Pd to the Ru catalyst improved the selectivity to *n*-propylbenzene 2-fold and reached the level for Ir (Figure 2.10). The monometallic Pt catalyst gives the highest selectivity to *n*-propylbenzene because of a different RO mechanism via the olefin flat-lying model; on the other hand, it promotes lights production and, thus, it underperforms the Ru4Pd1 catalysts at preserving the molecular weight of the cleaved indan.

Table 2.2. Catalytic Activities and Product Selectivities in Indan RO.

catalyst	conversion, %	activity, 10^{-2} $\mathrm{mol_{indan}/mol_{metal(s)}}$/min	selectivities, wt.%						
			2-ethyl-toluene	*n*-propyl-benzene	ethyl-benzene	*o*-xylene	ben-zene	to-luene	lights
Ru[a]	37	4 (0)	17 (0)	2 (0)	2 (0)	40 (3)	2 (0)	16 (0)	21 (3)
Pd[b]	8	1 (0)	73 (-)	10 (-)	1 (-)	2 (-)	2 (-)	8 (-)	5 (-)
Ir[c]	46	16 (4)	62 (5)	3 (0)	1 (0)	22 (0)	1 (0)	5 (0)	6 (1)
Pt[d]	1	1 (-)	8 (-)	13 (-)	1 (-)	1 (-)	7 (-)	57 (-)	13 (-)
Ru10Pd1[a]	41	5 (0)	26 (2)	2 (0)	3 (0)	34 (1)	2 (0)	16 (0)	18 (1)
Ru8Pd1[d]	20	2 (0)	37 (4)	2 (0)	2 (0)	29 (2)	2 (0)	14 (1)	14 (1)
Ru6Pd1[d]	17	2 (-)	44 (-)	2 (-)	2 (-)	25 (-)	1 (-)	12 (-)	13 (-)
Ru4Pd1[d]	27	4 (0)	59 (6)	4 (0)	2 (1)	21 (2)	1 (1)	2 (1)	7 (2)
Ru2Pd1[d]	19	3 (-)	60 (-)	4 (-)	1 (-)	20 (-)	2 (-)	8 (-)	7 (-)
Ru1Pd1[d]	8	1 (0)	50 (7)	5 (2)	1 (0)	16 (2)	7 (3)	13 (4)	8 (0)
Ru1Pd2[d]	5	1 (-)	52 (-)	5 (-)	1 (-)	13 (-)	9 (-)	13 (-)	8 (-)
Pd(c)Ru(s)[a]	33	5 (1)	44 (3)	3 (0)	2 (0)	31 (3)	1 (0)	9 (1)	9 (0)

[a] 2 mg of active metal(s). [b] 9 mg of active metal. [c] 1 mg of active metal. [d] 4 mg of active metals. Data in brackets correspond to one standard deviation.

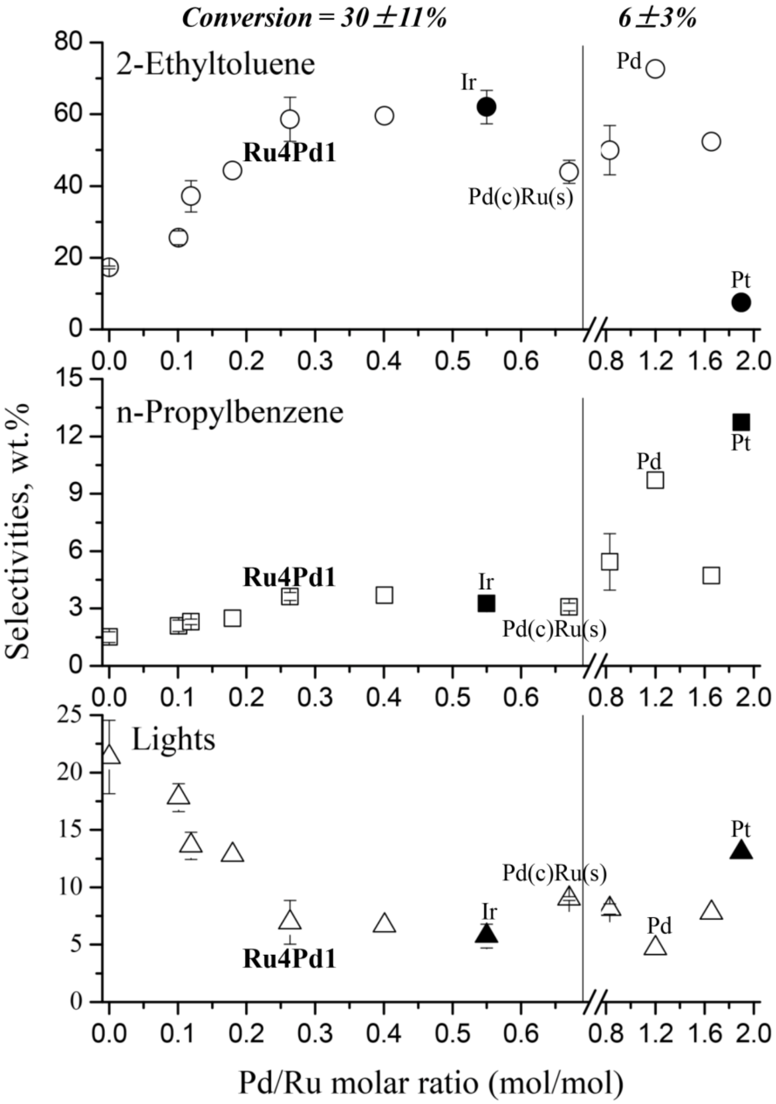

Figure 2.10. Selectivities vs. Pd-to-Ru molar ratio in the bimetallic and monometallic catalysts (monometallic Ir and Pt catalysts are included for comparison). The catalysts were grouped according to similar indan conversions for fair selectivity comparison.

Ruthenium, similar to Ir, exhibits a dicarbene path in RO, which requires perpendicular adsorption of a reactant on two metal atoms [1, 18]. Pd works through a flat-lying π-adsorbed olefin mode (with low activity); thus, its addition to Ru may dilute the Ru ensembles, decreasing the activity. On the other hand, the formed single cleavage products may adsorb on the Pd atoms in Ru−Pd systems via the π-olefin mode, which prevents their further dealkylation to *o*-xylene and toluene, characteristic for mono Ru. This results in the improved selectivity. The electronic effects due to the different electronic affinities may be also responsible for the observed synergism.

Thus, the most optimal Ru−Pd composition corresponding to the highest selectivity toward single cleavage at the minimal loss of activity is the Ru4Pd1 catalyst: its selectivities are either equal or outperform the monometallic Ir and Pt selectivities, which makes the Ru−Pd system a valid alternative to Ir for the RO reactions. The conclusion should not be extrapolated to any Ru−Pd systems with similar 4:1 molar ratios of metals because of the residuals of PVP adsorbed on the reported system, which may affect the catalytic behavior. According to the XPS analysis of the Ru4Pd1 catalyst, the N/Ru molar ratio dropped from 2.5 to 1.1 after the 200 °C calcination and 375 °C reduction, as used before the catalytic runs. The C/Ru ratio decreased from 0.3 to 0.2 after the treatment. The current study shows the possibility of avoiding rare and expensive Ir by introducing a more available and less expensive alternative bimetallic system that allows the same RO selectivity as Ir.

2.4. Conclusions

Bimetallic Ru−Pd nanoparticles of ∼ 2−3 nm size with varying molar ratio of Pd-to-Ru from 0 to 1.7 were synthesized in the presence of PVP, deposited on alumina and tested in the indan RO at atmospheric pressure. The synthetic methods allowed for preparing the nanoparticles with Ru abundance in the nanoparticle shell. The intrinsic bimetallic nature of the nanoparticles was consistent with the results of CO-TPD, CO-DRIFTS, thermal stability tests and a chemical probe reaction (olefin hydrogenation with only Pd atoms active). TEM revealed nanoparticle monodispersity, which was maintained after the high-temperature PVP removal for bimetallic systems, with pronounced sintering in the case of mono-forms. A study of the PVP removal at different calcination temperatures, performed by comparing the RO activities with the metallic surface available for CO chemisorption, showed that the amount of the adsorbed CO is not indicative of the most optimal pretreatment temperature found as 200−250 °C for the maximized catalytic activity. The catalytic tests of indan RO showed the dramatic 3-fold increase in the selectivity to 2-ethyltoluene when the Pd-to-Ru molar ratio increased from 0 to 0.25, with no further improvement in selectivity and loss of activity because of the high proportion of low-active Pd. The Ru4Pd1 catalyst displayed the same high single cleavage selectivity and as low lights formation as iridium, which is known as the most selective RO metal.

Acknowledgments

We thank the Centre for Oil Sands Innovation at the University of Alberta and Canada Foundation for Innovation (New Leaders Opportunities) for financial support, Dr. Mainak Ghosh (Imperial Oil Resources, Calgary, Canada) for fruitful discussions, Dr. Dimitre Karpuzov (U of A) for XPS measurements, Dr. J. Duke (U of A) and Becquerel Laboratory (Ontario, Canada) for the NAA analyses.

2.5. References

[1] G.B. McVicker, M. Daage, M.S. Touvelle, C.W. Hudson, D.P. Klein, W.C.B. Jr., B.R. Cook, J.G. Chen, S. Hantzer, D.E.W. Vaughan, E.S. Ellis, O.C. Feeley, J. Catal. 210 (2002) 137-148.
[2] R.C. Santana, P.T. Do, M. Santikunaporn, W.E. Alvarez, J.D. Taylor, E.L. Sughrue, D.E. Resasco, Fuel. 85 (2006) 643-656.
[3] H. Du, C. Fairbridge, H. Yang, Z. Ring, Appl. Catal. A. 294 (2005) 1-21.
[4] P.T. Do, W.E. Alvarez, D.E. Resasco, J. Catal. 238 (2006) 477-488.
[5] R. Moraes, K. Thomas, S. Thomas, S. van Donk, G. Grasso, J.P. Gilson, M. Houalla, J. Catal. 286 (2012) 62-77.
[6] S. Dokjampa, T. Rirksomboon, S. Osuwan, S. Jongpatiwut, D.E. Resasco, Catal. Today. 123 (2007) 218-223.
[7] D.G. Blackmond, J.G. Goodwin, J.E. Lester, J. Catal. 78 (1982) 34-43.
[8] D. Kubicka, N. Kumar, P. Maki-Arvela, M. Tiitta, V. Niemi, H. Karhu, T. Salmi, D.Y. Murzin, J. Catal. 227 (2004) 313-327.
[9] C. Marcilly, J. Catal. 216 (2003) 47-62.
[10] M. Santikunaporn, J.E. Herrera, S. Jongpatiwut, D.E. Resasco, J. Catal. 228 (2004) 100-113.
[11] M. Kangas, D. Kubicka, T. Salmi, D.Y. Murzin, Top. Catal. 53 (2010) 1172-1175.
[12] F.G. Gault, Adv. Catal. 30 (1981) 1-95.
[13] A. Piegsa, W. Korth, F. Demir, A. Jess, catal. lett. 142 (2012) 531-540.
[14] S. Lecarpentier, v.G. Gestel J., K. Thomas, J.P. Gilson, M. Houalla, J. Catal. 254 (2008) 49-63.
[15] J.H. Sinfelt, US Patent. US3953368 A (1976).
[16] A. Djeddi, I. Fechete, F. Garin, Appl. Catal. A. 413-414 (2012) 340-349.

[17] Z.J. Zhao, L.V. Moskaleva, N. Rösch, ACS Catal. 3 (2013) 196-205.

[18] P. Samoila, M. Boutzeloit, C. Especel, F. Epron, P. Marécot, Appl. Catal. A. 369 (2009) 104-112.

[19] B. Coq, F. Figueras, J. Mol. Catal. A. 173 (2001) 117-134.

[20] P. Samoila, M. Boutzeloit, C. Especel, F. Epron, P. Marécot, J. Catal. 276 (2010) 237-248.

[21] C. Poupin, L. Pirault-Roy, C. La Fontaine, L. Tóth, M. Chamam, A. Wootsch, Z. Paál, J. Catal. 272 (2010) 315-319.

[22] G. Espinosa, G. Del Angel, J. Barbier, P. Bosch, V. Lara, D. Acosta, J. Mol. Catal. A. 164 (2000) 253-262.

[23] D. Teschner, L. Pirault-Roy, D. Naudb, M. Guérin, Z. Paál, Appl. Catal. A. 252 (2003) 421-426.

[24] H. Ziaei-azad, C.X. Yin, J. Shen, Y. Hu, D. Karpuzov, N. Semagina, J. Catal. 300 (2013) 113-124.

[25] L. Piccolo, S. Nassreddine, M. Aouine, C. Ulhaq, C. Geantet, J. Catal. 292 (2012) 173-180.

[26] F. Xu, L.J. Bauer, R.D. Gillespie, M.L. Bricker, S.A. Bradley, US Patent. WO2007041605 A1 (2007).

[27] F. Le Normand, k. Kili, J.L. Schmitt, J. Catal. 139 (1993) 234-255.

[28] A.B. Gaspar, L.C. Dieguez, Appl. Catal. A. 201 (2000) 241-251.

[29] G. Del Angel, B. Coq, R. Dutartre, F. Figueras, J. Catal. 87 (1984) 27-35.

[30] C. Pan, F. Dassenoy, M.J. Casanove, K. Philippot, C. Amiens, P. Lecante, A. Mosset, B. Chaudret, J. Phys. Chem. B. 103 (1999) 10098-10101.

[31] J. Shen, X. Yin, D. Karpuzov, N. Semagina, Catal. Sci. Technol. 3 (2013) 208-221.

[32] T. Teranishi, M. Miyake, Chem. Mater. 10 (1998) 594-600.

[33] Y. Chen, K.Y. Liew, J. Li, Mater. Lett. 62 (2008) 1018-1021.

[34] Y. Borodko, S.E. Habas, M. Koebel, P. Yang, H. Frei, G.A. Somorjai, J. Phys. Chem. B. 110 (2006) 23052-23059.

[35] M. Liu, J. Zhang, J. Liu, W.W. Yu, J. Catal. 278 (2011) 1-7.

[36] R. Ma, N. Semagina, J. Phys. Chem. C. 114 (2010) 15417-15423.

[37] U. Nylen, L. Sassu, S. Melis, S. Järås, M. Boutonnet, Appl. Catal. A. 299 (2006) 1-13.

[38] Y. Li, E. Boone, M.A. El-Sayed, Langmuir. 18 (2002) 4921-4925.

[39] N. Toshima, H. Yan, Y. Shiraishi, in: B. Corain, G. Schmid, N. Toshima (Ed.), **Metal Nanoclusters in Catalysis and Materials Science: The Issue of Size Control**, Elsevier B.V., Amesterdam, 2008, pp. 49-75.

[40] L.C. Ciacchi, W. Pompe, J. Phys. Chem. B. 107 (2003) 1755-1764.

[41] R. van Hardeveld, F. Hartog, Surf. Sci. 15 (1969) 189-230.

[42] M. Crespo-Quesada, A. Yarulin, M. Jin, Y. Xia, L. Kiwi-Minsker, J. Am. Chem. Soc. 133 (2011) 12787-12794.

[43] R. Huang, Y.H. Wen, Z.Z. Zhu, S.G. Sun, J. Phys. Chem. C. 116 (2012) 8664-8671.

[44] R. Strobel, J.D. Grunwaldt, A. Camenzind, S.E. Pratsinis, A. Baiker, Catal. Lett. 104 (2005) 9-16.

[45] S. Dokjampa, T. Rirksomboon, D.T.M. Phuong, D.E. Resasco, J. Mol. Catal. A. 274 (2007) 231-240.

[46] J.W. Niemantsverdriet (Ed.), Spectroscopy in Catalysis, Wiley-vch, Weinheim, 2007.

[47] U. Nylen, B. Pawelec, M. Boutonnet, J.L.G. Fierro, Appl. Catal. A. 299 (2006) 14-29.

[48] M. Kappers, C. Dossi, R. Psaro, S. Recchia, A. Fusi, Catal. lett. 39 (1996) 183-189.

[49] B.A. Riguetto, J.M.C. Bueno, L. Petrov, C.M.P. Marques, Spectrochimica Acta Part A. 59 (2003) 2141-2150.

[50] R.M. Rioux, H. Song, M. Grass, S. Habas, K. Niesz, J.D. Hoefelmeyer, P. Yang, G.A. Somorjai, Top. Catal. 39 (2006) 167-174.

[51] J. Shen, N. Semagina, ACS Catal. 4 (2014) 268-279.

Chapter 3. Is it always necessary to remove a metal nanoparticle stabilizer before catalysis?[2]

3.1. Introduction

Numerous methods involving colloidal chemistry techniques are well established for the synthesis of metal nanoclusters using protecting agents [1, 2]. One can maximize catalytic activity and selectivity through precisely controlled nanoparticle morphology, as opposed to the traditional impregnation methods resulting in broad particle size distributions.

Among the capping agents, poly(vinylpyrrolidone) (PVP) is the most commonly used organic stabilizer for the preparation of various metal nanoparticles [3]. As shown for Pt and Rh nanoparticles of < 7 nm size, PVP molecules act as electron donors that cap the surface atoms of the metallic clusters via C═O, C−N and/or CH_2 functional groups [4]; whereas, for larger particles (Pt > 25 nm), charge transfer occurs from the metal to the side chain of PVP [5]. For Pd nanoparticles, PVP molecules chemisorb via oxygen atoms in the pyrrolidone rings on small nanoparticles but with both O and N atoms on the larger particles [6]. Such interactions, which are necessary to provide efficient stabilizing action, become a drawback in terms of further catalytic applications, as the chemisorbed species could block active sites and deteriorate catalytic performance. Therefore, removal of these capping agents is critical for efficient catalysis [7], which is a general consensus.

---

[2] Chapter 3 of the thesis has been published as: **J. Shen**, H. Ziaei-Azad and N. Semagina, "Is it always necessary to remove a metal nanoparticle stabilizer before catalysis", *Journal of Molecular Catalysis A: Chemical* 391 (2014) 36-40. Dr. Dimitre Karpuzov performed XPS analysis at Alberta Centre for Surface Engineering and Science (ACSES), University of Alberta. The coauthor, Dr. Hessam Ziaei-Azad, performed indan-TPD and CO-TPD experiments. Shiraz Merali performed XRD analysis at the department of Chemical and Material Engineering, University of Alberta. NAA analysis was performed by Becquerel Laboratories Inc., Maxxam Analytics, Ontario. The author performed all syntheses, reactions, analyses and other characterizations. This paper was reprinted with Permissions from Hessam Ziaei-Azad and Ref [24]. Copyright © 2014 Elsevier B.V.

The excess PVP used during synthesis is usually removed by solvent washing before or after deposition on a catalyst support [8]. However, the removal of chemisorbed organic species from a metal surface is challenging. Thermal treatment is the most common method of PVP removal [7]. Free PVP decomposes at 330 °C; the presence of metal nanoparticles may catalyze the combustion of PVP and bring down the decomposition temperature [9]. Rioux et al. concluded that calcination in dilute oxygen (20% O_2/He) is a more effective method than thermal treatment in inert atmosphere for cleaning Pt surfaces. Ethylene hydrogenation activity was maximized with an in situ oxidation-reduction cycle at 200 °C [9]. The nature of the metal being protected has a strong effect on the decomposition behavior of PVP, as each metal interacts with PVP in a unique way; for example, the PVP-Rh interaction is stronger than that of Pt nanoparticles [4]. The strength of the inter-action also depends on the size of nanoparticles due to the different chemisorption modes of the pyrrolidone rings on metal surfaces.

Other strategies such as chemical [8], UV-ozone [10] and plasma treatments [11] are also used for the removal of organic capping agents. For chemical treatments, there may be specific procedures for the removal of each organic capping agent [12]. Blavo et al. reported that triple washings in ethanol/hexane cycles removed the majority of organic species (PVP) from the surface of Pt nanoparticles [13]. Naresh et al. found that ethanol/hexane washing followed by prolonged treatment with tertbutylamine provides a PVP- and Br-free Pd surface [14]. Furthermore, treatments in strong acid or base solutions have also been investigated for the removal of polymers [12] and surfactants [15], respectively. However, chemical treatments may lead to metal loss during repetitive washing. Further removal of chemical additives could also lead to a complicated process, which may not be a preferred industrial practice. Vig reviewed that UV-ozone exposure is an effective method of removing a variety of contaminants from surfaces [16]. This method uses UV light with wavelengths of 184.9 nm and 253.7 nm. The 184.9 nm wavelength is absorbed by oxygen and thus generates ozone; the 253.7 nm wavelength is absorbed by most hydrocarbons and ozone, which is responsible for the oxidation of the carbon-containing compounds into carbon dioxide and water [16]. The UV-ozone technique has been applied in catalysis, allowing the decomposition of organic capping agents from metallic nanoparticles at room temperature. Somorjai's group reported that UV-ozone treatment could successfully eliminate TTAB and PVP from the surface of Pt nanoparticles; the absence of the capping agent was confirmed by XPS and DRIFTS [10]. Organic ligands on the surface of nanoparticles can also be removed by nitrogen, hydrogen, and oxygen plasmas through a combination of sputtering, electron-induced reactions, and etching with free radicals [17]. However, plasma techniques require special equipment [11].

Thus, a stabilizer removal is considered necessary for efficient catalysis, and a variety of techniques have been proposed. The general disadvantages of these procedures are that there is at least one additional step in the catalyst preparation, they require extensive energy and/or materials consumption, and they involve possible structural metal nanoparticle changes due to high temperature or chemical etching. Complete PVP removal without any change in nanoparticle morphology is challenging.

In this study, we report examples in which stabilizer removal is not necessary for efficient catalysis. The two reported cases involve monometallic Ru and Ir nanoparticles stabilized by PVP, deposited on alumina, washed with acetone to remove excess PVP and pretreated at different calcination temperatures before the ring opening reaction of indan (benzocyclopentane) at 350 °C in hydrogen atmosphere. These should be considered exceptions but are of high practical value to show that the necessity of stabilizer removal should be evaluated on a case-by-case basis and, as will be shown below, is dependent on the metal nature.

3.2. Experimental section

Ruthenium(III) nitrosylnitrate and hydrogen hexachloroiridate(IV) hydrate were reduced in ethylene glycol in the presence of PVP (MW 40,000) as described earlier [18]. The PVP-to-metal molar ratio was 10/1, which is the minimum amount needed to provide highly monodispersed Ru and Ir nanoparticles without agglomeration according to our experience. The PVP-stabilized Ru and Ir nanoparticles were precipitated with acetone and deposited on γ-Al_2O_3 (150 mesh, 58 Å pore size) by wet impregnation. The products obtained were then washed with acetone three−five times to remove solvents, unreduced metal salts, and excess PVP. Finally, the catalysts were dried in a fume hood. Prior to the catalytic reactions, the catalysts were calcined in a furnace at 200 °C, 250 °C and 300 °C for Ru catalysts and at 200 °C, 300 °C and 400 °C for Ir catalysts. The pre-calcined catalysts were then reduced at 375 °C under H_2 flow for 1 h.

X-ray powder diffraction (**XRD**) measurements were performed to show the crystallinity of the catalysts. XRD patterns were recorded on a Bruker AXS diffractometer with Cu-Kα

radiation (λ = 1.54059 Å) at 40 kV and 44 mA. Continuous X-ray scans were carried out from 2θ of 10° to 110° with a step width of 0.05° and a scan speed of 2°/min. Monometallic Ru and Ir nanoparticles for XRD samples were prepared following the experimental procedures described previously [18, 19], but without further deposition on alumina support. The obtained colloidal solutions were concentrated by rotary evaporation of solvents under vacuum; and drying was carried out in a vacuum oven at 60 °C to preserve the nanoparticle structures.

As-prepared nanoparticles and/or supported catalysts were analyzed by transmission electron microscopy (**TEM**), neutron activation analysis (**NAA**), and **CO chemisorption** as described earlier [18, 19]. Before the CO chemisorption, the as-deposited catalysts were calcined in a furnace at 200 °C, 250 °C and 300 °C for Ru catalysts, and 200 °C, 300 °C and 400 °C for Ir catalysts. The pre-calcined catalysts were then reduced at 375 °C under H_2 flow for 1 h.

Exemplary **CO-TPD** and **indan-TPD** analyses were performed on the deposited Ir catalysts after 400 °C calcination. The pre-calcined Ir catalyst was packed in a tubular reactor (ring opening setup, as described below) and reduced at 375 °C for 1 h in a hydrogen flow. The reduced sample was cooled down to room temperature. Indan was introduced to the pretreated Ir sample by bubbling H_2 (120 mL/min) through an indan bubbler at room temperature. The indan-Ir/γ-Al_2O_3 sample was then packed in a quartz reactor and heated up under He flow (10 mL/min) from room temperature to 400 °C. TCD signals of indan desorption were recorded as a function of temperature. The experimental procedures for CO-TPD can be found elsewhere [18]. Ir catalyst for TPD experiments were prepared in ethanol/water system, and followed by acetone precipitation and deposition on alumina support, as described earlier [19].

In order to trace PVP residuals and coke formation during indan ring opening, **CHN** and **XPS** analyses were performed on a series of Ru/γ-Al_2O_3 catalysts under different pretreatment conditions, that is, fresh, calcined at 200 °C in air for 1 h, calcined at 200 °C in air for 1 h followed by hydrogen reduction at 375 °C for 1 h, calcined at 250 °C in air for 1 h, and calcined at 250 °C in air for 1 h followed by hydrogen reduction at 375 °C for 1 h, as well as the spent catalysts after ring opening reactions. The fresh Ru catalyst was prepared by rinsing the as-prepared Ru catalyst with acetone five times to remove ethylene glycol and excess PVP. Analytical conditions for CHN and XPS can be found elsewhere [20, 21].

For the catalytic ring opening reaction, the procedure described elsewhere was used [18, 19]. In this study, the pre-calcined catalyst loading corresponds to 2.2 mg active Ru or 2.0 mg active Ir. Indan (95%, Sigma-Aldrich) was fed into the catalytic system by bubbling 120 mL/min H_2 through indan at a constant bath temperature of 10 °C, giving a indan flow rate of $(4.7\pm0.6)\times10^{-6}$ mol/min. Before the reaction, the catalysts were pretreated in situ in hydrogen flow for 1 h at 375 °C. The catalytic reactions were performed at an internal temperature of 350 °C and atmospheric pressure. Steady state was established after 80 min time on stream; and the reaction rates are reported for the 80- to 200-min time on stream with negligible deactivation.

3.3. Results and discussion

XRD patterns of the synthesized Ru and Ir nanoparticles are shown in Figure 3.1 and confirm the particles' crystallinity. The Ru (101) and Ir (111) diffraction peaks are broad, due to incomplete destructive interference in scattering directions, thus, small particle sizes. The crystalline sizes calculated using Scherrer equation are 1.4 nm for Ru and 1.2 nm for Ir, which are smaller than those obtained from TEM (Fig. 3.2). Similar observation was made by Somorjai et al. for Ru nanoparticles and was ascribed to the polycrystalline nature of the particles [22].

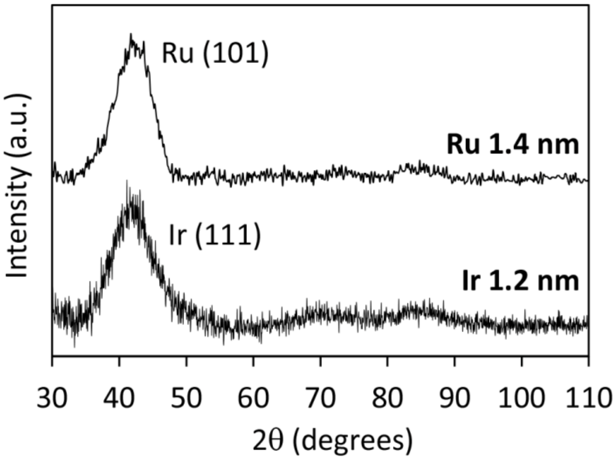

Figure 3.1. XRD patterns of as-synthesized PVP-Ru and Ir nanoparticles.

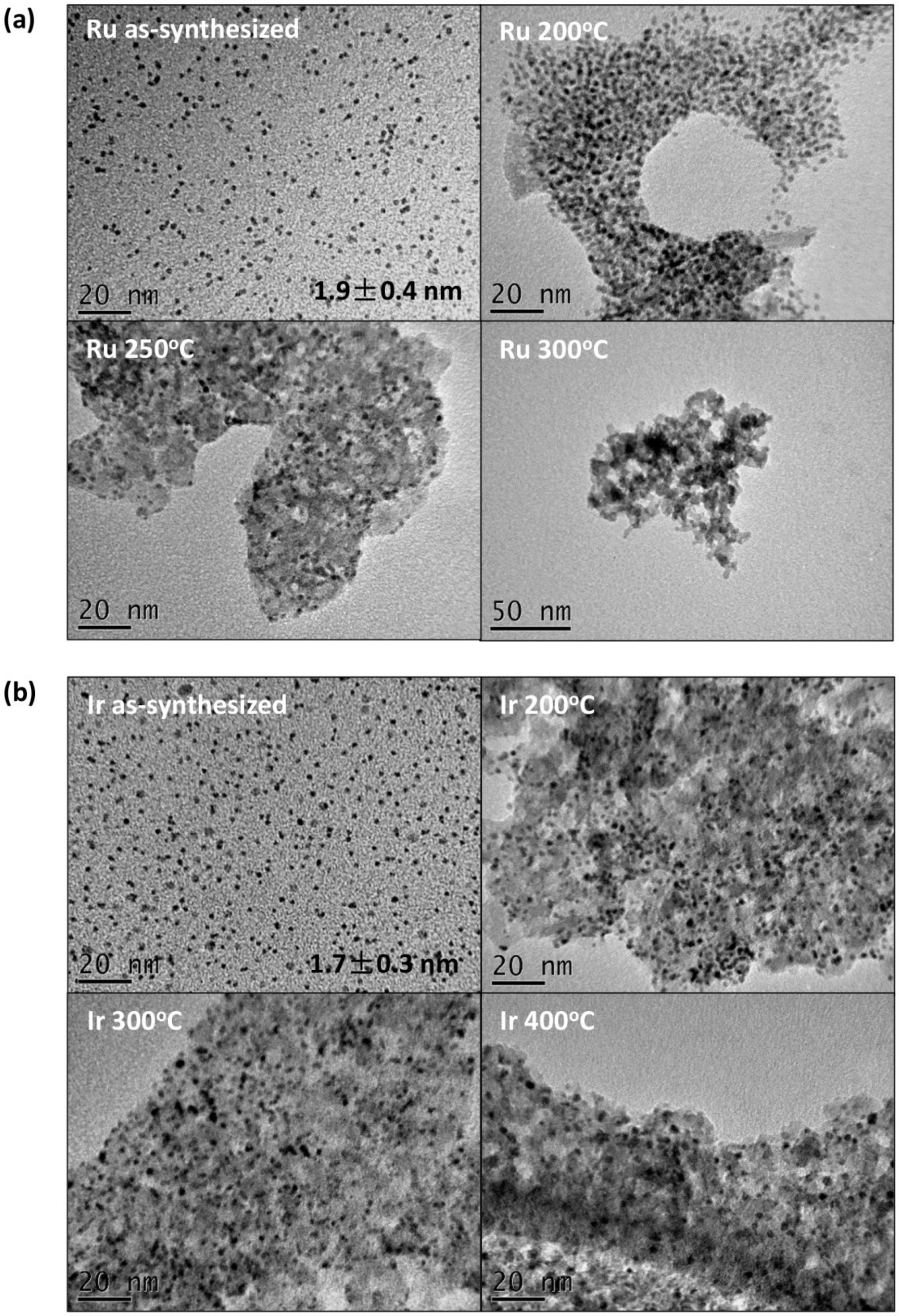

Figure 3.2. TEM images of (a) PVP-stabilized Ru colloids and Ru/γ-Al_2O_3 catalysts after precalcination in air at 200 °C, 250 °C and 300 °C and (b) PVP-stabilized Ir colloids and Ir/γ-Al_2O_3 catalysts after precalcination in air at 200 °C, 300 °C and 400 °C.

The effect of calcination treatment on the Ru and Ir catalysts was examined by transmission electron microscopy, **CO chemisorption**, and **CHN** and **XPS** analyses. TEM images were obtained from the as-synthesized and pre-calcined catalysts. CO chemisorption experiments were performed after calcination-reduction pretreatment to investigate the extent of PVP removal. Low-pressure indan ring opening was employed to evaluate the effectiveness of the proposed pretreatment temperatures. In this study, the lowest calcination temperature for PVP removal was 200 °C, which was chosen according to Somorjai's finding that an in situ oxidation-reduction cycle at 200 °C could maximize Pt activity in ethylene hydrogenation. The highest calcination temperature that does not cause significant sintering is different for each metal, i.e., 250 °C for Ru and 300 °C for Ir, which were verified by TEM (Fig. 3.2). Mild nanoparticle sintering can be seen for Ir catalyst after 400 °C calcination. CO chemisorption showed that the average diameter of Ir nanoparticles increased by less than 1 nm after 400 °C calcination comparing to the size obtained from TEM of as-synthesized nanoparticles. Unlike Ir, Ru sintered severely after being subjected to thermal treatment at above 250 °C [18].

The CO uptake of pure alumina support is negligible ($< 0.1\ \mu mol_{CO}/g_{alumina}$). The CO uptakes obtained were corrected from support uptake and shown in Figure 3.3. The CO uptakes were almost negligible when Ru and Ir catalysts were calcined at 200 °C in air and reduced at 375 °C in hydrogen, indicating the active sites were still blocked by a significant amount of residual PVP. When Ru and Ir were calcined at 250 °C and 300 °C in air and reduced at 375 °C in hydrogen, respectively, CO uptakes increased dramatically. Figure 3.3 also shows theoretical CO uptakes (dash lines), calculated based on the TEM-found nanoparticle size, metal crystal statistics [23] and 1:1 CO-to-surface metal ratio. The last assumption over estimates the amount of the theoretical CO in the presence of other than linear surface CO complexes on the metal. However, even with such over-estimation, Figure 3.3 shows that the 250 °C calcination temperature for Ru and 300 °C for Ir followed by the reduction treatment at 375 °C provided complete surface cleaning from the polymer residuals.

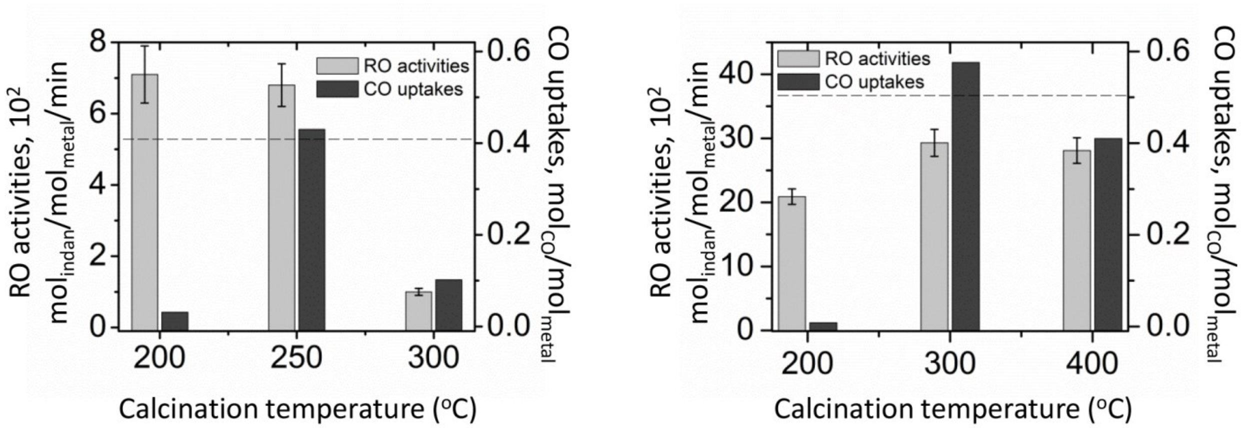

(a) Ru/γ-Al_2O_3 (b) Ir/γ-Al_2O_3

Figure 3.3. The effect of calcination temperature on catalytic activities in indan ring opening and CO uptakes from CO chemisorption: (a) Ru/γ-Al_2O_3 catalysts and (b) Ir/γ-Al_2O_3 catalysts. Dash lines indicate theoretical CO uptakes.

Surprisingly, neither treatment affected the catalytic ring opening activities at all (with the exception of Ru calcined at 300 °C), as seen from Figure 3.3. It seems that the PVP residuals did not prevent the adsorption of indan on Ru or Ir surfaces, which is opposed to the chemisorption of CO molecules. RO activity dropped dramatically when subjecting Ru to 300 °C calcination, as Ru nanoparticles sintered to a large extent (Fig. 3.2). The different chemisorption strengths of indan and CO on clean Ir particles after 400 °C calcination and 375 °C reduction are obvious from the **TPD** profiles (Fig. 3.4). Less strong indan bonding to the surface, necessary for its activation as compared to the CO, might be advantageous in terms of less clean surface requirements for indan adsorption.

A probable reason for the high catalytic activities could be an in situ cleaning of the surface during the catalytic reaction, since the RO activities were reported at 350 °C after ~ 2 h on stream. It is important, though, that the CO chemisorptions were carried out after 375 °C reduction in hydrogen, which simulates the reaction conditions, apart from the presence of a low amount of indan. To verify the influence of the reaction conditions on the polymer removal, CHN and XPS analyses of some fresh, treated and spent Ru catalysts were performed, and the results are presented in Table 3.1.

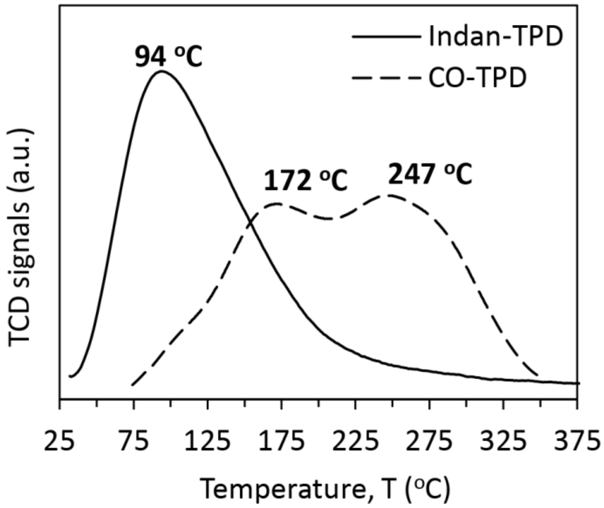

Figure 3.4. (a) Indan- and (b) CO-TPD spectra for Ir/γ-Al_2O_3 catalysts precalcined at 400 °C followed by hydrogen reduction at 375 °C.

Table 3.1. Nitrogen (from XPS) and carbon (from CHN analysis) content of the fresh and treated Ru/γ-Al_2O_3 catalysts.

catalyst pretreatment	N content[a], wt.%	C content, wt.%
Fresh	4.31	4.21
200 °C air	3.33	3.54
200 °C air + 375 °C H_2	0.55	1.00
200 °C air + 375 °C H_2 + after RO reaction	0.52	1.09
250 °C air	1.59	2.13
250 °C air + 375 °C H_2	0.04	0.93
250 °C air + 375 °C H_2 + after RO reaction	0.02	0.72

[a] Corrected for N content of the alumina support (0.24 wt.%, irrespective of the treatment); error ±0.02 wt.%.

As can be seen, only solvent washing was not efficient for polymer removal: 4.3 wt.% N was detected on the surface. The N content before and after the reaction shows that no further polymer removal during the reaction was achieved, and according to the CHN analysis carbon content did not change, indicating that significant coking did not occur under the applied conditions. Air-only treatment, irrespective of temperature, did not result in the surface cleaning; the reductive treatment produced the most cleaning effect. The results also confirm our above hypothesis that for Ru, the 250 °C treatment followed by reduction allows almost complete surface cleaning from the polymer residuals, as opposed to the 200 °C treatment: the N content drops from 0.55 wt.% to a negligible 0.04 wt.%. Thus, there is no evidence that surface cleaning from the polymer residuals occurs during the course of the catalytic reaction, so indan may adsorb and react even in the presence of the stabilizing polymer residuals: the same catalytic activities are observed when 0.55 wt.% and 0.04 wt.% of N is present on the Ru surface, while CO chemisorption was significantly suppressed for the 0.55 wt.% N presence. The outcome is that for some catalytic reactions, such as indan ring opening, the chemisorption of reactant molecules on nanoparticles may not require polymer-free surfaces. A mild thermal treatment temperature would be preferable to preserve the nanoparticle structures.

3.4. Conclusions

For the ring opening reaction of indan, complete removal of a metal nanoparticle stabilizer is not necessary, as evidenced by the catalytic tests and XPS, CHN, TEM, TPD and CO chemisorption analyses for PVP-stabilized Ru and Ir catalysts. On the contrary, if a reaction requires CO activation, the surface must be completely clean. Thus, depending on a catalyzed reaction and metal nature, a mild thermal pretreatment temperature would be preferable to preserve the nanoparticle structure. The conditions should be evaluated on a case-by-case basis, but this study shows that for some metal-reaction combinations, it is possible to achieve high catalytic reaction rates without complete stabilizer removal.

Acknowledgements

Financial support was provided by the Institute of Oil Sands Innovation (IOSI) Grant no (2011-01) at the University of Alberta. We also thank Dr. D. Karpuzov (Alberta Centre for Surface Engineering and Science) for the XPS measurements and Dr. Xiaoli Tan (IOSI) for the CHN analyses.

3.5. References

[1] T.K. Sau, C.J. Murphy, Am. Chem. Sci. J. 20 (2004) 6414-6420.

[2] T. Teranishi, M. Miyake, Chem. Mater. 10 (1998) 594-600.

[3] N. Toshima, H. Yan, Y. Shiraishi, in: B. Corain, G. Schmid, N. Toshima (Ed.), **Metal Nanoclusters in Catalysis and Materials Science: The Issue of Size Control**, Elsevier B.V., Amesterdam, 2008, pp. 49-75.

[4] Y. Borodko, S.M. Humphrey, T.D. Tilley, H. Frei, G.A. Somorjai, J. Phys. Chem. C. 111 (2007) 6288-6295.

[5] L. Qiu, F. Liu, L. Zhao, W. Yang, J. Yao, Langmuir. 22 (2006) 4480-4482.

[6] J. Xian, Q. Hua, Z. Jiang, Y. Ma, W. Huang, Langmuir. 28 (2012) 6736-6741.

[7] Z.L. Wang, J.M. Petroski, T.C. Green, M.A. El-Sayed, J. Phys. Chem. B. 102 (1998) 6145-6151.

[8] C.K. Tsung, J.N. Kuhn, W. Huang, C. Aliaga, L.I. Hung, G.A. Somorjai, P. Yang, J. Am. Chem. Soc. 131 (2009) 5816-5822.

[9] R.M. Rioux, H. Song, M. Grass, S. Habas, K. Niesz, J.D. Hoefelmeyer, P. Yang, G.A. Somorjai, Top. Catal. 39 (2006) 167-174.

[10] C. Aliaga, J.Y. Park, Y. Yamada, H.S. Lee, C.K. Tsung, P. Yang, G.A. Somorjai, J. Phys. Chem. C. 113 (2009) 6150-6155.

[11] H. Wang, H. Tang, J. He, Q. Wang, Mater. Res. Bull. 44 (2009) 1676-1680.

[12] J. Monzo, M.T.M. Koper, P. Rodriguez, ChemPhysChem. 13 (2012) 709-715.

[13] S.O. Blavo, E. Qayyum, L.M. Baldyga, V.A. Castillo, M.D. Sanchez, K. Warrington, M.A. Barakat, J.N. Kuhn, Top. Catal. 56 (2013) 1835-1842.

[14] N. Naresh, F.G.S. Wasim, B.P. Ladewig, M. Neergat, J. Mater. Chem. A. 1 (2013) 8553-8559.

[15] H. Eriksona, A. Sarapuua, N. Alexeyevaa, K. Tammeveskia, J. Solla-Gullónb, J.M. Feliu, Electrochimica Acta. 59 (2012) 329-335.

[16] J.R. Vig, J. Vac. Sci. Technol. A. 3 (1985) 1027-1034.

[17] B. Gehl, A. Fromsdorf, V. Aleksandrovic, T. Schmidt, A. Pretorius, J.I. Flege, S. Bernstorff, A. Rosenauer, J. Falta, H. Weller, M. Baumer, Adv. Funct. Mater. 18 (2008) 2398-2410.

[18] J. Shen, N. Semagina, ACS Catal. 4 (2014) 268-279.

[19] H. Ziaei-azad, N. Semagina, ChemCatChem. 6 (2014) 885-894.

[20] H. Ziaei-azad, C.X. Yin, J. Shen, Y. Hu, D. Karpuzov, N. Semagina, J. Catal. 300 (2013) 113-124.

[21] J. Shen, X. Yin, D. Karpuzov, N. Semagina, Catal. Sci. Technol. 3 (2013) 208-221.

[22] S.H. Joo, J.Y. Park, J.R. Renzas, D.R. Butcher, W. Huang, G.A. Somorjai, Nano Lett. 10 (2010) 2709-2713.

[23] R. van Hardeveld, F. Hartog, Surf. Sci. 15 (1969) 189-230.

[24] J. Shen, H. Ziaei-Azad, N. Semagina, J. Mol. Catal. A. 391 (2014) 36-40.

Chapter 4. 100° temperature reduction of wet methane combustion: highly active Pd−Ni/Al_2O_3 catalyst versus Pd/$NiAl_2O_4$[3]

4.1. Introduction

Recently revived interest in catalytic methane combustion is brought by the increasing demand in natural gas operated vehicles, heating devices and gas turbines [1, 2]. The release of methane is an environmental concern, because it is the second most significant greenhouse gas with a global warming potential of 23 times higher than that of CO_2. The use of heterogeneous catalysts allows complete methane oxidation at relatively low temperatures as compared to thermal combustion. Alumina-supported palladium catalysts are generally accepted as the most active CH_4 oxidation catalysts, and have been extensively studied, including methods to improve Pd nanoparticle stability towards sintering [1-3]. The methane combustion catalysts must achieve ignition temperature of 200−300 °C [1] and complete oxidation temperature below 500−550 °C [3]. However, maintaining low-temperature Pd stability in the presence of water is challenging [4], because inactive palladium hydroxide could be retained at temperatures up to 450 °C [3, 5].

---

[3] Chapter 4 of the thesis has been published as: **J, Shen**, R. E. Hayes, X. Wu and N. Semagina, "100° temperature reduction of wet methane combustion: highly active Pd−Ni/Al_2O_3 catalyst versus Pd/$NiAl_2O_4$", *ACS Catalysis* 5 (2015) 2916-2920. The reaction setup for methane oxidation was originally designed and built by Dr. Long Wu and Dr. Robert E. Hayes. The developed catalysts were tested in methane oxidation with collaboration with a master student, Xiaoxing Wu. Methane oxidation experiments performed by Xiaoxing Wu are: Pd-COL at 450 °C, $PdNi_{12}$-COL at 375, 400 and 415 °C, and $PdNi_{12}$-IMP at 450 °C. Dr. Xuejun Sun collected HRTEM images of $PdNi_{12}$-COL catalyst at the department of Oncology, Alberta Cross Cancer Institute, University of Alberta. Dr. Dimitre Karpuzov performed XPS analysis at Alberta Centre for Surface Engineering and Science (ACSES), University of Alberta. NAA analysis was performed by Becquerel Laboratories Inc., Maxxam Analytics, Ontario. The author performed all syntheses, most of the reactions, analyses and other characterizations. This paper was reprinted with Permissions from Robert E. Hayes and Xiaoxing Wu. This paper was reprinted with Permissions from Robert E. Hayes, Xiaoxing Wu and Ref [33]. Copyright © 2015 American Chemical Society.

One of the proposed solutions to improve the hydrothermal stability of Pd/Al_2O_3 catalysts is to use metal oxide additives to the alumina support [6-11].

Introducing a second metal component into a heterogeneous catalyst support has been widely accepted as one of the ways to increase activity, selectivity and/or stability of the deposited catalytic metal nanoparticles [12]. For the catalysts to be stable in a high-temperature oxidizing atmosphere, least lattice mismatch between the supported Pd or Pt nanoparticles and spinels of nickel [6] or magnesium [12], respectively, has been shown to be responsible for the enhanced nanoparticle stability towards sintering. This approach, however, requires high amounts of the second metal, often more than a half of the support weight, it brings complexity to the large-scale support production and increases the material's price. Nickel−oxide promoted alumina has received particular attention due to improved Pd catalyst stability in methane combustion, including in the presence of water. The enhancement is ascribed to the Pd dispersion stabilizing effect by $NiAl_2O_4$ spinel [6-8], while some observations claim the opposite effect due to the lowered surface area of alumina support by Ni [13]. The Ni content in alumina support must be extremely high to achieve a notable improvement in Pd activity, e.g., a 35 °C reduction in the 90% methane conversion temperature was obtained by adding 36:1 NiO to the alumina support [7]. Several attempts were made to validate experimentally the effect of alloying Pd and Ni with similar loadings and ensure their close contact, but because the catalysts were prepared by conventional co-precipitation or impregnation, Ni was consumed in spinel formation and/or did not yield a noticeable improvement in the catalytic performance [13-15]. Such traditional methods for bimetallic catalyst synthesis are known to be inefficient in providing nanoparticle structure control [16].

In this study, we report a successful preparation of modified Pd catalysts with ultra-low Ni content (12:1 molar ratio of Ni to Pd) yielding PdO−NiO bimetallic catalyst, which allowed methane combustion at 430 °C in the presence of 5 mol.% water in the feed. The Pd−Ni particles were prepared before deposition on the support by a colloidal chemistry technique with poly(vinylpyrrolidone) (PVP) as a stabilizer. The method of Ni incorporation is shown to be paramount: when the same Ni amount was introduced via traditional support impregnation, it was consumed into spinel formation and did not show any improvement in catalytic activity versus monometallic Pd catalyst. The diagram depicting the two approaches in the catalyst preparation is provided in Figure 4.1.

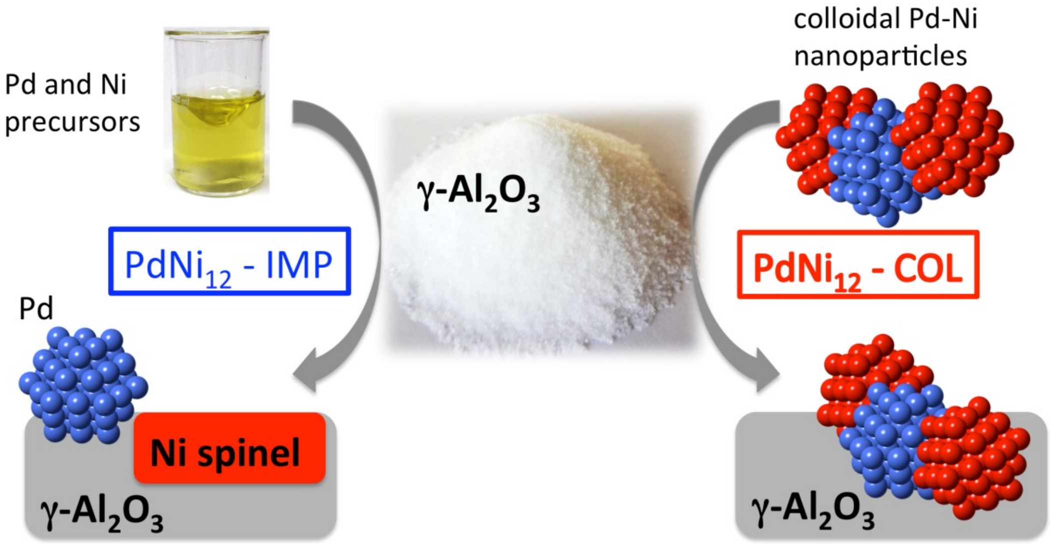

Figure 4.1. Schematic of bimetallic catalyst preparation via traditional impregnation-calcination ($PdNi_{12}$-IMP) and colloidal techniques ($PdNi_{12}$-COL) resulting in monometallic particles on a binary support (left) and Pd and Ni nanoparticles on the parent support (right).

4.2. Experimental section

4.2.1. Experimental details for catalyst preparation

Colloidal Pd-COL, Ni-COL and $PdNi_{12}$-COL nanoparticles were synthesized in alcohol media in the presence of poly(vinylpyrrolidone) (PVP, MW 40,000, Sigma-Aldrich). Metal precursors were nickel(II) nitrate hexahydrate ($Ni(NO_3)_2 \cdot 6H_2O$, 98.5%, Sigma-Aldrich) and palladium(II) chloride ($PdCl_2$, 5% w/v solution, Acros); for the chlorine effect study, palladium(II) acetate was also used ($Pd(OAc)_2$, 99.98%, Sigma-Aldrich). The Pd-COL nanoparticles were synthesized in ethanol/water system using Teranishi and Miyake's one-step alcohol reduction methods [17] with some modifications [18] as described in the following. A mixture of $PdCl_2$, PVP (0.444 g, 4 mmol, PVP-to-Pd molar ratio = 20/1) and 170 mL of 40 vol.% ethanol/water solution (reagent alcohol, 95%, Fisher Scientific; Milli-Q water) was stirred and refluxed for 3 h under air. For the $PdNi_{12}$-COL preparation, Ni–Pd bimetallic nanoparticles were synthesized by simultaneous reduction of both Pd and Ni precursors using a modified polyol reduction method [19] in the presence of PVP, in which nickel and palladium precursors were reduced at high temperature by sodium borohydride ($NaBH_4$, > 99%, Sigma-Aldrich). Target Ni-to-Pd molar ratio was 9:1. For a typical synthesis, $Ni(NO_3)_2 \cdot 6H_2O$, $PdCl_2$ and PVP (0.888 g, 8 mmol, PVP-to-metals molar ratio = 40/1) were dissolved in 200 mL ethylene glycol (EG, 99.8%, Sigma-Aldrich) in a 500 mL 3-neck round bottom flask under stirring. The PVP-metals-EG mixture was heated to 140 °C, and then $NaBH_4$ (0.378 g, 10 mmol, $NaBH_4$-to-metals molar ratio = 50/1) was introduced to the synthesis solution under vigorous stirring. A transparent dark brown solution was observed immediately after $NaBH_4$ addition. The system was then heated to the reflux point of EG (198 °C), and maintained at this temperature for 2 h for complete reduction. The Ni-COL nanoparticles were prepared using the same sodium borohydride reduction method as for the synthesis of $NiPd_{12}$-COL colloids. A 200 mL of PVP-Ni^{2+}-EG solution (PVP-to-Ni molar ratio of 40/1) was prepared at room temperature and heated to 140 °C under stirring. The reduction reaction of Ni^{2+} to Ni^0 was initiated by adding $NaBH_4$ (0.378 g, 10 mmol, $NaBH_4$-to-Ni molar ratio = 50/1) to the reaction mixture at 140 °C under vigorous stirring. The reaction continued for 2 h at 198 °C.

For the deposition on a catalyst support, γ-Al_2O_3 support (150 mesh, 58 Å pore size, Sigma-Aldrich) was calcined under static air at 500 °C for 2 h. The PVP-stabilized $PdNi_{12}$-COL and Ni-COL nanoparticles prepared in EG were precipitated with acetone (> 95%, Fisher Scientific, acetone-to-colloidal dispersion volumetric ratio = 4/1), and deposited on γ-Al_2O_3 by wet impregnation. The colloidal solution of PVP-Pd prepared in ethanol/water was concentrated by vacuum evaporation of solvents, followed by incipient wetness impregnation on γ-Al_2O_3 support.

$PdNi_{12}$-IMP catalyst was prepared by incipient wetness impregnation of the γ-alumina support with a 0.05M aqueous solution of $PdCl_2$ and $Ni(NO_3)_2 \cdot 6H_2O$ precursors followed by drying in a oven at 60 °C overnight. To study the chlorine effect, $PdNi_{12}$-IMP catalyst was also prepared by impregnating γ-Al_2O_3 support with $Pd(OAc)_2$ and $Ni(NO_3)_2 \cdot 6H_2O$ solution. The solution (0.05 M) was prepared by mixing an aqueous solution of $Ni(NO_3)_2 \cdot 6H_2O$ with a dioxane (99.8%, Sigma-Aldrich) solution of $Pd(OAc)_2$.

4.2.2. Characterization

Transmission electron microscopy (**TEM**) and high-resolution TEM (**HRTEM**) were performed at 200 kV acceleration voltage on a JEOL 2100 transmission electron microscope. The mean diameter and standard deviation of nanoparticles were calculated by counting more than 200 particles from TEM images using ImageJ software. For each HRTEM image, average lattice spacing value was calculated from more than 10 data measured at different regions using ImageJ software. All lattice spacings were corrected by gold standard (lattice spacing = 2.3 Å), which was used for HRTEM calibration.

Temperature-programmed reduction (**TPR**) analyses were performed for the same metal loadings in the reactor (3.8 mg Ni and/or 0.6 mg Pd) with 10% H_2/Ar gas mixture using an AutoChem II 2920 instrument (Micromeritics) equipped with a quartz U-tube reactor and a thermal conductivity detector (TCD). A series of oxidation-reduction-oxidation-reduction experiments were performed; and the final reduction profiles were reported. Prior to the TPR analysis, the catalysts were calcined at 550 °C in air for 16 h, which simulates the pretreatment procedure before methane oxidation reactions. The pre-calcined catalysts were reduced in a flow of 10% H_2/Ar (25 mL/min) at 550 °C for 1h. After the calcination-reduction pretreatment, the samples were flushed with inert (Ar) for 30 min at 550 °C and cooled to ambient temperature under inert. The catalysts were then oxidized in 10% O_2/He gas mixture at 900 °C and then flushed with inert (He) for 30 min at 900 °C and cooled to room temperature in He. This oxidation procedure was then followed by a TPR analysis using 10% H_2/Ar from room temperature to 900 °C with a temperature ramping rate of 10 °C/min. The TCD signals for the reported TPR profiles are inverted; thus, positive peaks refer to the consumption of hydrogen.

CO chemisorption experiments were performed to estimate the metal dispersions of the 0.03 wt.% and 0.24 wt.% Pd catalysts. The catalysts were calcined at 550 °C for 16 h in a furnace. The calcined samples were packed in a quartz U-tube reactor and then loaded to a AutoChem II 2920 instrument. Prior to CO chemisorption, the catalysts were reduced in situ in a flow of 10% H_2/Ar (25 mL/min) for 1 h. CO chemisorption experiments were performed by dosing 3% CO/He gas mixture at room temperature. The volumetric flow rates of 3% CO/He loop and the He carrier gas were 25 mL/min. Nanoparticle dispersions were calculated using a molar ratio of CO-to-Pd of 0.6 [20].

The actual loadings of Pd and Ni on γ-Al_2O_3 were determined by neutron activation analysis (**NAA**) at Becquerel Laboratories (Maxxam Company, Canada). Samples were irradiated for 20 min in the Cd shielded, epi-thermal site of the reactor core. Palladium and nickel were counted 15 min and 25 min, respectively, after 24 h decay on an Aptec CS13– A31C gamma detector.

X-ray photoelectron spectroscopy (**XPS**) measurements were performed on an AXIS-165 spectrometer (Kratos Analytical) at the Alberta Centre for Surface Engineering and Science (ACSES), University of Alberta. Monochromatic Al Kα source (hν = 1486.6 eV) was used at a power of 168 W. The survey scans were collected for binding energy spanning from 1100 to 0 eV with analyzer pass-energy of 160 eV and a step of 0.4 eV. For the high resolution spectra, the pass-energy was 20 eV with a step of 0.1 eV. Electron flood neutralizer was applied to compensate sample charging. Instrument software was used to calculate the composition with RSF of Scofield and Shirley background from the high resolution spectra. CasaXPS software was used for the deconvolution of Ni 2*p3/2* and Pd $3d_{5/2}$ peaks. Binding energies were referenced to carbon 1s (284.7 eV). The analyses were performed on the calcined samples (550 °C, 16 h). The aged samples were not used to avoid Ni hydroxide formation, whose peaks interfere the $NiAl_2O_4$ spinel peaks.

X-ray powder diffraction (**XRD**) patterns were recorded on a Bruker AXS diffractometer with a Cu-Kα radiation source (λ = 1.54059 Å) operated at 40 kV and 44 mA. Continuous X-ray scans were carried out from 2θ of 30° to 90° with a step width of 0.01° and a count time of 2.4 s. The peak identification was performed using MDI Jade 9.0 software combined with the ICDD database. $PdNi_{12}$-COL nanoparticles for XRD analysis were collected by acetone precipitation from the colloidal dispersion without the support to avoid the interference with alumina peaks. The particles were calcined in air at 550 °C for 16 h.

4.2.3. Wet methane combustion

Wet methane combustion in the presence of 5 mol.% of water was investigated according to the previous study [21] with some modifications. A tubular reactor was packed with 4 g of calcined catalyst (550 °C, 16 h under static air) corresponding to 1.2 mg active Pd and 7.6 mg Ni (0.029 wt.% Pd and 0.190 wt.% Ni loadings in relevant catalysts). Methane (10% balanced in nitrogen, Praxair, 8.5 ml/min) and air (extra-dry, Praxair, 200 ml/min) were pre-mixed and fed into the reactor (4100 ppm CH_4 in N_2 and air mixture). The reactions were carried out at 1.1 barg pressure. Ignition and extinction curves were obtained by increasing and decreasing the reaction temperature stepwise (50 °C for each step), respectively, with a ramping rate of 60 °C/min; the system was held at each temperature for 30 min. The ignition curves were initiated at 200 °C and ended at 550 °C, the latter being the highest combustion temperature in this study. The extinction was performed vice versa to investigate the catalytic performance during cooling down.

First, two ignition-extinction experiments (without and with 5 mol.% water, respectively) were performed to pre-condition the catalyst, followed by the hydrothermal aging in the wet methane/air feed by increasing reaction temperature to 550 °C (60 °C/min ramping rate) and then cooling the reactor to the temperature that gives about 50% CH_4 conversion (unless indicated otherwise). The high-low temperature cycling was repeated 8 times (about 22 hours). Each temperature stage was held for 1 h. After the cycling was completed, the reactor temperature was then held at the selected temperature for another 18 hours. Finally, a third ignition-extinction test (with 5 mol.% water) was performed to check the activity of aged catalyst. The gas outlet from the reactor was analyzed online every 15 min using an Agilent HP 7890A gas chromatograph equipped with series TCD and FID.

4.2.4. Dry methane combustion

Methane combustion was also performed at dry conditions to compare the activity of Pd-COL catalyst with literature data. The reactor was packed with 0.5 g of calcined (550 °C, 16 h) 0.24 wt.% Pd-COL catalyst corresponding to 1.2 mg active Pd. Dry methane oxidation was investigated at similar conditions as described above in the wet methane combustion, but without water addition. Two ignition-extinction experiments in the 200−550 °C temperature range were performed to pre-condition the catalyst, and followed by a thermal aging test in dry methane/air gas mixture by increasing the reactor temperature to 550 °C and then cooling the reactor to 350 °C that gives about 50% methane conversion. Finally, a third ignition-extinction experiment was performed to check the activity of the aged 0.24 wt.% Pd-COL catalyst. The turnover frequency was evaluated at differential conditions (1.5% conversion, 254 °C) in the third ignition-extinction curve, and Pd dispersion measured by CO chemisorption.

4.3. Results and discussion

Colloidal Pd-COL, Ni-COL and $PdNi_{12}$-COL nanoparticles were synthesized by the reduction of $PdCl_2$ and/or $Ni(NO_3)_2 \cdot 6H_2O$ precursors in alcohol media in the presence of poly(vinylpyrrolidone) (PVP) followed by deposition on γ-Al_2O_3 support. The metal loadings were found by neutron activation analysis as 0.190 wt.% Ni and 0.029 wt.% Pd, with the 12-to-1 Ni-to-Pd molar ratio. The notation $PdNi_{12}$-COL only indicates the overall catalyst molar composition, not the phase composition. $PdNi_{12}$-IMP catalyst was prepared by incipient wetness impregnation of the support with an aqueous solution of the same precursors. The Pd-COL, $PdNi_{12}$-IMP and Ni-COL catalysts were prepared with the same loadings for fair comparison (0.029 wt.% Pd and 0.190 wt.% Ni). All catalysts were calcined under static air at 550 °C for 16 h.

Catalytic wet methane combustion was conducted in the presence of 5 mol.% of water in the feed (4100 ppm CH_4 in N_2 and air mixture) at 1.1 barg pressure. All experiments were performed with the same total catalyst amount in the reactor with the same loadings corresponding to 1.2 mg Pd and/or 7.6 mg Ni. Ignition and extinction curves were obtained between 200 °C and 550 °C. First, two ignition-extinction experiments (without and with 5 mol.% water, respectively) were performed to pre-condition the catalyst, followed by the hydrothermal aging in the wet methane/air feed by increasing reaction temperature to 550 °C and then cooling the reactor to the temperature that gives about 50% CH_4 conversion. The high-low temperature cycling was repeated 8 times (about 22 hours). After the cycling was completed, the reactor temperature was then held at the selected temperature for another 18 hours. Finally, a third ignition-extinction test (with 5 mol.% water) was performed to check the activity of aged catalyst. These data are reported in Figure 4.2.

As seen from Figure 4.2, the use of colloidal $PdNi_{12}$-COL catalyst lowers the complete methane combustion temperature by approximately 100 °C as compared to monometallic Pd (Pd-COL) at the same Pd loading in the reactor and in the supported catalysts. Remarkably, Ni addition by co-impregnation with metal precursors ($PdNi_{12}$-IMP) did not show any improvement in the catalytic activity versus Pd. The same trend was observed during the hydrothermal aging of the three catalysts: both Pd-COL and $PdNi_{12}$-IMP showed 10 ÷ 40% conversions in the temperature range of 415 to 450 °C, while the $PdNi_{12}$-COL catalyst allowed 80% conversion at 435 °C. The $PdNi_{12}$-COL catalyst did not deactivate for at least 40 hours on stream at temperatures of 375 ÷ 435 °C. This temperature window indicates the outstanding colloidal catalyst stability in the presence of water: the effect of water on Pd catalysts is known to be significant at lower temperatures and almost negligible at 450 °C and above [5]. Colloidal monometallic nickel catalyst (Ni-COL) displayed the least activity (38% conversion at 550 °C at the same loading as in the bimetallic catalysts).

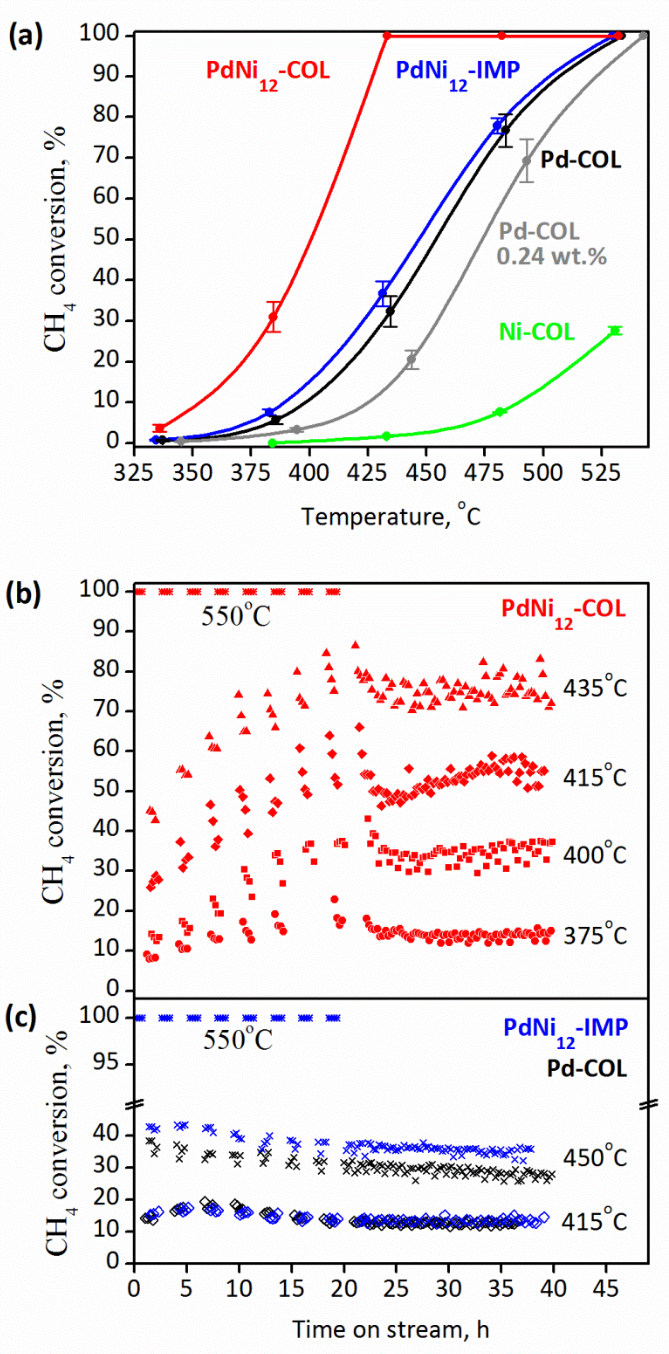

Figure 4.2. Wet methane combustion, 4100 ppm methane, 5 mol.% water, 1.1 barg pressure, 1.2 mg Pd, 7.6 mg Ni (0.029 wt.% Pd and 0.190 wt.% Ni loading in relevant catalysts, except for the 0.24 wt.% Pd catalyst): (a) ignition-extinction curves after 40 hours on stream (no hysteresis was observed), (b), (c) hydrothermal aging. Error bars represent one standard deviation from average for all ignition-extinction curves (b, c) after 40 hours on stream.

Chlorine-containing Pd precursor was used for the catalyst preparation and it can be poisonous for the catalytic activity [3], so its content was verified via X-ray photoelectron spectroscopy (XPS). The $PdNi_{12}$-COL catalyst contains negligible amount of Cl (0.1 wt.%) after calcination at 550 °C for 16 hours, which is likely due to washing of the preformed nanoparticles. The $PdNi_{12}$-IMP catalyst had quite a significant chlorine content (0.7 wt.%) after the calcination, but it was below the detection limit for the sample after the hydrothermal aging for 40 hours, most likely due to the cleaning effect of steam-air mixture. To confirm that the lower activity of the $PdNi_{12}$-IMP catalyst is not due to the chlorine presence, another impregnated catalyst was prepared with palladium acetate and tested at 450 °C: the catalytic results were the same (< 3% conversion difference) as those for the $PdNi_{12}$-IMP catalyst prepared from palladium chloride. Thus, the chlorine effect can be considered negligible.

Because bimetallic catalysts may show improved stability against sintering [22], the addition of Ni to Pd during the colloidal synthesis could potentially prevent growth of Pd nanoparticles known to occur at high-temperature oxidation processes. The ability to control collective properties of nanoparticles is crucial for their stable performance [23]. Herein, the as-prepared nanoparticle sizes are comparable for both catalysts in the range of 2−3 nm as seen from their transmission electron microscopy (**TEM**) images (Figure 4.3), being on the higher side for the $PdNi_{12}$-COL sample. Both Pd-COL and $PdNi_{12}$-COL catalysts exhibited similar sintering behavior after calcination and hydrothermal aging. Higher degree of agglomeration for the bimetallic catalyst is due to overall higher metal loading (0.03 wt.% Pd in Pd-COL and 0.03 wt.% Pd–0.19 wt.% Ni in $PdNi_{12}$-COL). Thus, nickel addition does not noticeably improve the nanoparticle stability against sintering.

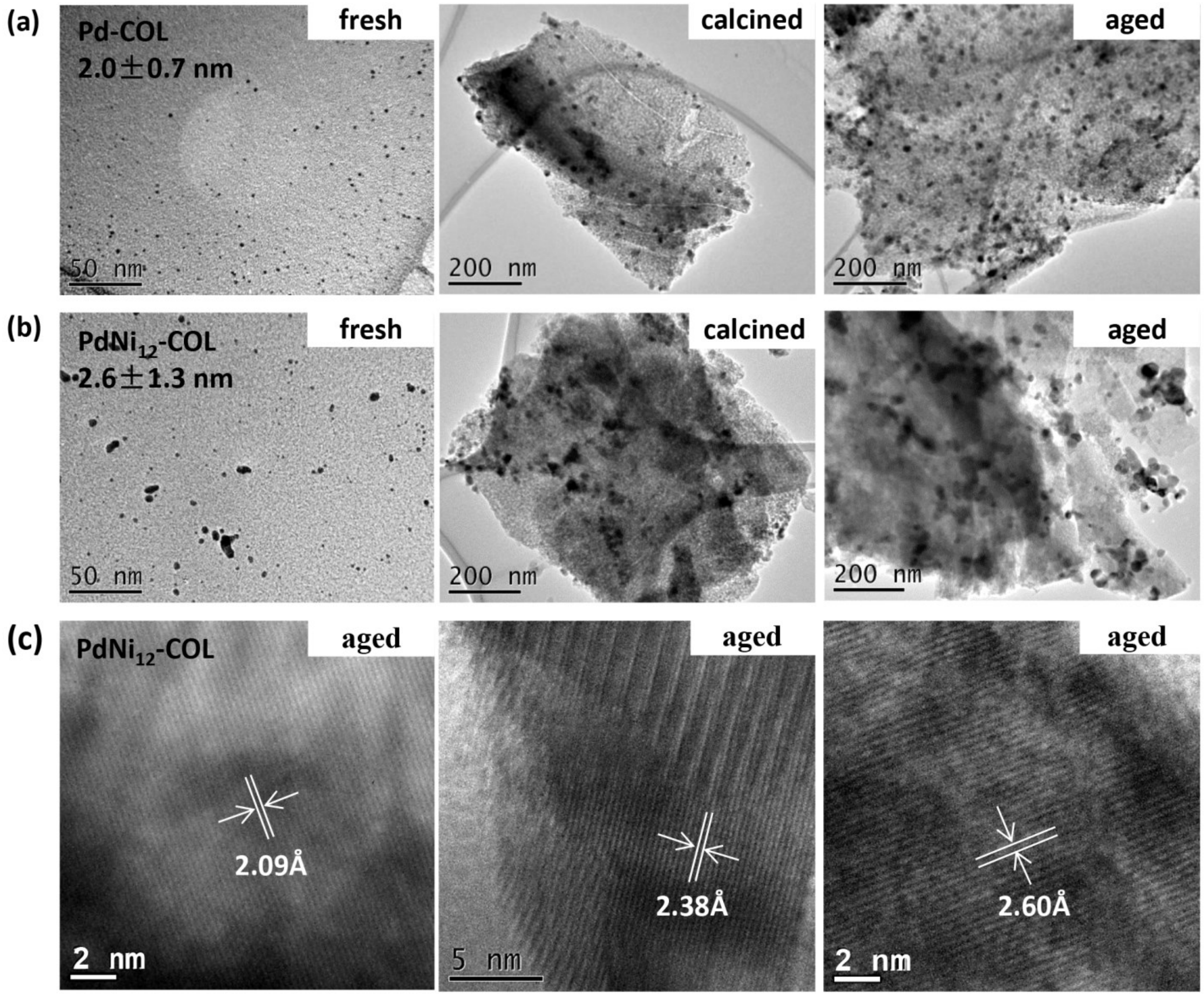

Figure 4.3. TEM images of Pd-COL (a) and PdNi$_{12}$-COL (b, c) catalysts: nanoparticles before deposition on the support ("fresh"); after deposition and calcination for 16 h at 550 °C ("calcined"), and after hydrothermal aging (methane combustion) for 40 h ("aged").

A plausible explanation of the enhanced activity of the bimetallic colloidal catalyst could be related to its enhanced agglomeration versus the monometallic Pd-COL. Indeed, it is known that turnover frequency of Pd catalysts in methane combustion increases as high as two orders of magnitude with decreasing dispersion [24-27]. To verify this hypothesis, we prepared a higher loading Pd-COL 0.24 wt.% catalyst, so that the catalyst approaches the bimetallic catalyst by the metal(s) weight loading. As found by CO chemisorption, after 16 h calcination at 550 °C, the Pd dispersion in 0.24 wt.% Pd-COL catalyst is 10% (13 nm particle size) versus 28% (4.8 nm particle size) for the 0.03 wt.% Pd-COL catalyst. TEM of the higher loading Pd catalyst (Figure 4.4) confirmed the excessive sintering and resembled the image for the $PdNi_{12}$-COL catalyst (Figure 4.3(b)). However, when tested in the wet methane combustion with the same Pd amount in the reactor (Figure 4.2(a)), the higher loading catalyst was not only much less active than the $PdNi_{12}$-COL catalyst, but also exhibited lower activity as opposed to the lower loading Pd-COL catalyst. Thus, the activity enhancement effect for the $PdNi_{12}$-COL catalyst cannot be explained by higher overall metal loading and decreased dispersion.

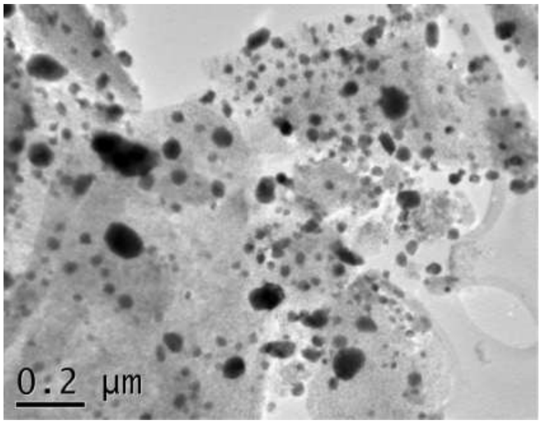

Figure 4.4. TEM image of 0.24 wt.% Pd-COL catalyst after calcination at 550 °C for 16 h.

In order to compare our findings with the literature data, we evaluated TOF for dry methane combustion at differential conditions at 254 ^{o}C as 0.008 s^{-1} (for the 0.24 wt.% Pd-COL catalyst with 10% Pd dispersion, 13 nm particle size; the TOF is for the third ignition-extinction curve after 40 h on stream). Using the activation energy value of 117 kJ/mol [27], the extrapolated exemplary reported TOFs for Pd/Al_2O_3 catalysts at 254 °C are 0.0082 s^{-1} (2.2 wt.% Pd loading, 14 nm particle size) [25], and are in the range of 0.0017 s^{-1} (0.46 wt.% Pd loading, 35% Pd dispersion) to 0.094 s^{-1} (2.3 wt.% Pd loading, 10% Pd dispersion) [27]. Our 0.24 wt.% Pd-COL catalyst prepared via the colloidal technique showed 14 times higher TOF than the reported impregnated Pd catalyst with the same loading (0.2 wt.%) [27]. The enhancement is likely due to the lower Pd dispersion in the colloidal catalyst (10% versus 84% for the reported catalyst), because the 2-nm Pd nanoparticles were formed before deposition on the support.

To understand the observed differences between the colloidal $PdNi_{12}$-COL and impregnated $PdNi_{12}$-IMP catalysts, the materials were subjected to temperature programmed reduction (TPR) and revealed distinctively different profiles (Figure 4.5(a)). Pd-COL catalyst shows only a hydrogen evolution peak below 100 °C, indicative of hydride decomposition [18]. The reduction of the $PdNi_{12}$-COL catalyst occurs at 383 °C that can be assigned to the reduction of NiO [28]. Although the TPR test for the $PdNi_{12}$-COL catalyst was performed with the same Pd loading as the monometallic Pd-COL sample, the negative hydrogen evolution peak corresponding to Pd disappeared in the $PdNi_{12}$-COL catalyst; this could be an indication of Ni−Pd interactions in the latter. The $PdNi_{12}$-IMP catalyst showed only a small broad peak at 383 °C and a strong reduction peak with a maximum of 850 °C, which is characteristic of $NiAl_2O_4$ spinels for catalysts prepared by co-impregnation of Ni and Pd precursors on alumina support [6, 28]. Thus, as TPR shows the method of Pd−Ni catalyst preparation is crucial for the final catalyst structure: no spinel formation occurred when nanoparticles were formed in the absence of alumina.

The XPS analysis of the calcined samples confirmed the TPR findings (Figure 4.5(b)): the Ni $3p_{3/2}$ peaks from NiO (main 854.2 eV and its satellite 861.1 eV [29]) are insignificant for the impregnated sample, as opposed to the colloidal catalyst. The 856.1 eV peak may be ascribed both to NiO shoulder and spinel $NiAl_2O_4$, with a satellite at 863.1 eV [29], but in the impregnated sample the two peaks represent virtually all present Ni states, without NiO at 854.2 eV, indicating that nickel in the impregnated sample is consumed in the spinel formation, in agreement with the TPR data. Pd $3d_{5/2}$ peaks in all three Pd-COL, $PdNi_{12}$-COL and $PdNi_{12}$-IMP samples (Figure 4.5(c)) could be assigned to PdO (336.5 eV) and PdO_x (337.4 eV) The peak ratios of PdO/PdO_x are identical for the colloidal mono- and bimetallic catalysts, but the impregnated catalyst exhibit the significantly lower value. Smaller Pd crystallites, such as in the impregnated sample, are known to be oxidized to a larger extent versus larger particles, which leads to the decreased catalytic activity [27], in agreement with our data. No shifts in Pd binding energy because of possible alloying with Ni were observed.

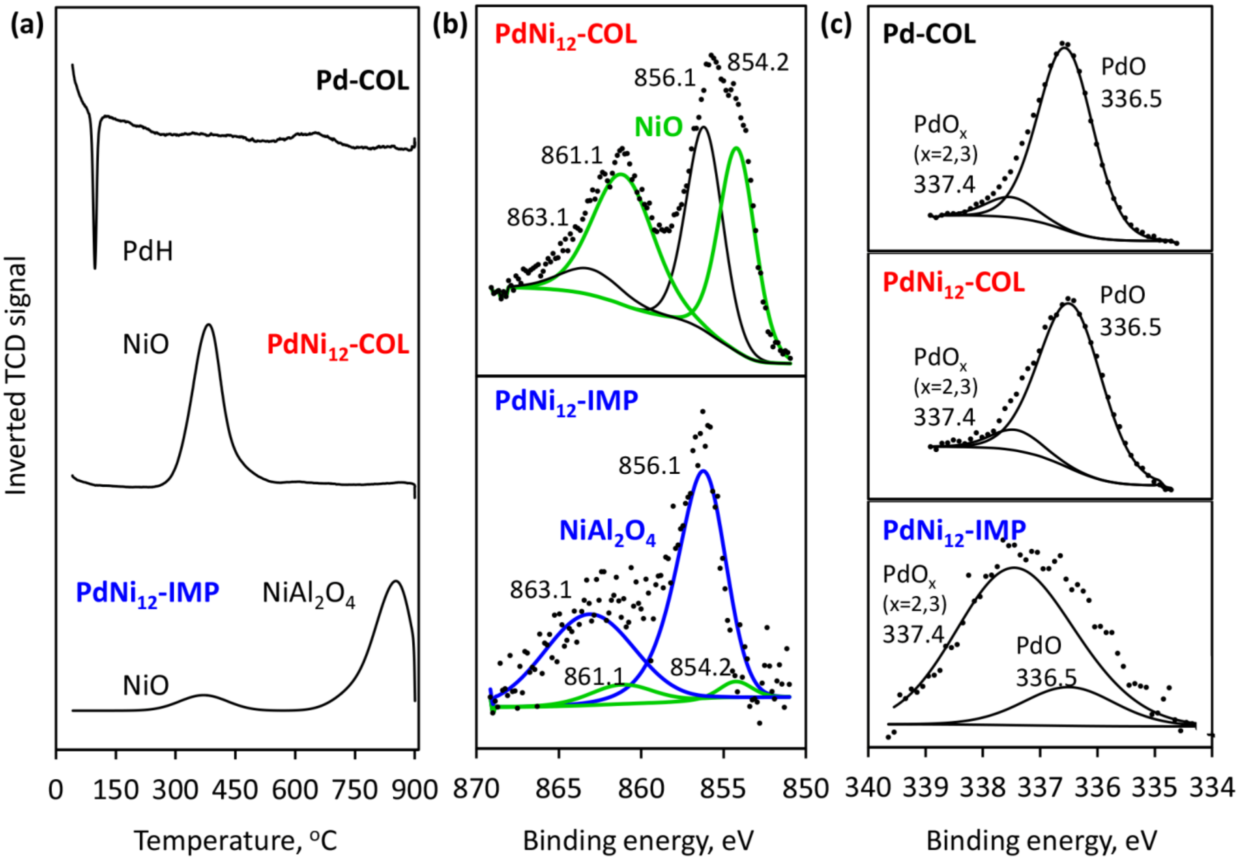

Figure 4.5. Spinel and NiO phase formation in the catalysts after calcination at 550 °C, 16 h: temperature programmed reduction profiles with the same loadings of Pd and Ni in H_2/Ar flow (negative inverted TCD signal indicates hydrogen evolution) (a); high-resolution X-ray photoelectron spectra of Ni $2p_{3/2}$ (b) and Pd $3d_{5/2}$ (c).

The PdNi$_{12}$-COL catalyst was further investigated via high-resolution TEM (**HRTEM**) after the hydrothermal aging to gain more insight into the possible alloy structure of Ni−Pd bimetallic nanoparticles (Figure 4.3(c)). The lattice spacings of 0.209 nm, 0.241 nm and 0.264 nm are characteristic of cubic NiO (200), NiO (111) and tetragonal PdO (101), respectively. An **XRD** pattern (Figure 4.6) also shows the presence of tetragonal PdO and cubic NiO phases, with no shifts that could suggest the intrinsic Pd−Ni alloy structure. Although Pd and Ni form alloys of unlimited mutual miscibility, similar segregation of Pd and Ni oxides supported on alumina were observed in their temperature-programmed oxidation and reduction study [30]. Nevertheless, the catalytic results are indicative of the interactions between the PdO and NiO phases in the PdNi$_{12}$-COL catalyst. The nature of such interactions is currently under study, with a hypothesis that NiO particles participate in the redox Mars and van Krevelen mechanism [31, 32], when reduced Pd is reoxidized with oxygen from NiO and Al_2O_3. The NiO presence may become beneficial in the wet combustion because water was suggested to decrease the oxygen exchange with the support [31].

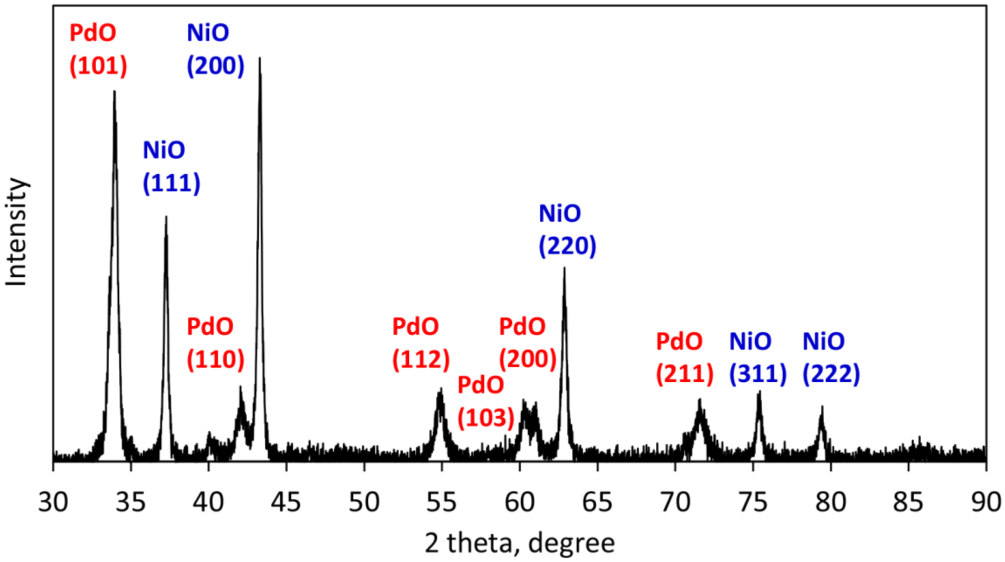

Figure 4.6. XRD pattern of unsupported PdNi$_{12}$-COL nanoparticles, dried and calcined at 550 °C for 16 h. Cubic NiO and tetragonal PdO are detected.

4.4. Conclusions

Therefore, when the bimetallic catalyst was prepared by traditional impregnation method, Ni precursor reacts with alumina support and forms inactive $NiAl_2O_4$ spinel during high temperature treatment, which explains no improvement in methane oxidation activity as compared to the monometallic Pd. Previous studies of impregnated Pd−Ni catalysts on alumina support also reported the formation of $NiAl_2O_4$ spinel phase and small amount of NiO with no improvement of Pd performance in CH_4 oxidation [13, 15]. The improved performance was only noticed if very high Ni content was employed (36:1 NiO/Al_2O_3) [7].

Our study demonstrates a dramatic importance of the synthetic strategy for effective promotion of supported metal nanoparticles by low-quantity metal promoter. In the present state, however, the developed bimetallic catalyst cannot be applied for realistic space velocities because of the low Pd loading, and bottom-up strategies must be developed to increase the loading of preformed Pd−Ni nanoparticles on the support [2]. The conversions reported in Figure 4.2 for the $PdNi_{12}$-COL, $PdNi_{12}$-IMP and Pd-COL were measured for the same space velocities for fair comparison. The value of our findings is in the dramatically increased activity of Pd catalyst in the presence of water, caused by Ni addition at the lowest reported in literature weight ratio of Ni to Pd (6.5-to-1 versus, for example, 70 as was shown previously for only 35-degree temperature reduction [7]). In general, the results indicate that it is possible to reevaluate binary supports effect on supported metal nanoparticles' catalytic performance by introducing a relevant support component into the alloy (or segregated alloy) structure with the supported nanoparticles, thus, reducing the support cost and localizing the desired effects on the catalyst surface.

Acknowledgements

Financial support from NSERC–Strategic program grant STPGP 430108-12 is acknowledged. We thank Dimitre Karpuzov for the XPS analysis and Becquerel Laboratory of Maxxam Analytics (Ontario, Canada) for NAA analysis.

4.5. References

[1] G. Centi, J. Mol. Catal. A. 173 (2001) 287-312.
[2] M. Cargnello, J.J. Delgado Jaen, J.C. Hernandez Garrido, K. Bakhmutsky, T. Montini, J.J. Calvino Gamez, R.J. Gorte, P. Fornasiero, Sci. 337 (2012) 713-717.
[3] P. Gelin, M. Primet, Appl. Catal. B. 39 (2002) 1-37.
[4] R.J. Farrauto, Sci. 337 (2012) 659-660.
[5] R. Burch, F.J. Urbano, P.K. Loader, Appl. Catal. A. 123 (1995) 173-184.
[6] Y. Liu, S. Wang, T. Sun, D. Gao, C. Zhang, S. Wang, Appl. Catal. B. 119-120 (2012) 321-328.
[7] H. Widjaja, K. Sekizawa, K. Eguchi, H. Arai, Catal. Today. 47 (1999) 95-101.
[8] B. Yue, R. Zhou, Y. Wang, X. Zheng, Appl. Surf. Sci. 252 (2006) 5820-5828.
[9] K. Sekizawa, K. Eguchi, H. Widjaja, M. Machida, H. Arai, Catal. Today. 28 (1996) 245-250.

[10] H. Widjaja, K. Sekizawa, K. Eguchi, H. Arai, Catal. Today. 35 (1997) 197-202.

[11] L. Yang, C. Shi, X. He, J. Cai, Appl. Catal. B. 38 (2002) 117-125.

[12] W.Z. Li, L. Kovarik, D. Mei, J. Liu, Y. Wang, C.H.F. Peden, Nat. Commun. 4:2481 (2013).

[13] X. Pan, Y. Zhang, Z. Miao, X. Yang, J. Energy Chem. 22 (2013) 610-616.

[14] X. Pan, Y. Zhang, B. Zhang, Z. Miao, T. Wu, X. Yang, Chem. Res. Chin. Univ. 29 (2013) 952-955.

[15] K. Persson, A. Ersson, K. Jansson, N. Iverlund, S. Jaras, J. Catal. 231 (2005) 139-150.

[16] J. Lu, K.B. Low, Y. Lei, J.A. Libera, A. Nicholls, P.C. Stair, J.W. Elam, Nat. Commun. 5:3264 (2014).

[17] T. Teranishi, M. Miyake, Chem. Mater. 10 (1998) 594-600.

[18] J. Shen, N. Semagina, ACS Catal. 4 (2014) 268-279.

[19] G.G. Couto, J.J. Kleinb, W.H. Schreiner, D.H. Mosca, A.J.A. de Oliveira, A.J.G. Zarbina, J. Colloid Interface Sci. 311 (2007) 461-468.

[20] I. Yuranov, P. Moeckli, E. Suvorova, P. Buffat, L. Kiwi-Minsker, A. Renken, J. Mol. Catal. A. 192 (2003) 239-251.

[21] R. Abbasi, L. Wu, S.E. Wanke, R.E. Hayes, Chem. Eng. Res. Des. 90 (2012) 1930-1942.

[22] A. Cao, G. Veser, Nat. Mater. 9 (2010) 75-81.

[23] G. Prieto, J. Zecevic, H. Friedrich, K.P. de Jong, P.E. de Jongh, Nat. Mater. 12 (2013) 34-39.

[24] C.A. Muller, M. Maciejewski, R.A. Koeppel, A. Baiker, J. Catal. 166 (1997) 36-43.

[25] D. Roth, P. Gelin, A. Kaddouri, E. Garbowski, M. Primet, E. Tena, Catal. Today. 112 (2006) 134-138.

[26] K. Fujimoto, F.H. Ribeiro, M. Avalos-Borja, E. Iglesia, J. Catal. 179 (1998) 431-442.

[27] R.F. Hicks, H. Qi, M.L. Young, R.G. Lee, J. Catal. 122 (1990) 280-294.

[28] J. Guo, H. Zhao, D. Chai, X. Zheng, Appl. Catal. A. 273 (2004) 75-82.

[29] F. Qin, J.W. Anderegg, C.J. Jenks, B. Gleeson, D.J. Sordelet, P.A. Thiel, Surf. Sci. 602 (2008) 205-215.

[30] T. Paryjczak, J.M. Farbotko, K.W. Jozwiak, React. Kinet. Catal. Lett. 20 (1982) 227-231.

[31] W.R. Schwartz, L.D. Pfefferle, J. Phys. Chem. 116 (2012) 8571-8578.

[32] C.A. Muller, M. Maciejewski, R.A. Koeppel, A. Baiker, Catal. Today. 47 (1999) 245-252.

[33] J. Shen, R.E. Hayes, X. Wu, N. Semagina, ACS Catal. 5 (2015) 2916-2920.

Chapter 5. Structural evolution of bimetallic Ru−Pd catalysts in oxidative and reductive applications[4]

5.1. Introduction

Introducing a second metal component to supported catalysts is widely recognized as an efficient way to increase catalyst activity, selectivity, and stability. Numerous large-scale industrial productions benefit from synergism phenomena in bimetallic catalysis [1-5]. Two metals may form intrinsic alloys with or without preferential shell or core segregation of one of the metals, or individual monometallic nanoparticles. Such structures, however, often are not maintained during catalysis [6], leading to unstable catalyst performance and even deactivation. The changes are driven by thermodynamics (the metal with lower surface energy segregates to the surface of bimetallic nanoparticles) and/or chemically activated selective metal diffusion ("adsorbent-induced segregation") due to different metal affinities to the reaction mixture components [7, 8]. Thermodynamic considerations predict that nanoparticles with the same metal ratios but initially different structures at high enough temperatures transform into one most-thermodynamically-

---

[4] Chapter 5 of the thesis was submitted to Applied Catalysis A: General as: "Structural evolution of bimetallic Ru−Pd catalysts in oxidative and reductive applications", **J. Shen**, R. W. J. Scott, R. E. Hayes and N. Semagina, *Applied Catalysis A: General* (2015), under revision. The reaction setup for methane oxidation was originally designed and built by Dr. Long Wu and Dr. Robert E. Hayes. The EXAFS work was performed with technical support by Dr. Ning Chen at the Canadian Light Source, Saskatchewan and Dr. Robert W.J. Scott (and his PhD student, Atal Shivhare) at University of Saskatchewan, Saskatchewan. Dr. Robert W. J. Scott provided training on IFEFFIT software package for EXAFS data processing, as well as collaborated with EXAFS modeling. Dr. Xuehai Tan collected HRTEM images and performed SAED analyses at University of Alberta. Shiraz Merali performed XRD analysis at the department of Chemical and Material Engineering, University of Alberta. NAA analysis was performed by Becquerel Laboratories Inc., Maxxam Analytics, Ontario. The author performed all syntheses, reactions, analyses and other characterizations. This paper was reprinted with Permissions from Robert W. J. Scott and Robert E. Hayes.

stable configuration [9]. At different metal ratios, nanoparticles may be stabilized in different core−shell or alloyed structures even at temperatures above 1600 K [10].

In thermodynamically driven changes, achieving prolonged catalyst stability is still feasible (especially in low-temperature regions) because the structural evolution is often kinetically limited. The adsorbent-induced segregation [7, 8], on the contrary, may happen on the same time scale as the catalytic reaction and requires lower temperatures and shorter times to modify the parent bimetallic nanoparticles. For example, a ternary CuPdY alloy did not segregate in a vacuum, but in the presence of oxygen, Y oxides were formed on the surface, driven by preferential oxygen-induced Y segregation [11]. Similarly, parent alloy Pt−Co nanoparticles evolved into Pt(shell)/Pt−Co(core) particles upon annealing in CO [7].

Studies of the particle structural evolution during pre-treatment or catalysis are complicated not only by the limited availability of operando and in situ catalyst characterization techniques but also by the nature of the catalysts themselves. The traditional preparation methods that support impregnation with metal precursor solutions followed by calcination do not allow the production of well-defined uniform nanoparticles, so their structural evolution studies are complicated by the wide polydispersity of the original nanoparticles. At present, the steadily increasing number of colloidal chemistry techniques to prepare structure- and size-controlled metal nanoparticles [12-15] enable experimental studies of the bimetallic nanoparticle rearrangement, including structure inversion during synthesis or after thermal activation and/or catalysis [16-18]. The structural changes depend on the atmosphere (for example, oxidizing or reducing) and may or may not take place depending on the involved metals [15].

The objective of this work is to demonstrate the structural changes of well-defined bimetallic nanoparticles in reductive and oxidative catalytic reactions. We start with two different Ru−Pd nanostructures synthesized with a protective stabilizer either via simultaneous reduction of the metal precursors ("alloy" Ru2Pd1) or via Ru atom deposition on the core of preformed Pd nanoparticles ("core−shell" Pd(c)Ru(s) sample), as depicted in Scheme 5.1. The overall metal ratio is the same in both structures so that their structural evolution is not affected by their composition [10]. We further use these nanoparticles as catalysts for the hydrogenolysis of indan at 350 °C and combustion of methane in air at up to 550 °C. In the former case, the structural evolution is minimal, and the alloy and Pd(core)−Ru(shell) nanoparticles' performance is distinctively different. In methane combustion, both structures transform into the very same nanoparticle structure with a Pd-enriched shell and show similar catalytic performance. This comparative study demonstrates the advantages and limitations of the structure-controlled bimetallic nanoparticle synthesis for different catalytic applications.

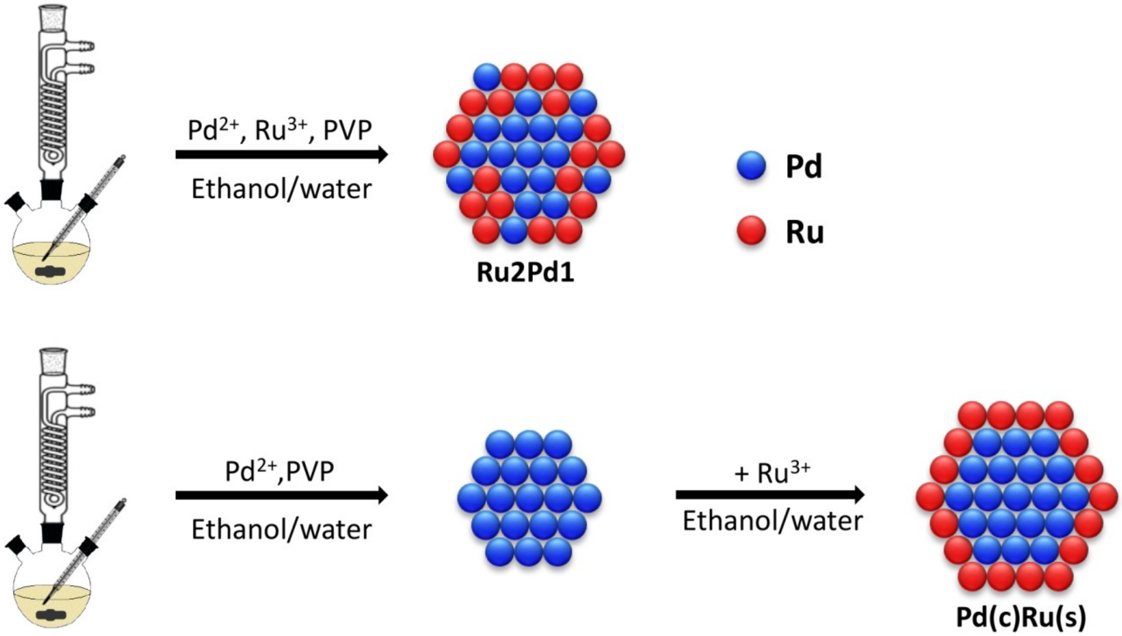

Scheme 5.1. Structure-controlled synthesis of alloy and core−shell bimetallic nanoparticles.

5.2. Experimental section

5.2.1. Materials

Ruthenium(III) nitrosylnitrate ($Ru(NO)(NO_3)_3$, Ru 31.3% min, Alfa Aesar), palladium(II) chloride solution ($PdCl_2$, 5% w/v, Acros), poly(vinylpyrrolidone) (PVP) (MW 40,000, Sigma-Aldrich), reagent alcohol (ethanol, 95 vol.%, Fisher Scientific), ethylene glycol (EG, 99.8%, Sigma-Aldrich), gamma aluminum oxide (γ-Al_2O_3, 150 mesh 58Å pore size, Sigma-Aldrich), and acetone (99.7%, Fisher Scientific) were used as received. Milli-Q water was used throughout the work.

5.2.2. Catalyst preparation

All catalysts were prepared by synthesizing PVP-stabilized 2−3 nm nanoparticles in colloidal solutions, followed by deposition on γ-Al_2O_3 support with 5.8 nm pores. Monometallic Ru nanoparticles were prepared using the ethylene glycol reduction method [19] with some modifications [20]. At room temperature, 0.2 mmol $Ru(NO)(NO_3)_3$ and PVP (2 mmol, PVP-to-Ru molar ratio = 10/1) were dissolved in 200 mL EG in a 500 mL single-neck round-bottom flask. The reaction temperature was increased from room temperature to the reflux point of EG (198 °C), and maintained at 198 °C for 3 h under stirring. Monometallic Pd nanoparticles were synthesized by the one-step alcohol reduction method [21] with some modifications [20]. A mixture containing 0.2 mmol $PdCl_2$, PVP (4 mmol, PVP-to-Pd molar ratio = 20/1) and 170 mL of ethanol/water (41 vol.% ethanol) was stirred and refluxed in a 500 mL single-neck round-bottom flask for 3 h under air.

Bimetallic Ru−Pd nanoparticles with different surfaces were prepared according to our previously published synthesis techniques as shown in Scheme 5.1 [20]. For the Ru2Pd1 alloy, the monometallic Pd synthetic procedure was followed using 0.133 mmol of Ru and 0.067 mol Pd precursors. The Pd(core)−Ru(shell) nanoparticles were synthesized by Teranishi and Miyake's stepwise growth-reaction method in ethanol/water [21] with some modifications [20]. The Pd core colloids were prepared using the synthesis method for monometallic Pd nanoparticles. The pre-synthesized Pd seed colloidal solution (0.05 mmol Pd, 42.5 mL) and 0.1 mmol $Ru(NO)(NO_3)_3$ were dissolved in 170 mL ethanol/water (41 vol.% ethanol) at room temperature, without more fresh PVP addition. The mixture was then stirred and refluxed for 3 h to allow the formation of the Ru shell.

The catalyst support, γ-Al_2O_3, was dried in static air at 500 °C for 3 h. The PVP-stabilized monometallic Ru nanoparticles prepared in EG were precipitated with acetone (acetone-to-colloidal solution volumetric ratio = 4/1), and deposited on γ-Al_2O_3 by incipient wetness impregnation. The ethanol/water colloidal solutions of PVP-stabilized monometallic Pd and bimetallic Ru−Pd nanoparticles were concentrated by vacuum evaporation of solvents, followed by incipient wetness impregnation on the γ-Al_2O_3 support. Finally, all catalysts were dried in static air at 60 °C overnight. The target total metal(s) loading was 0.3 wt.%.

The actual loadings in the supported catalysts were determined by neutron activation analysis as 0.250 wt.% Ru/γ-Al_2O_3; 0.240 wt.% Pd/γ-Al_2O_3; 0.154 wt.% Ru, 0.065 wt.% Pd in

Ru2Pd1/γ-Al_2O_3; and 0.200 wt.% Ru, 0.072 wt.% Pd in Pd(c)Ru(s) catalysts. The Ru-to-Pd molar ratios in the final catalysts are 2.4 and 2.8 for the Ru2Pd1 and Pd(c)Ru(s) samples.

5.2.3. Catalyst characterization

The PVP-stabilized nanoparticles and/or pretreated catalysts were characterized by transmission electron microscopy (**TEM**), selected area electron diffraction (**SAED**), and high-resolution TEM (**HRTEM**) at 200 kV on a JEOL 2100 transmission electron microscope (Cell Imaging Facility, University of Alberta). The mean diameter and standard deviation of nanoparticles were calculated by counting more than 200 particles from TEM images using ImageJ software. X-ray powder diffraction (**XRD**) patterns were recorded on a Bruker AXS diffractometer (Department of Chemical and Material Engineering, University of Alberta) with a Cu-Kα radiation source (λ = 1.54059 Å) at 40 kV and 44 mA. Continuous X-ray scans were carried out from 2θ of 10° to 110° with a step width of 0.05° and a scan speed of 2°/min. XRD peak identification and data processing were performed using MDI Jade 9.0 software combined with the ICDD database. The colloidal solutions were concentrated by rotary evaporation of solvents under vacuum, followed by drying in an oven at 60 °C under air for a day. Nanoparticle powders (without further deposition on alumina support) were collected for XRD analyses.

The actual loadings of Ru and Pd on γ-Al_2O_3 before and after pretreatment were determined by neutron activation analysis (**NAA**) at Becquerel Laboratories (Maxxam Company, Ontario). Samples were irradiated for 20 min in the Cd shielded, epithermal site of the reactor core. Palladium and ruthenium were counted for 15 min after 24 h decay on an Aptec CS13-A31C gamma detector.

CO chemisorption analyses were performed by dosing 3% CO/He gas mixture at room temperature with an AutoChem 2950HP instrument equipped with a quartz U-tube reactor and a thermal conductivity detector (TCD). The volumetric flow rates of CO/He loop gas and the He carrier gas were 25 mL/min. Prior to CO chemisorption experiments, the catalysts were calcined at 550 °C in air for 16 h in a furnace. The precalcined catalysts were reduced in a flow of 10% H_2/Ar (25 mL/min) at 550 °C for 1 h. After the calcination-reduction pretreatment, the samples were purged with argon for 30 min at 550 °C and cooled to ambient temperature under inert atmosphere. The results were corrected by subtracting the CO uptakes of alumina support.

Diffuse reflectance infrared spectra of the adsorbed CO (**CO-DRIFTS**) were obtained using NEXUS 670 FT-IR fitted with a Smart Diffuse Reflectance accessory. DRIFT spectra were recorded against a KBr standard (256 scans, 4 cm^{-1} resolution). Data processing was performed with OMNIC software. The detailed experimental procedures including catalyst pretreatment can be found in our previous work [20]. Monometallic Pd and Ru and bimetallic Pd(c)Ru(s) samples were calcined at 200 °C for 1 h in air, and followed by reduction in a flow of 10% H_2/Ar at 375 °C for 30 min to simulate conditions of pretreatment before the catalytic indan ring opening. Prior to CO treatment, the sample was purged with Ar at 375 °C, and cooled down to room temperature in Ar. Then 3% CO/He was passed through the sample for 30 min, followed by degassing in an Ar environment to remove the physically adsorbed CO.

The **hydrogenation of 2-methyl-3-buten-2-ol (MBE) to 2-methylbutan-2-ol (MBA)** that is catalyzed by Pd only was selected to elucidate whether Pd atoms are present in the outermost layer of bimetallic Ru−Pd nanoparticles, as described previously [20]. A semibatch stainless reactor was filled with 0.04 M MBE in 200 mL ethanol and 0.5 g of as-prepared catalyst. The MBE hydrogenation reaction was carried out at 40 °C, 0.45 MPa absolute pressure and 1,200 rpm stirring speed. During the reaction, the hydrogen pressure drop in the gas burette was recorded. The initial reaction rate was calculated from the slope of the hydrogen consumption graph after complete dissolution of hydrogen in ethanol.

Extended X-ray absorption fine structure spectroscopy (**EXAFS**) was performed at Canadian Light Source (Saskatchewan). X-ray absorption spectra at the Pd K-edge and the Ru K-edge were recorded at the HXMA beamline 061D-1 (energy range, 5−30 keV; resolution, 1×10^{-4} $\Delta E/E$) at the Canadian Light Source (CLS, 2.9 GeV storage ring, ~ 250 mA current). All samples were pressed into pellets and measured in transmission mode at room temperature. Samples for EXAFS analyses were prepared with an expected metal(s) loading of 2 wt.%. The Ru−Pd catalysts for EXAFS study were pre-calcined at 550 °C for 16 hours under air followed by H_2 reduction at 400 °C, which is confirmed to be enough to reduce oxidized Ru−Pd nanoparticles to metallic forms by our previous TPR analysis [20]. After the reduction the catalysts were kept at ambient temperature under air atmosphere for one week. A double-crystal Si(220) monochromator was employed for energy selection. Higher harmonics were eliminated by detuning the double-crystal Si(220) by using a Pt-coated 100 mm long KB mirror.

The IFEFFIT software package was used for EXAFS data processing [22]. More details about obtaining EXAFS function can be found in previous publications [23, 24]. The EXAFS fitting was performed in R-space using theoretical phase shifts and amplitudes generated by FEFF. Lattice parameters and first shell coordination numbers of 12 for bulk fcc Pd and (or hcp Ru) were used to generate the amplitude reduction factor for Pd (or Ru) by fitting Pd foil (or Ru foil). The amplitude reduction factors found from Pd and Ru foils were 0.828 and 0.773, respectively. Ru−Pd bimetallic systems were fitted using bulk Pd lattice parameters, as XRD and SAED confirmed the fcc structures of the bimetallic nanoparticles. Additionally, the lattice spacings for the Ru−Pd bimetallic catalysts calculated from (111) diffractions are very close to that of monometallic Pd nanoparticles, which will be discussed later.

5.2.4. Catalysis in reductive atmosphere: indan ring opening in hydrogen, 350 °C

The developed monometallic and bimetallic Ru−Pd catalysts were studied in a low-pressure indan ring opening, as described in our previous study [20]. The PVP-stabilized catalysts were calcined at 200 °C in static air, followed by in situ reduction at 375 °C in a flow of hydrogen (80 mL/min). The catalytic indan ring opening was carried out at an internal temperature of 350 °C and 1 atm pressure. Indan ($(4.7\pm0.6)\times10^{-6}$ mol/min flow rate) was fed into the catalytic system by bubbling 120 mL/min hydrogen through indan at a constant temperature of 10 °C. The gas outlet from the reactor was analyzed online using a Varian 430 gas chromatograph equipped with FID. As reported previously [20], the ring opening products are 2-ethyltoluene, *n*-propylbenzene, *o*-xylene, ethylbenzene, toluene, benzene, and lights (mainly C1 and C2), in which only 2-ethyltoluene and *n*-propylbenzene are the desired ring opening products with a naphthenic ring being cleaved once.

5.2.5. Catalysis in oxidative atmosphere: methane combustion in air, up to 550 °C

Methane combustion was investigated over the developed Ru−Pd nanocatalysts according to the previous study published by Abbasi et al. [25]. A 20 in. long tubular reactor with an inner diameter of 3/8 in. was packed with calcined catalysts (550 °C, 16 h in static air) corresponding to 1.2 mg active Pd (and/or 3.1±0.4 mg Ru). Layers of quartz wool were placed at both ends of the catalyst bed to hold the catalyst in place. The reactor was then placed inside a furnace equipped with a temperature controller. The internal reaction temperatures were measured by two thermocouples at each end of the catalyst bed. The flow rates of the feed gases (10% CH_4/N_2 and air) were regulated by mass flow controllers (Matheson and MKS). Methane (10% balanced in nitrogen, 8.5 mL/min) and air (extra-dry, 200 mL/min) were pre-mixed and fed into the catalytic system. The concentration of CH_4 in the gas mixture was 4100 ppm.

Methane oxidation reactions in this study were performed as described in our previous work [26], except the catalysts were tested at dry conditions. Methane oxidation was carried out at a constant pressure of 30 psi. Ignition and extinction curves were obtained by increasing and decreasing the reaction temperature stepwise (50 °C for each step; 60 °C/min ramping rate), respectively. The ignition curves were initiated at 200 °C and ended at 550 °C, which refer to the lowest and highest combustion temperatures in the present work, respectively. The extinction curves were performed in the opposite direction to investigate the catalytic performance during cooling. Two ignition-extinction experiments were performed to stabilize the catalysts. This was then followed by a 40-hour thermal aging test in 4100 ppm methane by increasing reaction temperature to 550 °C (60 °C/min ramping rate) and then cooling the reactor to 375 °C. The 550-375 °C temperature cycling was repeated 8 times (~ 25 hours); after this cycling, the catalyst was aged at 375 °C for another 15 hours. Finally, the catalytic test in methane combustion was terminated by a third ignition-extinction cycle to check the catalytic activities after 40 hours thermal aging. During methane combustion, the temperature at each stage was held for 30 min in ignition-extinction tests and 1 h in thermal aging tests. The gas outlet from the reactor was analyzed online every 15 min using an Agilent HP 7890A gas chromatograph equipped with series TCD and FID. The reported curves in the results section represent the initial 1st ignition-extinction, cycling and ignition-extinction results after the cycling.

5.3. Results and discussion

5.3.1. Characterization of as-synthesized nanoparticles

We intentionally selected two different procedures for the bimetallic catalyst preparation to obtain nanoparticles with different structures, as outlined in Scheme 5.1. The ruthenium precursor, without the palladium seeds present, could not be reduced in ethanol, so no monometallic Ru nanoparticles could be obtained in the ethanol solution used for syntheses. The presence of palladium nanoparticles facilitated Ru^{3+} reduction by an autocatalytic surface-growth mechanism, as suggested by Liu et al. for similar Pt−Ru systems [27].

Figure 5.1 shows **HRTEM** images and **SAED** patterns of PVP-stabilized Pd(c)Ru(s) and Ru2Pd1 nanoparticles; the samples were prepared from colloidal solutions without further treatment. Both materials are single crystals with an fcc structure as follows from the comparison of the observed ring diffraction patterns with the simulated fcc pattern. No monometallic hcp Ru structures were found, as expected from the synthetic procedure. Statistical analysis of the nanoparticle size distribution based on **TEM** revealed the sizes for monometallic Pd, monometallic Ru, Pd(c)Ru(s) and Ru2Pd1 systems to be 2.0±0.5 nm, 2.0±0.3 nm, 2.3±0.7 nm and 2.6±0.6 nm, respectively, as reported in our previous work [20]. Larger sizes of the bimetallic samples as compared to the monometallic forms suggest the formation of intrinsic bimetallic structures. As-synthesized Ru−Pd catalysts were in metallic form; however, a small degree of Pd and Ru surface oxidation was possible after exposing to air for few weeks (at room temperature), as shown in our previous XPS analysis [28].

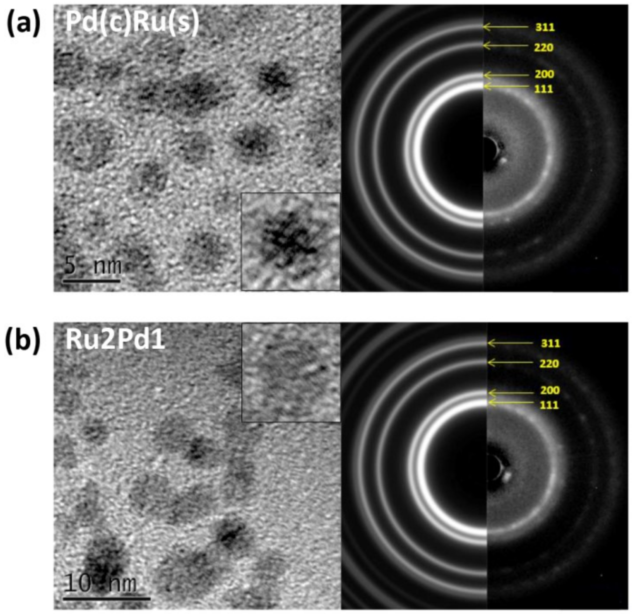

Figure 5.1. HRTEM images and SAED patterns of as-synthesized Pd(c)Ru(s) (a) and Ru2Pd1 (b) nanoparticles.

The crystal structures of the mono- and bimetallic nanoparticles were further investigated by **XRD** (Figure 5.2). Pd and Ru nanoparticles display an fcc and hcp structure, respectively. Both bimetallic samples with the same Ru-to-Pd molar ratio of 2:1 reveal (111), (200), (220) and (311) fcc peaks, which are consistent with the SAED patterns (Figure 5.1). This observation is similar to a previous study on the structural change when alloying Pt with Ru [29]: Ru−Pt bimetallic systems revealed fcc structures up to 75 mol.% of Ru in the bimetallic particles, as was shown by XRD and HRTEM [29]. The fcc (111) lattice spacings of our bimetallic samples were 2.23 Å for both samples using Bragg's law, higher than that of pure Ru (2.14 Å) and very close to that of pure Pd (2.24 Å). The TEM, XRD and SAED observations are consistent with the proposed intrinsic bimetallic nature of the synthesized nanoparticles.

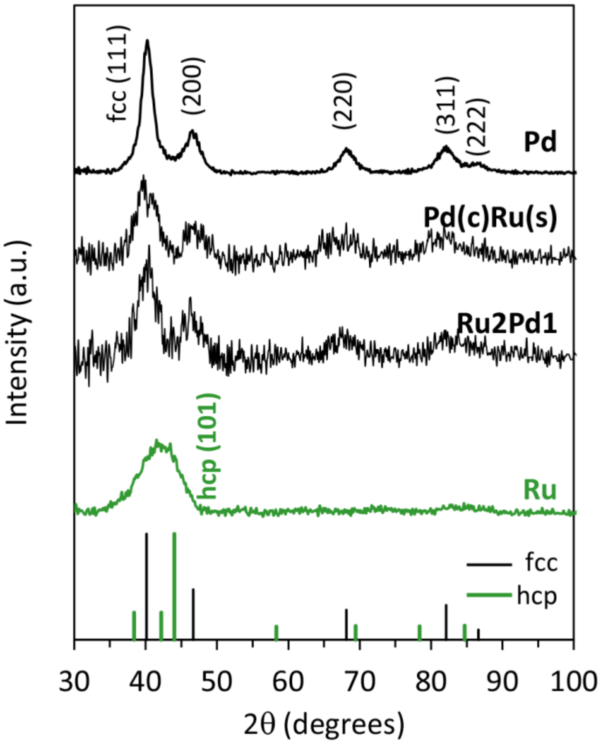

Figure 5.2. XRD patterns of as-synthesized Ru, Pd, Pd(c)Ru(s) and Ru2Pd1 nanoparticles.

For the Pd(c)−Ru(s) nanoparticle preparation, the palladium seeds were formed first followed by ruthenium precursor addition to form a Ru shell. Indeed, the size change of the Pd seeds from 2.0±0.5 nm to 2.3±0.7 nm after the Ru deposition indicates the proposed structure is likely (no monometallic Ru nanoparticles were observed, as shown above). The indicated sizes were calculated based on length; the mass/volume average for the monometallic Pd particles is 2.1 nm. 80% by mass of all Pd(core)−Ru(shell) particles are larger than 2.6 nm diameter with an average diameter (by mass) of 3.0 nm. Using crystal statistics for 2.1 nm Pd core and 3.0 nm bimetallic particles [29], the predicted molar ratio in the core−shell sample is 2.2 : 1 Ru to Pd, that is consistent with the ratio used for synthesis and found by NAA in the final catalysts.

However, core−shell structure inversion may occur even during catalyst synthesis due to the rearrangement of high-energy corner and edge atoms on ultra-small particles (< 2 nm) [16]. To verify whether Pd atoms are present on the surface of the as-synthesized Pd(c)Ru(s) nanoparticles, a selective chemical probe surface reaction was used. The three-phase liquid phase hydrogenation of an allylic alcohol (**2-methyl-3-buten-2-ol to 2-methylbutan-2-ol**) was performed at 40 ^{o}C, 0.45 MPa absolute pressure and 1200 rpm stirring speed. As-prepared monometallic and bimetallic Ru−Pd catalysts were studied in MBE hydrogenation without any further thermal treatment to minimize structural rearrangements so that the as-synthesized structures can be evaluated. Only initial rates were evaluated to avoid in-situ structural evolution. The Pd catalyst initial activity was 2.7±0.2 mol_{H_2}/mol_{Pd}/min [20], while Ru catalyst had relatively negligible MBE hydrogenation activity. Ru is known to be active in many catalytic applications, such as hydrogenolysis, methanation, oxidations, etc [30]. However, ruthenium, with its lower d-band occupancy, is relatively inactive in hydrogenations at low temperature and pressure as compared to Pd and Pt, for example, in hydrogenations of 2-methyl-3-butyn-2-ol and 1,4-butynediol [31] or hydrogenation of *o*-chloronitrobenzene in methanol at 303 K and 0.1 MPa [32], which is in line with our observations. The Pd(c)Ru(s) catalyst also did not show any activity confirming that there are no surface Pd atoms in the material and Pd nanoparticles are covered by a Ru shell in the as-synthesized nanoparticles.

5.3.2. Catalysis in a reductive atmosphere: hydrogenolysis at 350 °C

The as-synthesized particles were deposited on γ-Al_2O_3, and for this particular reductive application, they were pretreated by calcination at 200 ^{o}C followed by reduction in hydrogen flow at 375 ^{o}C. This particular treatment for surface stabilizer removal resulted in the maximized catalytic activity even in the presence of PVP residuals on the surface, as we reported earlier [20]; higher calcination temperatures caused sintering and/or undesired Pd/Ru rearrangement on the nanoparticle surface. According to our previous TPR analysis, Ru−Pd catalysts showed reduction peak at 80–85 °C [20]. Thus, the in situ hydrogen reduction at 375 °C is enough to provide metallic surfaces for both Ru2Pd1 and Pd(c)Ru(s) catalysts, which are the active sites for indan hydrogenolysis. The catalytic reaction in a reductive (hydrogen) atmosphere was indan ring opening (selective hydrogenolysis) carried out in a packed-bed reactor with gas feed at 350 °C. The reaction serves as a model reaction for fuel upgrading [33]. We already reported these results earlier and details can be found in ref. [20]. Here we provide a brief summary with a focus on the nanoparticle surface structure only for a sake of comparison with an oxidative application (following Section 5.3.3, not reported previously).

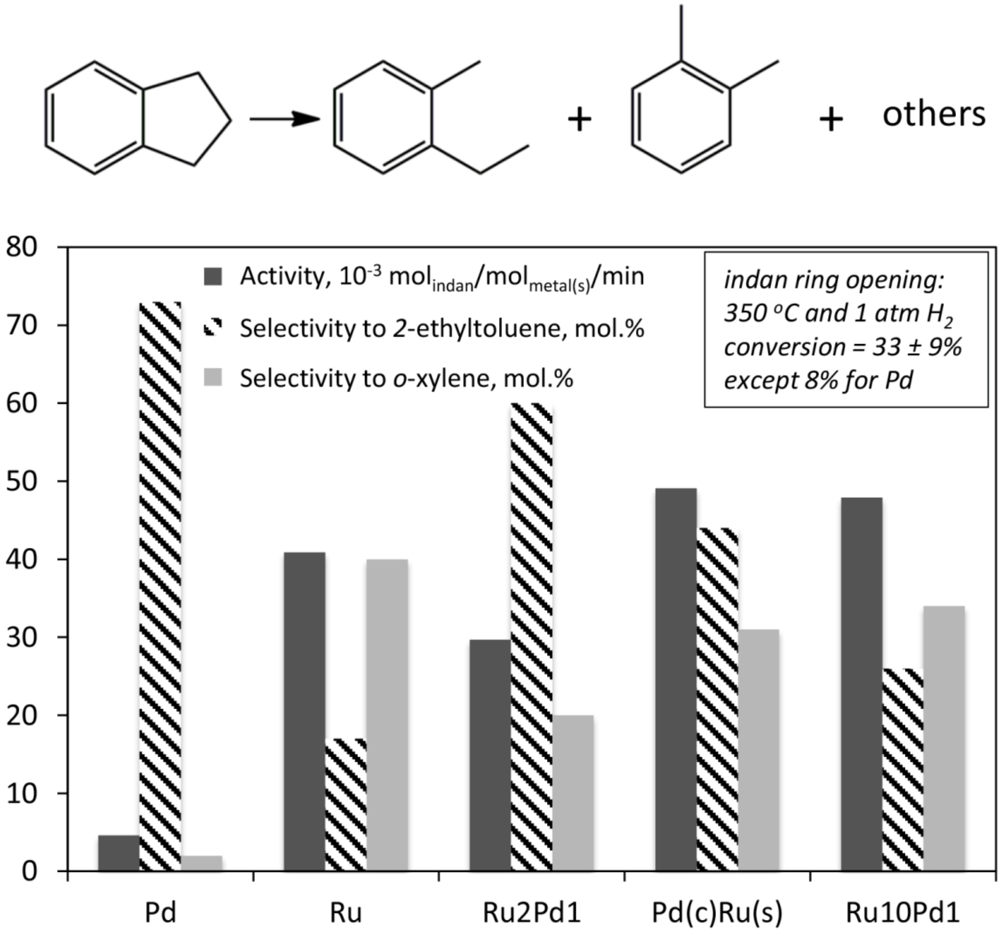

Figure 5.3. Catalytic activities and product selectivities over mono- and bimetallic Ru–Pd catalysts in indan hydrogenolysis [20]. Catalysts were calcined at 200 °C and followed by reduction in hydrogen at 375 °C for polymer removal.

Monometallic Ru is highly active in indan hydrogenolysis, unlike palladium, but the latter allows selective ring opening to 2-ethyltoluene without successive dealkylation. Ruthenium favors deeper hydrogenolysis to *o*-xylene (Figure 5.3). When the two metals are alloyed together either into an Ru2Pd1 or Pd(c)Ru(s) structure, they show intermediate behavior between the two metals (with one exception) but are distinctively different from each other. The exception is that the activity of Pd(c)Ru(s) even surpasses the activity of monometallic Ru, indicating that active ruthenium is more accessible to reactants being dispersed on the Pd core, versus monometallic Ru particles with lower Ru dispersion. The Ru2Pd1 sample shows Ru-like activity but Pd-like selectivity, suggesting the close contact between the two metals in one nanostructure: if Ru is not promoted by Pd on the nanoparticle surface, the Ru2Pd1 will not show suppressed selectivity to *o*-xylene and enhanced selectivity to 2-ethyltoluene as compared to monometallic Ru. The Pd(c)Ru(s) selectivity is closer to the monometallic Ru selectivity, indicating the shell enrichment with Ru. Figure 5.3 also presents the results of earlier reported alloyed Ru10Pd1 catalyst (molar ratio of Ru to Pd = 10) only to show how the catalytic properties of Pd(c)Ru(s) (2:1 molar ratio) are close to the Ru-enriched nanoparticles with both Ru and Pd present on the surface. Thus, the catalytic results in indan hydrogenolysis indicate that the two Ru−Pd catalysts with the same molar ratio but initially different structures (alloy Ru2Pd1 and core−shell) still behave differently in the reaction in accordance with their nanoparticle surface enrichment, but the core−shell sample does undergo some structural evolution. If initially, in low-temperature MBE hydrogenation the core−shell sample displays purely Ru behaviour, then at high-temperature hydrogenolysis, Pd behavior also manifests, i.e., some Pd migration to the nanoparticle surface occurred. This behaviour is expected from thermodynamics: Pd has lower heat of vaporization (380 kJ/mol) as compared to Ru (580 kJ/mol), thus, it tends to segregate to the surface to lower the surface free energy. **CO-DRIFTS** of the core−shell catalyst (Figure 5.4) confirms such structural evolution. Prior to CO-DRIFTS analysis, Ru−Pd catalysts were calcined at 200 ^{o}C in air and followed by in situ hydrogen reduction at 375 ^{o}C to simulate the pretreatment procedures before indan RO. The low wavenumber adsorption bands corresponding to bridged adsorbed CO mode on Ru (1946 cm^{-1}) and Pd (2026 and 1995 cm^{-1}) are significantly different for the core−shell structure: the bridged adsorption on Ru atoms is suppressed (low intensity of 1951 cm^{-1} peak) with no bridged adsorption on Pd atoms, but a high-intensity new peak at 1980 cm^{-1} can be most likely ascribed to the bridged adsorption of CO on adjacent Pd and Ru atoms, which is in line with our hypothesis of the core−shell structure evolution into a surface containing both elements.

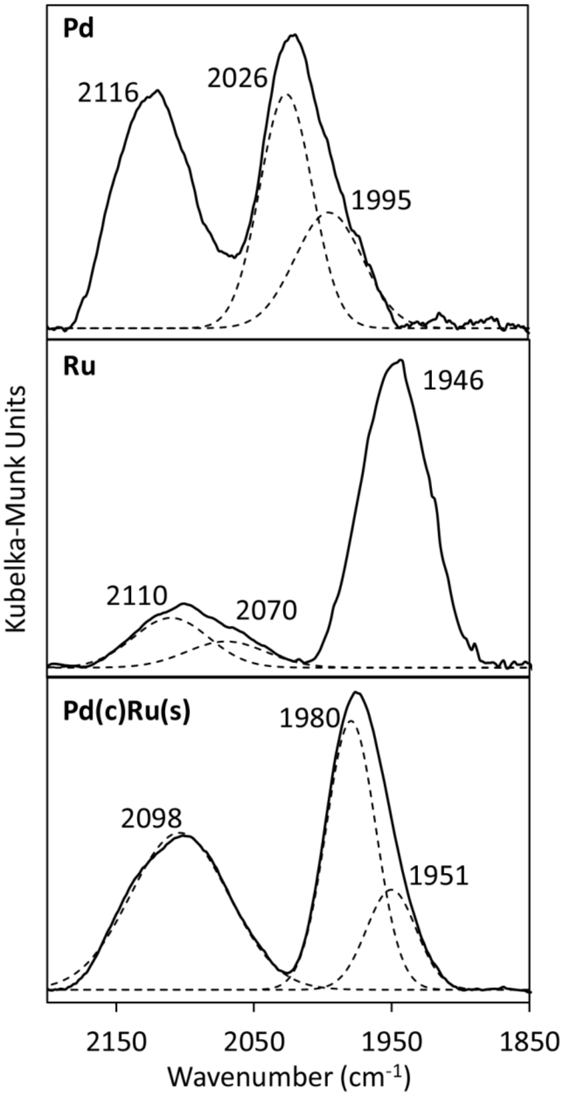

Figure 5.4. DRIFT spectra of CO adsorbed on Ru, Pd and Pd(c)Ru(s) catalysts after reductive atmosphere treatment. Catalysts were calcined at 200 °C and followed by reduction in hydrogen at 375 °C for polymer removal. Reprinted with permission from Ref [20]. Copyright © 2014 American Chemical Society.

To conclude, the catalytic results and CO-DRIFTS indicate structural rearrangement of parent Pd(c)Ru(s) structure via Pd segregation to the surface under indan hydrogenolysis conditions. However, there are still significant differences in behavior of the Ru2Pd1 and Ru(c)Pd(s) sample in the reaction regardless of their identical Pd-to-Ru molar ratio. The occurred structural rearrangements thus did not result in the very same structure; the use of initially applied different synthetic procedures (Scheme 5.1) is paramount for this particular application: to achieve high single cleavage selectivity to 2-ethyltoluene (Figure 5.3), shell enrichment with Ru is undesirable and the alloy structure preparation is preferred.

5.3.3. Catalysis in an oxidative atmosphere: combustion at 550 °C

Prior to the methane combustion reactions, all catalysts were calcined at 550 ^{o}C for 16 h, which is an accepted de-greening procedure for automotive catalysts [25]. Since methane combustion was carried out in oxygen-rich environment, the calcined Ru−Pd catalysts were packed in the reactor without further reduction by hydrogen. Methane oxidation follows Mars-van Krevelen redox mechanism on site pairs consisting of adjacent Pd and PdO species [34, 35]. Metallic Pd dissociatively adsorbs CH_4 producing H and CH_x species; while PdO is responsible for oxidation [34, 36]. Thus, according to the redox mechanism, the surface state of catalysts should be partially oxidized during methane oxidation. This is confirmed by XPS analysis over a spent Pd catalyst as shown in Figure 5.5: the Pd $3d_{5/2}$ peaks could be assigned to PdO (336.5 eV), PdO_x (337.3 eV) and Pd (335.4 eV), indicating the coexistence of metallic Pd and Pd oxides.

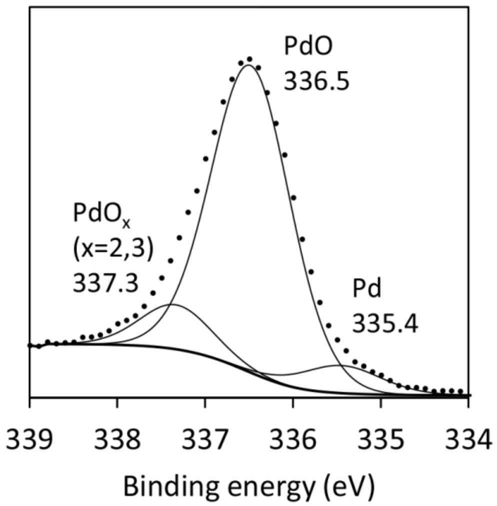

Figure 5.5. Pd *$3d_{5/2}$* XPS of the spent monometallic Pd catalyst (after the reaction from Figure 5.6).

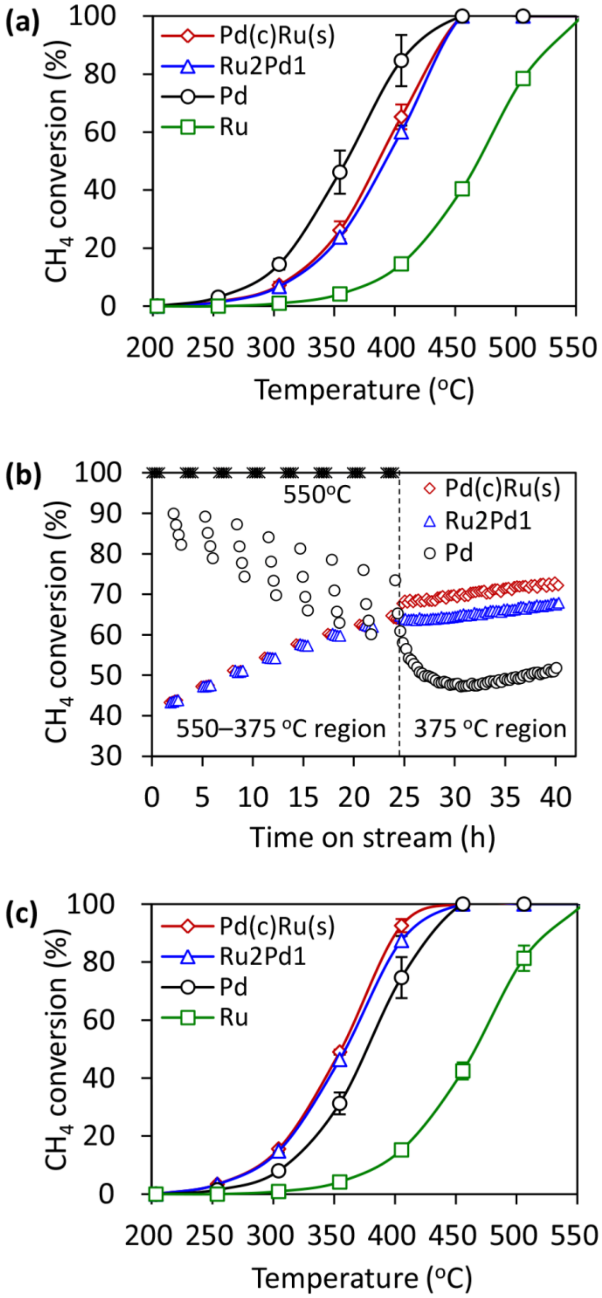

Figure 5.6. Methane combustion over mono- and bimetallic Ru−Pd catalysts, 4100 ppm methane, 1.1 barg pressure, 1.2 mg Pd and/or 3.1±0.4 mg Ru: (a) thermal aging at 375–550 °C (Ru is not shown because of < 10% conversion at 375 °C); (b) ignition-extinction curves after 40 hours thermal aging. Error bars represent one standard deviation from average for ignition-extinction curves (no significant hysteresis was observed). Catalysts were calcined at 550 °C for 16 h under static air.

Figure 5.6 compares the activities of monometallic and bimetallic catalysts in methane combustion during initial ignition-extinction, low-high temperature cycling (375 and 550 °C), followed by ignition-extinction curve measurements as described in the experimental section. The monometallic Pd catalyst is the most active methane oxidation catalyst [34, 37]. The monometallic Ru displays the lowest activity, with less than 10% conversion at 375 °C; initial activity of the bimetallic catalysts in the first ignition-extinction cycle is lower than for the pure Pd (Figure 5.6(a)), but it improves under the reaction conditions and surpasses the Pd activity after 25 hours on stream (Figures 5.6(b) and 5.6(c)). Indeed, as seen for the cycling experiments (Figure 5.6(b)), 550 °C temperature conditioning leads to progressive deactivation of Pd, while the bimetallic catalysts do not deactivate with cycling and even increase their activity. However, as opposed to the previous case with a reductive atmosphere, both Pd(c)Ru(s) and Ru2Pd1 catalysts display exactly the same behavior for methane combustion during and after structural evolution.

As seen from the TEM images (Figure 5.7) of the fresh, calcined (550° C for 16 h), and spent monometallic Pd (after all the cycling experiments) and Ru2Pd1 catalysts (after all the cycling experiments as in Figure 5.6), mono-Pd sintered to a large extent after exposure to 550 °C, which is one of the known reasons for Pd catalyst deactivation during methane combustion [34]. The bimetallic catalyst possesses improved thermal stability, with no visible agglomerates above 30 nm. The **CO chemisorption** showed the CO/metal(s) molar ratios of 0.19, 0.15 and 0.33 for Pd, Ru and Ru2Pd1 catalysts, respectively. Monometallic and bimetallic Ru−Pd samples for CO chemisorption experiments were also calcined at 550 °C for 16 h to simulate the pretreatment procedure before methane combustion; this is then followed by in situ hydrogen reduction at 550 °C for 1 h, as CO adsorption requires metallic surfaces of Pd and Ru. The higher thermal stability and surface area of the bimetallic catalyst may partly explain the higher observed methane combustion activity versus the monometallic Pd.

One of other feasible hypotheses of the bimetallic catalysts activity improvement over the course of the reaction (Figure 5.6) could be volatilization of inactive Ru as oxides, leading to the progressive increase in the Pd atom exposure. To check the hypothesis's validity, the Ru and Ru2Pd1 samples were analyzed by **NAA** after two different calcination treatments: i) 550 °C, 16 h, and ii) 550 °C, 16 h followed by 600 °C, 72 h. Monometallic Ru content dropped from 0.28±0.02 wt.% to 0.22±0.01 wt.% after the 600 °C treatment, confirming the oxide volatility.

However, when Ru was alloyed with Pd in the Ru2Pd1 sample, the loading remained constant as 0.17±0.01 wt.%. This result is in line with the improved thermal stability of the alloyed Ru−Pd catalysts (Figure 5.7), and leads to a rejection of the hypothesis of increasing Pd exposure due to Ru oxides volatilization. Monometallic Ru and bimetallic Ru2Pd1 catalysts treated at 600 ^{o}C were used only to the study the possible Ru oxides volatility, so they were not used in the catalytic tests.

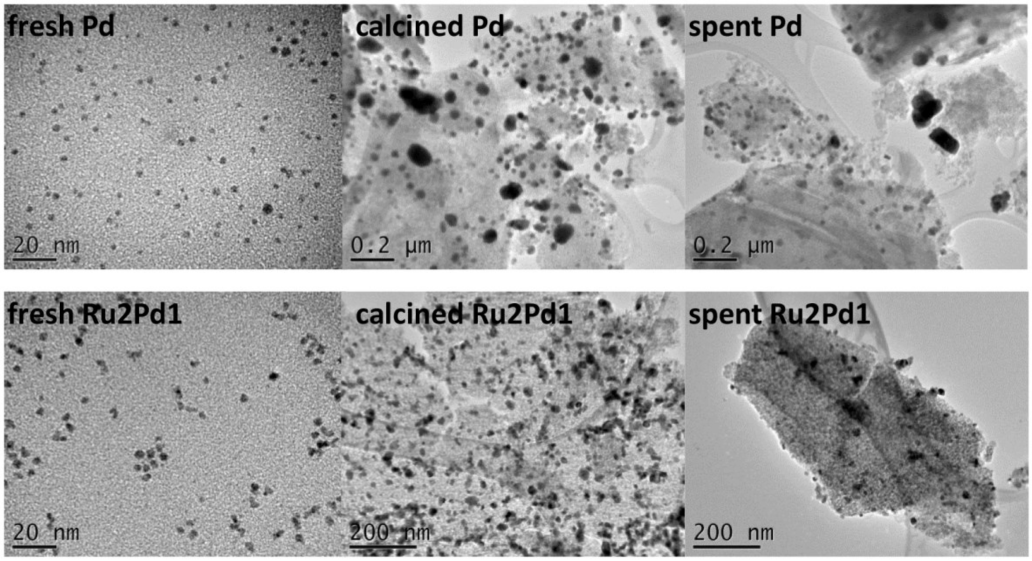

Figure 5.7. TEM images of as-synthesized nanoparticles, calcined catalysts (550 °C, 16 h) and spent catalysts (after the reactions from Figure 5.6).

Another reason for the bimetallic catalyst activity improvement could be in situ nanoparticle reconstruction and Pd atom diffusion to the surface driven by the minimization of surface free energy. Indeed, the heat of vaporization of Pd (380 kJ/mol) is lower than the one for Ru (580 kJ/mol), so the progressive nanoparticle shell enrichment with Pd is expected during high-temperature applications. Such a hypothesis may also explain the same observed activity of the Pd(c)Ru(s) and Ru2Pd1 bimetallic samples in the methane combustion: regardless of the initial particle structures, they both restructure to the most thermodynamically favourable material. The variation in bimetallic activities with prolonged time on stream could be related to the progressive change in surface oxygen composition as Pd diffuses to the bimetallic surface. Different metals may display different combustion activities not only because of their nature but also due to different metal-to-metal oxide ratios. For example, PdO forms in low temperature range (300−400 °C), being stable up to 800 °C, whereas, PtO_2 decomposes at a much lower temperature (400 °C) [37]. Since PtO_2 is highly unstable, significant amount of metallic Pt may still exist even after calcination at 500 °C in air [37], which explains the poor methane combustion activity of supported Pt catalyst under fuel-lean conditions comparing to Pd metal. According to the Mars-van Krevelen redox mechanism, an optimal surface oxidation state is required for methane activation. In the case of bimetallic Ru−Pd system, Ru binds oxygen too strongly (the heat of formation for RuO_2 is higher than PdO), which can lead to a lower surface density of oxygen vacancies for CH_4 dissociative adsorption. Eventually, the active Pd in bimetallic catalysts became more accessible being dispersed on Ru core, which explains the increasing activities in both bimetallic Ru−Pd catalysts. The Ru2Pd1 and Pd(c)Ru(s) catalysts should have similar surface oxygen compositions during methane combustion, because they both transformed into Ru(c)Pd(s) structure as was shown by EXAFS analysis in the following.

EXAFS of the high-temperature-treated Pd(c)Ru(s) and Ru2Pd1 samples was performed to verify their structures. The Ru−Pd catalysts for EXAFS study were treated using the same procedure as in catalyst test that is pre-calcination at 550 °C for 16 hours under air; this was followed by H_2 reduction at 400 °C, which is confirmed to be enough to reduce oxidized Ru−Pd nanoparticles to metallic forms by our previous TPR analysis [20]. Prior to EXAFS analysis, samples were stored under ambient conditions for a week and then reduced in hydrogen to avoid complications by the metal-oxygen contributions when estimating coordination numbers. The reductive pre-treatment did not lead to the changes in methane oxidation catalysis: both reduced and oxidized Ru2Pd1 samples showed identical light-off temperature (temperature for 50% methane conversion) of 385±10 °C.

Figures 5.8 (a) and (b) show the Pd K-edge and Ru K-edge EXAFS spectra in K-space for mono-Ru and Pd and bimetallic nanoparticles. The amplitudes of the signal for Pd(c)Ru(s) and Ru2Pd1 nanoparticles are significantly lower than those of mono-Pd nanoparticles (Figure 5.8(a)), indicating lower coordination numbers around Pd in the bimetallic particles [24]. The EXAFS oscillation patterns of bimetallic nanoparticles at the Ru K-edge are similar in amplitude but differ slightly in periodicity from the pure Ru sample (Figure 5.8(b)); this could be ascribed to alloying between Pd and Ru in the bimetallic structure. Similar changes in the EXAFS oscillation patterns as a result of the formation of Au−Pd bonds have been reported by Liu et. al.

[38]. The negligible change in amplitude of the Ru edge in the bimetallic samples, combined with the decreasing amplitude on the Pd edge, is strong evidence of Ru(c)Pd(s) formation after calcination/reduction; i.e. an inversion of the original structure in the case of Pd(c)Ru(s) particles.

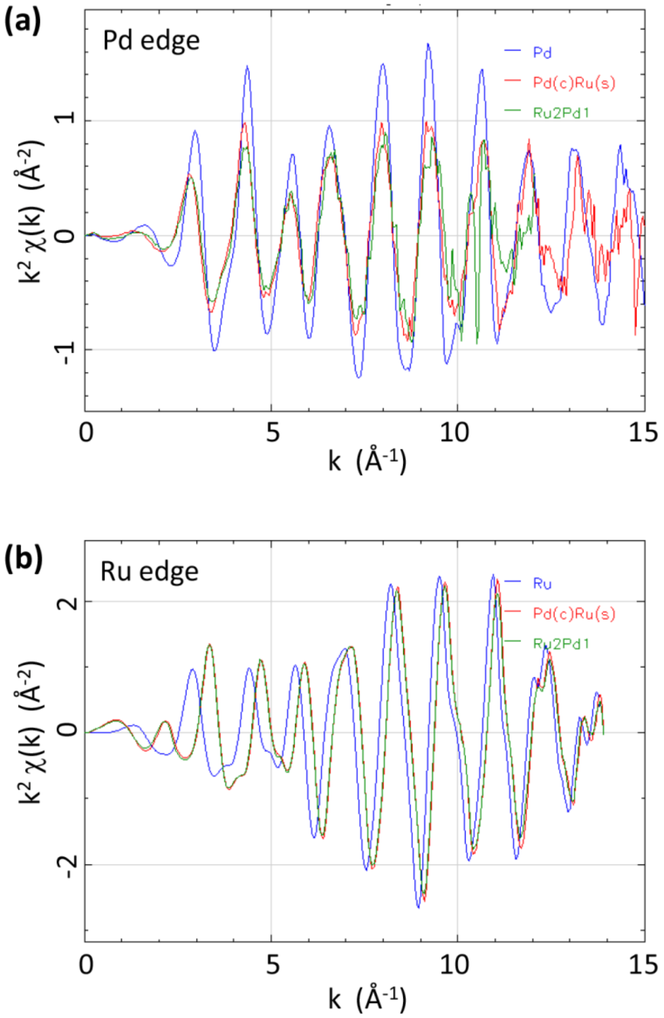

Figure 5.8. EXAFS spectra in K-space for monometallic Ru and Pd and bimetallic Pd(c)Ru(s) and Ru2Pd1 nanoparticles in Pd K-edge (a) and Ru K-edge (b). Catalysts were calcined at 550 °C for 16 h and followed by reduction in hydrogen at 400 °C.

Figure 5.9 shows high quality EXAFS R-space data with single-shell theoretical fits for monometallic Ru and Pd and bimetallic Pd(c)Ru(s) and Ru2Pd1 nanoparticles. The Pd and Ru experimental EXAFS data of the bimetallic samples were fit by the theoretical phase-shift and amplitudes generated by FEFF [23, 24]. The structural parameters of the mono-and bimetallic

Ru−Pd nanoparticles generated using IFEFFIT software package are shown in Table 5.1. The shoulders observed on the Pd edge at low R values are most likely due to the presence of small amounts of surface Pd oxidation [24]. The EXAFS analyses were performed on the samples exposed to air (at room temperature) for about 1 week; Pd surface oxidation was possible; this was also observed by XPS in our previous work [28]. The most useful information on the local structure obtained from EXAFS fits is coordination number, presented in Table 5.1. The coordination numbers for the bulk fcc and hcp structures are 12. As compared to the reference foils, monometallic Pd and Ru nanoparticles have lower coordination numbers of 9.7±0.7 (N_{Pd-Pd}) and 10.6±1.6 (N_{Ru-Ru}), respectively. These are indications of the existence of large portions of atoms on the surface of the nanoparticles [38]. The higher coordination number seen for Ru after the high temperature treatment agrees with CO chemisorption/TEM evidence that Ru tends to sinter to a greater degree than Pd.

For the bimetallic nanoparticles, N_{Pd-M} and N_{Ru-M} correspond to the total coordination numbers around Pd and Ru, respectively, where M refers both to Ru and Pd. The Pd−Pd and Pd−Ru contributions cannot be well differentiated because of their similar atomic numbers. For core−shell structures, the total coordination number for the core metal should be high, normally close to 12, whereas the total coordination number for the shell metal would be much smaller [38]. For our catalysts, after calcination in air at 550 ^{o}C for 16 hours, and subsequent reduction, the N_{Pd-M} for Pd(c)Ru(s) and Ru2Pd1 samples were found to be 7.5±0.7 and 8.0±1.0, respectively, while the total coordination numbers around Ru atoms, N_{Ru-M}, were higher (11.3±1.4 for Pd(c)Ru(s) and 11.5±1.3 for Ru2Pd1). This shows that both structures transformed into a final Ru(c)Pd(s) structure. Only small amounts of Pd oxidation are seen in these samples, and no Ru oxidation, which is further evidence of the migration of Pd atoms to nanoparticle shells. Note that the monometallic catalyst coordination numbers differ significantly from those of the bimetallic samples. TEM evidence shows much more moderate sintering in bimetallic nanoparticles compared to their mono- Pd or Ru counterparts; which confirms that the bimetallic nanoparticles do not segregate into much larger Ru and small Pd monometallic particles. The structural inversion of the parent Pd(c)Ru(s) particle occurred most likely due to the thermodynamics-induced Pd segregation to the surface because of its lower heat of vaporization. The fact that the shell becomes enriched with Pd is in line with the catalytic results: the bimetallic catalysts display dramatically enhanced activity over time as compared to monometallic Pd (Figure 5.6), which is consistent with Pd diffusion to the surface over time.

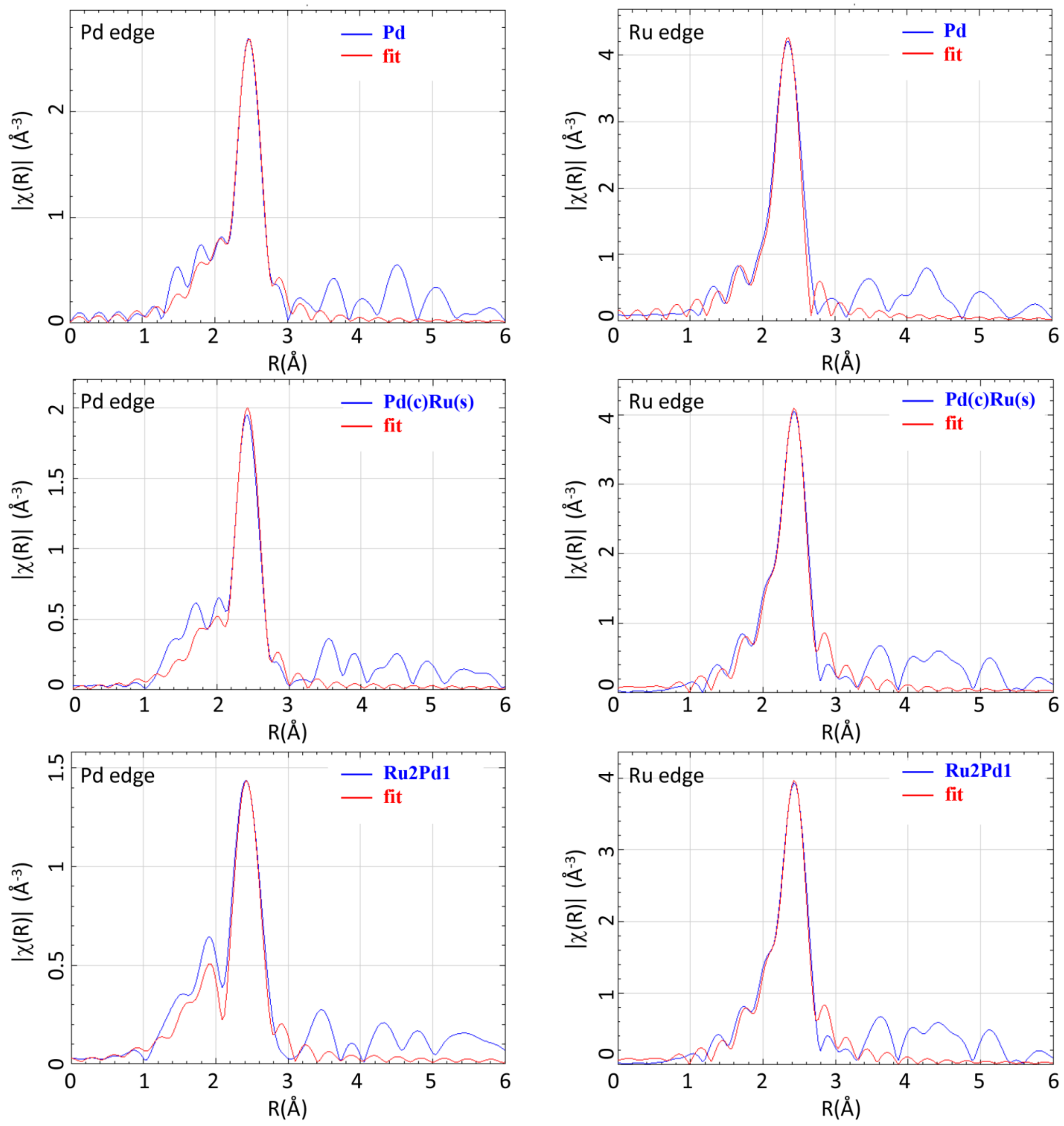

Figure 5.9. EXAFS single-shell fits in R-space for monometallic Pd and Ru and bimetallic Pd(c)Ru(s) and Ru2Pd1 nanoparticles. Catalysts were calcined at 550 °C for 16 h and followed by reduction in hydrogen at 400 °C.

Table 5.1. EXAFS fitting parameters.

Catalyst	Shell	N	R_j (Å)	ΔE^0 (eV)	$\sigma^2 \cdot 10^3$ ($Å^2$)	R-factor
Pd foil	Pd−Pd	12	2.741 (0.002)	2.3 (0.5)	5.7 (0.4)	0.005
Ru foil	Ru−Ru	12	2.671 (0.002)	2.9 (1.2)	4.2 (0.9)	0.016
Pd	Pd−Pd	9.7 (0.7)	2.735 (0.001)	-5.0 (0.5)	6.1 (0.4)	0.009
Ru	Ru−Ru	10.6 (1.6)	2.670 (0.006)	-7.5 (1.2)	4.0 (0.8)	0.023
Pd(c)Ru(s)	Pd−M	7.5 (0.7)	2.713 (0.002)	-9.1 (0.7)	6.5 (0.7)	0.017
	Ru−M	11.3 (1.4)	2.672 (0.002)	3.7 (1.0)	4.6 (0.7)	0.016
Ru2Pd1	Pd−M	8.0 (1.0)	2.699 (0.004)	-9.2 (1.0)	9.0 (1.0)	0.046
	Ru−M	11.5 (1.3)	2.673 (0.002)	3.4 (0.9)	4.9 (0.6)	0.015

Thus, both samples' methane combustion catalytic results (Figure 5.6) and EXAFS evidence show that irrespective of the preparation method (Scheme 5.1) and differences in parent bimetallic nanostructures (but recall their constant bulk metal ratio), both Pd−Ru systems transform into one structure with Pd-enriched shells. The structural evolution was the most pronounced in the high-temperature oxidative application versus the above-discussed indan hydrogenolysis at 350 °C.

5.4. Conclusions

Ru−Pd bimetallic nanoparticles with the same bulk metal ratio were synthesized using two different colloidal chemistry techniques. One resulted in particles with mixed surface (alloy), and another with Ru-shell particles. Several catalytic applications were considered:

- A low-temperature liquid-phase hydrogenation of an allylic alcohol showed that the presumably core−shell structure indeed displays the properties of only the shell metal while the alloy sample displayed intermediate properties between the monometallic counterparts.
- In a high-temperature gas-phase hydrogenolysis, the core−shell sample underwent some structural evolution with Pd segregation to the surface, as seen from the catalytic behavior and CO-DRIFTS; however, the two samples still exhibited distinctively different behaviors;
- A high-temperature combustion reaction revealed identical catalytic properties of both samples, and EXAFS confirmed that both parent nanoparticle types evolved into one structure with Pd-enriched shells.

The results show that the structure control in bimetallic nanoparticle preparation is crucial for some applications while others do not benefit because of thermodynamically and probably adsorbent-induced structural evolution into one type of structure. The results for methane oxidation showed that nanoparticle structural evolution is kinetically limited even at 550 °C and thus bimetallic catalysts to be evaluated under prolonged times on stream.

Acknowledgements

Financial support from NSERC-Strategic program grant STPGP 430108-12 is acknowledged. We thank Becquerel Laboratory of Maxxam Analytics (Ontario, Canada) for NAA analysis, Dr. Xuehai Tan (University of Alberta) for his help with high resolution TEM and SAED analyses, and Shiraz Merali (University of Alberta) for performing XRD analyses. EXAFS work *described in this paper was performed at the Canadian Light Source, which is supported by the Canadian Foundation for Innovation, Natural Sciences and Engineering Research Council of Canada, the University of Saskatchewan, the Government of Saskatchewan, Western Economic Diversification Canada, the National Research Council Canada, and the Canadian Institutes of Health Research.*

5.5. References

[1] B. Coq, F. Figueras, J. Mol. Catal. A. 173 (2001) 117-134.
[2] M. Sankar, N. Dimitratos, P.J. Miedziak, P.P. Wells, C.J. Kiely, G.J. Hutchings, Chem. Soc. Rev. 41 (2012) 8099-8139.
[3] O.G. Ellert, M.V. Tsodikov, S.A. Nikolaev, V.M. Novotortsev, Russ. Chem. Rev. 83 (2014) 718-732.
[4] A.K. Singh, Q. Xu, ChemCatChem. 5 (2013) 652-676.
[5] D.M. Alonso, S.G. Wettstein, J.A. Dumesic, Chem. Soc. Rev. 41 (2012) 8075-8098.
[6] C. Cui, L. Gan, M. Heggen, S. Rudi, P. Strasser, Nat. Mater. 12 (2013) 765-771.
[7] K.J.J. Mayrhofer, V. Juhart, K. Hartl, M. Hanzlik, M. Arenz, Angew. Chem. Int. Ed. 48 (2009) 3529-3531.
[8] B. Zhu, G. Thrimurthulu, L. Delannoy, C. Louis, C. Mottet, J. Creuze, B. Legrand, H. Guesmi, J. Catal. 308 (2013) 272-281.

[9] H.B. Liu, U. Pal, J.A. Ascencio, J. Phys. Chem. C. 112 (2008) 19173-19177.

[10] R. Huang, Y.H. Wen, Z.Z. Zhu, S.G. Sun, J. Phys. Chem. C. 116 (2012) 8664-8671.

[11] D.N. Tafen, J.B. Miller, Ö.N. Doğan, J.P. Baltrus, P. Kondratyuk, Surf. Sci. 608 (2013) 61-66.

[12] J. Gu, Y.W. Zhang, F. Tao, Chem. Soc. Rev. 41 (2012) 8050-8065.

[13] N. Toshima, H. Yan, Y. Shiraishi, in: B. Corain, G. Schmid, N. Toshima (Ed.), **Metal Nanoclusters in Catalysis and Materials Science: The Issue of Size Control**, Elsevier B.V., Amesterdam, 2008, pp. 49-75.

[14] A.U. Nilekar, S. Alayoglu, B. Eichhorn, M. Mavrikakis, J. Am. Chem. Soc. 132 (2010) 7418-7428.

[15] L. D'Souza, S. Sampath, Langmuir. 16 (2000) 8510-8517.

[16] R.M. Anderson, L. Zhang, J.A. Loussaert, A.I. Frenkel, G. Henkelman, R.M. Crooks, ACS Nano. 7 (2013) 9345-9353.

[17] A.I. Frenkel, Chem. Soc. Rev. 41 (2012) 8163-8178.

[18] S. Alayoglu, P. Zavalij, B. Eichhorn, Q. Wang, A.I. Frenkel, P. Chupas, ACS Nano. 3 (2009) 3127-3137.

[19] Y. Chen, K.Y. Liew, J. Li, Mater. Lett. 62 (2008) 1018-1021.

[20] J. Shen, N. Semagina, ACS Catal. 4 (2014) 268-279.

[21] T. Teranishi, M. Miyake, Chem. Mater. 10 (1998) 594-600.

[22] E.A. Stern, M. Newville, B. Ravel, Y. Yacoby, D. Haskel, Physica B. 208&209 (1995) 117-120.

[23] P. Dash, T. Bond, C. Fowler, W. Hou, N. Coombs, R.W.J. Scott, J. Phys. Chem. C. 113 (2009) 12719-12730.

[24] T. Balcha, J.R. Strobl, C. Fowler, P. Dash, R.W.J. Scott, ACS Catal. 1 (2011) 425-436.

[25] R. Abbasi, L. Wu, S.E. Wanke, R.E. Hayes, Chem. Eng. Res. Des. 90 (2012) 1930-1942.

[26] J. Shen, R.E. Hayes, X. Wu, N. Semagina, ACS Catal. 5 (2015) 2916-2920.

[27] M. Liu, J. Zhang, J. Liu, W.W. Yu, J. Catal. 278 (2011) 1-7.

[28] J. Shen, X. Yin, D. Karpuzov, N. Semagina, Catal. Sci. Technol. 3 (2013) 208-221.

[29] C. Pan, F. Dassenoy, M.J. Casanove, K. Philippot, C. Amiens, P. Lecante, A. Mosset, B. Chaudret, J. Phys. Chem. B. 103 (1999) 10098-10101.

[30] J.K. Norskov, T. Bligaard, J. Rossmeisl, C.H. Christensen, Nat. Chem. 1 (2009) 37-46.

[31] P. Rylander, Catalytic Hydrogenation Over Platinum Metals, Academic Press Inc., New York, 1967.

[32] M. Liu, W. Yu, H. Liu, J. Zheng, J. Colloid Interface Sci. 214 (1999) 231-237.

[33] U. Nylen, L. Sassu, S. Melis, S. Järås, M. Boutonnet, Appl. Catal. A. 299 (2006) 1-13.

[34] G. Centi, J. Mol. Catal. A. 173 (2001) 287-312.

[35] K. Fujimoto, F.H. Ribeiro, M. Avalos-Borja, E. Iglesia, J. Catal. 179 (1998) 431-442.

[36] J.N. Carstens, S.C. Su, A.T. Bell, J. Catal. 176 (1998) 136-142.

[37] P. Gelin, M. Primet, Appl. Catal. B. 39 (2002) 1-37.

[38] F. Liu, D. Wechsler, P. Zhang, Chem. Phys. Lett. 461 (2008) 254-259.

Chapter 6. Enhancement of direct desulfurization in the hydrodesulfurization of a refractory sulfur compound[5]

6.1. Introduction

Ultra-low sulfur diesel with a 15 ppm sulfur specification was phased since 2006, and became mandatory in 2010, according to United State Environmental Protection Agency (EPA) [1]. Environment Canada sets regulations for the maximum level of sulfur in gasoline (30 ppm) and diesel fuel (15 ppm) [2, 3], which are referred to now as low-sulfur and ultra-low sulfur fuels, respectively. Increasing stringent regulations on the quality of fuels in terms of sulfur content challenge refineries either to enhance the activity, selectivity and stability of existing catalysts, decrease the process severity, or find new catalyst combinations [4]. The enormous body of knowledge that has accumulated in the refineries for many decades can deal with targets of 200−500 ppm. Below this limit, there are mainly most stubborn (refractory) sulfur compounds left whose desulfurization rates are orders of magnitude lower than in the more abundant easily-removed S. It is estimated that either pressure or reactor volumes must be tripled for ultra-deep desulfurization [4]. No doubt, many studies have been focused recently on the reactor and/or catalyst technology improvements for ultra-low hydrodesulfurization (HDS), and industrial companies developed and implemented several successful Ni, Mo and/or Co-based catalysts [5]. All these technologies and catalysts, however, still require significant hydrogen pressures (30−100 atm) because they rely mostly on the hydrogenation pathway for S removal, with low contribution from the hydrogen-saving direct desulfurization path.

---

[5] Chapter 6 of the thesis was written as a paper manuscript as "Enhancement of direct desulfurization in the hydrodesulfurization of a refractory sulfur compound", **J. Shen** and N. Semagina; and it will be submitted for a publication in a due course. The high pressure reaction setup for hydrodesulfurization was built by Dr. Long Wu and Dr. Hessam Ziaei-Azad. The lab view program to communicate with reaction setup was written by Les Dean. Shiraz Merali performed XRD analysis at the department of Chemical and Material Engineering, University of Alberta. NAA analysis was performed by Becquerel Laboratories Inc., Maxxam Analytics, Ontario. The author performed all syntheses, reactions, analyses and other characterizations.

Diesel feed contains various types of sulfur containing compounds. These individual sulfur compounds can be summarized into two groups: alkyl-substituted benzothiophenes (BT) and alkyl-substituted dibenzothiophenes (DBT). Among them, DBT contains alkyl groups in the 4 and 6 positions (close to S atom) is the least reactive and the most refractory sulfur compound. During desulfurization, the access to the catalyst sites becomes sterically hindered, and the rate of reaction drops considerably [6]. Thus, to produce fuels with ultra-low sulfur content, it is necessary to remove the most refractory sulfur compounds; thus 4,6-dimethyl-dibenzothiophene (4,6-DMDBT) is commonly chosen as a model compound in the study of deep desulfurization. The reaction mechanism of the HDS of 4,6-DMDBT is now very well established in literatures [6-8]. The 4,6-DMDBT molecule can be desulfurized via one of the two parallel reaction pathways (Scheme 6.1): direct extraction of sulfur (direct desulfurization route, DDS), or hydrogenation of one of the aromatic rings followed by sulfur extraction (hydrogenation route, HYD) [6]. The DDS occurs through a perpendicular σ-adsorption of the reactants via the sulfur atoms; and the HYD proceeds through a flat-lying π-adsorption of the reactants through the aromatic rings [9]. According to the different adsorption configurations, the presence of alkyl groups strongly hinders the DDS rate; especially when these alkyl groups are adjacent to the sulfur atoms at 4 and 6 positions. On the other hand, HYD reaction path way is hardly affected by the alkyl groups in the 4 and 6 positions [6]. Hence, HYD route is generally considered dominant for the HDS of alkyl-substituted DBT molecules.

The distribution of the proposed reaction mechanisms for sulfur-removal from 4,6-DMDBT is strongly affected by thermodynamics. The pre-hydrogenation of one of the aromatic rings before sulfur-removal is a highly exothermic and reversible reaction, so the HYD route favors a decrease in reaction temperature and an increase in hydrogen partial pressure [6]. For example, in the HDS of 4,6-DMDBT, 90% of sulfur removal proceeded through HYD route at 300 °C; while at 380 °C the DDS rate is more dominant over conventional Mo-based catalysts [10]. Hence, HDS at high hydrogen partial pressures (4.5−6.5 MPa) is mostly considered as an important option for producing ULSD in refining industries [6]. Alumina-supported sulfided Mo promoted by Co or Ni is traditional hydrotreating catalyst in refining industries. Conventional Co−Mo and Ni−Mo catalysts play an important role in enhancing the sulfur removal and promoting hydrodesulfurization in hydrotreating processes; however, they are not sufficient to further desulfurize diesel feeds to ultra-low sulfur level to meet the new regulations on fuel quality. At severe operating conditions, such as high temperatures and high pressures, sulfided catalysts may show higher activity, but also rapid deactivation and shorter cycle length [6].

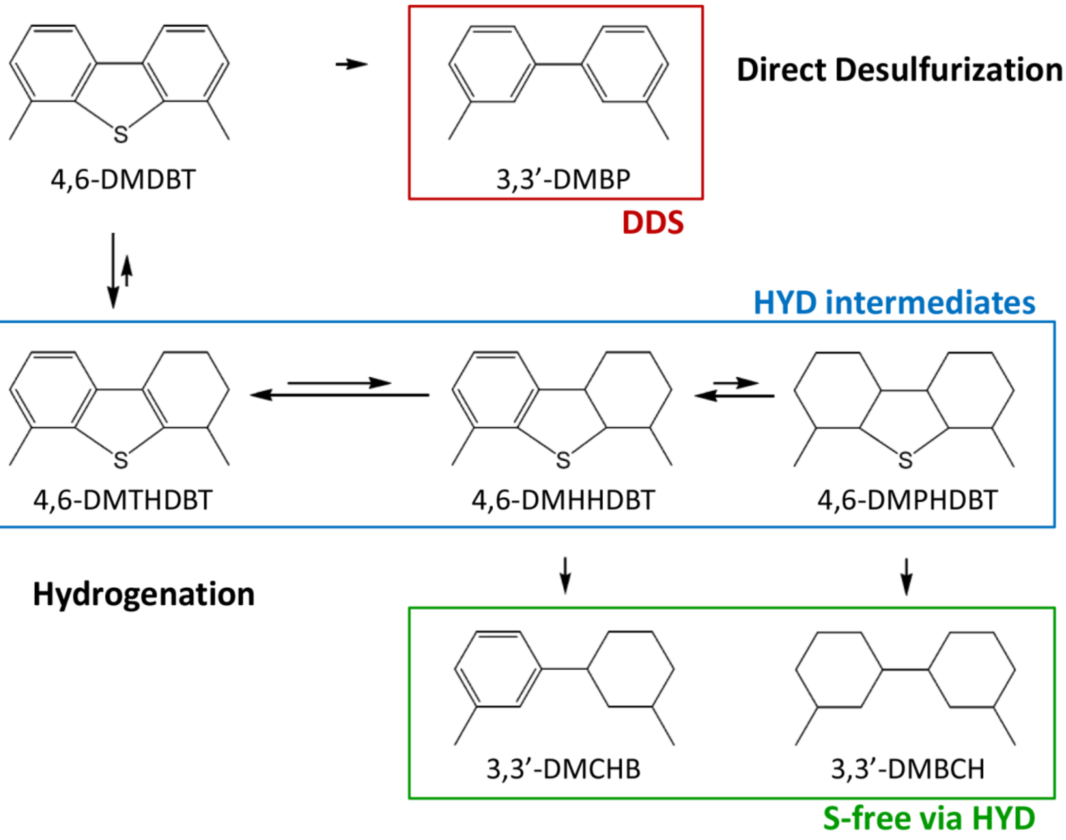

Scheme 6.1. Reaction pathways for HDS of 4,6-DMDBT at 300 °C and 5 MPa [6].

Over the past decades, attention has been drawn to noble metal catalysts for ultra-deep desulfurization [7-9, 11-13]. As discussed above, HDS of 4,6-DMDBT occurs predominately through hydrogenation pathway, and therefore rely on the hydrogenation properties of noble metals required for the flat-lying π-adsorption of benzene rings [8, 9] (although the goal of this study is to improve DDS selectivity). Among the noble metals, Pd- and Pt- containing catalysts have been well studied in HDS reactions using model compounds like DBT and 4,6-DMDBT [7-9], because of the great advantage of their hydrogenation capabilities. It has been concluded that the catalytic activity of noble metals decreases in the order of Pd ≈ Pt−Pd > Pt > Rh > Ru−Rh >> Ru for 4,6-DMDBT hydrodesulfurization [12]. Another important advantage of using Pd- (or Pt-) based catalysts is their better sulfur resistance comparing to other metals. In a study on the mechanism and site requirements of thiophene HDS, Wang et al. observed a higher turnover frequency over Pt nanoparticles than that on Ru, and related to the relatively weak sulfur binding on Pt surfaces (low S coverage/less S poisoning effect) [14, 15].

Many efforts has been made to improve the long term performances of the active Pd and Pt metals in the view points of enhanced sulfur removal rates and better sulfur resistance. One approach is to alloy the active metal with a second metal, and the finding has been applied successfully by Exxon since 1970 s when bimetallic Pt−Ir catalysts were introduced into the refining units [16]. The bimetallic Pt−Pd catalysts were much more active than the physical combination of their mono-forms, which was claimed as a synergetic effect between the alloyed metals [9]. Sulfur resistance of noble metal catalysts is related to the electron density of metal, and could be improved by alloying as well. The addition of Pd on Pt would decrease the electron density of Pt, and therefore weaken the S−Pt chemisorption bond [11]. As for another approach, the reactivity of the refractory sulfur molecules might be improved by introducing acidic supports in the catalytic system, such as amorphous Si−Al or zeolites [6]. Acidic function of the catalysts enables dealkylation and isomerization reactions of the alkyl substituents, and may transform refractory sulfur molecules to more reactive species [8]. In the study of 4,6-DMDBT hydrodesulfurization, Guo et al. demonstrated the catalytic performances of Pt supported on HZSM-5 (high acidity) and SBA-15 (low acidity) and compared with a Pt/γ-Al_2O_3 catalyst. However, catalysts showed either lower activity (Pt/SBA-15) than Pt/γ-Al_2O_3, or sever hydrocracking and coking (Pt/HZSM-5) [8].

Nevertheless, previous studies often dealt with the reaction networks of the HDS of refractory sulfur molecules over noble metals, thermodynamic limitations, and general improvement in sulfur removal rates, or report on the DDS-to-HYD ratios observed over different metals or at different experimental conditions. A common agreement in literatures is that the sulfur removal of 4,6-DMDBT over Pd-based catalysts can hardly occur via DDS pathway, owning to the fact of the alkyl group-induced steric hindrances and plus the great hydrogenation properties of Pd over conventional Mo-based catalysts. Hence, there is very few groups attempted to enhance the DDS selectivity/rate for the HDS of sterically hindered DBT molecules in open literatures [17, 18]. One of the recent studies reported an unprecedented selectivity to the DDS pathway over a FeNi phosphide catalyst, which requires less consumption of expensive hydrogen. The author stated that low coordination sites are particularly active for direct sulfur extraction, which was confirmed by EXAFS analysis [17]. The problem is the low activity of Fe−Ni−P phase, so the reactor volumes must be increased several times to achieve comparable conversions with the existing Ni−Mo catalyst.

Therefore we demonstrated the DDS enhancement over Pd-based catalysts, by maintaining their high dispersions during HDS reactions. The idea is originated from the importance of nanoparticle size control. Metal nanoparticles in the range of 1−10 nm are believed to work as effective catalysts due to their uniform size and shape distribution in nanometers, as well as their large surface-to-volume ratios [19]. Nanoparticles with different sizes have different surface atom distributions. If catalytic activity or selectivity is enhanced over some specific atoms (for example defect or face atoms), then a monodispersed catalyst will lead to the overall improved catalytic performances. For example, thiophene conversion through DDS pathway induced by the perpendicular α-adsorption mode is greater on smaller Pt clusters than that over larger ones [14]; similar trend was also observed with Ru dispersion changes [15]. The reason is in the surface configurations: the proportion of atoms on edges and corners increases with the particle dispersions increase. The concept of nanoparticle size control using advanced nanotechnologies is far from conventional impregnation method that reported in most of literatures; the later method resulted in wide polydispersed catalysts.

The advanced nanotechnologies for nanoparticle size control are well developed, which involve the use of various stabilizing agents (such as dendrimers [20, 21] and capping agents [22, 23]), allowing the synthesis of highly monodispersed nanoparticles as small as ~ 1 nm [24]. However, nanoparticles tend to sinter to lower their surface free energies during many catalytic reactions even at moderate temperatures. A feasible way to improve the thermal stability of Pd toward nanoparticle sintering is to add a second component, creating a bimetallic catalyst. According to our previous work, the monodispersity of bimetallic Pd−Ru nanoparticles was maintained after the high-temperature treatment upto 400 °C [25], thus showed superior catalytic performance in a low-pressure indan ring opening reaction. This was claimed as the textural synergetic effect when alloying Pd with Ru, as both monometallic Pd and Ru cannot tolerate thermal treatment [25]. Our group also observed similar trend in the viewpoint of the thermal stability improvement when Ir was added to Pd or Ni [26, 27]. Another effective method to improve the thermal stability of noble metal nanoparticles is the application of binary supports, such as $MgAl_2O_4$ spinel material. The relatively strong interaction between supported nanoparticles and spinels is responsible for the enhanced thermal stability of catalysts [28]. It has been shown that well-defined $MgAl_2O_4$ spinel support is capable of stabilizing Pt clusters in the range of 1−3 nm after extremely high temperature treatment at 800 °C. Like alumina, $MgAl_2O_4$ spinel material is characterized as low acidity [29] and has been long known for their ability to enhance catalyst performances by chemical modifications of the supported metallic nanoparticles.

Therefore, the combination of nanotechnologies and support material selection allowed us to thermally stabilize Pd-based catalysts and maintain their high nanoparticle dispersions during catalytic reactions. As will be discussed below, the developed bimetallic Pd6Ru1/γ-Al_2O_3 and Pd1.5/$MgAl_2O_4$ catalysts yielded a significantly improved selectivity toward DDS route in addition to the great hydrogenation ability of Pd, in the HDS of 4,6-DMDBT, reaching the level of Ir addition (known as the best hydrogenolysis catalyst for C−S cleavage). The beneficial effect is lower hydrogen consumption. According to the reaction Scheme 6.1, the direct desulfurization route consumes only one mole of hydrogen versus 7 moles in the hydrogenation route.

6.2. Experimental section

6.2.1. Materials

Palladium(II) chloride solution ($PdCl_2$, 5% w/v, Acros), sodium tetrachloropalladate(II) (Na_2PdCl_4, 98%, Sigma-Aldrich), Ruthenium(III) nitrosylnitrate ($Ru(NO)(NO_3)_3$, Ru 31.3% min, Alfa Aesar), hydrogen hexachloroiridate(IV) (H_2IrCl_6, 99.98%, Sigma-Aldrich), poly(vinylpyrrolidone) (PVP) (MW 40,000, Sigma-Aldrich), generation 4 poly(amidoamine)-hydroxyl dendrimer (G4OH, 10 wt.% in methanol, Dendritech Inc), potassium bromide (KBr, > 99%, Sigma-Aldrich), ethyl alcohol (denatured, Sigma-Aldrich), reagent alcohol (ethanol, 95 vol.%, Fisher Scientific), ethylene glycol (EG, 99.8%, Sigma-Aldrich), ascorbic acid (≥ 99%, Sigma-Aldrich), sodium borohydride ($NaBH_4$, > 99%, Sigma-Aldrich), gamma aluminum oxide (γ-Al_2O_3, 150 mesh, 58 Å pore size, Sigma-Aldrich), aluminum isopropoxide ($Al(OCH(CH_3)_2)_3$, ≥ 98%, Sigma-Aldrich), magnesium nitrate hexahydrate ($Mg(NO_3)_2 \cdot 6H_2O$, ≥ 98%, Sigma-Aldrich), acetone (99.7%, Fisher Scientific), 4,6-dimethyl-dibenzothiophene (4,6-DMDBT, 97%, Sigma-Aldrich), decane (≥ 99%, Sigma-Aldrich) and dodecane (≥ 99%, Sigma-Aldrich) were used as received. Milli-Q water was used throughout the work.

6.2.2. Catalyst preparation

A summary of the prepared catalysts is presented in Table 6.1. The PVP-stabilized bimetallic **Pd−Ru** nanoparticles with mean diameters of 2−3 nm were synthesized using a modified synthetic procedure for the preparation of Ru−Pt nanoparticles [30], as described in our previous work [25]. In this study, catalysts with high Pd-to-Ru ratios were prepared, because of the high activity of Pd. A series of Pd−Ru nanoparticles with varying Pd-to-Ru weight ratios (Pd6Ru1, Pd5Ru1, Pd3Ru1, Pd2Ru1 and Pd1Ru1) were synthesized in ethanol/water system in the presence of PVP. For a typical synthesis reaction, a mixture, in a 500 mL 3-neck round-bottom flask, containing 0.2 mmol of Pd and Ru precursors, 170 mL ethanol/water solution (41 vol.% ethanol) and 0.4 mmol PVP (PVP-to-metals molar ratio = 20/1) was stirred and refluxed for 3 h under air. PVP-stabilized **Ru** nanoparticles were prepared by ethylene glycol reduction method [25, 31]. In a 500 mL 3-neck round-bottom flask, 0.2 mmol Ru precursor and 4 mmol of PVP (PVP-to-Ru molar ratio = 20/1) were well dissolved in 200 mL ethylene glycol at room temperature. Then the PVP-Ru^{3+}-EG solution was stirred and refluxed under air for 3 h for complete reduction. Transparent dark-brown colloidal solutions of monometallic Ru and bimetallic Pd−Ru nanoparticles were obtained without any precipitate.

Ultra-small Pd nanoparticles with < 2 nm mean diameter were prepared using a dendrimer-templating strategy, originally developed by Crooks and his coworkers [24], with some modifications. The synthetic procedure for the G4OH-stabilized Pd nanoparticles (**Pd1.5**) was described as following. A 10 mL of 0.25 mM G4OH solution was prepared by diluting 0.357 g of 10 wt.% G4OH methanol solution (0.0025 mmol) by water. A 100 mL of 1 mM $PdCl_2$ methanol solution was prepared by adding 0.356 mL of $PdCl_2$ 5% w/v solution (0.1 mmol) in methanol in a 250 mL round-bottom flask. Then the G4OH solution was added into the reaction flask containing the $PdCl_2$ methanol solution (molar ratio of G4OH-to-Pd = 1/40). The complexing process between Pd^{2+} and the internal amine groups of dendrimer is shown in Figure 6.1 [24]. After 1 hour of complexation, 2 mL of 1 M $NaBH_4$ solution (2 mmol; $NaBH_4$-to-Pd molar ratio = 20/1; prepared and kept at 0 °C) was added to the reaction mixture drop by drop under vigorous stirring. The color of Pd^{2+}-G4OH solution changed from pale yellow to dark brown indicating the reduction of Pd ions to metallic Pd. The reaction continued for 1 h for complete reduction. To study the intrinsic effect of second metal addition on DDS selectivity in the HDS of 4,6-DMDBT, G4OH-stabilized Pd2Ir1 nanoparticles were prepared by a simultaneous reduction of Pd and Ir precursors, according to the synthetic procedures for Pd1.5 nanoparticles, as described above. In the reaction solution, the total amount of $PdCl_2$ and H_2IrCl_6 salts was 0.1 mmol (0.075 mmol $PdCl_2$ and 0.025 mmol H_2IrCl_6), with a G4OH-to-(Pd+Ir) molar ratio of 1/40.

Table 6.1. Summary of the synthesized nanoparticles and supported catalysts.

catalyst	metal precursor(s)	Capping agent	Reducing agent[a]	Catalyst support	Pd loading[b], wt.%	Ru (or Ir) loading[b], wt.%	Pd/Ru (or Ir) weight ratio[c]
Ru	$Ru(NO)(NO_3)_3$	PVP	EG	γ-Al_2O_3	-	0.22	0/1
Pd1Ru1	$PdCl_2$/ $Ru(NO)(NO_3)_3$	PVP	EtOH/H_2O	γ-Al_2O_3	0.096	0.111	0.9/1
Pd2Ru1		PVP	EtOH/H_2O	γ-Al_2O_3	0.143	0.082	1.7/1
Pd3Ru1		PVP	EtOH/H_2O	γ-Al_2O_3	0.177	0.055	3.2/1
Pd5Ru1		PVP	EtOH/H_2O	γ-Al_2O_3	0.164	0.031	5.3/1
Pd6Ru1		PVP	EtOH/H_2O	γ-Al_2O_3	0.180	0.029	6.2/1
Pd1.5	$PdCl_2$	G4OH	$NaBH_4$	$MgAl_2O_4$	0.200	-	-
Pd2.8	$PdCl_2$	PVP	EtOH/H_2O	γ-Al_2O_3	0.240	-	-
Pd7.0	$PdCl_2$	PVP	EG	γ-Al_2O_3	0.240	-	-
Pd16	Na_2PdCl_4	PVP/KBr	Ascorbic acid	γ-Al_2O_3	0.210	-	-
Pd2Ir1	$PdCl_2$ /H_2IrCl_6	G4OH	$NaBH_4$	$MgAl_2O_4$	0.165	0.075	2.2/1

[a] EtOH, ethanol; EG, ethylene glycol. [b] metal loadings determined by NAA. [c] exact weight ratios of Pd-to-Ru calculated from NAA results.

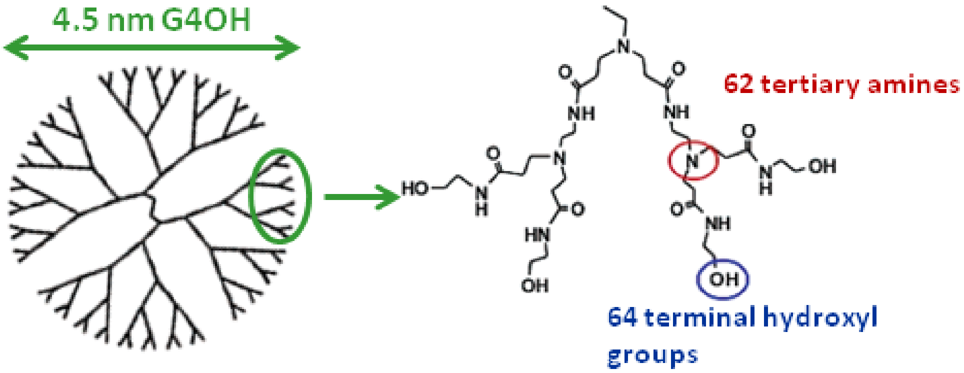

Figure 6.1. A structure of a fourth generation hydroxyl terminated dendrimer (G4OH) [24]. Reprinted with Permission from Ref [24]. Copyright © 2005 American Chemical Society.

The PVP-stabilized Pd nanoparticles with mean diameter of 2.8 nm (**Pd2.8**) was prepared using Teranish and Miyake's one-step alcohol reduction method [23], with minor modifications [25]. The experimental conditions were the same as the synthesis for PVP-stabilized Pd−Ru nanoparticles in ethanol/water system as described above, except 0.2 mmol of $PdCl_2$ in the reaction solution.

The PVP-stabilized Pd nanoparticles with mean diameters of 7.0 nm (**Pd7.0**) were prepared by ethylene glycol reduction method [25]. The synthetic procedures were the same as for the synthesis of monometallic Ru nanoparticles, as described above, except 0.2 mmol of $PdCl_2$ in the reaction solution.

The PVP-stabilized Pd nanocubes with average edge length of 16 nm (**Pd16**) were prepared using slow reduction by ascorbic acid in the presence of PVP and KBr, following the synthetic procedure described by Xia and coworkers [32] with some modifications. In a 50 mL round-bottom flask, 1 mmol PVP, 5.2 mmol KBr and 0.2 mmol of ascorbic acid were dissolved in 20 mL water at 80 °C (solution temperature). Then, 5 mL aqueous solution containing 0.2 mmol $NaPdCl_4$ was added to the reaction solution while stirring. The molar ratios of PVP, KBr and ascorbic acid to Pd are 5/1, 2/1 and 26/1, respectively. The color of the reaction solution changed from yellow to dark brown, indicating the reduction of Pd^{2+} to metallic Pd. The reaction was continued for 3 h at 80 °C for complete reduction. Transparent dark-brown colloidal dispersions of monometallic Pd nanoparticles were obtained without any precipitate.

The **$MgAl_2O_4$ spinel support** was prepared following the synthetic procedures proposed by Li et al. [28]. In a 1,000 mL Pyrex bottle (autoclavable), 0.1 mol $Al(OCH(CH_3)_2)_3$ and 0.05 mol $Mg(NO_3)_2 \cdot 6H_2O$ were well dissolved in 300 mL denatured ethanol under stirring until complete dissolution (at least 1 h). The reaction bottle was sealed and the reaction mixture was heated to 150 °C (hot plate digital display) for 12 h. The solvent, denatured ethanol, was evaporated at 100 °C (hot plate digital display) under stirring, and the resulted gel was then dried in an oven at 90 °C for overnight. To obtain $MgAl_2O_4$ spinel material, the dry powder was calcined in a furnace under static air at 800 °C for 12 h.

Catalyst support, γ-Al_2O_3, was pre-dried in a furnace at 500 °C for 2 h. The PVP-stabilized monometallic Pd2.8 and bimetallic Pd−Ru nanoparticles prepared in ethanol/water were deposited on γ-Al_2O_3 by incipient impregnation. The PVP-stabilized monometallic Ru, Pd7.0 and Pd16 were precipitated with acetone and deposited on γ-Al_2O_3 by wet impregnation. The G4OH-stabilized Pd1.5 and Pd2Ir1 nanoparticles were precipitated with acetone and deposited on $MgAl_2O_4$ spinel support by wet impregnation. Finally, all catalysts were dried in an oven at 60 °C for overnight. The target loading was 0.3 wt.%. Table 6.1 shows metal loadings for the synthesized catalysts and the actual weight ratios of Pd-to-Ru, determined by neutron activation analysis at Becquerel Laboratories (A Maxxam Company, Canada).

6.2.3. Catalyst characterization

Transmission electron microscopy (**TEM**), high-resolution TEM (**HRTEM**), neutron activation analysis (**NAA**), **CO chemisorption** and temperature programmed reduction (**TPR**) of as-synthesized nanoparticles and/or supported catalysts were performed as described earlier [25]. For TEM analysis, 100−200 nanoparticles per sample were counted from TEM images using ImageJ software. Prior to CO chemisorption and TPR analyses, catalysts were calcined at 350 °C for 2 h in air and followed by in situ reduction in 10% H_2/Ar at 300 °C for 1 h. The reported TPR profiles refer to the final reduction step after a series of oxidation-reduction-oxidation-reduction.

X-ray powder diffraction (**XRD**) pattern of $MgAl_2O_4$ was recorded on a Bruker AXS diffractometer (Department of Chemical and Material Engineering, University of Alberta) with a Cu-Kα radiation source (λ = 1.54059 Å) at 40 kV and 44 mA. Continuous X-ray scan was carried out from 2θ of 10° to 110° with a step width of 0.05° and a scan speed of 2°/min. XRD peak identification and data processing were performed using MDI Jade 9.0 software combined with the ICDD database.

6.2.4. Hydrodesulfurization of 4,6-dimethyl-dibenzothiophene

Hydrodesulfurization of 4,6-DMDBT was performed in a packed bed reactor (22" long stainless steel tube with an inner diameter of 1/2"), according to the pioneering works published by Prins's group [7, 9] with some modifications later by our group [33]. The PVP- and G4OH-stabilized catalysts were calcined at 350 °C for 2 h in a furnace under static air to removal polymer. In the initial evaluation of catalytic activity, HDS reactions were carried out at 300 °C and 50 bar with hydrogen flow rate of 100 mL/min (STP conditions). For a typical reaction, 0.18 g calcined catalyst (diluted in 150 mesh SiC, total catalyst bed volume 4 g) was packed in the reactor and then reduced in situ at 300 °C and 50 bar for 1 h under a hydrogen flow (100 mL/min). The 4,6-DMDBT was fed into the catalytic system by pumping an oil solution containing 0.5 wt.% 4,6-DMDBT and 3.5 wt.% dodecane (internal standard) balanced in decane (solvent) with a flow rate of 0.05 mL/min (WHSV = 15 h^{-1}). Later, in order to compare product selectivities at similar 4,6-DMDBT conversions, the developed catalysts were also tested at different WHSVs in the range of 5−56 h^{-1}, by changing the amount of catalysts (0.09−0.54 g) and/or varying the flow rates of hydrogen (100−200 mL/min) and oil solution (0.05−0.10 mL/min) proportionally. In this study the molar ratio of hydrogen-to-oil is always constant at 28 mol./mol..

Catalytic performances were analyzed after 16 h stabilization when steady-state was achieved. A stainless steel condenser (150 mL) is equipped for liquid sample collection. The gas phase product went through a sulfur scrubber and then vented to the fumehood. Prior to sampling, the condenser was emptied after the 16 hours stabilization; liquid samples were then collected after 2 h (at 18 h time on stream). Liquid samples were analyzed offline by a Varian 430 gas chromatogram (GC) equipped with a flame ionization detector (FID). The GC capillary column is a CP-Sil 8 CB column, 50 m length × 0.25 mm inner diameter. Initially, the oven temperature was stabilized at 50 °C for 1 min, and then increased to 300 °C with a rate of 10 °C/min.

The final products of 4,6-DMDBT hydrodesulfurization contain S-free product via DDS route: 3,3'-dimethyl-biphenyl (DMBP), S-free products via HYD route: 3,3'-dimethyl-cyclohexylbenzene (DMCHB) and 3,3'-dimethyl-bicyclohexyl (DMBCH), and S-intermediates via HYD route: 4,6-dimethyl-tetrahydro-dibenzothiophene (DMTHDBT), 4,6-dimethyl-hexahydro-dibenzothiophene (DMHHDBT) and 4,6-dimethyl-perhydro-dibenzothiophene (DMPHDBT), as shown in Scheme 6.1. The observed HDS products from GC spectra were identified by GC-MS [33], and are in agreement with results reported in literatures [7, 9].

For the off-line product analysis, after steady state was reached (16 h), no more than 10% deviation in the mass balance (including HDS products, unconverted 4,6-DMDBT, and H_2S) was observed (typically, 1−6%) as compared to the mass flow of incoming 4,6-DMDBT. Thus, **4,6-DMDBT conversion** was calculated as the amount of 4,6-DMDBT converted in HDS over the amount in the feed solution. The **selectivity** is integral selectivity (reported on molar basis; produced H_2S not included) that was determined as the amount of each HDS product formed divided by the total amount of HDS products (except H_2S). In the following discussion, the **selectivity to DDS** is the selectivity to DMBP; the **selectivity to HYD** is the summation of the selectivities to DMBCH, DMCHB, DMHHDBT, DMPHDBT and DMTHDBT; the **selectivity to S-free via HYD** is the summation of the selectivities to DMBCH and DMCHB; the **selectivity to S-free** is the summation of selectivities to DMBP, DMBCH and CMCHB; and the **selectivity to HYD intermediates** are the summation of DMHHDBT, DMPHDBT and DMTHDBT (Scheme 6.1).

6.3. Result and discussion

6.3.1. Catalyst characterizations of as-synthesized nanoparticles and catalyst support

PVP stabilized monometallic Pd and Ru nanoparticles with mean diameters of 2.8 nm (Fig. 6.3(b)) and 2.0 nm (Fig. 6.2(c)) were synthesized by alcohol and polyol reduction methods, respectively, and are consistent with the results in our previous publications [25, 31, 34]. The bimetallic Pd−Ru nanoparticles with similar sizes (within 2−3 nm range) were synthesized in ethanol/water system with the presence of PVP. The **TEM** images and size distribution histograms of the as-synthesized Pd−Ru nanoparticles are shown in Figure 6.2. For TEM, 100−200 nanoparticles per sample were counted from TEM images using ImageJ software. The synthetic method for bimetallic Pd−Ru nanoparticles was reported previously [25, 30]. In this study, bimetallic Pd−Ru nanoparticles with high Pd fractions (Pd6Ru1, Pd5Ru1, Pd3Ru1, Pd2Ru1 and Pd1Ru1) were prepared. The precursors of Pd and Ru metals were sequentially reduced in ethanol/water at reflux. During the synthesis reaction, Pd precursors were reduced to zerovalent Pd, that act with seeds to autocatalyze the reduction of Ru^{3+} and remaining Pd^{2+} on the surfaces of Pd seed nanoparticles. On average, the mean diameter of Pd6Ru1, Pd5Ru1, Pd3Ru1, Pd2Ru1 and Pd1Ru1 nanoparticles, prepared by ethanol/water reduction, is 2.9±0.4 nm. The larger bimetallic size explains the growth of Ru atoms on Pd seeds; this trend is consistent with the previous results for high Ru fraction catalysts [25]. The surface Ru-to-Pd ratios are expected higher than the bulk distribution, as per our synthetic method.

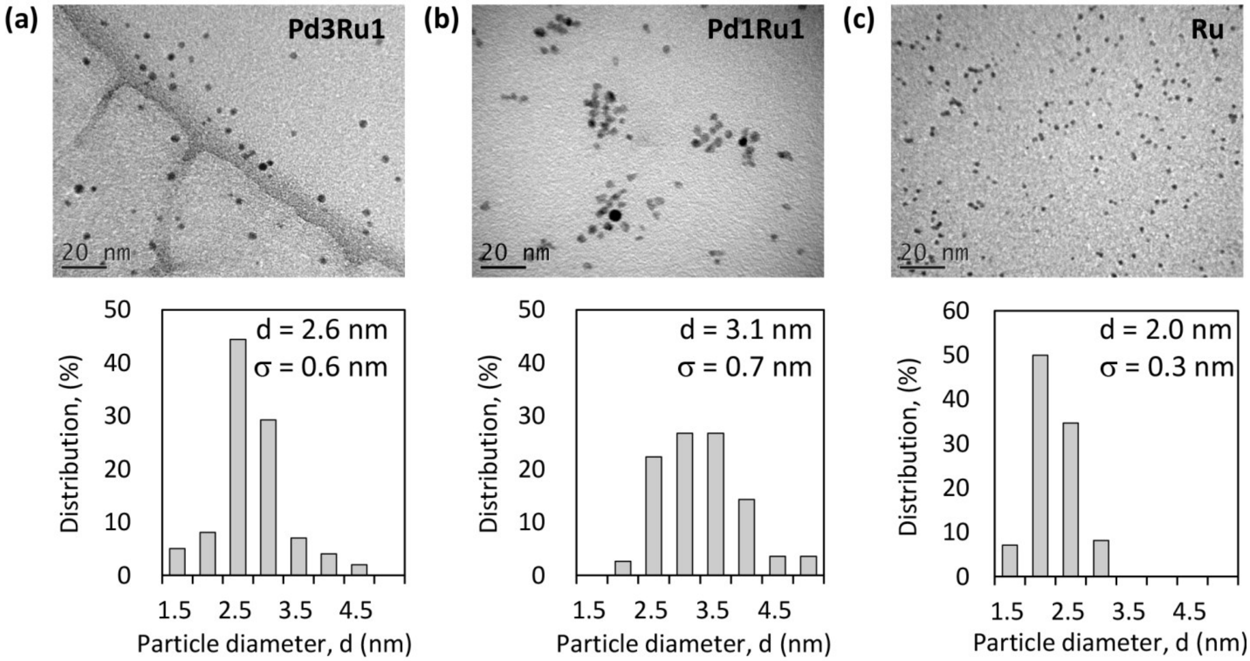

Figure 6.2. TEM images of selected as-synthesized Pd–Ru colloid: Pd3Ru1 (a), Pd1Ru1 (b) and Ru (c) and corresponding size distribution histograms. All scale bars are 20 nm.

The reduction of Pd precursors in alcohol with the presence of PVP is an excellent method to prepare nanoparticles with mean diameter s in the range of 2−8 nanoparticles [23]. However, it is difficult to synthesize ultra-small nanoparticles (such as 1.5 nm Pd in Fig. 6.3(a)) or large Pd particle with different shapes (such as 16 nm Pd cubes in Fig. 6.3(d)). The size distribution of large Pd nanoparticles obtained by applying several growth steps might be relatively wide, as only Pd precursors were added in each growth step, without more stabilizers introduced [35]. For shape control, a shape-directing agent (such as KBr or bromide in CTAB) is required, because it adsorbs selectively on specific surface atoms and prevents their further growth [36]. This way, Pd cubes could be synthesized with (100) terraces [37].

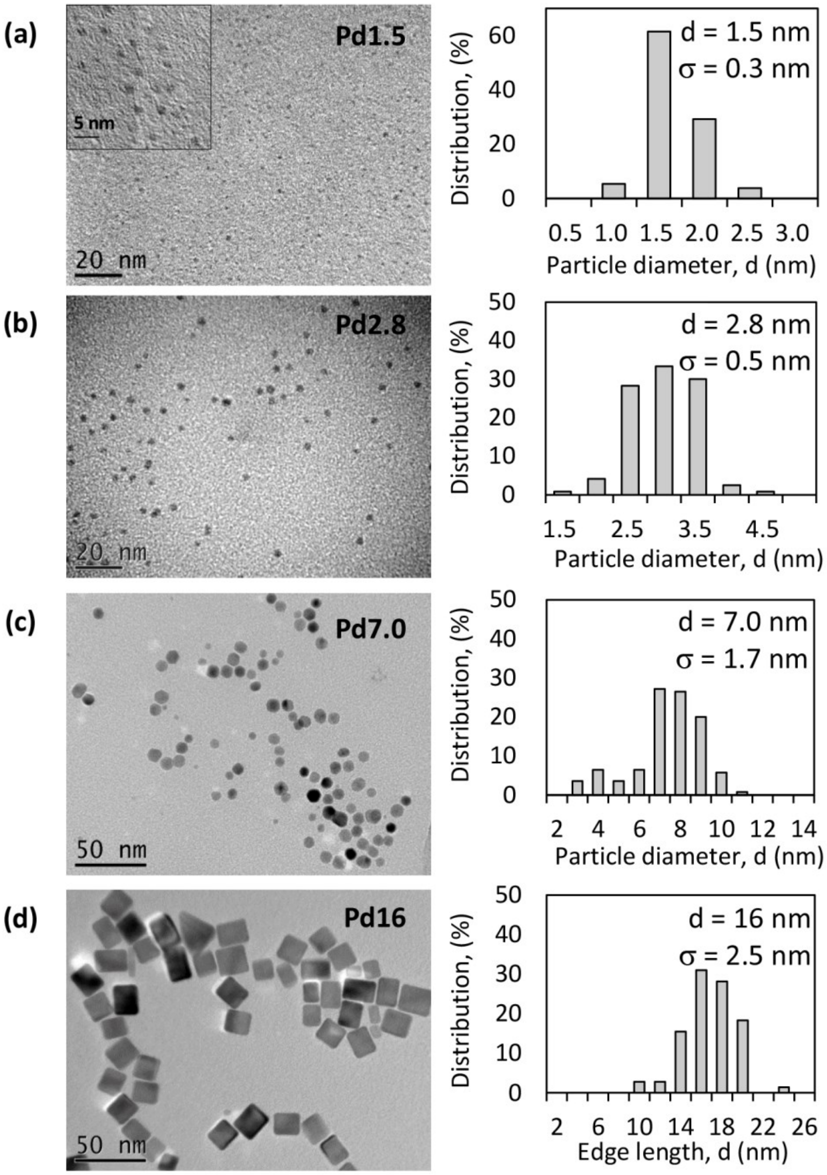

Figure 6.3. TEM images of as-synthesized G4OH-Pd1.5 (a), PVP-Pd2.8 (b), PVP-Pd7.0 (c) and PVP-Pd16 nanoparticles, and corresponding size distribution histograms.

In this study, Pd nanoparticles were synthesized by using various nanotechnologies that allow the precise preparation of Pd nanoparticles with different sizes and shapes. Figure 6.3 displays the TEM images of highly monodispersed Pd nanoparticles from 1.5−16 nm with nearly spherical (Fig. 6.3(a) and (b)), cuboctahedral (Fig. 6.3(c)) and cubic (Fig. 6.3(d)) shapes. The numbers in the catalyst notation (such as Pd1.5) correspond to the mean diameter (or edge length for cubes). In this study, we did not study or elucidate the mechanism of Pd size/or shape control during the nanoparticle formation.

Dendrimer-templating strategy was used to prepare ultra-small Pd nanoparticles (**Pd1.5** in Fig. 6.3(a)). The size control using G4OH was achieved by the complexation of Pd^{2+} with 64 interior amine groups of G4OH, and followed by the reduction by $NaBH_4$. The G4OH dendrimer is approximately 4.5 nm in diameter (Fig. 6.1); and the unique tree-like structure of dendrimers restricts the further growth to larger particles [24]. The mean diameter of 1.5 nm for Pd is in agreement with previous results: 1.3−1.7 nm of G4OH-stabilized Pd nanoparticles for similar preparation method [38, 39]. The **Pd2.8** (Fig. 6.3(b)) nanoparticles were prepared by low-boiling alcohol reduction method in the presence of PVP, which is a well established method to yield near spherical nanoparticles with mean diameter of 2–3 nm [23]. The **Pd7.0** (Fig. 6.3(c)) cuboctahedral particles were prepared using modified polyol reduction method with the presence of PVP. The observed uniform cuboctahedrons agrees with the previously published results by Xia and coworkers [40]. The author claimed that the selective etching of the early stage twinned particles by Cl^-/O_2 is responsible for purifying and thus the Pd shape control. The **Pd16** (Fig. 6.3(d)) cubic nanoparticles were synthesized by slow reduction via ascorbic acid in the presence PVP and shape directing agent, KBr. The formation of final large Pd cubes is a sequential reduction reaction. The initial step is the reduction of Pd precursors to form small Pd seeds. Ascorbic acid serves as a weak reducing agent, provides slow nucleation rate to form low concentration Pd seeds relative to the unreduced Pd ions. In the second step, bromide selectively chemisorbed on the (100) faces of Pd seeds, which promotes the nanoparticle growth along the (111) direction to form large Pd cubes [37]. Our results are in line with the Pd cubes (18 nm) synthesized by similar method, reported by Xia's group [32].

The crystal structure of synthesized $MgAl_2O_4$ was investigated by **XRD**, as shown in Figure 6.4. The XRD pattern confirms the formation of $MgAl_2O_4$ spinel after annealed at 800 °C for 12 h, as indicated by the presence of (111), (220), (311), (400), (511) and (440) reflections, which is consistent with the previous result, when $MgAl_2O_4$ was synthesized using similar method [28].

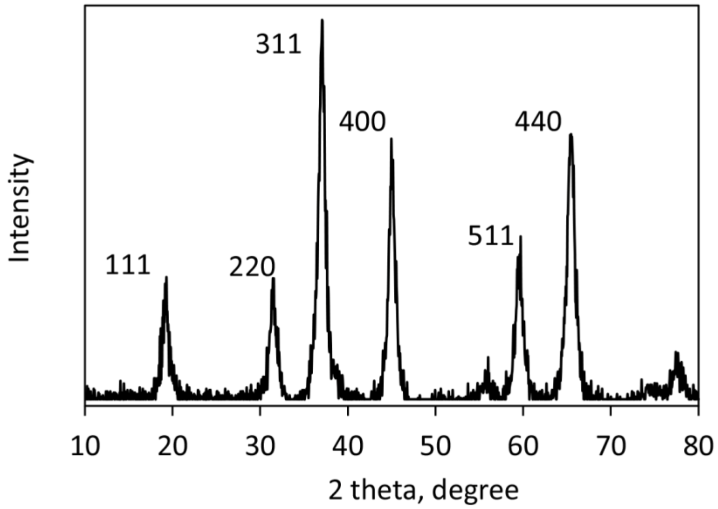

Figure 6.4. XRD pattern for $MgAl_2O_4$ spinel support.

6.3.2. Catalyst characterizations of calcined/spent catalysts

Table 6.2 presents nanoparticle mean diameters and dispersions estimated by **CO chemisorption** experiments of the pretreated catalysts (350 °C calcination in air for 2 h and 300 °C reduction in 10% H_2/Ar for 1 h). The nanoparticle sizes and dispersions were calculated from CO uptake values by assuming CO-to-metal(s) stoichiometry of 1. Monometallic Pd2.8 (synthesized by the same method as for bimetallic Pd−Ru nanoparticles) and Ru nanoparticles cannot survive high temperature treatment, resulting in increasing nanoparticle sizes due to sever sintering, as reported previously [41]. When alloying Ru with Pd, dispersions of all bimetallic nanoparticles increased remarkably. The improvement is consistent with our previous results on high Ru fraction bimetallic samples [25], indicating the intrinsic bimetallicity. The optimal Pd-to-Ru weight ratio for the most distinct improvement in thermal stability is observed in low Ru fraction bimetallic samples: Pd6Ru1 and Pd5Ru1 with mean diameters of 2.4 nm and 3.1 nm, respectively, after polymer removal.

All alumina supported Pd nanoparticles (Pd2.8, Pd7.0 and Pd16) show sintering after subjecting to thermal treatment (Table 6.2), i.e., low Pd dispersions in the range of 1−9%. The trend is that the nanoparticle size was originally large (Pd16, 16 nm in edge length) reveals large extent of sintering (145 nm in edge length after treatment). Particles with sizes larger than alumina pore size (6.8 nm in average) reside outside the pores; while the sintering of small particles can be partially restricted by alumina pores. The $MgAl_2O_4$-supported Pd1.5 sample is the most stable catalyst with 6.8 nm of mean diameter after thermal treatment at 350 °C. The enhanced thermal stability is attributed to the strong interaction between $MgAl_2O_4$ spinel and Pd1.5 nanoparticles [28], leading to the maintenance of high Pd dispersions. In the previous study of stable Pt nanoparticles on specific $MgAl_2O_4$ spinel facets, the author observed that the $MgAl_2O_4$ spinel support is capable of stabilizing Pt particles in the range of 1−3 nm on its (111) facets. The superior property of spinel is related to the interaction between Pt (111) facets and oxygen on spinel (111) facets [28].

Table 6.2. Nanoparticle sizes from CO chemisorption analyses of the supported catalysts after 350 °C calcination in air for 2 h and 300 °C reduction in 10% H_2/Ar for 1 h.

Catalysts	Nanoparticle sizes, nm	Dispersions, %
Ru	9.7	11
Pd1Ru1	4.8	22
Pd2Ru1	7.0	16
Pd3Ru1	8.4	13
Pd5Ru1	3.1	36
Pd6Ru1	2.4	46
Pd1.5	6.8	17
Pd2.8	13.3	9
Pd7.0	21.4	5
Pd16	145	1

TEM of supported spent catalysts was performed to evaluate possible sintering of the selected catalysts after HDS reactions. Figure 6.5 shows the TEM images of spent Pd2.8/γ-Al_2O_3, Pd6Ru1/γ-Al_2O_3 and Pd1.5/$MgAl_2O_4$ catalysts after 22 hours HDS reactions at 300 °C and 50 bar H_2; the latter two catalysts were found as remarkably promising in 4,6-DMDBT hydrodesulfurization, while the Pd2.8 catalyst is a reference sample without any thermal stability enhancement. The alumina-supported Pd2.8 catalyst (Fig. 6.5(a)) displays severe sintering after HDS reaction at 300 °C. This is agreed with our previous findings that monometallic Pd and Ru are not resistant to sintering and showed agglomerates in the 300−400 °C range [25]. As expected from the CO chemisorption results (Table 6.2) of calcined samples, bimetallic Pd6Ru1/γ-Al_2O_3 and Pd1.5/$MgAl_2O_4$ catalysts (Figs. 6.5(b)−(d)) did not show visible agglomerates of more than 5 nm. The improved thermal stabilities are indicative of intrinsic bimetallicity and strong support effect in Pd6Ru1/γ-Al_2O_3 and Pd1.5/$MgAl_2O_4$ catalysts, respectively. The high nanoparticle dispersions seen from TEM, together with the CO chemisorption results, explicate the enhancement in DDS selectivity (will be discussed in section 6.6).

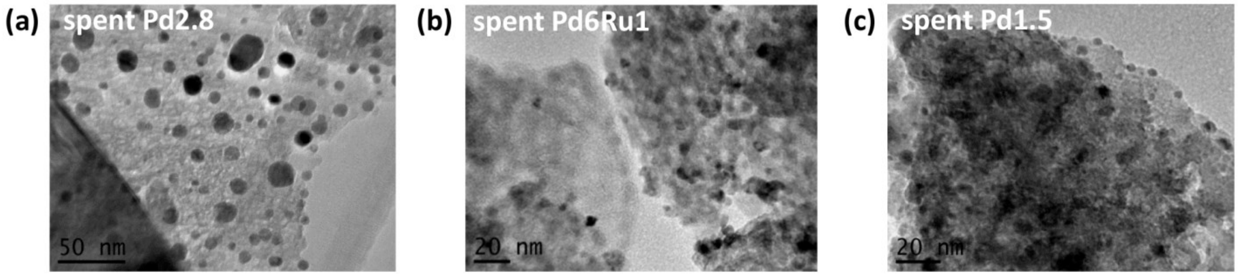

Figure 6.5. TEM images of spent catalysts: Pd2.8/γ-Al_2O_3 (a), Pd6Ru1/γ-Al_2O_3 (b) and Pd1.5/$MgAl_2O_4$ (c) after HDS reactions at 300 °C for 22 h in 50 bar H_2. Scale bars are 20 nm except 50 nm for Pd2.8/γ-Al_2O_3.

TPR was carried out also after calcination at 350 °C in air for 2 h and followed by in situ reduction in a flow of 10% H_2/Ar at 300 °C for 1 h, which imitates the catalyst pretreatment prior to HDS reactions. Figure 6.6 shows the TPR profiles of alumina-supported Pd2.8 and Pd16 nanoparticles with particle sizes of 13 and 145 nm after calcination, respectively. It is known that Pd could be easily reduced and forms Pd hydrides below room temperature [25, 42] while the system waits for a stable TCD baseline, thus TPR profiles show only hydrogen evolution peaks. The Pd2.8 catalyst reveals single hydrogen desorption peak centered at 87 °C. The Pd16 sample exhibits a broad hydrogen evolution peak, which can be deconvoluted into 122 °C and 140 °C peaks. The higher hydrogen desorption temperatures is an indicative of more stable hydrides in the Pd16 sample comparing to the Pd2.8 catalyst. The hydrogen desorption behaviors observed in TPR experiments characterize only the different sites and binding strengths between small Pd spheres and large cubes, and do not correlate with the HDS activity trend.

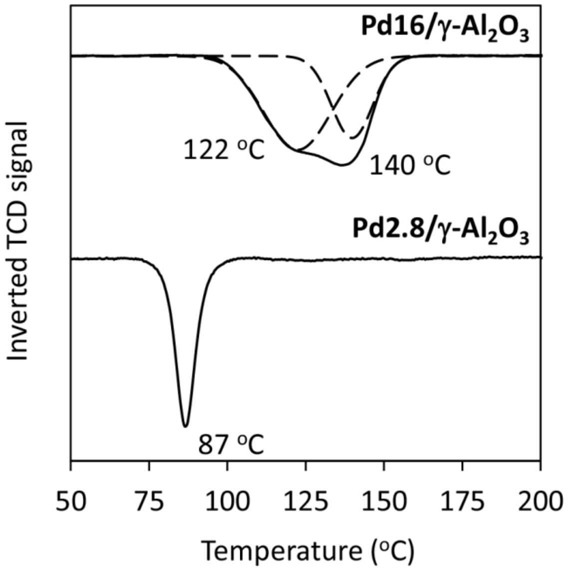

Figure 6.6. TPR profiles of Pd2.8/γ-Al_2O_3 and Pd16/γ-Al_2O_3 catalysts. Catalysts were calcined at 350 °C for 2 h.

6.3.3. HDS of 4,6-DMDBT

The developed mono- and bimetallic Pd-based catalysts were studied in the hydrodesulfurization of 4,6-DMDBT. Catalyst performances were reported at steady state (after 16 hours time on stream), with no more than 10% deviation in the carbon mass balance (typically, 1−6%). Each data is presented as an average obtained from 2−3 GC runs with one standard deviation. The absence of external mass transfer limitation for 4,6-DMDBT HDS was proved experimentally over a monometallic Pd2.8 catalyst, by varying the reactant flow rates (H_2 and oil) and catalyst loading on the reactor at constant weight hourly space velocity (WHSV = 31 h^{-1}) (Table 6.3). A constant activity ($(5.1\pm0.2)\times10^{-3}$ $mol_{4,6\text{-DMDBT}}/mol_{Pd}/s$) validated the absence of external mass transfer limitations in a wide range of H_2 (50−200 mL/min) and oil (0.025−0.100 mL/min) flow rates [43]. The Madon-Boudart technique was applied to verify the absence of internal mass transfer limitations by changing the Pd loading (0.21 and 0.12 wt.% determined from NAA) of the Pd2.8 catalyst (Table 6.3). A constant activity calculated as per surface Pd atoms ((21.8±1.6)×10^{-3} $mol_{4,6\text{-DMDBT}}/mol_{surf\ Pd}/s$) suggests the absence of internal mass transfer limitations. Hence, the reported catalytic performances in the following discussions are in kinetic regime. The activities refer to integral reactor operation and were determined based on the exit stream composition, typically at the same conversions unless otherwise stated. The differential reactor operation for intrinsic turnover frequency calculations [44] was not performed in this work because the presented study is focused on DDS/HYD product distribution at high conversions.

Table 6.3. Evaluation of the absence of mass transfer limitations in the HDS of 4,6-DMDBT over Pd2.8/γ-Al_2O_3 catalyst at 300 °C, 50 bar, 31 h^{-1} WHSV and 18 h time on stream. Data in brackets are one standard deviation.

Catalyst weight, g	Pd loading, wt.%	H_2 flow rate, mL/min	Oil flow rate, mL/min	Activity, 10^{-3} $mol_{4,6\text{-DMDBT}}/mol_{Pd}/s$	Activity, 10^{-3} $mol_{4,6\text{-DMDBT}}/mol_{surf\ Pd}/s$
External mass transfer limitations					
0.045	0.21	50	0.025	5.04 (0.15)	20.9 (0.6)
0.090	0.21	100	0.050	4.99 (0.10)	20.7 (0.4)
0.180	0.21	200	0.100	5.27 (-)	21.9 (-)
Internal mass transfer limitations					
0.090	0.21	100	0.050	4.99 (0.10)	20.7 (0.4)
0.090	0.12	100	0.050	5.08 (0.03)	23.0 (0.1)

Figure 6.7(a) shows product selectivities as a function of 4,6-DMDBT conversion, in the range of 40−70 %, over a Pd2.8/γ-Al_2O_3 catalyst. It can be seen that the selectivity to DDS is unchanged with varying 4,6-DMDBT conversions. The selectivity to S-free product via HYD route increases with increasing 4,6-DMDBT conversion, because more HYD intermediates were cleaved to S-free products at higher 4,6-DMDBT conversions. As a result, the selectivity to S-free products increases with increasing 4,6-DMDBT conversion. Thus, valid comparison of catalytic selectivities must be performed and reported at similar 4,6-DMDBT conversions. The catalyst performances (in Fig. 6.7) were reported in a wide range of WHSV (15−56 h^{-1}) by

changing the catalyst weights or reactant flow rates, due to the different activities over the developed catalysts. Figure 6.7(b) shows the trend that 4,6-DMDBT conversion decreases as WHSV increases.

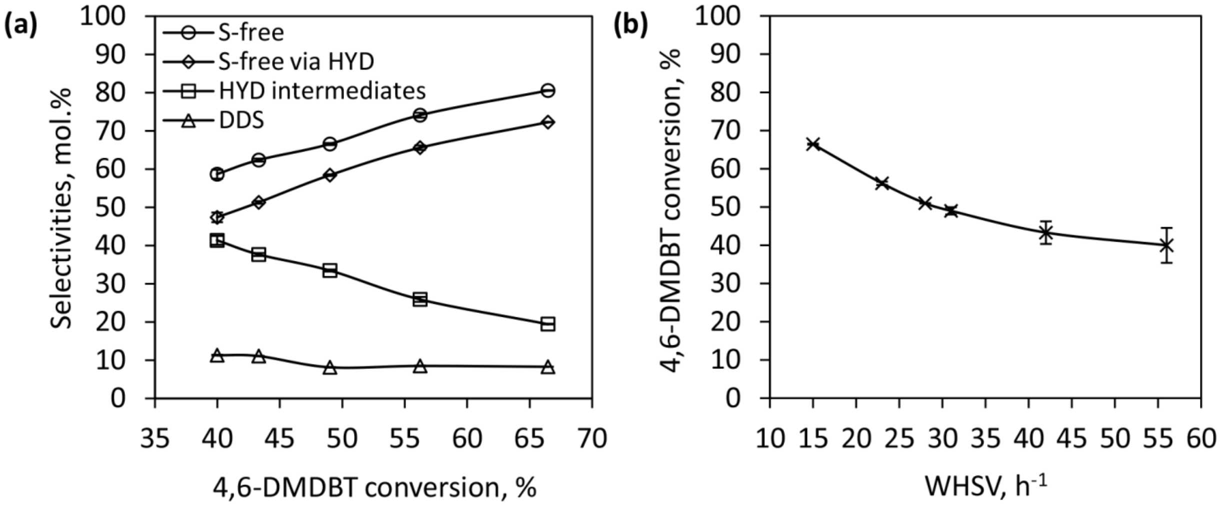

Figure 6.7. HDS selectivities vs. 4,6-DMDBT conversion (a) and 4,6-DMDBT conversions vs. WHSV (b) over a Pd2.8/γ-Al_2O_3 catalyst. Different WHSVs were obtained by varying H_2 and oil flow rates simultaneously (molar ratio of H_2-to-oil = 28/1) or changing the amount of Pd2.8/γ-Al_2O_3 catalyst. HDS operating conditions are 300 °C and 50 bar H_2. The error bars correspond to one standard deviation.

6.3.4. DDS enhancement: Ru addition to Pd

The catalytic performances of alumina-supported bimetallic Pd−Ru catalysts were compared with a monometallic Ru and Pd2.8/γ-Al_2O_3 (Pd2.8 was prepared in ethanol/water; similar particle size as bimetallic Pd−Ru nanoparticles before calcination) catalysts. Figure 6.8 shows the activities and selectivities to S-free products (divided into DDS and HYD routes) for the developed catalysts. Monometallic Pd is known an active HDS catalyst; the Pd2.8 catalyst converts $(2.35\times10^{-3})\pm0.02$ $mol_{4,6\text{-DMDBT}}/mol_{Pd}/s$ versus negligible activity over the monometallic Ru catalyst. Alloys display intermediate activities between their mono-forms, except Pd6Ru1 reaching the value of monometallic Pd2.8 catalyst (Fig. 6.8(a)). Activity per mole of surface atoms was not calculated for Pd−Ru catalysts, because of the existential uncertainties with the surface sites. The Pd-to-Ru ratio on the nanoparticle surfaces might be higher that the values in the bulk, as per our synthetic method. In addition, due to the synergistic effects upon alloying Pd with Ru, it is not clear that whether it is Pd atoms or the presence of new sites (Pd and Ru ensembles) responsible for the activity of the bimetallic nanoparticles.

Catalytic selectivities were compared at similar 4,6-DMDBT conversions (40±3%), except 14% for monometallic Ru catalyst. The addition of Ru to Pd can potentially enhance the Pd stability and bring better hydrogenolysis property of the alloys. Between 3.2−6.2 Pd-to-Ru weight ratios, the selectivity to S-free products improves by a maximum of 34% (Fig. 6.8(b)), with corresponding 2-fold increase in the DMBP formation (DDS product) (Fig. 6.8(c)), comparing to the monometallic Pd2.8 catalyst. The trend is that an increase in Pd content in the bimetallic catalyst leads to better performances in terms of selectivity to S-free products. The highest selectivity to DDS (19 mol.%) is observed over the Pd6Ru1 catalyst with the smallest particle size of 2.4 nm after 2 h calcination at 350 °C (Table 6.2). Alloying Pd with Ru improves the thermal stability of Pd (for all Pd-to-Ru ratios studied), thus tempers the severe sintering of the bimetallic nanoparticles. The CO chemisorption results show increase in nanoparticle dispersions (Table 6.2), which is also verified by TEM of spent catalysts (Fig. 6.5): no sign of nanoparticle sintering after 22 hours HDS reaction at 300 °C and 50 bar H_2. The DDS selectivity is strongly dependent on nanoparticle size. The appearance of more corner and edge atoms in small Pd−Ru nanoparticles vs. Pd2.8 catalyst allows more perpendicular adsorption of 4,6-DMDBT molecules on the nanoparticle surfaces via S atoms, which is required for DDS mechanism.

However, the change in nanoparticle dispersion upon alloying Pd with Ru seems to show no impact on the selectivity toward sulfur removal via HYD route. For instance, bimetallic Pd−Ru catalysts reveal constantly improved selectivity to S-free product via HYD route by an average of 19 mol.% (Fig. 6.8(d)), regardless the final nanoparticle sizes after calcination. The better selectivity toward DMBCH and DMCHB formations (S-free via HYD) is most likely due to the presence of Ru atoms in the nanoparticle surfaces. It is known that Ru has better hydrogenolysis property than Pd, while Pd works as a good hydrogenation catalyst [25] from our previous study in low-pressure indan ring opening. The addition of Ru dilutes the Pd ensembles, thus enhances the C−S cleavage of the pre-hydrogenated HYD intermediates.

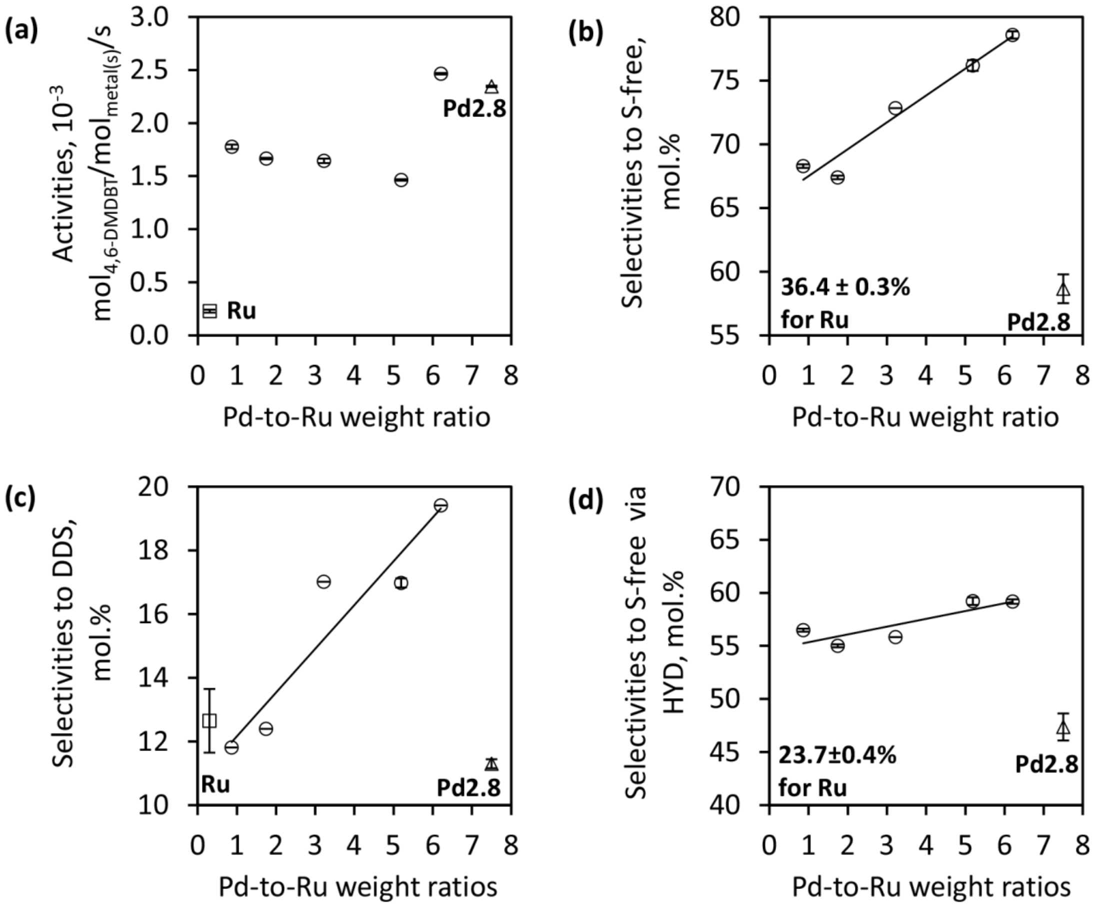

Figure 6.8. Catalytic performances of Pd−Ru alloys with varying Pd-to-Ru weight ratios compared with monometallic Pd2.8 and Ru catalysts: activity (a); selectivity to S-free (b), selectivity to DDS (c); and selectivity to S-free via HYD (d) in the HDS of 4,6-DMDBT at 300 °C and 50 bar H_2; conversion = 40±3% (except 14% for Ru); and WHSV = 23 h^{-1} (except 56 and 8 h^{-1} for Pd2.8 and Ru catalysts, respectively). Activities were compared at WHSV = 23 h^{-1}.

Similar trend observed in the activity and selectivities over Pd−Ru catalysts are also observed in the 4,6-DMDBT consumption rate and HDS products formation rates per mass of alumina-supported catalyst at the constant WHSV (23 h^{-1}), as shown in Figure 6.9. The Pd6Ru1 catalyst (most promising Pd−Ru catalyst for DDS enhancement) converts similar amount of 4,6-DMDBT (5×10^{-8} $mol_{4,6\text{-DMDBT}}/g_{catalyst}/s$) as Pd2.8 catalyst at the same 1.8 g catalyst packed in the reactor (Fig. 6.9(a)). Remarkably, the Pd6Ru1 catalyst outperforms Pd2.8 with a 3-fold increase in the DMBP formation rate (Fig. 6.9(c)) and a same high S-free products yield rate (Fig. 6.9(b)). In addition, the addition of a small portion of Ru to Pd (Pd6Ru1) maintains the formation rate of

S-free products via HYD route at the similar level of Pd2.8 (known as the most active hydrogenation catalyst) (Fig. 6.9 (d)).

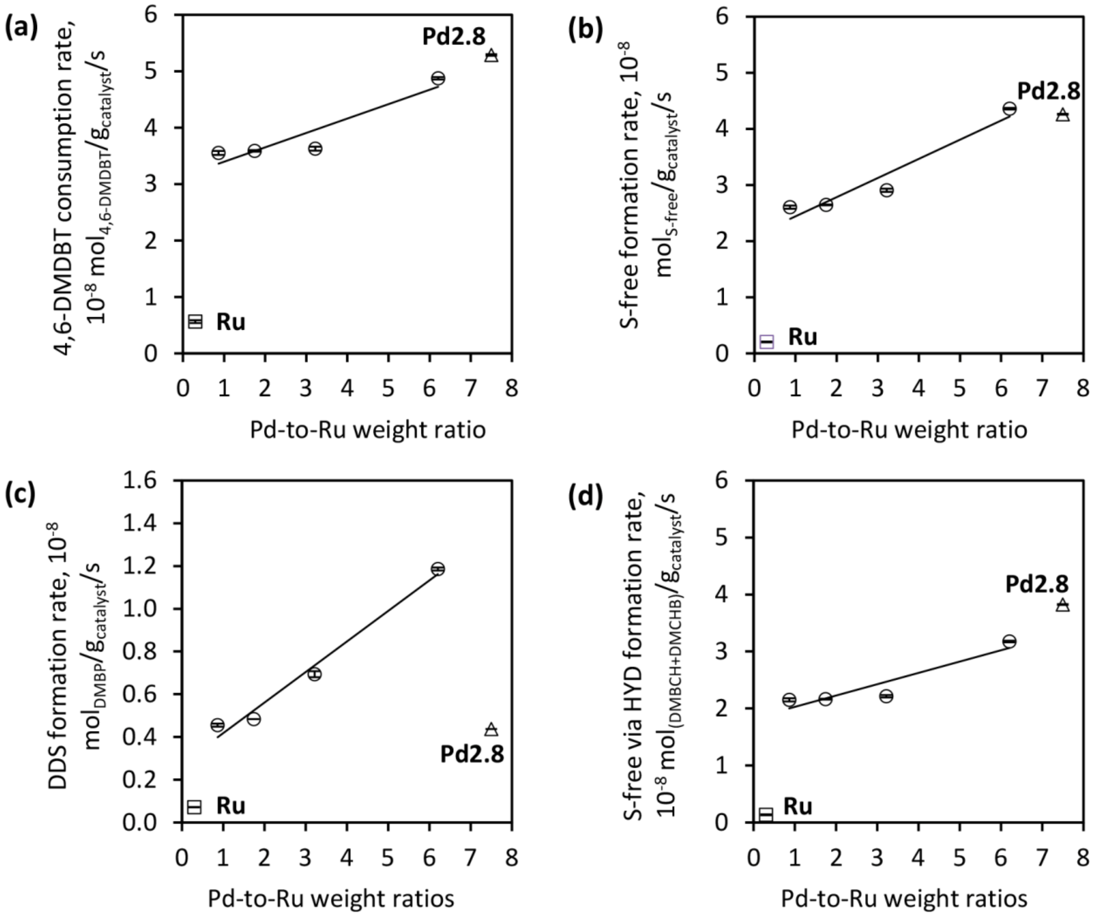

Figure 6.9. 4,6-DMDBT consumption rate (a), S-free product formation rate (b), DDS formation rate (c), and S-free via HYD formation rate (d) over Pd−Ru catalysts in the HDS of 4,6-DMDBT at 300 °C and 50 bar H_2; and WHSV = 23 h^{-1}.

Based on the catalyst selectivities (and distribution of the two HDS mechanisms) over Pd−Ru catalysts, a feasible hypothesis could be the HYD mechanism depends on the nature of the second metal added in the nanoparticle shells; while the selectivity to DDS over Pd-containing catalysts is dependent only on the nanoparticle dispersions. The latter is contrary to literature findings that 4,6-DMDBT conversion through DDS pathway almost not occur over Pd catalysts. Niquille-Rothlisberger reported that HDS of 4,6-DMDBT proceeded exclusively via the HYD route with only 1% selectivity to DDS over a Pd/γ-Al_2O_3 catalyst [7, 9]; the HDS was carried out at 300 °C and 50 MPa, which is similar to the HDS reaction conditions in our work. Therefore, to check the hypothesis validity, the intrinsic size effect on DDS selectivity is studied over monometallic Pd catalysts in the following section.

6.3.5. Selectivity enhancement: Pd size and shape control

Figure 6.10 shows the catalytic activity and selectivities of monometallic Pd nanocatalysts with different sizes and shapes. The numbers of active sites after calcination were estimated using CO uptake values, so the catalyst activities were calculated as the amount of 4,6-DMDBT converted per surface Pd atoms per second based on the 4,6-DMDBT flow rate and its conversion at the reactor exit. The Pd16 catalyst shows activity of 70×10^{-3} $\mathrm{mol}_{4,6\text{-DMDBT}}/\mathrm{mol}_{\mathrm{surf\ Pd}}/\mathrm{s}$ vs. 39×10^{-3} and 26×10^{-3} $\mathrm{mol}_{4,6\text{-DMDBT}}/\mathrm{mol}_{\mathrm{surf\ Pd}}/\mathrm{s}$ for Pd7.0 and Pd2.8 spheres, respectively (Fig. 6.10(a)), because hydrogenations are known to be structure-sensitive and require large terraces to proceed [36, 45]. Among the three Pd spheres, Pd1.5 catalyst displays the lowest activity (5.8×10^{-3} $\mathrm{mol}_{4,6\text{-DMDBT}}/\mathrm{mol}_{\mathrm{surf\ Pd}}/\mathrm{s}$), confirming that the 4,6-DMDBT mostly lay flat on the surface, which requires larger terraces. Our findings are consistent with the conclusions made in previous studies of HDS of thiophene molecules over Pt and Ru nanoparticles with sizes ranging from 2−8 nm. Smaller Pt or Ru clusters exhibit lower activity vs. larger particles, which is related to the too strong reactant binding on the coordinatively unsaturated atoms of small particles [14, 15, 46]. The too strong binding, according to the Sabatier's principle ("volcano plot"), prevents product formation.

The mentioned activities were calculated based on the total conversion of 4,6-DMDBT, which contains S-free products as well as S-containing pre-hydrogenated HYD intermediates. The fact is that a catalyst shows high activity might not allow fast sulfur removal rate; for example, 70 mol.% of HDS products are S-containing molecules over the Pd16 catalyst (Fig. 6.10(b)). Thus, high selectivity toward S-removal should be considered as a more important factor than activity when evaluating new catalysts.

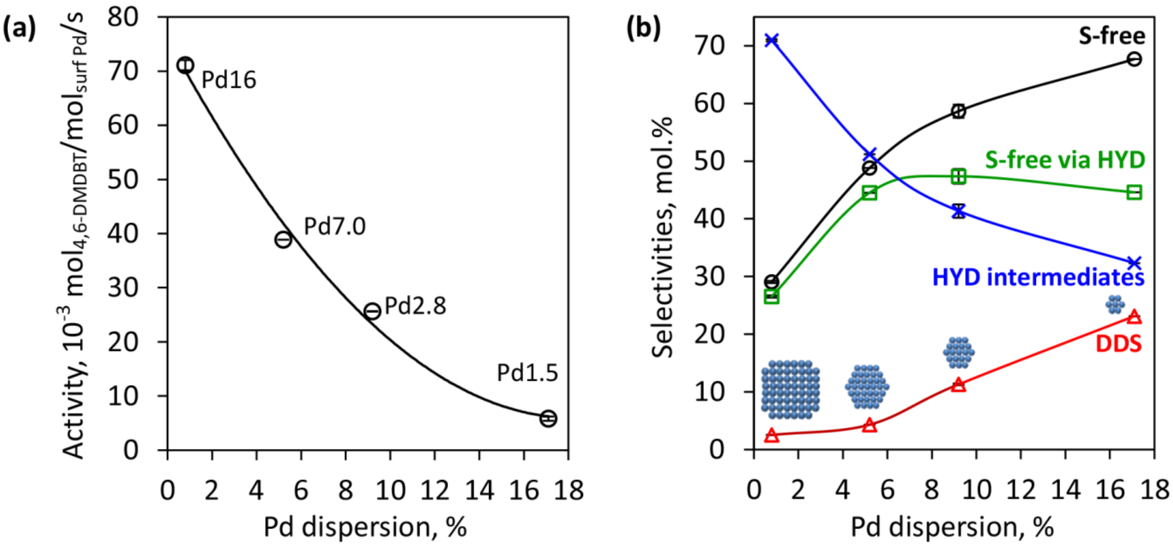

Figure 6.10. Catalytic performances of monometallic Pd catalysts with varying particle dispersions at similar conversions: activities (a); and selectivities (b) in the HDS of 4,6-DMDBT at 300 °C and 50 bar H_2; conversion = 39±8%; and WHSV = 5, 56, 15 and 5 h^{-1} for Pd1.5, Pd2.8, Pd7.0 and Pd16 catalysts, respectively.

The comparison of HDS selectivities over a series of monometallic Pd nanoparticles with different sizes and shapes was shown in Figure 6.10(b). The Pd16 catalyst displays the lowest selectivity to S-free products (30 mol.%), due to the slow C−S cleavage rate of pre-hydrogenated HYD intermediates on large Pd surfaces. For the similar 4,6-DBDMT conversions, the selectivity to S-free products improves up to 2-fold over smaller spherical Pd nanoparticles (Pd2.8 and Pd1.5 catalysts). This improved sulfur removal rate is contributed by enhanced C−S bond hydrogenolysis via both reaction mechanisms. The improvement in the DDS selectivity is ascribed to the presence of more corner and edge atoms in small Pd spheres, which eliminates the alkyl group-induced steric hindrance, therefore, enhances the perpendicular adsorption of 4,6-DMDBT molecules through sulfur atoms. While the increase in S-free selectivity through HYD route is due to the changes in electronic properties from large Pd to small Pd nanoparticles, consequently optimizing the strength of 4,6-DMDBT adsorption (through aromatic rings) over Pd terrace atoms. The differences in surface configurations and binding strengths between large and small Pd particles can be also seen from the different hydrogen desorption behaviors over alumina-supported Pd2.8 and Pd16 catalysts (TPR analysis, Fig. 6.6, strong hydrogen bonding on Pd16 sample was observed).

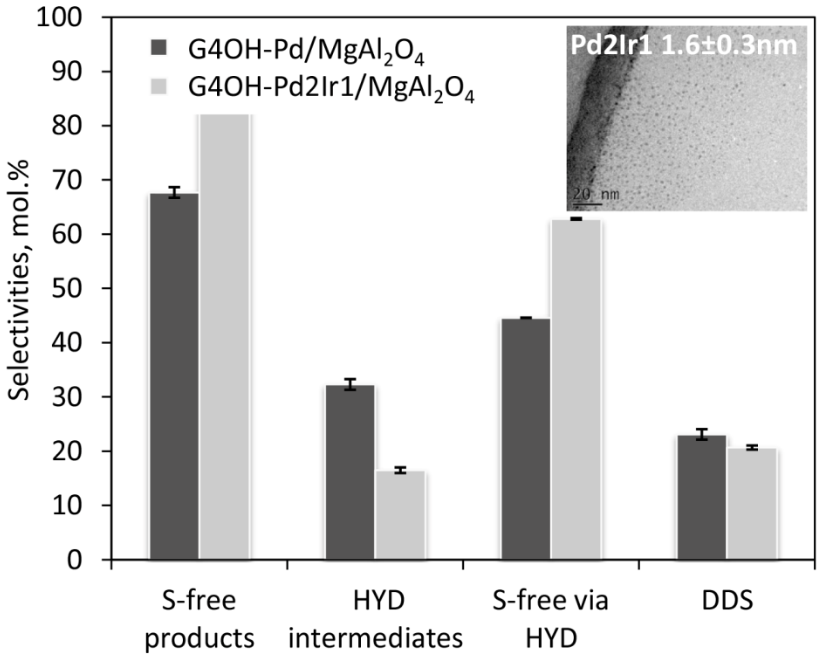

Figure 6.11. Catalytic performances of Pd1.5/$MgAl_2O_4$ vs. Pd2Ir1/$MgAl_2O_4$ at 300 °C and 50 bar H_2 pressure; conversion = 33±6%; and WHSV = 5 h^{-1}.

Among all three spherical Pd nanoparticles, Pd1.5 displays the highest selectivity toward S-free products formation (67 mol.% in Fig. 6.10(b)). Maintaining high Pd dispersion by introducing a strong metal-support interaction, $MgAl_2O_4$-supported Pd1.5 allows a 5-fold increase in DMBP formation (21 mol.%) comparing to Pd7.0 (4 mol.%), reaching the value of Pd6Ru1 (19 mol.%) catalyst at similar 4,6-DMDBT conversions. The selectivity to sulfur removal via HYD route remains constant (46±1 mol.%) with nanoparticle sizes in the range of 7−21 nm (calculated from CO chemisorption results). Therefore, it can be concluded that the selectivity to DDS over Pd catalysts depends largely on nanoparticle size. This supports the proposed hypothesis made from Pd−Ru behaviors. The hydrogenolysis property of Ru did not promote DDS rate; it is the change in nanoparticle dispersions (presence of more defect atoms) governs the selectivity to DMBP formation. Similar trend was also observed with Ir addition to Pd (Fig. 6.11). The Pd2Ir1 (rounded Pd-to-Ir weight ratio of 2.2/1, confirmed by NAA) nanoparticles prepared by dendrimer-templating method were deposited on $MgAl_2O_4$ spinel support. Thus, Figure 6.11 reveals the intrinsic effect of Ir addition to Pd, with negligible size or support effects. Ir, known as the most active hydrogenolysis catalyst, surprisingly, its addition to

Pd did not further improve the selectivity to DDS (21 mol.%, similar to Pd1.5). Like Ru, Ir promotes only the S-removal in HYD route. This result validates the importance of Pd size control in the HDS of 4,6-DMDBT. The understanding of intrinsic size effect on HDS selectivity avoids the use of rare or expensive elements on earth (such as Pd, Ru and Ir), thus may leading to an alternative route in catalyst design in refining industries.

Figure 6.12 compares 4,6-DMDBT consumption rates and the formation rates of HDS products over monometallic Pd catalysts with four different particle dispersions. The optimal Pd dispersion for the highest 4,6-DMDBT consumption rate is 9% (Pd2.8). Pd catalyst with either too large or too small particle sizes displays low 4,6-DMDBT consumption rate, due to the loss in surface Pd atom in large nanoparticles or too strong sulfur binding on coordinatively unsaturated atoms presence in small nanoparticles, respectively. The H_2S effect on monometallic Pd nanoparticles is currently under study, with the hypothesis that sulfur poisoning is size sensitive. The formation rate of S-free products is also maximized over Pd2.8 catalyst, accompanied with the highest yield of S-free product via HYD pathway. The Pd1.5 catalyst with the highest selectivity toward S-free product formation (Fig. 6.10(b)) underperforms Pd2.8 catalyst, when considering the S-free product formation rates because of its low activity. The catalyst volume for Pd1.5 must be increased several times more to reach the comparable 4,6-DMDBT conversion with Pd2.8. However, these results are not in conflict with the conclusion that HDS selectivity depends strongly on Pd dispersion: the more edge atoms the higher the selectivity to DDS.

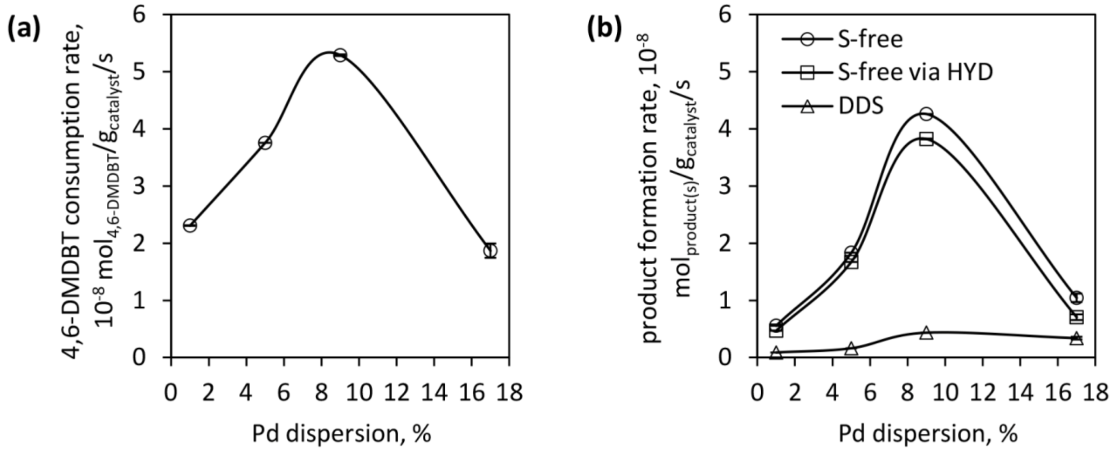

Figure 6.12. 4,6-DMDBT consumption rate (a) and products formation rate over monometallic Pd catalysts with varying particle dispersions in HDS at 300 °C and 50 bar H_2; WHSV = 15 h^{-1}.

6.4. Conclusions

Bimetallic Pd−Ru nanoparticles of 2−3 nm sizes with varying Pd-to-Ru weight ratios from 6.2−0 were synthesized in the presence of PVP. Monometallic Pd nanoparticles of varying particle sizes from 1.5−16 nm with spherical or cubic shapes were prepared. The size control of Pd nanoparticles was accomplished by a series of advanced colloidal methods, including dendrimer-templating and polymer protection techniques in alcohols, as well as the use of shape directing agent, bromide, for Pd cubes. Magnesium aluminate spinel support was prepared by hydrolysis of aluminum isopropoxide with magnesium nitrate hexahydrate in ethanol, followed by drying and high temperature calcination to form pure spinel crystal phase, as XRD shown. Bimetallic Pd−Ru nanoparticles and monometallic Pd nanoparticles were deposit on alumina support or $MgAl_2O_4$ spinel support. The developed catalysts were tested in the hydrodesulfurization of 4,6-DMDBT at 300 °C and 50 bar H_2 pressure.

Alloying Pd with Ru and introducing a strong Pd-support interaction (by $MgAl_2O_4$ spinel) dramatically improved the thermal stability of active Pd. CO chemisorption and TEM revealed that the nanoparticle dispersions were maintained after high-temperature calcination and after 22 h HDS reactions, respectively. To correlate the Pd size effect on HDS selectivities, TPR showed the difference in binding strengths between small Pd spheres and large cubes.

The catalytic tests of HDS of 4,6-DMDBT showed the dramatic 2-fold increase in the selectivity to sulfur-removal via direct desulfurization pathway, when the thermal stability of Pd was modified by a small amount of Ru addition or strong interaction with $MgAl_2O_4$ spinel support. The alumina-supported Pd6Ru1 and $MgAl_2O_4$-supported Pd1.5 catalysts displayed the same high DDS selectivity. Maintaining high Pd dispersions is crucial for the enhancement in DDS route. A study of the Pd size effect on HDS selectivities validated the hypothesis that the selectivity to DDS depends exclusively on Pd dispersions; however, adding a second metal, such as Ru or Ir, only promotes the sulfur extraction through HYD route, which consumes more hydrogen.

6.5. References

[1] United State Environmental Protection Agency-Diesel Fuel http://www.epa.gov/OTAQ/fuels/dieselfuels/index.htm.

[2] Sulphur in Gasoline Regulations-Air-Environment Canada, http://www. ec. gc. ca/energie-energy/default. asp?lang=En&n=BEA13229-1. (2014).

[3] Environment Canada-Air-Sulphur in Diesel Fuel Regulations, https://www. ec. gc. ca/energie-energy/default. asp?lang=En&n=7A8F92ED-1. (2014).

[4] G. Breysse, G. Diega-Mariadassou, S. Pessayre, C. Geantet, M. Vrinat, G. Perot, M. Lemaire, Catal. Today. 84 (2003) 129-138.

[5] R. Prins, in: G. Ertl, H. Knozinger, F. Schuth, J. Weitkamp (Ed.), Handbood of Heterogeneous Catalysis, 2nd ed., Wiley-VCH, 2008.

[6] A. Stanislaus, A. Marafi, M.S. Rana, Catal. Today. 153 (2010) 1-68.

[7] A. Röthlisberger, R. Prins, J. Catal. 235 (2005) 229-240.

[8] H. Guo, Y. Sun, R. Prins, Catal. Today. 130 (2008) 249-253.

[9] A. Niquille-Röthlisberger, R. Prins, J. Catal. 242 (2006) 207-216.

[10] D.D. Whitehurst, H. Farag, T. Nagamatsu, K. Sakanishi, I. Mochida, Catal. Today. 45 (1998) 299-305.

[11] W. Qian, Y. Yoda, Y. Hirai, A. Ishihara, T. Kabe, Appl. Catal. A. 184 (1999) 81-88.

[12] A. Ishihara, F. Dumeignil, J. Lee, K. Mitsuhashi, E.W. Qian, T. Kabe, Appl. Catal. A. 289 (2005) 163-173.

[13] R. Navarro, B. Pawelec, J.L.G. Fierro, P.T. Vasudevan, J.F. Cambra, P.L. Arias, Appl. Catal. A. 137 (1996) 269-286.

[14] H. Wang, E. Iglesia, ChemCatChem. 3 (2011) 1166-1175.

[15] H. Wang, E. Iglesia, J. Catal. 273 (2010) 245-256.

[16] J.L. Carter, G.B. McVicker, W. Weissman, W.S. Kmak, J.H. Sinfelt, Appl. Catal. 3 (1982) 327-346.

[17] S. Ted Oyama, H. Zhao, H.J. Freund, K. Asakura, R. Wlodarczyk, M. Sierka, J. Catal. 285 (2012) 1-5.

[18] Y. Xu, H. Shang, R. Zhao, C. Liu, Prepr. Pap. -Am. Chem. Soc. , Div. Fuel Chem. 49 (2004) 343-345.

[19] N. Toshima, in: Lyshevski, S.E., Contescu, C.I. and Putyera, K. (Eds.), Dekker Encyclopedia of Nanoscience and Nanotechnology, second ed., Taylor & Francis, 2009, pp. 2052-2063.

[20] R.W.J. Scott, A.K. Datye, R.M. Crooks, J. Am. Chem. Soc. 125 (2003) 3708-3709.

[21] W. Huang, J.N. Kuhn, C.K. Tsung, Y. Zhang, S.E. Habas, P. Yang, G.A. Somorjai, Nano Lett. 8(7) (2008) 2027-2034.

[22] Y. Wang, N. Toshima, J. Phys. Chem. B. 101 (1997) 5301-5306.

[23] T. Teranishi, M. Miyake, Chem. Mater. 10 (1998) 594-600.

[24] R.W.J. Scott, O.M. Wilson, R.M. Crooks, J. Phys. Chem. B. 109 (2005) 692-704.

[25] J. Shen, N. Semagina, ACS Catal. 4 (2014) 268-279.

[26] H. Ziaei-azad, C.X. Yin, J. Shen, Y. Hu, D. Karpuzov, N. Semagina, J. Catal. 300 (2013) 113-124.

[27] H. Ziaei-azad, N. Semagina, ChemCatChem. 6 (2014) 885-894.

[28] W.Z. Li, L. Kovarik, D. Mei, J. Liu, Y. Wang, C.H.F. Peden, Nat. Commun. 4:2481 (2013).

[29] J. Guo, H. Zhao, D. Chai, X. Zheng, Appl. Catal. A. 273 (2004) 75-82.

[30] M. Liu, J. Zhang, J. Liu, W.W. Yu, J. Catal. 278 (2011) 1-7.

[31] J. Shen, X. Yin, D. Karpuzov, N. Semagina, Catal. Sci. Technol. 3 (2013) 208-221.

[32] M. Jin, H. Liu, H. Zhang, Z. Xie, J. Liu, Y. Xia, Nano Res. 4 (2011) 83-91.

[33] H. Ziaei-azad, Bimetallic Ir-based Catalysts for Ring Opening and Hydrodesulfurization Reactions, University of Alberta, Edmonton, Canada, PhD thesis. (2015 unpublished).

[34] N. Semagina, X. Yin, J. Shen, K. Loganathan, US Patent. US20130248414 A1 (2013).

[35] J. Shen, Bimetallic catalysts for low-pressure ring opening, University of Alberta, Edmonton, Canada, MSc thesis. (2011).

[36] N. Semagina, L. Kiwi-Minsker, Catal. Rev. 51 (2009) 147-217.

[37] C.K. Tsung, J.N. Kuhn, W. Huang, C. Aliaga, L.I. Hung, G.A. Somorjai, P. Yang, J. Am. Chem. Soc. 131 (2009) 5816-5822.

[38] M. Zhao, R.M. Crooks, Angew. Chem. Int. Ed. 38 (1999) 364-366.

[39] J.C. Garcia-Martinez, R.W.J. Scott, R.M. Crooks, J. Am. Chem. Soc. 125 (2003) 11190-11191.

[40] Y. Xiong, J. Chen, B. Wiley, Y. Xia, J. Am. Chem. Soc. 127 (2005) 7332-7333.

[41] J. Shen, H. Ziaei-Azad, N. Semagina, J. Mol. Catal. A. 391 (2014) 36-40.

[42] R. Strobel, J.D. Grunwaldt, A. Camenzind, S.E. Pratsinis, A. Baiker, Catal. Lett. 104 (2005) 9-16.

[43] M.A. Vannice (Ed.), Kinetics of Catalytic Reactions, 1st ed., Springer, 2005.

[44] M. Boudart, Chem. Rev. 95 (1995) 661-666.

[45] R. Ma, N. Semagina, J. Phys. Chem. C. 114 (2010) 15417-15423.

[46] L.M. Baldyga, S.O. Blavo, C.H. Kuo, C.K. Tsung, J.N. Kuhn, ACS Catal. 2 (2012) 2626-2629.

Chapter 7. Conclusions and future work

7.1. Conclusions

The presented thesis focused on the preparation of bimetallic Pd-based nanocatalysts and the investigation of their catalyst performances in three catalytic applications: ring opening of benzocyclopentane, hydrodesulfurization of 4,6-dimethyl-dibenzothiophene and methane combustion. The hypothesis was that the precise size and structure controls of bimetallic nanoparticles can enhance the catalytic activity, selectivity and/or stability of the existing active catalysts and prepare new bimetallic combinations without using rare or expensive elements (such as Pt and Ir). The conclusions about the research works were summarized following the logical order of the important aspects mentioned in this thesis (but not the order of the chapters): **catalyst synthesis**, **importance of synthetic strategy**, **beneficial effects of structure and size controls in catalytic applications**, **efficient catalysis, and structure evolution during catalysis**.

The syntheses of Pt- and Ir- free nanoparticles using size- and structure-controlled synthetic strategies are discussed throughout Chapters 2−6 in this thesis. Chapter 2, 5 and 6 include a comprehensive study on the best-suited synthetic methods for Pd−Ru bimetallic systems with a wide Pd-to-Ru ratios (0.1−6.2 wt./wt.) in the presence of PVP. On the basis of successful nanoparticle size control (2−3 nm), it has been found that the synthetic methods allowed the fine-tuning of surface compositions of metals. The resulted Pd−Ru nanoparticles revealed random alloys (Chapter 2), Pd core−Ru shell (Chapters 2 and 5), and Ru-enriched surfaces (Chapters 2 and 6) relative to their bulk compositions. The obtained sizes and structures of the mono- and bimetallic nanoparticles with the selected reducing methods are consistent with their intrinsic bimetallic natures. The bimetallic formation and surface compositions were confirmed by a combination of characterization techniques: CO chemisorption, CO-TPD, CO-DRIFTS, TEM, thermal stability tests, and a chemical probe reaction (olefin hydrogenation with only Pd atoms active), as well as the applied catalytic reactions (selective hydrogenolysis).

Chapter 4 proved the dramatic importance of the synthetic strategy for bimetallic catalysts. When the bimetallic catalyst was prepared by traditional impregnation method, Ni precursor was consumed by alumina support to form inactive $NiAl_2O_4$ spinels during high temperature treatment at 550 °C, which did not improve the Pd activity in methane oxidation. Our study demonstrated that a successful preparation of modified Pd catalyst yielded PdO−NiO bimetallic catalyst, which lowered methane combustion temperature by 100 °C, as comparing to a monometallic Pd catalyst. The differences between two catalysts prepared by traditional impregnation-calcination and colloidal technique methods were characterized by TPR and supported by XPS. Although there was no evidence from XRD or XPS for intrinsic Pd−Ni alloy structure after calcination, the hypothetic conclusion is that the close contact of NiO with Pd/PdO provided oxygen during the Mars and van Krevelen redox reaction.

The success in nanocatalyst preparation is fundamentally and practically important. The monodispersed and ultra-fine nanostructures have become a powerful tool in the presented thesis in revealing the active sites for chemical reactions. The developed Pd−Ru catalysts with relatively low Pd-to-Ru ratios (0.1−1.7 wt./wt.) were tested in selective hydrogenolysis of indan at 350 °C and atmospheric pressure (Chapter 2). This reaction serves as a model reaction for fuel upgrading. Monometallic Ru is highly active, but shows successive dealkylation (high *o*-xylene formation). Unlike Ru, Pd is less active, but allows selective ring opening to 2-ehtyltoluene without undesired cracking. When the two metals are alloyed, the Ru4Pd1 catalyst with Ru-enriched surfaces showed a dramatic 3-fold increase in the selectivity to 2-ethyltoluene, with the same high single cleavage selectivity and low lights formation as Ir (the most selective ring opening metal).

The same Pd−Ru bimetallic combination discussed above, but with relatively high Pd-to-Ru ratio (6.2−0.9 wt./wt.), were tested in the HDS of 4,6-DMDBT at 300 °C and 50 bar (Chapter 6). This is a model reaction to upgrade fuels to meet ultra-low sulfur level (15 ppm). Similar beneficial effect was observed like in the case of low-pressure indan ring opening. Bimetallic Pd6Ru1 catalyst showed a 2-fold increase in the selectivity to direct desulfurization while maintaining the same activity as compared to monometallic Pd catalyst. The reason is that adding Ru to Pd improved Pd stability, and the appearance of relatively more edge and corner atoms in small particles promoted the direct desulfurization rate. Chapter 6 also explained the importance of size control using examples of bimetallic Pd−Ru and monometallic Pd catalysts in hydrodesulfurization. In order to get deep insights into the particle size effects on HDS selectivities, monometallic Pd nanoparticles in the range of 1.5−16 nm were prepared using different colloidal chemistry methods, including dendrimer-templating and PVP-stabilizing techniques for nanospheres of different sizes, as well as a shape-directing agent, KBr, for nanocube formation. Monometallic Pd tends to sintering severely during calcination (for polymer removal) and catalysis at even moderate temperatures (300−400 °C) (learned from Chapter 2). In order to preserve high dispersion of ultra-small Pd nanoparticles, Pd nanoparticles with original mean diameters of 1.5 nm were stabilized on synthetic $MgAl_2O_4$ spinel support. The nanoparticle sizes and morphologies were characterized by TEM. TPR revealed the difference in binding strengths between small and large Pd particles when interacting with hydrogen. By maintaining high Pd dispersions, same 2-fold increase in the selectivity to DDS was obtained for monometallic Pd catalyst as Pd catalysts prepared by Ru or Ir addition. The conclusion is that selectivity of DDS depends strongly on Pd dispersion; however, adding a second metal (Ru or Ir) only promotes the sulfur removal via HYD route. This finding avoids the use of rare or expensive elements on earth, and may pave the way toward an alternative route in catalyst design.

The accessibility of the active sites is always an issue in many applications when involving catalysts prepared by wet chemistry with the presence of stabilizers. Thus, capping agent removal is critical for efficient catalysis. An interesting result found in Chapter 2 was that the amount of CO adsorbed is not indicative of the most optimal polymer removal temperature for maximizing catalytic activity in indan ring opening. This motivated the study on the effect of PVP removal temperature on ring opening activity (Chapter 3). The fact is catalytic indan ring opening does not require PVP-free Ru or Ir surfaces, which was evidenced by a combination of chemical and physical characterization analyses, including XPS, CHN, TEM, CO chemisorption, CO-TPD and indan-TPD. The balance between "clean" catalyst surfaces and preserving high nanoparticle dispersion is essential for optimizing catalyst performances. Chapter 3 explained that for some metal-catalyzed reactions, high catalytic activities might be achieved with mild polymer removal temperature, and thus, complete removal of capping agents might be unnecessary.

A question that has been frequently asked is "does the bimetallic nanoparticle always maintain its original structure during catalysis?" The answer is no, because bimetallic nanoparticles may undergo structural evolution during high temperature treatment. By careful selection of colloidal chemistry techniques, Pd−Ru bimetallic nanoparticles with the same bulk metal ratio were synthesized with completely different surface structures. One resulted in particles with mixed surfaces (alloy); and another led to Pd core−Ru shell, which were characterized by a liquid-phase hydrogenation of an allylic alcohol at room temperature. Both catalysts displayed distinctively different behaviors in indan ring opening at 350 °C and atmospheric pressure. However, minor diffusion of Pd atoms to the bimetallic surfaces was seen in the Pd core−Ru shell sample by CO-DRIFTS. In methane combustion at temperature range of 200−550 °C, identical catalytic performance was observed in both types of catalysts. Later EXAFS confirmed the segregation of Pd atoms to the bimetallic nanoparticle shells for both catalysts with initially alloy and core−shell structures. Chapter 5 explained that for some reactions, like low-temperature hydrogenation and hydrogenolysis at mild conditions, the catalytic performances are beneficial from the structure-controlled synthesis. However, such synthetic strategy becomes unnecessary when structural evolution is driven by thermodynamics or induced by reaction absorbents.

7.2. Future work

The future work relating to the present thesis is summarized into two directions: catalyst design toward stable performance, and in situ catalyst characterization; the details are listed as following:

- To evaluate the promising catalysts in HDS of 4,6-DMDBT with the presence of inhibitors, such as H_2S and nitrogen-containing molecules.
- To improve the stability of Pd-based catalysts in combustion with the presence of water through alloying Pd with other metals or modifying the catalyst support.
- To design bimetallic systems using cheap and abundant metals (such as Fe and Cu).
- in situ reaction and characterization to understand the active sites and mechanism for catalytic methane oxidation over Pd-based catalysts. In situ analysis is not limited by methane oxidation but is believed to open another opportunity for rational catalyst design.

Bibliography

R. Abbasi, L. Wu, S.E. Wanke, R.E. Hayes, Chem. Eng. Res. Des. 90 (2012) 1930-1942.

S. Alayoglu, P. Zavalij, B. Eichhorn, Q. Wang, A.I. Frenkel, P. Chupas, ACS Nano. 3 (2009) 3127-3137.

C. Aliaga, J.Y. Park, Y. Yamada, H.S. Lee, C.K. Tsung, P. Yang, G.A. Somorjai, J. Phys. Chem. C. 113 (2009) 6150-6155.

D.M. Alonso, S.G. Wettstein, J.A. Dumesic, Chem. Soc. Rev. 41 (2012) 8075-8098.

R.M. Anderson, L. Zhang, J.A. Loussaert, A.I. Frenkel, G. Henkelman, R.M. Crooks, ACS Nano. 7 (2013) 9345-9353.

T. Ando, Y. Isobe, D. Sunohara, Y. Daisho, J. Kusaka, JSAE Review. 24 (2003) 33-40.

T. Balcha, J.R. Strobl, C. Fowler, P. Dash, R.W.J. Scott, ACS Catal. 1 (2011) 425-436.

L.M. Baldyga, S.O. Blavo, C.H. Kuo, C.K. Tsung, J.N. Kuhn, ACS Catal. 2 (2012) 2626-2629.

D.G. Blackmond, J.G. Goodwin, J.E. Lester, J. Catal. 78 (1982) 34-43.

S.O. Blavo, E. Qayyum, L.M. Baldyga, V.A. Castillo, M.D. Sanchez, K. Warrington, M.A. Barakat, J.N. Kuhn, Top. Catal. 56 (2013) 1835-1842.

H. Bonnemann, K.S. Nagabhushana, in: B. Corain, G. Schmid, N. Toshima (Ed.), **Metal Nanoclusters in Catalysis and Materials Science: The Issue of Size Control** , Elsevier B.V., Amsterdam, 2008, pp. 21-48.

Y. Borodko, S.M. Humphrey, T.D. Tilley, H. Frei, G.A. Somorjai, J. Phys. Chem. C. 111 (2007) 6288-6295.

Y. Borodko, S.E. Habas, M. Koebel, P. Yang, H. Frei, G.A. Somorjai, J. Phys. Chem. B. 110 (2006) 23052-23059.

M. Boudart, Chem. Rev. 95 (1995) 661-666.

G. Breysse, G. Diega-Mariadassou, S. Pessayre, C. Geantet, M. Vrinat, G. Perot, M. Lemaire, Catal. Today. 84 (2003) 129-138.

R. Burch, D.J. Crittle, M.J. Hayes, Catal. Today. 47 (1999) 229-234.

R. Burch, F.J. Urbano, P.K. Loader, Appl. Catal. A. 123 (1995) 173-184.

A. Cao, R. Lu, G. Veser, Phys. Chem. Chem. Phys. 12 (2010) 13499-13510.

A. Cao, G. Veser, Nat. Mater. 9 (2010) 75-81.

M. Cargnello, J.J. Delgado Jaen, J.C. Hernandez Garrido, K. Bakhmutsky, T. Montini, J.J. Calvino Gamez, R.J. Gorte, P. Fornasiero, Sci. 337 (2012) 713-717.

J.N. Carstens, S.C. Su, A.T. Bell, J. Catal. 176 (1998) 136-142.

J.L. Carter, G.B. McVicker, W. Weissman, W.S. Kmak, J.H. Sinfelt, Appl. Catal. 3 (1982) 327-346.

G. Centi, J. Mol. Catal. A. 173 (2001) 287-312.

J. Chen, X. Zhang, H. Arandiyan, Y. Peng, H. Chang, J. Li, Catal. Today. 201 (2013) 12-18.

Y. Chen, K.Y. Liew, J. Li, Mater. Lett. 62 (2008) 1018-1021.

Y.H. Chin, D.E. Resasco, Catal. 14 (1999) 1-39.

L.C. Ciacchi, W. Pompe, J. Phys. Chem. B. 107 (2003) 1755-1764.

B. Coq, F. Figueras, J. Mol. Catal. A. 173 (2001) 117-134.

G.G. Couto, J.J. Kleinb, W.H. Schreiner, D.H. Mosca, A.J.A. de Oliveira, A.J.G. Zarbina, J. Colloid Interface Sci. 311 (2007) 461-468.

M. Crespo-Quesada, A. Yarulin, M. Jin, Y. Xia, L. Kiwi-Minsker, J. Am. Chem. Soc. 133 (2011) 12787-12794.

C. Cui, L. Gan, M. Heggen, S. Rudi, P. Strasser, Nat. Mater. 12 (2013) 765-771.

P. Dash, T. Bond, C. Fowler, W. Hou, N. Coombs, R.W.J. Scott, J. Phys. Chem. C. 113 (2009) 12719-12730.

G. Del Angel, B. Coq, R. Dutartre, F. Figueras, J. Catal. 87 (1984) 27-35.

DieselNet-China-Emission Standards, https://www. dieselnet. com/standards/cn/. (2014).

DieselNet-China-Fuel regulations, https://www. dieselnet. com/standards/cn/fuel. php. (2013).

Directive 2009/30/EC of the European parliament and the council of 23 April 2009, Official Journal of the European Union. L 140/88.

A. Djeddi, I. Fechete, F. Garin, Appl. Catal. A. 413-414 (2012) 340-349.

A. Djeddi, I. Fechete, F. Garin, Catal. Commun. 17 (2012) 173-178.

P.T. Do, W.E. Alvarez, D.E. Resasco, J. Catal. 238 (2006) 477-488.

S. Dokjampa, T. Rirksomboon, S. Osuwan, S. Jongpatiwut, D.E. Resasco, Catal. Today. 123 (2007) 218-223.

S. Dokjampa, T. Rirksomboon, D.T.M. Phuong, D.E. Resasco, J. Mol. Catal. A. 274 (2007) 231-240.

L. D'Souza, S. Sampath, Langmuir. 16 (2000) 8510-8517.

H. Du, C. Fairbridge, H. Yang, Z. Ring, Appl. Catal. A. 294 (2005) 1-21.

O.G. Ellert, M.V. Tsodikov, S.A. Nikolaev, V.M. Novotortsev, Russ. Chem. Rev. 83 (2014) 718-732.

Environment Canada-Air-Sulphur in Diesel Fuel Regulations, https://www. ec. gc. ca/energie-energy/default. asp?lang=En&n=7A8F92ED-1. (2014).

H. Eriksona, A. Sarapuua, N. Alexeyevaa, K. Tammeveskia, J. Solla-Gullónb, J.M. Feliu, Electrochimica Acta. 59 (2012) 329-335.

G. Espinosa, G. Del Angel, J. Barbier, P. Bosch, V. Lara, D. Acosta, J. Mol. Catal. A. 164 (2000) 253-262.

R.J. Farrauto, Sci. 337 (2012) 659-660.

A.I. Frenkel, Chem. Soc. Rev. 41 (2012) 8163-8178.

K. Fujimoto, F.H. Ribeiro, M. Avalos-Borja, E. Iglesia, J. Catal. 179 (1998) 431-442.

J.C. Garcia-Martinez, R.W.J. Scott, R.M. Crooks, J. Am. Chem. Soc. 125 (2003) 11190-11191.

A.B. Gaspar, L.C. Dieguez, Appl. Catal. A. 201 (2000) 241-251.

F.G. Gault, Adv. Catal. 30 (1981) 1-95.

J. Ge, Q. Zhang, T. Zhang, Y. Yin, Angew. Chem. Int. Ed. 47 (2008) 8924-8928.

B. Gehl, A. Fromsdorf, V. Aleksandrovic, T. Schmidt, A. Pretorius, J.I. Flege, S. Bernstorff, A. Rosenauer, J. Falta, H. Weller, M. Baumer, Adv. Funct. Mater. 18 (2008) 2398-2410.

P. Gelin, M. Primet, Appl. Catal. B. 39 (2002) 1-37.

G. Groppi, C. Cristiani, L. Lietti, P. Forzatti, Stud. Surf. Sci. Catal. 130 (2000) 3801-3806.

J. Gu, Y.W. Zhang, F. Tao, Chem. Soc. Rev. 41 (2012) 8050-8065.

H. Guo, Y. Sun, R. Prins, Catal. Today. 130 (2008) 249-253.

J. Guo, H. Zhao, D. Chai, X. Zheng, Appl. Catal. A. 273 (2004) 75-82.

L. Guo, Q.J. Huang, X.Y. Li, S. Yang, Langmuir. 22 (2006) 7867-7872.

T.W. Hansen, A.T. Delariva, S.R. Challa, A.K. Datye, Acc. Chem. Res. 46 (2013) 1720-1730.

H. Hashemipour, M.E. Zadeh, R. Pourakbari, P. Rahimi, Int. J. Phy. Sci. 6 (2011) 4331-4336.

R.F. Hicks, H. Qi, M.L. Young, R.G. Lee, J. Catal. 122 (1990) 280-294.

D. Hu, J. Jiang, Journal of Environmental Protection. 4 (2013) 746-752.

R. Huang, Y.H. Wen, Z.Z. Zhu, S.G. Sun, J. Phys. Chem. C. 116 (2012) 8664-8671.

W. Huang, J.N. Kuhn, C.K. Tsung, Y. Zhang, S.E. Habas, P. Yang, G.A. Somorjai, Nano Lett. 8(7) (2008) 2027-2034.

A. Ishihara, F. Dumeignil, J. Lee, K. Mitsuhashi, E.W. Qian, T. Kabe, Appl. Catal. A. 289 (2005) 163-173.

T. Ishihara, H. Shigematsu, Y. Abe, Y. Takita, Chem. Lett. (1993) 407-410.

M. Jin, H. Liu, H. Zhang, Z. Xie, J. Liu, Y. Xia, Nano Res. 4 (2011) 83-91.

John C. Berg (Ed.), **An Introduction to INTERFACES & COLLOIDS: The Bridge to Nanoscience**, World Scientific Publishing Co. Pte. Ltd., Singapore, 2010.

S.H. Joo, J.Y. Park, J.R. Renzas, D.R. Butcher, W. Huang, G.A. Somorjai, Nano Lett. 10 (2010) 2709-2713.

S.H. Joo, J.Y. Park, C.K. Tsung, Y. Yamada, P. Yang, G.A. Somorjai, Nat. Mater. 8 (2009) 126-131.

M. Kangas, D. Kubicka, T. Salmi, D.Y. Murzin, Top. Catal. 53 (2010) 1172-1175.

M. Kappers, C. Dossi, R. Psaro, S. Recchia, A. Fusi, Catal. lett. 39 (1996) 183-189.

J.M. Khurana, K. Vij, catal. lett. 138 (2010) 104-110.

J.S. Kim, Soft Nanosci. Lett. 13 (2007) 566-570.

M.M. Koebel, L.C. Jones, G.A. Somorjai, J. Nanopart. Res. 10 (2008) 1063-1069.

D. Kubicka, M. Kangas, N. Kumar, M. Tiitta, M. Lindblad, D.Y. Murzin, Top. Catal. 53 (2010) 1438-1445.

D. Kubicka, N. Kumar, P. Maki-Arvela, M. Tiitta, V. Niemi, H. Karhu, T. Salmi, D.Y. Murzin, J. Catal. 227 (2004) 313-327.

R. Lanza, S.G. Jaras, P. Canu, Appl. Catal. A. 325 (2007) 57-67.

F. Le Normand, k. Kili, J.L. Schmitt, J. Catal. 139 (1993) 234-255.

S. Lecarpentier, v.G. Gestel J., K. Thomas, J.P. Gilson, M. Houalla, J. Catal. 254 (2008) 49-63.

M.J. Ledoux, O. Michaux, G. Agostini, J. Catal. 102 (1986) 275-288.

I. Lee, Q. Zhang, J. Ge, Y. Yin, F. Zaera, Nano Res. 4(1) (2011) 115-123.

W.Z. Li, L. Kovarik, D. Mei, J. Liu, Y. Wang, C.H.F. Peden, Nat. Commun. 4:2481 (2013).

Y. Li, E. Boone, M.A. El-Sayed, Langmuir. 18 (2002) 4921-4925.

B. Liu, M.D. Checkel, R.E. Hayes, Can. J. Chem. Eng. 79 (2001) 491-506.

F. Liu, D. Wechsler, P. Zhang, Chem. Phys. Lett. 461 (2008) 254-259.

H.B. Liu, U. Pal, J.A. Ascencio, J. Phys. Chem. C. 112 (2008) 19173-19177.

M. Liu, J. Zhang, J. Liu, W.W. Yu, J. Catal. 278 (2011) 1-7.

W. Liu, D. Guo, X. Xu, China Petroleum Processing and Petrochemical Technology. 14 (2012) 1-9.

Y. Liu, S. Wang, T. Sun, D. Gao, C. Zhang, S. Wang, Appl. Catal. B. 119-120 (2012) 321-328.

J. Lu, K.B. Low, Y. Lei, J.A. Libera, A. Nicholls, P.C. Stair, J.W. Elam, Nat. Commun. 5:3264 (2014).

P. Lu, N. Toshima, Bull. Chem. Soc. Jpn. 73 (2000) 751-758.

P. Lu, T. Teranishi, K. Asakura, M. Miyake, N. Toshima, J. Phys. Chem. B. 103 (1999) 9673-9682.

R. Ma, N. Semagina, J. Phys. Chem. C. 114 (2010) 15417-15423.

C. Marcilly, J. Catal. 216 (2003) 47-62.

O.M. Masloboishchikova, T.V. Vasina, E.G. Khelkovskaya-Sergeeva, L.M. Kustov, P. Zeuthen, Russ. Chem. Bull. 51 (2002) 249-254.

K.J.J. Mayrhofer, V. Juhart, K. Hartl, M. Hanzlik, M. Arenz, Angew. Chem. Int. Ed. 48 (2009) 3529-3531.

G.B. McVicker, M. Daage, M.S. Touvelle, C.W. Hudson, D.P. Klein, W.C.B. Jr., B.R. Cook, J.G. Chen, S. Hantzer, D.E.W. Vaughan, E.S. Ellis, O.C. Feeley, J. Catal. 210 (2002) 137-148.

D. Mei, V.M. Lebarbier, R. Rousseau, V.A. Glezakou, K.O. Albrecht, L. Kovarik, M. Flake, R.A. Dagle, ACS Catal. 3 (2013) 1133-1143.

P.J. Mitchell, R.M. Siewart, US Patent. US5131224 A (1992).

A. Molnar, A. Sarkany, M. Varga, J. Mol. Catal. A. 173 (2001) 185-221.

J. Monzo, M.T.M. Koper, P. Rodriguez, ChemPhysChem. 13 (2012) 709-715.

R. Moraes, K. Thomas, S. Thomas, S. van Donk, G. Grasso, J.P. Gilson, M. Houalla, J. Catal. 286 (2012) 62-77.

J.A. Moulijn, A.E. van Diepen, F. Kapteijn, Appl. Catal. A. 212 (2001) 3-16.

D.L. Mowery, M.S. Graboski, T.R. Ohno, R.L. McCormick, Appl. Catal. B. 21 (1999) 157-169.

C.A. Muller, M. Maciejewski, R.A. Koeppel, A. Baiker, Catal. Today. 47 (1999) 245-252.

C.A. Muller, M. Maciejewski, R.A. Koeppel, A. Baiker, J. Catal. 166 (1997) 36-43.

N. Naresh, F.G.S. Wasim, B.P. Ladewig, M. Neergat, J. Mater. Chem. A. 1 (2013) 8553-8559.

R. Navarro, B. Pawelec, J.L.G. Fierro, P.T. Vasudevan, J.F. Cambra, P.L. Arias, Appl. Catal. A. 137 (1996) 269-286.

J.W. Niemantsverdriet (Ed.), Spectroscopy in Catalysis, Wiley-vch, Weinheim, 2007.

A.U. Nilekar, S. Alayoglu, B. Eichhorn, M. Mavrikakis, J. Am. Chem. Soc. 132 (2010) 7418-7428.

A. Niquille-Röthlisberger, R. Prins, J. Catal. 242 (2006) 207-216.

U. Nylen, B. Pawelec, M. Boutonnet, J.L.G. Fierro, Appl. Catal. A. 299 (2006) 14-29.

U. Nylen, L. Sassu, S. Melis, S. Järås, M. Boutonnet, Appl. Catal. A. 299 (2006) 1-13.

Z. Paal, P. Tetenyi, Nat. 267 (1977) 234-236.

C. Pan, F. Dassenoy, M.J. Casanove, K. Philippot, C. Amiens, P. Lecante, A. Mosset, B. Chaudret, J. Phys. Chem. B. 103 (1999) 10098-10101.

X. Pan, Y. Zhang, Z. Miao, X. Yang, J. Energy Chem. 22 (2013) 610-616.

X. Pan, Y. Zhang, B. Zhang, Z. Miao, T. Wu, X. Yang, Chem. Res. Chin. Univ. 29 (2013) 952-955.

T. Paryjczak, J.M. Farbotko, K.W. Jozwiak, React. Kinet. Catal. Lett. 20 (1982) 227-231.

K. Persson, A. Ersson, K. Jansson, N. Iverlund, S. Jaras, J. Catal. 231 (2005) 139-150.

L. Piccolo, S. Nassreddine, M. Aouine, C. Ulhaq, C. Geantet, J. Catal. 292 (2012) 173-180.

A. Piegsa, W. Korth, F. Demir, A. Jess, catal. lett. 142 (2012) 531-540.

C. Poupin, L. Pirault-Roy, C. La Fontaine, L. Tóth, M. Chamam, A. Wootsch, Z. Paál, J. Catal. 272 (2010) 315-319.

G. Prieto, J. Zecevic, H. Friedrich, K.P. de Jong, P.E. de Jongh, Nat. Mater. 12 (2013) 34-39.

R. Prins, in: G. Ertl, H. Knozinger, F. Schuth, J. Weitkamp (Ed.), Handbood of Heterogeneous Catalysis, 2nd ed., Wiley-VCH, 2008.

W. Qian, Y. Yoda, Y. Hirai, A. Ishihara, T. Kabe, Appl. Catal. A. 184 (1999) 81-88.

F. Qin, J.W. Anderegg, C.J. Jenks, B. Gleeson, D.J. Sordelet, P.A. Thiel, Surf. Sci. 602 (2008) 205-215.

L. Qiu, F. Liu, L. Zhao, W. Yang, J. Yao, Langmuir. 22 (2006) 4480-4482.

B.A. Riguetto, J.M.C. Bueno, L. Petrov, C.M.P. Marques, Spectrochimica Acta Part A. 59 (2003) 2141-2150.

R.M. Rioux, H. Song, M. Grass, S. Habas, K. Niesz, J.D. Hoefelmeyer, P. Yang, G.A. Somorjai, Top. Catal. 39 (2006) 167-174.

D. Roth, P. Gelin, A. Kaddouri, E. Garbowski, M. Primet, E. Tena, Catal. Today. 112 (2006) 134-138.

A. Röthlisberger, R. Prins, J. Catal. 235 (2005) 229-240.

C.K. Ryu, M.W. Ryoo, I.S. Ryu, S.K. Kang, Catal. Today. 47 (1999) 141-147.

P. Samoila, M. Boutzeloit, C. Especel, F. Epron, P. Marécot, Appl. Catal. A. 369 (2009) 104-112.

P. Samoila, M. Boutzeloit, C. Especel, F. Epron, P. Marécot, J. Catal. 276 (2010) 237-248.

M. Sankar, N. Dimitratos, P.J. Miedziak, P.P. Wells, C.J. Kiely, G.J. Hutchings, Chem. Soc. Rev. 41 (2012) 8099-8139.

R.C. Santana, P.T. Do, M. Santikunaporn, W.E. Alvarez, J.D. Taylor, E.L. Sughrue, D.E. Resasco, Fuel. 85 (2006) 643-656.

M. Santikunaporn, J.E. Herrera, S. Jongpatiwut, D.E. Resasco, J. Catal. 228 (2004) 100-113.

T.K. Sau, C.J. Murphy, Am. Chem. Sci. J. 20 (2004) 6414-6420.

G. Schmid, in: B. Corain, G. Schmid, N. Toshima (Ed.), **Metal Nanoclusters in Catalysis and Materials Science: The Issue of Size Control** , Elsevier B.V., Amsterdam, 2008, pp. 3-20.

W.R. Schwartz, L.D. Pfefferle, J. Phys. Chem. 116 (2012) 8571-8578.

R.W.J. Scott, O.M. Wilson, R.M. Crooks, J. Phys. Chem. B. 109 (2005) 692-704.

R.W.J. Scott, O.M. Wilson, R.M. Crooks, Chem. Mater. 16 (2004) 5682-5688.

R.W.J. Scott, O.M. Wilson, S.H. Oh, E.A. Kenik, R.M. Crooks, J. Am. Chem. Soc. 136 (2004) 15583-15591.

R.W.J. Scott, A.K. Datye, R.M. Crooks, J. Am. Chem. Soc. 125 (2003) 3708-3709.

J. Sehested, A. Garlsson, T.V.W. Janssens, P.L. Hansen, A.K. Datye, J. Catal. 197 (2001) 200-209.

K. Sekizawa, K. Eguchi, H. Widjaja, M. Machida, H. Arai, Catal. Today. 28 (1996) 245-250.

N. Semagina, X. Yin, J. Shen, K. Loganathan, US Patent. US20130248414 A1 (2013).

N. Semagina, L. Kiwi-Minsker, Catal. Rev. 51 (2009) 147-217.

J. Shen, R.E. Hayes, X. Wu, N. Semagina, ACS Catal. 5 (2015) 2916-2920.

J. Shen, N. Semagina, ACS Catal. 4 (2014) 268-279.

J. Shen, H. Ziaei-Azad, N. Semagina, J. Mol. Catal. A. 391 (2014) 36-40.

J. Shen, X. Yin, D. Karpuzov, N. Semagina, Catal. Sci. Technol. 3 (2013) 208-221.

J. Shen, Bimetallic catalysts for low-pressure ring opening, University of Alberta, Edmonton, Canada, MSc thesis. (2011).

T. Shimizu, A.D. Abid, G. Poskrebyshev, H. Wang, J. Nabity, J. Engel, J. Yu, D. Wickham, B. Van Devener, S.L. Anderson, S. Williams, Comb. and Flame. 157 (2010) 421-435.

J.H. Sinfelt, US Patent. US3953368 A (1976).

A.K. Singh, Q. Xu, ChemCatChem. 5 (2013) 652-676.

C. Song, Catal. Today. 86 (2003) 211-263.

C. Song, A.D. Schmitz, Energy Fuels. 11 (1997) 656-661.

A. Stanislaus, A. Marafi, M.S. Rana, Catal. Today. 153 (2010) 1-68.

E.A. Stern, M. Newville, B. Ravel, Y. Yacoby, D. Haskel, Physica B. 208&209 (1995) 117-120.

R. Strobel, J.D. Grunwaldt, A. Camenzind, S.E. Pratsinis, A. Baiker, Catal. Lett. 104 (2005) 9-16.

Sulphur in Gasoline Regulations-Air-Environment Canada, http://www. ec. gc. ca/energie-energy/default. asp?lang=En&n=BEA13229-1. (2014).

D.N. Tafen, J.B. Miller, Ö.N. Doğan, J.P. Baltrus, P. Kondratyuk, Surf. Sci. 608 (2013) 61-66.

F. Tao, M.E. Grass, Y. Zhang, D.R. Butcher, J.R. Renzas, Z. Liu, J.Y. Chung, B.S. Mun, M. Salmeron, G.A. Somorjai, Sci. 322 (2008) 932-934.

S. Ted Oyama, H. Zhao, H.J. Freund, K. Asakura, R. Wlodarczyk, M. Sierka, J. Catal. 285 (2012) 1-5.

T. Teranishi, M. Miyake, Chem. Mater. 10 (1998) 594-600.

D. Teschner, L. Pirault-Roy, D. Naudb, M. Guérin, Z. Paál, Appl. Catal. A. 252 (2003) 421-426.

N. Toshima, in: Lyshevski, S.E., Contescu, C.I. and Putyera, K. (Eds.), Dekker Encyclopedia of Nanoscience and Nanotechnology, second ed., Taylor & Francis, 2009, pp. 2052-2063.

N. Toshima, H. Yan, Y. Shiraishi, in: B. Corain, G. Schmid, N. Toshima (Ed.), **Metal Nanoclusters in Catalysis and Materials Science: The Issue of Size Control**, Elsevier B.V., Amesterdam, 2008, pp. 49-75.

N. Toshima, T. Yonezawa, New J. Chem. 22 (1998) 1179-1201.

N. Toshima, P. Lu, Chem. Lett. 25 (1996) 729-730.

N. Toshima, T. Yonezawa, K. Kushihashi, J. Chem. Soc. , Faraday Trans. 89 (1993) 2537-2543.

TransportPolicy.net-EU: Fuels: Diesel and Gasoline, http://transportpolicy. net/index. php?title= EU:_Fuels:_Diesel_and_Gasoline. (2013).

C.K. Tsung, J.N. Kuhn, W. Huang, C. Aliaga, L.I. Hung, G.A. Somorjai, P. Yang, J. Am. Chem. Soc. 131 (2009) 5816-5822.

United State Environmental Protection Agency-Diesel Fuel http://www.epa.gov/OTAQ/fuels/ dieselfuels/index.htm.

B. Van Devener, S.L. Anderson, T. Shimizu, H. Wang, J. Nabity, J. Engel, J. Yu, D. Wickham, S. Williams, J. Phys. Chem. C. 113 (2009) 20632-20639.

R. van Hardeveld, F. Hartog, Surf. Sci. 15 (1969) 189-230.

M.A. Vannice (Ed.), Kinetics of Catalytic Reactions, 1st ed., Springer, 2005.

J.R. Vig, J. Vac. Sci. Technol. A. 3 (1985) 1027-1034.

H. Wang, E. Iglesia, ChemCatChem. 3 (2011) 1166-1175.

H. Wang, E. Iglesia, J. Catal. 273 (2010) 245-256.

H. Wang, H. Tang, J. He, Q. Wang, Mater. Res. Bull. 44 (2009) 1676-1680.

Y. Wang, N. Toshima, J. Phys. Chem. B. 101 (1997) 5301-5306.

Z.L. Wang, J.M. Petroski, T.C. Green, M.A. El-Sayed, J. Phys. Chem. B. 102 (1998) 6145-6151.

M.G. Weir, M.R. Knecht, A.I. Frenkel, R.M. Crooks, Langmuir. 26 (2010) 1137-1146.

D.D. Whitehurst, H. Farag, T. Nagamatsu, K. Sakanishi, I. Mochida, Catal. Today. 45 (1998) 299-305.

H. Widjaja, K. Sekizawa, K. Eguchi, H. Arai, Catal. Today. 47 (1999) 95-101.

H. Widjaja, K. Sekizawa, K. Eguchi, H. Arai, Catal. Today. 35 (1997) 197-202.

WWF-for a living planet-Living planet report (2008).

Y. Xia, Y. Xiong, B. Lim, S.E. Skrabalak, Angew. Chem. Int. Ed. 48 (2009) 60-103.

J. Xian, Q. Hua, Z. Jiang, Y. Ma, W. Huang, Langmuir. 28 (2012) 6736-6741.

Y. Xiong, J. Chen, B. Wiley, Y. Xia, J. Am. Chem. Soc. 127 (2005) 7332-7333.

F. Xu, L.J. Bauer, R.D. Gillespie, M.L. Bricker, S.A. Bradley, US Patent. WO2007041605 A1 (2007).

Y. Xu, H. Shang, R. Zhao, C. Liu, Prepr. Pap. -Am. Chem. Soc. , Div. Fuel Chem. 49 (2004) 343-345.

L. Yang, C. Shi, X. He, J. Cai, Appl. Catal. B. 38 (2002) 117-125.

H. Ye, R.W.J. Scott, R.M. Crooks, Langmuir. 20 (2004) 2915-2920.

B. Yue, R. Zhou, Y. Wang, X. Zheng, Appl. Surf. Sci. 252 (2006) 5820-5828.

I. Yuranov, P. Moeckli, E. Suvorova, P. Buffat, L. Kiwi-Minsker, A. Renken, J. Mol. Catal. A. 192 (2003) 239-251.

M. Zanolettia, D. Klvana, J. Kirchnerovaa, M. Perriera, C. Guya, Chem. Eng. Sci. 64 (2009) 945-954.

P. Zhang, Y. Hu, B. Li, Q. Zhang, C. Zhou, H. Yu, X. Zhang, L. Chen, B.W. Eichhorn, S. Zhou, ACS Catal. 5 (2015) 1335-1343.

M. Zhao, R.M. Crooks, Angew. Chem. Int. Ed. 38 (1999) 364-366.

Z.J. Zhao, L.V. Moskaleva, N. Rösch, ACS Catal. 3 (2013) 196-205.

B. Zhu, G. Thrimurthulu, L. Delannoy, C. Louis, C. Mottet, J. Creuze, B. Legrand, H. Guesmi, J. Catal. 308 (2013) 272-281.

H. Ziaei-azad, Bimetallic Ir-based Catalysts for Ring Opening and Hydrodesulfurization Reactions, University of Alberta, Edmonton, Canada, PhD thesis. (2015 unpublished).

H. Ziaei-azad, N. Semagina, ChemCatChem. 6 (2014) 885-894.

H. Ziaei-azad, C.X. Yin, J. Shen, Y. Hu, D. Karpuzov, N. Semagina, J. Catal. 300 (2013) 113-124.